

Universidade de São Paulo – USP
Escola de Engenharia de São Carlos – EESC
Departamento de Engenharia Mecânica – SEM

Willian Caruso de Brito

A Proposed Framework for Minimum Energy Consumption in
Electric VTOL Aircrafts

São Carlos

2020

Willian Caruso de Brito

A Proposed Framework for Minimum Energy Consumption in
Electric VTOL Aircrafts

Corrected Version

Dissertation presented to the
Graduation Program in Mechanical
Engineering at the Escola de Engenharia
de São Carlos, Universidade de São
Paulo, Brazil to obtain the degree of
Master in Science.

Concentration area: Aeronautics

Advisors:

Prof. Dr. Hernan Dario Ceron Muñoz

São Carlos

2020

AUTORIZO A REPRODUÇÃO TOTAL OU PARCIAL DESTE TRABALHO,
POR QUALQUER MEIO CONVENCIONAL OU ELETRÔNICO, PARA FINS
DE ESTUDO E PESQUISA, DESDE QUE CITADA A FONTE.

Ficha catalográfica elaborada pela Biblioteca Prof. Dr. Sérgio Rodrigues Fontes da
EESC/USP com os dados inseridos pelo(a) autor(a).

B862a Brito, Willian Caruso de
A proposed framework for minimum energy consumption
in electric VTOL aircrafts / Willian Caruso de Brito;
orientador Hernan Dario Ceron Muñoz. São Carlos, 2020.

Dissertação (Mestrado) - Programa de
Pós-Graduação em Engenharia Mecânica e Área de
Concentração em Aeronáutica -- Escola de Engenharia de
São Carlos da Universidade de São Paulo, 2020.

1. Optimization. 2. Electric Aircraft. 3.
Performance improvement. 4. Machine learning. 5.
Genetic algorithm. 6. eVTOL. 7. Energy consumption. 8.
Air taxi travel. I. Título.

FOLHA DE JULGAMENTO

Candidato: Bacharel **WILLIAN CARUSO DE BRITO**.

Título da dissertação: "Uma Proposta de Projeto para Minimização de Consumo de Energia em Aeronaves VTOL elétricas".

Data da defesa: 29/10/2020

Comissão Julgadora

Prof. Dr. **Hernan Dario Ceron Muñoz**
(Orientador)

(Escola de Engenharia de São Carlos/EESC-USP)

Resultado

APROVADO

Prof. Dr. **Roberto Gil Annes da Silva**

(Instituto Tecnológico de Aeronáutica/ITA)

APROVADO

Dr. **Celso Braga de Mendonça**

(Empresa Brasileira de Aeronautica/EMBRAER)

APROVADO

Coordenador do Programa de Pós-Graduação em Engenharia Mecânica:

Prof. Associado **Carlos de Marqui Junior**

Presidente da Comissão de Pós-Graduação:

Prof. Titular **Murilo Araujo Romero**

AGRADECIMENTOS

Este trabalho é um resultado de um conjunto de ideias levantadas por professores, amigos, colegas de trabalho e família, além de nossa própria determinação. Por isso, o nosso esforço se deu principalmente na agregação dos conhecimentos com que cada um contribuiu, para então compilarmos esta dissertação. Não se limitam aos nomes citados os nossos agradecimentos, e pedimos desculpas de antemão pela possível falta de citação de pessoas que também contribuíram de alguma maneira para este projeto.

Primeiramente, agradeço a todos os professores que me acolheram na Universidade, Dr. Carlos De Marqui Junior, Dr. Álvaro Martins Abdalla, e a meu orientador e amigo Hernan Dario Ceron Muñoz. À cooperação técnica e precisa dos professores Dr. Antonio Carlos Canale e Dr. Paulo Celso Greco Júnior.

A grandes amigos que foram essenciais durante todo o projeto, sem os quais este trabalho não teria se concretizado, Erlan Viera Cavalcanti Carvalho, Helder Luiz Costa de Oliveira e também aos queridos Rosângela e Lamartine Califani.

A todos os colegas de trabalho da Embraer S.A. e, em especial, Alexandre Filgueiras Cruz, com o qual tive o prazer de dividir as primeiras discussões técnicas e ideias do projeto e também a Sérgio Louzada Júnior pelo direcionamento na questão aerodinâmica do modelo de aeronave usado neste trabalho.

E, por fim, a todos os meus familiares que, como sempre, me apoiaram e incentivaram para o bom êxito desta dissertação.

RESUMO

BRITO, Willian Caruso de. **Uma Proposta de Projeto para Minimização de Consumo de Energia em Aeronaves VTOL Elétricas**. 2020. 198 p. Dissertação (Mestrado em Engenharia Mecânica) – Escola de Engenharia de São Carlos, Universidade de São Paulo, São Carlos, 2020.

A fim de melhorar o tempo de deslocamento para viagens de curta distância e aliviar o tráfego nas grandes cidades, uma nova categoria de transporte tem sido tema de pesquisas e de novos projetos. O mercado de transporte por táxi aéreo poderá mudar a forma como as pessoas vivem e se locomovem por meio do conceito de veículos com a habilidade de decolar e pousar verticalmente e que também promovem um transporte equivalente a um carro, com mobilidade dentro de grandes cidades e também entre cidades. O transporte aéreo civil de hoje permanece custoso e representa 2% das emissões de CO₂ provocadas pelo homem. Aproveitando esse cenário, muitas empresas desenvolveram seu próprio projeto de decolagem e aterrissagem vertical (VTOL), buscando atender conforto, segurança, baixo custo e tempo de voo de maneira sustentável. Portanto, o uso de fontes de energia renováveis, especialmente baterias e sistemas de propulsão totalmente elétricos, são a escolha mais comum para essas aeronaves que surgem neste mercado. No entanto, ainda é um desafio encontrar uma maneira viável de utilizar baterias e não mais os tradicionais combustíveis à base de petróleo. As baterias são pesadas e têm uma densidade energética menor que a da gasolina, diesel ou querosene. Portanto, apesar de todas as vantagens claras, as aeronaves totalmente elétricas (AEA) ainda possuem baixa autonomia e alto custo operacional, uma vez que as baterias devem ser recarregadas ou substituídas. Nesse sentido, esta dissertação trás uma maneira de otimizar o consumo de energia em uma missão típica de uma aeronave de táxi aéreo. O procedimento de aproximação e aterrissagem é objeto de um algoritmo de otimização e o programa final pode ser adaptado às fases de mudanças de nível e de decolagem também. Uma aeronave VTOL de empuxo rotativo genérica com dados de propulsão totalmente elétrica foi usada como modelo de dinâmica de voo para derivar as equações do movimento. Embora um projeto de empuxo rotativo seja usado como prova de conceito, é possível adequar a otimização para outros tipos de projetos conceituais, mesmo

para aqueles com motores independentes para as fases de voo pairado e de cruzeiro. Para uma determinada trajetória, o melhor conjunto de variáveis de controle são calculadas de forma a prover a resposta no tempo para o RPM dos rotores, ângulo de tração e deflexão de profundores da aeronave que, se seguidos, resultam na mínima energia elétrica consumida para essa trajetória. A metodologia inclui a modelagem de uma aeronave de empuxo rotativo elétrica, solução da dinâmica de voo para a trajetória usando uma rotina de compensação, elaboração de métodos de aprendizagem para classificação para endereçar restrições de segurança, conforto e projeto e criação de um algoritmo genético para otimização. Para os casos testados, a melhoria de desempenho variou de 10 a 20% comparada à energia média das possíveis soluções. Os resultados são altamente dependentes das restrições.

Palavras-chave: Otimização. Aeronaves Elétricas. Melhoria de desempenho. Aprendizado de máquina. Algoritmo Genético. eVTOL. Consumo de energia. Táxi aéreo. Desempenho de pouso. Empuxo rotativo. Baterias

ABSTRACT

BRITO, Willian Caruso de. **A Proposed Framework for Minimum Energy Consumption in Electric VTOL Aircrafts**. 2020. 198 p. Dissertation (Master's Degree in Mechanical Engineering) – Escola de Engenharia de São Carlos, Universidade de São Paulo, São Carlos, 2020.

In order to improve commute time for small distance trips and relieve large cities traffic, a new transport category has been the subject of research and new designs worldwide. The air taxi travel market promises to change the way people live and commute by using the concept of vehicles with the ability to take-off and land vertically and to provide passenger's transport equivalent to a car, with mobility within large cities and between cities. Today's civil air transport remains costly and accounts for 2% of the man-made CO₂ emissions. Taking advantage of this scenario, many companies have developed their own Vertical Take Off and Landing (VTOL) design, seeking to meet comfort, safety, low cost and flight time requirements in a sustainable way. Thus, the use of green power supplies, especially batteries, and fully electric power plants is the most common choice for these arising aircrafts. However, it is still a challenge finding a feasible way to handle with the use of batteries rather than conventional petroleum-based fuels. The batteries are heavy and have an energy density still below from those of gasoline, diesel or kerosene. Therefore, despite all the clear advantages, All Electric Aircrafts (AEA) still have low flight autonomy and high operational cost, since the batteries must be recharged or replaced. In this sense, this dissertation addresses a way to optimize the energy consumption in a typical mission of an aerial taxi aircraft. The approach and landing procedure was chosen to be the subject of an optimization algorithm, while final programming can be adapted for take-off and flight level changes as well. A generic VTOL tiltrotor aircraft with full electric power plant model was used to fit the derived dynamic equations of motion. Although a tiltrotor design is used as a proof of concept, it is possible to adapt the optimization to be applied for other design concepts, even those with independent motors for hover and cruise flight phases. For a given trajectory, the best set of control variables are calculated to provide time history response for aircraft's rotors RPM, thrust direction and elevators deflexion that, if followed, results in the minimum electric power consumption through that

landing path. Methodology includes modeling an electric tiltrotor design, solving the aircraft dynamics through the trajectory using a trim routine, elaborating learning methods for classification to address safety, comfort and design constraints and creating a genetic algorithm for optimization. For the tested cases, performance improvement ranged from 10 to 20% compared with mean energy of possible solutions. Results are highly dependent on the constraints.

Keywords: Optimization. Electric Aircraft. Performance improvement. Machine learning. Genetic algorithm. eVTOL. Energy consumption. Air taxi travel. Landing performance. Tiltrotor. Batteries.

LIST OF FIGURES

Figure 1 - Commute time as function of cities number of inhabitants.	37
Figure 2 - Electric powerplant.	41
Figure 3 - Battery technology development over the next years.	44
Figure 4 - Hover vertical lift efficiency as a function of disc loading.....	47
Figure 5 - Aurora Flight Sciences' eVTOL in prototype version.....	48
Figure 6 - Aurora Flight Sciences' eVTOL in its final version.	49
Figure 7 - Kitty Hawk "Cora" eVTOL.	49
Figure 8 - First design of EmbraerX, Embraer's eVTOL.....	50
Figure 9 - Actual design of EmbraerX, Embraer's eVTOL.	50
Figure 10 - AirisOne eVTOL design	51
Figure 11 - Airbus' A ³ Vahana.	51
Figure 12 - HopFlyt's Venturi.....	52
Figure 13 - Lilium's Eagle.	53
Figure 14 - DeLorean Aerospace's DR-7.	53
Figure 15 - Minimum fuel consumption with design and touchdown constraints according to Heinrich G. Jacob.	57
Figure 16 - Cruise optimal path according to Mark D.Ardema.	58
Figure 17 - Landing Profile.....	59
Figure 18 - General layout of NASA XV-15.	63
Figure 19 - XV-15 Geometry.	64
Figure 20 - Airstream passing through a propeller with control surface.	67
Figure 21 - Blade element velocity and relative wind diagram.....	69
Figure 22 - Wing in combination with a propeller at an angle of attack ϕ	71
Figure 23 - Earth-axis and body-axis coordinate systems.	73
Figure 24 - Definition of the wind-axis system - longitudinal motion.....	74
Figure 25 - Mast-axis coordinate system.	75
Figure 26 - Sign convention for the forces, moments, airspeeds and angular rates on body-axis reference frame.....	77
Figure 27 - Velocities in body and earth-axis systems.	83

Figure 28 - Relation between aerodynamic forces in different aircraft fixed reference frames.	83
Figure 29 - Roulette algorithm diagram.....	86
Figure 30 - One-point crossover.	87
Figure 31 - N-point crossover (example with $n = 3$).	87
Figure 32 - Uniform crossover.	88
Figure 33 - Weight and Balance envelope for the eVTOL tiltrotor model.....	95
Figure 34 - CG variation with pylon tilt.	97
Figure 35 - IYY variation with pylon tilt.	97
Figure 36 - Pipistrel Taurus G4.....	100
Figure 37 - Propeller induced velocity versus speed and thrust angle.....	103
Figure 38 - w_i/w_0 determination diagram.	104
Figure 39 - Propeller Thrust vs $VNTPP$ and RPM.....	106
Figure 40 - Thrust coefficient CT for 400, 600, 800 and 1000 rpm.	107
Figure 41 - Thrust coefficient CT for 1200, 1400, 1600 and 1800 and 2000 rpm.....	107
Figure 42 - Thrust coefficient CT for 2200, 2400, 2600 and 2800 and 3000 rpm.	108
Figure 43 - Propeller power versus speed and thrust angle.....	109
Figure 44 - P_i/P_0 determination diagram.	109
Figure 45- Power coefficient CP for 400, 600, 800 and 1000 rpm.....	110
Figure 46 - Power coefficient CP for 1200, 1400, 1600, 1800 and 2000 rpm.....	111
Figure 47 - Power coefficient CP for 2200, 2400, 2600, 2800 and 3000 rpm.	111
Figure 48 –Power and thrust coefficients for the static case.	112
Figure 49 – Wind-tunnel mounting.....	113
Figure 50 - Fuselage lift, drag and pitching moment coefficients vs AoA.	115
Figure 51 - Flow chart of wing aerodynamics affected by rotor wake.	118
Figure 52 - Procedures for calculating wing area and CP location.	120
Figure 53 - Wing lift polar for different thrust angles.....	122
Figure 54 – Wing drag vs wing angle of attack for different thrust angles.	122
Figure 55 - Wing wake deflection angle on Horizontal Tail.	126
Figure 56 – HT lift coefficient variation with α_{HT} and δE	129
Figure 57 – HT drag coefficient variation with α_{HT} for $\delta E = 0$	130
Figure 58 – A 5-fold CV. Validation folds are shown in beige. Training folds in blue.	137

Figure 59 - Schematic of genetic algorithm.....	139
Figure 60 - Accuracy of KNN classifier for maximum pitch rate as a function of neighbors number.	142
Figure 61 - Accuracy of RF classifier for maximum pitch rate as a function of selected predictors.....	143
Figure 62 – Accuracy and Kappa of RF classifier for maximum pitch rate as a function of the number of trees.....	143
Figure 63 – Comparison of ROC plots for maximum pitch rate.	144
Figure 64 - Accuracy of KNN classifier for maximum sink rate as a function of neighbors' number.	145
Figure 65 - Accuracy of RF classifier for maximum sink rate as a function of selected predictors.	145
Figure 66 – Accuracy and Kappa of RF classifier for maximum sink rate as a function of the number of trees.....	146
Figure 67 - Comparison of ROC plots for maximum sink rate.	146
Figure 68 - Energy expenditure sample distribution (all solutions of spreadsheet data).....	147
Figure 69 - Accuracy of GAM for the training and the test sets.....	148
Figure 70 – RMSE of RF for energy expenditure as a function of selected predictors.	149
Figure 71 – RMSE and MAE of RF for energy prediction.....	149
Figure 72 – Accuracy of RF for the training and the test sets.	150
Figure 73 – Importance of variables on RF regression model. “AT” means attitude and “t” time.	150
Figure 74 – Dependence of energy on the last time step.	151
Figure 75 – RMSE and MAE for GAM and RMSE.	152
Figure 76 – Boxplots of R-squared for GAM and RF regression.	152
Figure 77 – Genetic Algorithm evolution.	153
Figure 63 - Landing path (Altitude Zt vs Range $X(t)$).....	156
Figure 64 - Speed horizontal component – earth-axis $X(t)$ time history.....	157
Figure 65 – Vertical speed – earth-axis $Z(t)$ time history.	157
Figure 66 - Horizontal acceleration – earth-axis $X(t)$ time history.	157
Figure 67 - Vertical acceleration time history.	158
Figure 68 – Pitch attitude time history.....	158

Figure 69 – Pitch Rate time history.....	158
Figure 70 – Pitch Acceleration time history.....	159
Figure 71 – Elevator deflexion time history.....	160
Figure 72 – Rotors RPM time history.....	160
Figure 73 – Thrust angle time history.....	161
Figure 74 - Moment of inertia <i>IYY</i> change due to pylon tilt.....	162
Figure 75 - CG displacement due to pylon tilt.....	163
Figure 76 – Total thrust time history.....	164
Figure 77 – Batteries power time history.....	165
Figure 78 – Fuselage AoA time history.....	166
Figure 79 – Fuselage lift time history.....	166
Figure 80 – Fuselage drag time history.....	167
Figure 81 – Fuselage pitching moment time history.....	167
Figure 82 – Wing AoA time history.....	169
Figure 83 – Wing lift time history.....	169
Figure 84 – Wing drag time history.....	169
Figure 85 – Wing pitching moment time history.....	170
Figure 86 – HT AoA time history.....	171
Figure 87 – HT lift time history.....	171
Figure 88 – HT drag time history.....	172
Figure 89 – HT pitching moment time history.....	172
Figure 90 – VT drag time history.....	172
Figure 91 – NLG drag time history.....	174
Figure 92 – MLG drag time history.....	174

LIST OF TABLES

Table 1 - Commute time.....	38
Table 2 - Limits assumed to the optimization algorithm.	60
Table 3 - Variables index).	77
Table 4 - Safety, Comfort and Design Constraints.....	82
Table 5 - Scale factors for incompressible flow assumption.....	93
Table 6 - Typical power loading by design.....	98
Table 7 - Trajectory data for positions, speeds, accelerations and attitude.....	155
Table 8 - Control variables after optimization.	159
Table 9 - Inertia and balance data for I_{YY} and CG displacement.....	162
Table 10 - Thrust, power and energy.	164
Table 11 - Fuselage AoA, lift, drag and pitching moment.	165
Table 12 - Wing-Pylon AoA, lift, drag and pitching moment.....	168
Table 13 - Empennage AoA, lift and Drag.....	171
Table 15 - Landing gears drag;.....	173
<hr/>	
Table A- 1 - Rotor wake on horizontal stabilizer, wiR/Hwi , $\varphi = 90 \text{ deg}$	185
Table A- 2 - Rotor wake on horizontal stabilizer, wiR/Hwi , $\varphi = 75 \text{ deg}$	185
Table A- 3 - Rotor wake on horizontal stabilizer, wiR/Hwi , $\varphi = 60 \text{ deg}$	186
Table A- 4 – Fuselage aerodynamics with angle of attack αF	186
Table A- 5 - Wing drag coefficient.	187
Table A- 6 - Wing lift coefficient.....	188
Table A- 7 - Wing pitching moment coefficient.	189
Table A- 8 - Wing-pylon interference drag coefficient.....	189
Table A- 9 - Wing Wake Deflection Angle on HT with αW and φ	189
Table A- 10 - Dynamic pressure ratio at the HT, rotors ON, $\varphi = 90 \text{ deg}$	190
Table A- 11 - Dynamic pressure ratio at the HT, rotors ON, $\varphi = 75 \text{ deg}$	190
Table A- 12 - Dynamic pressure ratio at the HT, rotors ON, $\varphi = 60 \text{ deg}$	191
Table A- 13 - Dynamic pressure ratio at the HT, rotors ON, $\varphi = 30 \text{ deg}$	191
Table A- 14 - Dynamic pressure ratio at the HT, rotors ON, $\varphi = 0 \text{ deg}$	192
Table A- 15 - Elevator Effectiveness factor XKE	192

Table A- 16 - MN effect on $\delta\varepsilon W/H / \delta\alpha WFS$	192
Table A- 17 - HT lift coeficiente $CLHT$	193
Table A- 18 - HT drag coefficient $CDHT$	194
Table A- 19- Sidewash Factor $(1 - \delta\sigma/\delta\beta F)$	195
Table A- 20 - Rotor sidewash factor $K\beta R$	195

LIST OF ABBREVIATIONS

MEA	More Electric Aircrafts
AEA	All Electric Aircrafts
DEP	Distributed Electric Propulsion
CNT	National Transport Confederation
VTOL	Vertical Take-off and Landing
MEE	More Electric Engines
ESG	Engine Starter Generator
APU	Auxiliary Power Unit
PMAD	Power Management And Distribution
STOL	Short Take Off and Landing
RPM	Rotations Per Minute
eVTOL	electrical Vertical Take-off and Landing
ACARE	Advisory Council for Aviation Research and innovation in Europe
LFAP	Long Final Approach Path
IP	Interception Point
TLP	Thrust Lifting Point
VDP	Vertical Descent Point
SFAP	Short Final Approach Path
HAP	Hovering Approach Path
LP	Landing Point
EOM	Equations Of Motion

CG Center of Gravity

VBA Visual Basic for Applications

GA Genetic Algorithms

AC Aerodynamic Center

CP Center of Pressure

AoA Angle of Attack

HT Horizontal Tail

VT Vertical Tail

NLG Nose Landing Gears

MLG Main Landing Gears

NOMAD Nonlinear Mesh Adaptive Direct Search

MADS Mesh Adaptive Direct Search

KNN K-Nearest Neighbors

QDA Quadratic Discriminant Analysis

CART Classification and Regression Tree

RF Random Forest

ROC Receiver Operating Characteristic

AUC Area Under the Curve

MSE Mean Squared Error

CV Cross Validation

GAM Generalized Additive Model

RMSE Root Mean Square Error

FMS Flight Management System

LIST OF SYMBOLS

γ	FLIGHT PATH ANGLE
μ	HEADING/BEARING ANGLE
ΔE_T	TOTAL ENERGY EXPENDITURE ALONG SFAP
$\Delta \varepsilon$	TIME STEP
P_{BATT}	BATTERIES POWER FOR EACH STEP
\dot{M}_{FLOW}	AIR MASS PER UNIT TIME
ρ	AIR DENSITY
A	PROPELLER DISC AREA
V_0	AIRFLOW NON-DISTURBED VELOCITY (PROPELLER INFLOW)
w_i	PROPELLER UNIFORM INDUCED VELOCITY (VELOCITY INCREMENT ADDED BY THE PROPELLER)
T	THRUST GENERATED BY THE PROPELLER
P_i	POWER INPUT (POWER THAT THE PROPELLER SUPPLIES TO THE FLUID)
P_{USE}	POWER OUTPUT (USEFUL POWER)
η_i	IDEAL EFFICIENCY
C_{MT}	THRUST COEFFICIENT FOR INDUCED VELOCITY
α_g	GEOMETRIC ANGLE OF ATTACK
α_i	ACTUAL ANGLE OF ATTACK OF BLADE ELEMENT
r_i	RADIUS FROM HUB TO BLADE ELEMENT
d_i	DIAMETER FROM ONE BLADE ELEMENT TO THE OPPOSITE ONE
Ω	ROTATION SPEED IN RAD/S OR DEGREES/S
n	ROTATION SPEED IN REV/S

J	ADVANCE RATIO
Q	PROPELLER TORQUE
C_T	THRUST COEFFICIENT
C_Q	TORQUE COEFFICIENT
C_P	POWER COEFFICIENT
φ	THRUST ANGLE
V'_0	RESULTANT VELOCITY IN THE PROPELLER
w_0	INDUCED VELOCITY IN THE PROPELLER (STATIC CONDITION)
P_0	POWER PRODUCED BY THE PROPELLER (STATIC CONDITION)
θ	EULER ANGLE WITH RESPECT TO PITCH MOTION, OR THE PITCH ANGLE
α_F	FUSELAGE ANGLE OF ATTACK
m	AIRCRAFT MASS
\vec{F}_R	RESULTANT FORCE
\vec{M}_R	RESULTANT MOMENT
\vec{L}	ANGULAR MOMENTUM
U	HORIZONTAL SPEED ALONG BODY X-AXIS
V	LATERAL SPEED ALONG BODY Y-AXIS
W	VERTICAL SPEED ALONG BODY Z-AXIS
P	ANGULAR RATE OVER BODY X-AXIS
Q	ANGULAR RATE OVER BODY Y-AXIS
R	ANGULAR RATE OVER BODY Z-AXIS
C	AERODYNAMIC FORCE ALONG BODY X-AXIS
Y	AERODYNAMIC FORCE ALONG BODY Y-AXIS

N	AERODYNAMIC FORCE ALONG BODY Z-AXIS
T_X	PROPULSIVE FORCE ALONG BODY X-AXIS
T_Y	PROPULSIVE FORCE ALONG BODY Y-AXIS
T_Z	PROPULSIVE FORCE ALONG BODY Z-AXIS
W_X	GRAVITATIONAL FORCE ALONG BODY X-AXIS
W_Y	GRAVITATIONAL FORCE ALONG BODY Y-AXIS
W_Z	GRAVITATIONAL FORCE ALONG BODY Z-AXIS
L	ROLLING MOMENT
M	PITCHING MOMENT
N	YAWING MOMENT
I_{XX}	MOMENT OF INERTIA ABOUT BODY X-AXIS
I_{YY}	MOMENT OF INERTIA ABOUT BODY Y-AXIS
I_{ZZ}	MOMENT OF INERTIA ABOUT BODY Z-AXIS
I_{YZ}	PRODUCT OF INERTIA WITH RESPECT TO Y AND Z BODY AXES
I_{XZ}	PRODUCT OF INERTIA WITH RESPECT TO X AND Z BODY AXES
I_{XY}	PRODUCT OF INERTIA WITH RESPECT TO X AND Y BODY AXES
F_X	COMPONENT OF RESULTANT FORCE IN BODY X-AXIS DIRECTION
F_Y	COMPONENT OF RESULTANT FORCE IN BODY Y-AXIS DIRECTION
F_Z	COMPONENT OF RESULTANT FORCE IN BODY Z-AXIS DIRECTION
M_X	COMPONENT OF RESULTANT MOMENTUM OVER BODY X-AXIS
M_Y	COMPONENT OF RESULTANT MOMENTUM OVER BODY Y-AXIS
M_Z	COMPONENT OF RESULTANT MOMENTUM OVER BODY Z-AXIS
\dot{U}	HORIZONTAL ACCELERATION ALONG BODY X-AXIS

\dot{V}	LATERAL ACCELERATION ALONG BODY X-AXIS
\dot{W}	VERTICAL ACCELERATION ALONG BODY X-AXIS
\dot{P}	ANGULAR ACCELERATION OVER BODY X-AXIS
\dot{Q}	ANGULAR ACCELERATION OVER BODY Y-AXIS
\dot{R}	ANGULAR ACCELERATION OVER BODY Z-AXIS
\dot{X}	HORIZONTAL SPEED ALONG EARTH X'-AXIS
\dot{Y}	LATERAL SPEED ALONG EARTH Y'-AXIS
\dot{Z}	VERTICAL SPEED ALONG EARTH Z'-AXIS, OR THE RATE OF SINK
g	GRAVITATIONAL ACCELERATION
W_{GROSS}	AIRCRAFT GROSS WEIGHT
M_{TCG}	PROPULSIVE PITCHING MOMENT WITH RESPECT TO THE CG
M_{ACG}	AERODYNAMIC PITCHING MOMENT WITH RESPECT TO THE CG
$\dot{\theta}$	PITCH RATE
$\ddot{\theta}$	PITCH ACCELERATION
ϕ	EULER ANGLE WITH RESPECT TO ROLLING MOTION, OR THE BANK ANGLE
$\dot{\phi}$	ROLL RATE
ψ	EULER ANGLE WITH RESPECT TO YAWING MOTION, OR THE YAW ANGLE
$\dot{\psi}$	YAW RATE
N_F	FUSELAGE AERODYNAMIC FORCE ALONG BODY X-AXIS
N_{iW}	WING AERODYNAMIC FORCE ON THE PORTION IN THE ROTOR WAKE ALONG BODY X-AXIS
N_{WFS}	WING AERODYNAMIC FORCE ON THE PORTION IN THE FREESTREAM ALONG BODY X-AXIS

N_{PYL}	PYLON AERODYNAMIC FORCE ALONG BODY X-AXIS
N_{SD}	SPINNER DRAG AERODYNAMIC FORCE ALONG BODY X-AXIS
N_{HT}	HORIZONTAL STABILIZER AERODYNAMIC FORCE ALONG BODY X-AXIS
N_{VT}	VERTICAL STABILIZER AERODYNAMIC FORCE ALONG BODY X-AXIS
N_{MG}	MAIN LANDING GEAR AERODYNAMIC FORCE ALONG BODY X-AXIS
N_{NG}	NOSE LANDING GEAR AERODYNAMIC FORCE ALONG BODY X-AXIS
C_F	FUSELAGE AERODYNAMIC FORCE ALONG BODY Z-AXIS
C_{iW}	WING AERODYNAMIC FORCE ON THE PORTION IN THE ROTOR WAKE ALONG BODY Z-AXIS
C_{WFS}	WING AERODYNAMIC FORCE ON THE PORTION IN THE FREESTREAM ALONG BODY Z-AXIS
C_{PYL}	PYLON AERODYNAMIC FORCE ALONG BODY Z-AXIS
C_{SD}	SPINNER DRAG AERODYNAMIC FORCE ALONG BODY Z-AXIS
C_{HT}	HORIZONTAL STABILIZER AERODYNAMIC FORCE ALONG BODY Z-AXIS
C_{VT}	VERTICAL STABILIZER AERODYNAMIC FORCE ALONG BODY Z-AXIS
C_{MG}	MAIN LANDING GEAR AERODYNAMIC FORCE ALONG BODY Z-AXIS
C_{NG}	NOSE LANDING GEAR AERODYNAMIC FORCE ALONG BODY Z-AXIS
M_F	FUSELAGE PITCHING MOMENT WITH RESPECT TO THE CG, BODY-AXIS
$M_F _{CA}$	FUSELAGE PITCHING MOMENT WITH RESPECT TO THE FUSELAGE AERODYNAMIC CENTER
M_{iW}	WING PITCHING MOMENT ON THE PORTION IN THE ROTOR WAKE WITH RESPECT TO THE CG, BODY-AXIS
M_{WFS}	WING PITCHING MOMENT ON THE PORTION IN THE FREESTREAM WITH RESPECT TO THE CG, BODY-AXIS

$M_{W CA}$	WING PITCHING MOMENT WITH RESPECT TO THE WING AERODYNAMIC CENTER
M_{PYL}	PYLON PITCHING MOMENT WITH RESPECT TO THE CG, BODY-AXIS
M_{SD}	SPINNER DRAG PITCHING MOMENT WITH RESPECT TO THE CG, BODY-AXIS
M_{HT}	HORIZONTAL STABILIZER PITCHING MOMENT WITH RESPECT TO THE CG, BODY-AXIS
$M_{HT CA}$	HORIZONTAL STABILIZER PITCHING MOMENT WITH RESPECT TO THE HT AERODYNAMIC CENTER
M_{VT}	VERTICAL STABILIZER PITCHING MOMENT WITH RESPECT TO THE CG, BODY-AXIS
M_{MG}	MAIN LANDING GEAR PITCHING MOMENT WITH RESPECT TO THE CG, BODY-AXIS
M_{NG}	NOSE LANDING GEAR PITCHING MOMENT WITH RESPECT TO THE CG, BODY-AXIS
X	HORIZONTAL POSITION, EARTH X' -AXIS
Z	VERTICAL POSITION, EARTH Z' -AXIS
V_T	TRUE AIRSPEED
X_0	HORIZONTAL POSITION AT THRUST LIFTING POINT, EARTH X' -AXIS
Z_0	VERTICAL POSITION AT THRUST LIFTING POINT, EARTH Z' -AXIS
V_{T0}	TRUE AIRSPEED AT THRUST LIFTING POINT
γ_0	FLIGHT PATH ANGLE AT THRUST LIFTING POINT
\ddot{X}	HORIZONTAL ACCELERATION, EARTH X' -AXIS
X_F	HORIZONTAL POSITION AT VERTICAL DESCENT POINT, EARTH-AXIS
Z_F	VERTICAL POSITION AT VERTICAL DESCENT POINT, EARTH-AXIS

\dot{X}_F	HORIZONTAL SPEED AT VERTICAL DESCENT POINT, EARTH-AXIS
\ddot{X}_F	HORIZONTAL ACCELERATION AT VERTICAL DESCENT POINT, EARTH-AXIS
θ_F	PITCH ANGLE AT VERTICAL DESCENT POINT
$\dot{\theta}_F$	PITCH RATE AT VERTICAL DESCENT POINT
$\ddot{\theta}_F$	PITCH ACCELERATION AT VERTICAL DESCENT POINT
$\dot{\phi}$	THRUST ANGLE RATE
θ_{MAX}	MAXIMUM PITCH ANGLE (LIMIT DURING SHORT FINAL APPROACH PATH)
θ_{MIN}	MINIMUM PITCH ANGLE (LIMIT DURING SHORT FINAL APPROACH PATH)
$\dot{\delta}_E$	ELEVATOR DEFLEXION RATE
\ddot{Z}	VERTICAL ACCELERATION FUNCTION IN RESPECT TO TIME, EARTH Z'-AXIS
U_{HM}	HORIZONTAL SPEED ALONG MAST X _M -AXIS
W_{HM}	VERTICAL SPEED ALONG MAST Z _M -AXIS
ϕ_M	LATERAL MAST TILT ANGLE
p_C	CROSSOVER PROBABILITY
p_M	MUTATION PROBABILITY
x_{LB}	LOWER BOUND OF THE POPULATION DOMAIN
y_{UB}	UPPER BOUND OF THE POPULATION DOMAIN
a_{n-j}	($n - j$)-th BIT (GENE) OF AN INDIVIDUAL'S BIT STRING
a	ELLIPSE SEMI-MAJOR AXIS
b	ELLIPSE SEMI-MINOR AXIS
n	RATIO OF MODEL-TO-FULL-SCALE DIMENSIONS

σ	RATIO OF AIR DENSITY
ν	KINEMATIC VISCOSITY
ν_0	KINEMATIC VISCOSITY AT SEA LEVEL
X_{CG}	CG FUSELAGE STATION DISPLACEMENT DUE TO PYLON TILT
Z_{CG}	CG WATER LINE DISPLACEMENT DUE TO PYLON TILT
W_{PYL}	WEIGHT OF BOTH PYLONS FOR A TILT ROTOR
FS_{NAC}	FUSELAGE STATION OF ENGINE NACELLE SHAFT PIVOT POINT FOR A TILT ROTOR
FS_{PYL}	FUSELAGE STATION OF PYLON CENTER OF GRAVITY FOR A TILT ROTOR
WL_{NAC}	WATER LINE OF PYLON CENTER OF GRAVITY FOR A TILT ROTOR
WL_{PYL}	WATER LINE OF ENGINE NACELLE SHAFT PIVOT POINT FOR A TILT ROTOR
$FS_{CG} _{\varphi=90^\circ}$	CG FUSELAGE STATION OF HOVER MODE
$WL_{CG} _{\varphi=90^\circ}$	CG WATER LINE OF HOVER MODE
$I_{YY} _{\varphi=90^\circ}$	HOVER MODE PITCHING MOMENT OF INERTIA, BODY-AXIS
K_I	PITCH INERTIA COEFFICIENT FOR VARYING INERTIA WITH THRUST ANGLE FOR A TILT ROTOR
ϕ_M	LATERAL MAST TILT ANGLE
$\phi_M _{\varphi=90^\circ}$	HOVER MODE LATERAL MAST TILT ANGLE
$\phi_M _{\varphi=0^\circ}$	AIRPLANE MODE LATERAL MAST TILT ANGLE
P_{ENG}	ENGINE POWER
R_W	ROTOR WAKE CONTRACTION RATIO
R_D	DISC RADIUS
l_M	MAST LENGTH

$w_i _{R/W}$	INDUCED VELOCITY AT THE WING IN MAST-AXIS DUE TO THE ROTOR
K_{0-4}	CONSTANTS IN THE ROTOR/WING WAKE EQUATION
μ	IN-PLANE VELOCITY RATIO AT THE MAST-AXIS $X_M Y_M$ PLANE
λ_i	INFLOW RATIO
w_i	UNIFORM INDUCED VELOCITY, MAST-AXIS
V_{TPP}	TRUE AIRSPEED TANGENTIAL COMPONENT TO THE MAST-AXIS $X_M Y_M$ PLANE
V_{NTPP}	TRUE AIRSPEED NORMAL COMPONENT TO THE MAST-AXIS $X_M Y_M$ PLANE
Ω'	ROTOR SPEED CORRECTED FOR ANGULAR RATE
V_{HM}	LATERAL SPEED ALONG MAST Y_M -AXIS
$U_i _{R/W}^B$	INDUCED X-VELOCITY AT THE WING IN BODY-AXIS DUE TO THE ROTOR
$W_i _{R/W}^B$	INDUCED Z-VELOCITY AT THE WING IN BODY-AXIS DUE TO THE ROTOR
$w_i _{R/H}$	INDUCED MAST Z_M -AXIS ROTOR WAKE VELOCITY ON THE HORIZONTAL STABILIZER
$\frac{w_i _{R/H}}{w_i}$	RATIO OF THE INDUCED MAST Z_M -AXIS ROTOR WAKE VELOCITY ON THE HORIZONTAL STABILIZER TO THE UNIFORM INDUCED VELOCITY AT THE ROTOR
S_{HT}	HORIZONTAL STABILIZER AREA
FS_{HT}	FUSELAGE STATION OF THE HORIZONTAL STABILIZER CENTER OF PRESSURE
$U_i _{R/H}^B$	INDUCED X-VELOCITY AT THE HORIZONTAL STABILIZER IN BODY-AXIS DUE TO THE ROTOR
$W_i _{R/H}^B$	INDUCED Z-VELOCITY AT THE HORIZONTAL STABILIZER IN BODY-AXIS DUE TO THE ROTOR

RPM	ROTATION SPEED IN RPM
$\eta_{POWCONT}$	POWER CONTROLLER EFFICIENCY
η_{MOTOR}	MOTOR EFFICIENCY
$\eta_{GEARBOX}$	GEARBOX EFFICIENCY
q_F	FUSELAGE DYNAMIC PRESSURE
L_F	FUSELAGE LIFT (WIND-AXIS)
L_α	FUSELAGE LIFT VARIATION WITH ANGLE OF ATTACK α_F
L_{BFO}	FUSELAGE LIFT AT $\alpha_F = 0 \text{ deg}$
L_{LANG}	EXTRA FUSELAGE LIFT
D_F	FUSELAGE DRAG (WIND-AXIS)
D_α	FUSELAGE DRAG VARIATION WITH ANGLE OF ATTACK α_F
D_{BFO}	FUSELAGE DRAG AT $\alpha_F = 0 \text{ deg}$
D_{LANG}	EXTRA FUSELAGE DRAG
L_F	FUSELAGE LIFT (WIND-AXIS)
L_α	FUSELAGE LIFT VARIATION WITH ANGLE OF ATTACK α_F
L_{BFO}	FUSELAGE LIFT AT $\alpha_F = 0 \text{ deg}$
M_F	FUSELAGE PITCHING MOMENT (WIND-AXIS)
M_α	FUSELAGE PITCHING MOMENT VARIATION WITH ANGLE OF ATTACK α_F
M_{BFO}	FUSELAGE PITCHING MOMENT AT $\alpha_F = 0 \text{ deg}$
S_{iW}	WING AREA AFFECTED BY ROTOR WAKE
X_{iW}	LONGITUDINAL CENTER OF PRESSURE LOCATION OF THE WING AFFECTED BY ROTOR WAKE
G, SG, CG, ZL	AUXILIARY PARAMETERS IN ROTOR WAKE DETERMINATION
U_W	AUXILIARY X-VELOCITY AT THE WING IN ROTOR WAKE DETERMINATION

W_W	AUXILIARY Z-VELOCITY AT THE WING IN ROTOR WAKE DETERMINATION
U_W	AUXILIARY X-VELOCITY AT THE WING IN ROTOR WAKE DETERMINATION
W_W	AUXILIARY Z-VELOCITY AT THE WING IN ROTOR WAKE DETERMINATION
K_{RW}	ROTOR SKEW ANGLE VELOCITY DISTRIBUTION FACTOR
X_{TE}	TRAILING EDGE DISTANCE IN CENTER OF PRESSURE LOCATION EQUATION
c_w	WING CHORD
FS_{WTE}	FUSELAGE STATION OF WING TRAILING EDGE
$X_{LE}, R_{WX}, R_{WY}, F_{RW}, S_{DEL}, C_{DEL}$	INITIALIZATION PARAMETERS IN PROCEDURES FOR CALCULATING X_{iW} AND S_{iW}
V_{TiW}	TRUE AIRSPEED IN WING ROTOR WAKE REGION
α_{iW}	ANGLE OF ATTACK OF THE WING PORTION IMMERSED IN ROTOR WAKE
L_{iW}	LIFT OF THE WING PORTION IMMERSED IN ROTOR WAKE
S_{iWT}	TOTAL WING AREA AFFECTED BY ROTOR WAKE
K_{FW}	ROTOR DOWNWASH/WING FOR FLAP EFFECTS FACTOR
D_{iW}	DRAG OF THE WING PORTION IMMERSED IN ROTOR WAKE
q_{iW}	DYNAMIC PRESSURE IN WING ROTOR WAKE REGION
K_{FW0}	CONSTANT IN ROTOR DOWNWASH/WING EQUATION FOR FLAP EFFECTS
K_{FWDF}	SLOPE IN ROTOR DOWNWASH/WING EQUATION FOR FLAP EFFECTS
δ_F	FLAPS POSITION
M_N	MACH NUMBER
S_{WFS}	WING AREA UPON THE FREESTREAM FLOW
S_W	TOTAL WING AREA

q_{WFS}	DYNAMIC PRESSURE IN WING REGION UPON FREESTREAM FLOW
α_{WFS}	ANGLE OF ATTACK OF THE WING IN FREESTREAM FLOW
$K_{XRW}, X_{RW}, X_{RW0}, X_{RW1}, X_{RW2}$	CONSTANTS IN ROTOR DOWNWASH/WING EQUATION
X_{RW}	ROTOR DOWNWASH/WING EFFECT ON AOA OF THE WING IN FREESTREAM FLOW
L_{WFS}	LIFT OF THE WING PORTION UPON THE FREESTREAM FLOW FIELD
C_{LW}	WING LIFT COEFFICIENT
D_{WFS}	DRAG OF THE WING PORTION UPON THE FREESTREAM FLOW FIELD
C_{DW}	WING DRAG COEFFICIENT
C_{LW}	WING PITCHING MOMENT COEFFICIENT
D_{PYLN}	DRAG BETWEEN THE INTERACTION OF THE TILT ROTOR PYLON AND WING
D_{PYINT}	WING-PYLON INTERFERENCE DRAG COEFFICIENT
U_{MSP}	HORIZONTAL SPEED ON SPINNER ALONG MAST X_M -AXIS
W_{MSP}	VERTICAL SPEED ON SPINNER ALONG MAST Z_M -AXIS
V_{TSP}	TRUE AIRSPEED UPON SPINNERS REGION
q_{SP}	DYNAMIC PRESSURE UPON SPINNERS REGION
α_{MSP}	ANGLE OF ATTACK UPON SPINNERS REGION, MAST AXIS
SD/q	COEFFICIENT TO ACCOUNT FOR THRUST ANGLE VARIATION IN SPINNERS DRAG EQUATION
$\epsilon_{W/H}$	WING WAKE DEFLECTION ANGLE AT THE HORIZONTAL STABILIZER
$\epsilon_{W/HOGE}$	WING WAKE DEFLECTION ANGLE AT THE HORIZONTAL STABILIZER

U_{HT}	HORIZONTAL SPEED ALONG BODY X-AXIS ON HT
W_{HT}	VERTICAL SPEED ALONG BODY Z-AXIS ON HT
V_{HT}	TRUE AIRSPEED MAGNITUDE ON HT
FS_{HT}	FUSELAGE STATION OF HT CENTER OF PRESSURE
WL_{HT}	WATER LINE OF HT CENTER OF PRESSURE
q_{HT}	DYNAMIC PRESSURE UPON HT REGION
K_{HNU}	HT LOSS MULTIPLIER OF DYNAMIC PRESSURE
η_{HS}	DYNAMIC PRESSURE RATIO AT THE HT
α_{HT}	HT ANGLE OF ATTACK
i_{HT}	HT INCIDENCE ANGLE
δ_E	ELEVATOR DEFLECTION ANGLE
τ_E	ELEVATOR EFFECTIVENESS
X_{KE}	ELEVATOR EFFECTIVENESS FACTOR
D_{KE}	ELEVATOR EFFECTIVENESS REDUCTION FACTOR FOR $ \delta_E > 15 \text{ deg}$
L_{HT}	HT LIFT
C_{LHT}	HT LIFT COEFFICIENT
C_{LHT_w}	HT STABILITY DERIVATIVE WITH VERTICAL ACCELERATION \dot{W} OR THE WING/BODY DAMPING
D_{HT}	HT DRAG
C_{DHT}	HT DRAG COEFFICIENT
C_{MHT}	HT PITCHING MOMENT COEFFICIENT
S_{HT}	HT REFERENCE AREA
c_{HT}	HT CHORD
D_{WB}	COEFFICIENT IN THE WING/BODY DAMPING EQUATION

$PCPM$	MACH NUMBER EFFECT ON THE $(\partial\epsilon_{W/H}/\partial\alpha_{WFS})$ DERIVATIVE
FS_{VT}	FUSELAGE STATION OF VT CENTER OF PRESSURE
WL_{VT}	WATER LINE OF VT CENTER OF PRESSURE
q_{VT}	DYNAMIC PRESSURE UPON VT REGION
K_{VNU}	VT LOSS MULTIPLIER OF DYNAMIC PRESSURE
η_{VS}	DYNAMIC PRESSURE RATIO AT THE VT
α_{VT}	VT ANGLE OF ATTACK
D_{VT}	VT DRAG
C_{DVT}	VT DRAG COEFFICIENT
S_{VT}	VT REFERENCE AREA
δ_R	RUDDER DEFLECTION ANGLE
$K_{\beta R}$	ROTOR SIDEWASH FACTOR ON DYNAMIC PRESSURE
$(1 - \frac{\partial\sigma}{\partial\beta_F})$	VT SIDEWASH FACTOR

SUMMARY

1	INTRODUCTION	37
1.1	SIDE EFFECT OF MODERN TRAFFIC USAGE	37
1.2	AIR TAXI TRAVEL MARKET.....	39
1.3	MODERN APPROACHES – TOWARD ALL ELECTRIC AIRCRAFTS	40
1.3.1	<i>Trends in Modern Aeronautics.....</i>	<i>40</i>
1.3.2	<i>Electric Propulsion Systems.....</i>	<i>41</i>
1.3.3	<i>Electric VTOL Aircrafts</i>	<i>45</i>
1.3.4	<i>Current Designs.....</i>	<i>48</i>
1.4	A MORE GREEN AVIATION.....	53
2	LITERATURE REVIEW.....	57
3	PROBLEM DESCRIPTION.....	59
3.1	LANDING PROFILE	59
3.2	OPTIMIZATION SCOPE	60
3.3	AIR TAXI TRAVEL MODEL	62
3.3.1	<i>The Concept.....</i>	<i>62</i>
3.3.2	<i>NASA XV-15 Project</i>	<i>63</i>
3.4	PROPELLERS	66
3.4.1	<i>Introduction</i>	<i>66</i>
3.4.2	<i>Momentum Theory.....</i>	<i>67</i>
3.4.3	<i>Blade Element Theory.....</i>	<i>69</i>
3.4.4	<i>Vecored Propellers.....</i>	<i>71</i>
3.5	AXIS DEFINITIONS.....	73
3.6	SHORT FINAL APPROACH PATH DEFINITIONS.....	75
3.6.1	<i>Introduction</i>	<i>75</i>
3.6.2	<i>Governing Equations.....</i>	<i>76</i>
3.6.3	<i>Conditions Described</i>	<i>81</i>
3.7	AXIS TRANSFORMATIONS.....	82
3.8	GENETIC ALGORITHMS.....	84
3.8.1	<i>Introduction</i>	<i>84</i>
3.8.2	<i>Representation</i>	<i>85</i>
3.8.3	<i>Fitness Function</i>	<i>85</i>
3.8.4	<i>Parent Selection.....</i>	<i>86</i>
3.8.5	<i>Crossover</i>	<i>87</i>
3.8.6	<i>Mutation.....</i>	<i>88</i>
3.8.7	<i>Stopping Criterion.....</i>	<i>88</i>

4	METHODOLOGY	89
4.1	INTRODUCTION	89
4.2	AIRCRAFT STATE PARAMETERS.....	90
4.3	INERTIA AND BALANCE	92
4.3.1	<i>Scaling</i>	92
4.3.2	<i>Modeling</i>	94
4.4	POWERPLANT	98
4.4.1	<i>Motors Selection</i>	98
4.4.2	<i>Rotor Aerodynamics</i>	100
4.4.3	<i>Engine Deck</i>	105
4.4.4	<i>Energy Expenditure</i>	108
4.5	FUSELAGE AERODYNAMICS	112
4.5.1	<i>Aerodynamics Structure</i>	112
4.5.2	<i>Equations</i>	113
4.6	WING-PYLON AERODYNAMICS.....	115
4.6.1	<i>Introduction</i>	115
4.6.2	<i>Wings Aerodynamics Affected by Rotor Wake</i>	115
4.6.3	<i>Wings Aerodynamics in Freestream</i>	123
4.6.4	<i>Wing-Pylon Interference Drag</i>	124
4.6.5	<i>Spinner Drag</i>	124
4.6.6	<i>Wing Wake Deflection on Horizontal Tail</i>	125
4.7	EMPENNAGE AERODYNAMICS	126
4.7.1	<i>Horizontal Stabilizer</i>	127
4.7.2	<i>Vertical Stabilizer</i>	130
4.8	LANDING GEARS AERODYNAMICS	132
4.8.1	<i>Nose Landing Gears</i>	132
4.8.2	<i>Main Landing Gears</i>	132
4.9	EQUATIONS OF MOTION	133
4.9.1	<i>Forces Summation</i>	133
4.9.2	<i>Pitching Moment Summation</i>	133
4.9.3	<i>Trim Routine</i>	134
4.9.4	<i>Controls Validation</i>	134
4.9.5	<i>Spreadsheet Data</i>	135
4.10	MACHINE LEARNING	135
4.10.1	<i>Methods for Classification</i>	136
4.10.2	<i>Methods for Regression</i>	137
4.10.3	<i>GA Algorithm for Optimization</i>	138

5	RESULTS.....	141
5.1	CODES IN R	141
5.1.1	<i>Introduction</i>	141
5.1.2	<i>Classification</i>	141
5.1.3	<i>Regression</i>	147
5.1.4	<i>Optimization</i>	153
5.2	EVOL MODEL BUILT.....	154
5.2.1	<i>Aircraft State Parameters</i>	155
5.2.2	<i>Control Variables</i>	159
5.2.3	<i>Inertia and Balance</i>	161
5.2.4	<i>Powerplant</i>	163
5.2.5	<i>Fuselage Aerodynamics</i>	165
5.2.6	<i>Wing-Pylon Aerodynamics</i>	167
5.2.7	<i>Empennage Aerodynamics</i>	170
5.2.8	<i>Landing Gears Aerodynamics</i>	173
6	CONCLUSION	175
	REFERENCES.....	177
	APPENDIX A – INPUT DATA FOR TILTROTOR MODEL	185
	APPENDIX B – VBA CODES FOR TILTROTOR MODEL	197

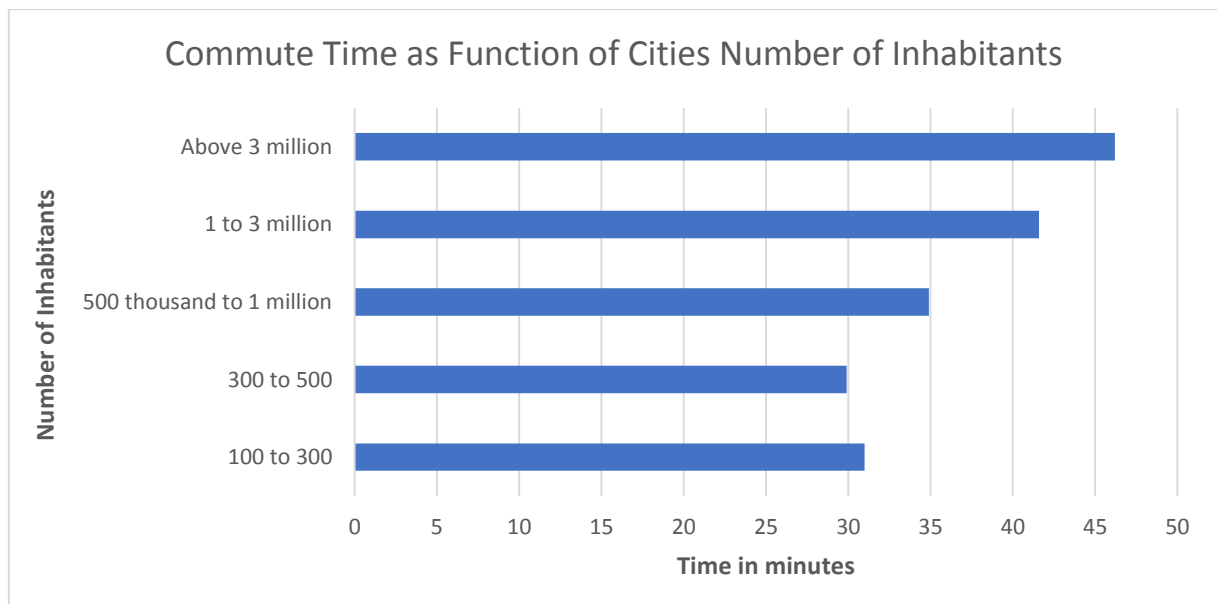
1 INTRODUCTION

1.1 SIDE EFFECT OF MODERN TRAFFIC USAGE

For many people worldwide, commuting to work for general reasons takes a good deal of daily time. In São Paulo, residents spend around 45 minutes commuting to work every day (PEREIRA; SCHWANEN, 2015) and 22% of all the commute time is spent in congestion (COOKSON; PISHUE, 2017).

The Brazilian National Transport Confederation (CNT) carried out a research related to the mobility of the urban population in Brazil and involved several small, medium and large cities. The survey covered more than 35 cities with a population greater than 100,000 inhabitants. Several mobility goals were raised, among them commuting for work, study and medical treatment. Also, the average time was raised based on the number of cities surveyed inhabitants. These results are shown in Table 1.

Figure 1 - Commute time as function of cities number of inhabitants.



Source:(NTU, 2017, p. 36).

While for cities between 100 and 300 thousand inhabitants the average mobility time is 31 min, for cities above 3 million inhabitants this time exceeds 45 min. More information is presented in Figure 1.

Table 1 - Commute time.

1 – Work	
Distance	Mean
Distance from home to work	13.3 km
Time	Mean
Time from home to work	37.7 min
2 – Study	
Distance	Mean
Distance from home to school	9.5 km
Time	Mean
Time from home to study activity	33.4 min
3 – Healthy Treatment	
Distance	Mean
Distance from home to healthy treatment local	11.4 km
Time	Mean
Time from home to healthy treatment local	38.7 min
4 – Other Reasons	
Distance	Mean
Distance of the route	8.4 km
Time	Mean
Time of the route	31.1 min

Source: (NTU, 2017, p. 36).

It was found that the high rate of congestion and the large fleet of vehicles contribute significantly to this increase in mobility time (NTU, 2017). This results in less quality of living for both work and personal time. In addition, it affects directly the people stress levels. According to the American Journal of Preventative Medicine, for instance, those who commute more than 10 miles a day are at increased odds of elevated blood pressure (HOEHNER et al., 2012)

Apart from higher commute time and worse health conditions, the consistent growth in cars and aircrafts circulation leads to heavier air pollution as long as fossil fuel burn prevails and higher transportation costs, due to oil's price growth (HEPPERLE, 2012).

1.2 AIR TAXI TRAVEL MARKET

In 2011, NASA launched a competition to improve passenger aircraft efficiency and stimulate the usage of greener energies sources, such as "bio fuels, hybrid electric propulsion systems, and fully electric" (BACCHINI; CESTINO, 2019). The top 2 awards were to fully electric aircrafts, demonstrating the great potential of this field and further growth of industry interest in green energy powered aircrafts (BACCHINI; CESTINO, 2019).

In order to incorporate these advantages improving commute time for small distance trips and relieving large cities traffic, a new transport category has been the subject of research and new designs worldwide. It is about vehicles with the ability to both take-off and land vertically and to provide passenger's transport equivalent to a car, with mobility within large cities and between cities. Vertical Take Off and Landing (VTOL) aircrafts would be able to departure from and land on small locations such as empty terrains, parking lots and others spaces naturally available in urban areas, sparing extra expenditures with infrastructure, roads and personnel.

VTOL aircrafts promise to change the way people live and commute, promoting a fast, clean and low noise of transportation (BACCHINI; CESTINO, 2019). Since it does not require a runaway, a VTOL will not be subjected to traffic jam or longer delays in case of an accident or any other kind of single interruption on traffic. Also, the area needed for its takeoff and landing site is minimal (some models require 15m x 15m) (LILIUM, 2019), enabling its implementation in urban areas with negligible impact. Initial propositions suggest using the roof of building as "vertstops" (a single VTOL pad) (UBER, 2016).

As this market strengthens, there will be more vertstops distributed throughout the city, easing traffic and making this transportation more readily accessible around town. This causes a positive feedback, increasing demand for VTOLs travels and lowering price, especially considering ridesharing uses (UBER, 2016).

In this scenario, on-demand transportation is easily achieved, lowering waiting time for users and idle time for VTOLs, and can be integrated with ridesharing land vehicles services, optimizing comfort, time, viability and pre-planned and pre-booked flights throughout the day. According to Bacchini & Cestino (2019, p. 1).

[...] most of the major aircraft companies are directly developing their own electric VTOL or have subsidiaries doing it. More than 130 electric VTOL concepts have been proposed and venture capitalists have invested more than 1 billion dollars into promising eVTOL startups.

A subsequent scenario foresees investments to build some “vertports” (multiples VTOL pads together) in strategic areas with high demand, allowing parking and maintenance space for several vehicles at the same time, lowering waiting time for users and having more infrastructure available (UBER, 2016). It also enables another market, similar for land vehicles: electric fuel stations – to recharge batteries or rent modulated fully charged ones.

1.3 MODERN APPROACHES – TOWARD ALL ELECTRIC AIRCRAFTS

1.3.1 Trends in Modern Aeronautics

Nowadays, novel ways of generating, distributing, and using power onboard are examined at the aircraft level. Hybrid or bleed-less air conditioning systems, "More Electric Engines" (MEEs) or fully electric engines, fuel cells, variable frequency generators, complex embedded digital systems and distributed system architectures are just a few of the technologies vying for space on forthcoming aircraft; the concept is known as "More Electric Aircraft" (MEA). In addition, it is believed that electrical systems have far more potential for future improvement than conventional architecture regarding energy efficiency. It is also expected that electrical subsystems lead to maintenance costs reduction, weight reductions, fewer unexpected delays due to failures in the power systems and production improvement (ROSETO et al., 2007).

According to Tariq “The last five decades have seen a tremendous growth in the power demand of aircraft, owing to more electric load in MEA” (TARIQ, 2017, p. 93), which has four cores:

1. Internal Engine Starter Generator (ESG) set;

2. Auxiliary Power Unit (APU), which includes battery and super/ultra-capacitor;
3. Flight controls actuation;
4. Fault tolerant Power Management and Distribution (PMAD) and motor drive system.

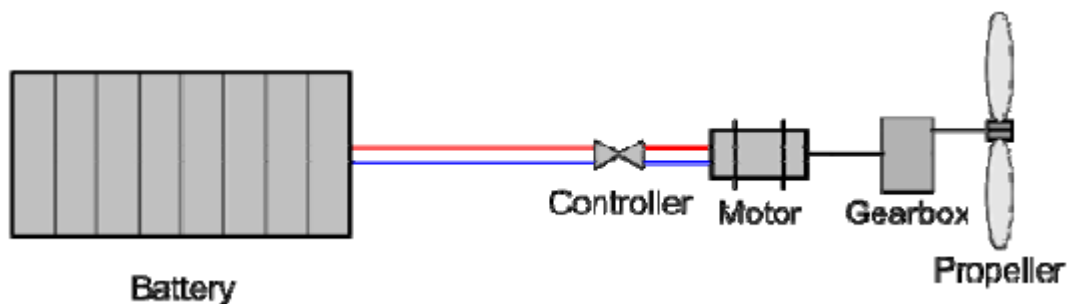
The latest advances in electric aircraft technologies has turned the ridesharing industry attention to new aircraft designs both for electric propulsive power and aircraft subsystems, which can significantly reduce pollution and noise generation, having major impact on flights near urban areas.

Nowadays, there is a numerous variety of designs and architectures of MEA VTOLs, including hover bikes, multicopters, flying cars, tilt-wing airplanes and others, each with its own benefits and drawbacks, better suiting different kinds of missions.

1.3.2 Electric Propulsion Systems

In aircraft propulsion design, an electric powerplant consists of a set of basic elements, namely: energy storage and conversion system, electric power controller, electric motor, gearbox and propeller. The two types of energy storage and conversion most commonly used are batteries and fuel cells. However, other power supplies, such as solar cells and beamed energy are also possible in electric propulsion systems.

Figure 2 - Electric powerplant.



Source: Adapted from Hepperle (2012, p. 6)

An electric powerplant is a common alternative to conventional propulsion, especially in the air taxi travel market growing concepts. A clear advantage of electric motors over the ones powered by petroleum-based fuels lies in the fact that they are a green option. Internal combustion engines emit pollutants. Today's civil air transport accounts for 2% of the man-

made CO₂ emissions (BOGLIETTI et al., 2009). Also, fuel burning releases lead on atmosphere. According to Tariq (2017, p. 93): “A resolution has been made by the Advisory Council for Aviation Research and innovation in Europe (ACARE) that by 2020, aircraft should be made cleaner and quieter”. Moreover, those fuels are naturally prone to fire and even explosion, which makes the conventional systems less safe options than the electric ones.

On the other hand, petroleum-based fuels, especially the processed aviation ones, have a great advantage over battery systems: high energy density. In other words, they weigh little for the power they can supply over a given amount of time. In addition, a fuel-based propulsion system is, in general, expected to be lighter than an equivalent electric system, including the power supply. Furthermore, conventional fuel powered airplanes usually take less time to refuel than the electric takes to recharge the batteries, not to mention that electric propulsion system currently costs more and the motors often need reduction drives due to their high rpm. Regarding noise generation, electric propulsion systems tend to be quieter.

It is worth mentioning that the aforementioned “green” aspect of electric propulsion does not take into account the fact that, if such systems use batteries as power supplies, the materials used in batteries are often harmful to the environment. If this fact is considered, the electric approach may be not as “green” as expected.

Despite recent technological innovations, the limited life and power of batteries remain two great drawbacks of battery-powered electric motors. Due to these factors and the others already mentioned, electric propulsion is still not on par with conventional one, especially in aspects of speed, range, endurance, and payload for a given weight or cost airplane. However, as technology evolves electric airplanes will become more common.

1.3.2.1 Electric Motors

An electric motor converts electrical into mechanical energy. Motors operate by means of the electromagnetic principle. In the motor, the current pass through a circuit loop that is immersed in a magnetic field. In addition, when an electric current flows through a coil, it generates a magnetic field. When two magnets get close together the North and the South poles attract, whereas the same poles will repel each other. These magnetic fields are combined generating magnetic forces in a rotor, and consequently, a torque to rotate it. There are two main different motor types used in model aircraft: (1) brushed and (2) brushless. From

another aspect, electric motors are divided into two groups: (1) direct current (DC) motors and (2) alternative current (AC) motors. The electric motor of an aircraft with an electric propulsion system is usually of DC type.

Electric motors can be deliberately overpowered for a short time, generating as much as three times their normal power (25% boost is more typical). This can be used for takeoff or emergency and allows the use of a motor with lower rated power than its equivalent gasoline engine.

Aircraft configuration flexibility is enhanced with electric power. The motors are small and can be placed away from the power supply. It has been proposed to use electrical generators and motors to remotely locate the fans of turbofan engines out to the wings or another location deemed beneficial. Some electric aircraft designs use multiple small motors on the wing and feed them varying amounts of power to attain yaw control. In fact, electric “bedpost” helicopters have no controls at all other than varying the power to their four motors. Some of the emerging VTOLs in the air taxi travel market work this way.

There can be weight savings for the propeller. When it comes to piston engines, the propeller is used as a flywheel to help damp out the intermittent internal cylinders. This might require additional mass in the blades that is avoided with an electric design. Also, if a propeller extension shaft is used with a reciprocating engine, it will be prone to torsional excitation and will need, as a result, to be manufactured stronger and heavier. Not so with the electric one. Furthermore, the electric engine is smaller and it might be possible to move it closer to the propeller, eliminating the need for a shaft in the first place. At the least, its smaller size should benefit cowling.

For battery power systems there are additional problems. There are temperature effects on the batteries. They lose power with great temperature variations. Attempting to use the power at too high of a rate causes resistance losses, which reduces the total energy available. There is some risk of explosion and fire for certain battery types.

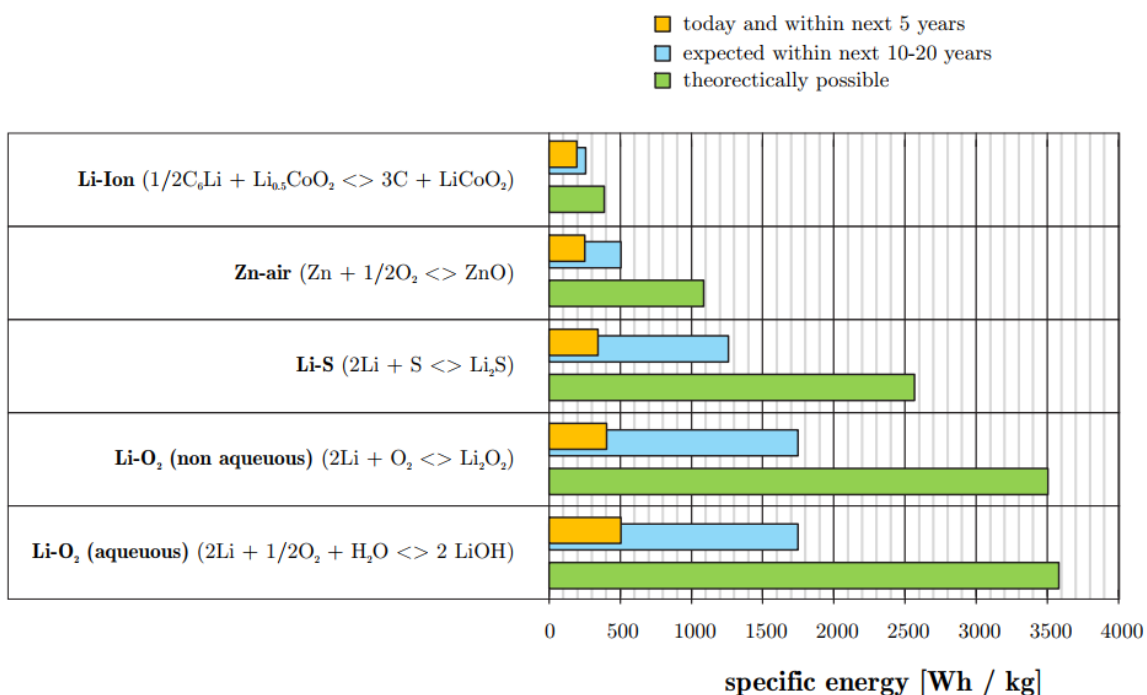
1.3.2.2 Battery Systems

Currently, most electric powered aircraft use battery systems. The most commonly used type of battery is the same as that used as power sources for mobile devices: the Lithium-ion type. An advantage of this type of battery is that its cost is relatively low and can even be

scaled to build systems with hundreds of kWh of energy capacity. Today's available systems are able to provide a mass specific energy content of up to 200 Wh/kg, but further developments may increase this value to the order of 250 Wh/kg, which is still significantly lower than the typical 11900 Wh/kg of jet fuel (PATTERSON; GERMAN, MOORE, 2012). Technologies of battery systems alternative to the Lithium-Ion type are in development, with Lithium-Sulfur and Lithium-Oxygen being examples of such systems. All of them offer energy densities larger than 3 to 10 times that of the Lithium-Ion type. For further information on Lithium based battery technology, see (HEPPERLE, 2012).

Despite the current drawback regarding energy density, the technology improvement plays a good expectation for batteries starting taking place in current and future airplane designs. Hepperle (2012) places the current and the expected development for batteries technology, as can be seen in Figure 3:

Figure 3 - Battery technology development over the next years.



Source: Hepperle (2012, p. 12)

Altogether, alternative fuel-using electrical designs, such as fuel cells and batteries, are projected as a good alternative to the growing demand for cleaner aviation, and still, aiming for an efficient performance as a goal.

1.3.3 Electric VTOL Aircrafts

Projects using small fuel-based VTOL aircrafts exists at least since the 50's (BACCHINI; CESTINO, 2019; NASA, 2018; VERTPEDIA, 2018). Initially for military purposes, like STOL (Short Take Off and Landing) aircrafts, but for more restricted uses (smaller landing sites) and with improved efficiency, compared to helicopters (AURORA, 2019; CAO et al., 2012). Recent researches are moving towards MEA (More Electric Aircraft) and even vehicles with no kind of fuel burn produced by any system, the AEA (All Electric Aircraft).

In addition, many companies worldwide have been developing their own all-electric VTOL designs, or eVTOLs. Some of them use the main idea of a multicopter (wingless multi-thrusted aircrafts) while others seek alternatives that take advantage of aerodynamics effects to increase cruise speed and autonomy (as the travel distance grows).

Winged aircrafts may become more efficient in cruise flight mode. They also present a great difference in thrust demand in comparison with wingless aircrafts. As the challenge for finding the best compromise persists, there are three general approaches for the winged ones:

- I. Separate motors for hover and cruise flight (independent propellers);
- II. Tilttable wings;
- III. Tilttable rotors.

The first type uses separate thrust for hover and cruise flight regimes, with minimal or inexistent mobility on them. This approach is the simplest one regarding design complexity, but tends to be less efficient, since it carries unused installed power weight in at least one regime.

Tiltwings join the thrust power attaching it to rotating wings, transitioning from hovering to cruise flight, or vice versa, controlling wings rotation. These designs must account the inertia and turbulence of rotating the entire wing during takeoff and landing procedures, in which the delay time is critical.

A third approach consists in fixed wings and tilting rotors, which can be spread in small rotors in each wing or condensed typically in one rotor per wing. This approach eases the transition from cruise to hover, while enabling more reliability (considering several rotors) in case of individual motor failure. Transition between hover and cruise flight can be smoothly controlled while rotating engines.

Tiltwings aircrafts enforce aerodynamically airflow direct on wings, reducing minimum speed achieved before stalling and enhancing aircraft's controllability on low speeds.

Tiltrotors aircrafts with multiple engines can have its rotors rotated independently, which can be used for stability and control, instead of surfaces control and typical aircraft stabilizers.

Modeling the aerodynamics interaction of blades and airframe while decelerating for hover or accelerating for cruise phase might be a great challenge for these latter two concepts. In addition, they are more expensive and might have greater empty weight, since they account for more control mechanisms to rotate the wings or rotors. Also, they require more studies to optimize the blades (shape and size) for both flight modes (cruise and hover) and a complex aeroelastic design that does not limit lateral-directional maneuvers. Finally, they might deliver more sophisticated “fly by wire” control laws to ensure optimal stability and controllability for the whole flying envelope applicable to the aircraft’s mission.

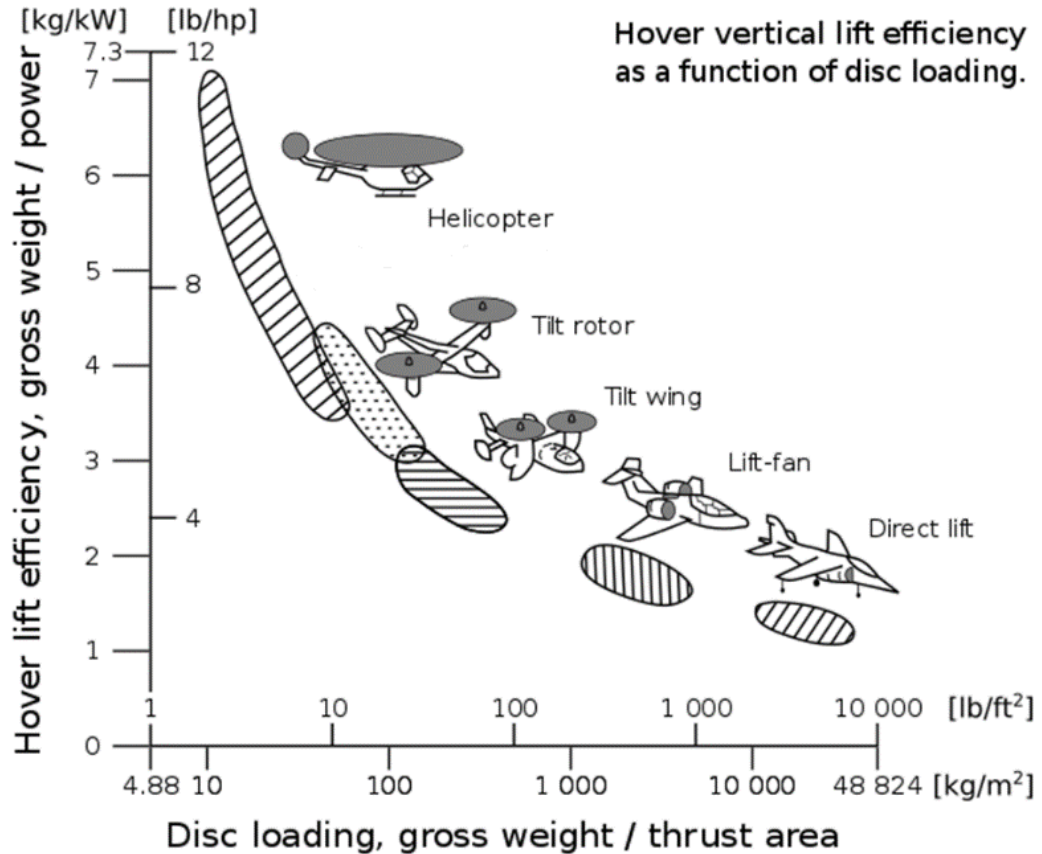
Electric VTOL aircrafts face an important trade off: safety (especially through motors redundancy) versus installed power efficiency (power installed per thrust provided). As for safety, Distributed Electric Propulsion (DEP) models are preferred, using multiple small rotors with equivalent thrust of one or two bigger ones. In DEP models, a single engine failure can be quickly compensated by the change in RPM of the other engines and realignment of the aircraft is achieved. This can be significant especially when facing situations where a departure could be imminent – a low speed situation, for instance, that could lead to a natural stall. An overpower might be needed and, as discussed in the previous section, this is feasible for electric motors. Finally, when DEP is the powerplant choice, turbulence or gusts are addressed with small lateral movements with minor changes in rotors RPM.

On the other hand, DEP’s will affect efficiency of power installed per thrust delivered. Smaller rotors can provide greater thrust if submitted to high rotations. This increases disc loading and also total power required. Figure 4 shows this correlation (MAISEL; GIULIANETI; DUGAN, 2000).

It is common to implement DEP on tiltwings and tiltrotors, greatly increasing safety and improving controllability. As for the first concept, the independent propellers approach, since it already has lower ratio of installed power to cruise flight power usage, DEP is rarely implemented.

Designs of VTOL with DEP can also show greatly reduction in rotor noise near and on the ground, by applying higher velocity on small rotors, but decreasing the tip velocity of the propellers¹ (KIMBERLIN, 2003; ROSERO et al., 2007)

Figure 4 - Hover vertical lift efficiency as a function of disc loading.



Source: Maisel, Giulianeti & Dugan (2000, p. 3)

An AEA has zero in-flight carbon emission. Furthermore, they have a simple logistic concerning recharging, overcoming the need for local fuel transportation and generalizing the type of fuel needed. On the other hand, present battery models require a very long time to fully recharge, limiting its operation due to a large idle time, prohibiting multiple flights per day per aircraft. This still is an unsolved problem for on-demand eVTOLs, since acquiring extra batteries per aircraft greatly increases cost.

There are other benefits and drawbacks to consider, such as aircraft and flight costs, certification and operational requirements, air traffic control and pilot training, but they are outside the main focus of this work.

¹ The main frequency of noise is typically a function of the fifth power of tip speed, allowing high frequency shifting by enough increase on smaller rotors velocity, providing less power dispersion through audible frequencies. Also, inside audible spectrum, the higher the frequency, the higher is the attenuation by atmosphere.

1.3.4 Current Designs

Next, a brief presentation is made on current forthcoming eVTOLs projects. The three previously presented concepts are explored.

1.3.4.1 Independent Motors eVTOL designs

The simplest solution to deliver different demands of thrust, easing manufacture and controllability, is the first type: designs using some rotors for hover, similar to a helicopter, and others as tractors or pushers for cruise flight (reducing lift thrust needed delivered by the hover rotors as speed increases). Several companies explored this idea, since it requires less control complexity and it has some degree of safety, compared to tiltwings and tiltrotors aircrafts.

In January 2019, a USA Boeing subsidiary performed its maiden flight of its eVTOL model. According to the company's website (AURORA, 2019):

Boeing NeXt, which leads the company's urban air mobility efforts, utilized Boeing subsidiary Aurora Flight Sciences to design and develop the electric vertical takeoff and landing (eVTOL) aircraft and will continue testing to advance the safety and reliability of on-demand autonomous air transportation.

Aurora Flight Sciences' eVTOL (earlier prototype shown in Figure 5 and latest one shown in Figure 6) is an AEA with 8 (eight) hovering rotors and 1 (one) pusher in the back, measuring approximately 9 m long to 8 m wide, designed for fully autonomous flight with range of up to 80 km.

Wisk (USA) used a similar design, but spreading its rotors throughout the wings, using 12 small rotors instead of 8 (WISK, 2019). Figure 7 shows Wisk (Kitty Hawk) Cora eVTOL.

Figure 5 - Aurora Flight Sciences' eVTOL in prototype version



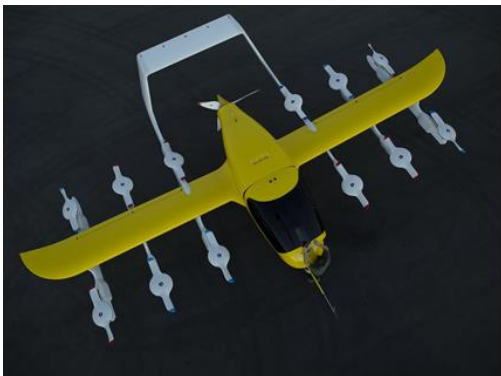
Source: Inside Nova (2019).

Figure 6 - Aurora Flight Sciences' eVTOL in its final version.



Source: Aurora: PAV - Passenger Air Vehicle (2019).

Figure 7 - Kitty Hawk "Cora" eVTOL.



Source: (VERTICAL FLIGHT SOCIETY, 2019d)

Embraer (Brazil) has also updated its first design (shown in Figure 8) now considering accessibility for wheel chair and baby's cars and added an extra pusher in the back. Also, it shows more aerodynamic usage for lift generation on extra wings, which support the hover rotors, above the vehicle (G1, 2019). Its most recent design (shown in Figure 9) it's a 5 (five) seater aircraft (pilot included), with 2 (two) separate wings, 8 (eight) hover rotors and 2 (two) pushers (EMBRAER, 2019).

Figure 8 - First design of EmbraerX, Embraer's eVTOL.



Source: Adapted from de (DEFESANET, 2018).

Figure 9 - Actual design of EmbraerX, Embraer's eVTOL.



Source: Adapted from de (EMBRAER, 2019)

Airis Aerospace (Bermudas) inverted this distribution (shown in Figure 10), using a larger central ducted fan for hover and eight small propellers (AIRIS AEROSPACE, 2019). Finally, Carter Copter SR/C model (USA) shows a winged helicopter whose tail rotor can turn backwards into a push rotor on cruise flight, lowering main's rotor rotation, reducing noise and drag (CARTER AVIATION TECHNOLOGIES, 2019). In any case, there is always one flight mode that can not harness all installed power efficiently (tractors or pushers are not able to help hover or hover thrust does not contribute on cruise flight).

Figure 10 - AirisOne eVTOL design



Source: (VERTICAL FLIGHT SOCIETY, 2019a).

1.3.4.2 Tiltwings and tilts rotors designs

The other two solutions have important differences regarding its manufacture, controllability, safety, redundancy and its flight modes efficiency. The first and clear benefit of these groups is that both flight modes can fully harness all installed power. These concepts implement fully vectored thrust, allowing controlled usage of all installed power on both flight modes, resulting in greater ratio of cruise flight speed per lift thrust.

When it comes to tiltwings eVTOL aircrafts, Airbus' A³ Vahana (USA) is a promising example. It has some redundancy on rotors, increasing safety and controllability, while does not require a tail rotor for torque balance (AIRBUS, 2019). Its design is shown in Figure 11, with approximately 6.3 m wide, 5.8 m long and 2.9 m of overall height.

Figure 11 - Airbus' A³ Vahana.

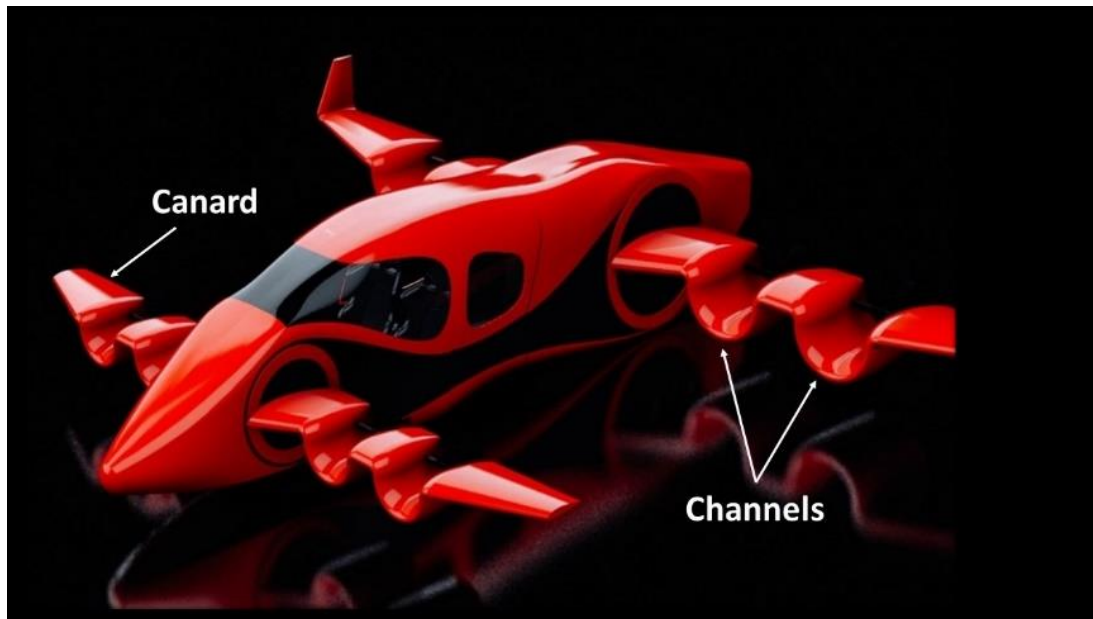


Source: (AIRBUS, 2019)

Airspace X's MOBi (USA) and Dufour Aerospace's aEro2 (Switzerland) have similar designs, using six and two rotors respectively (DUFOUR, 2019; TECHNOLOGIES, 2019).

HopFlyt's Venturi (USA) has a different design, with a longer and thinner fuselage, canards and channeled wings (VENTURI, 2019).

Figure 12 - HopFlyt's Venturi.



Source: Venturi (2019).

Regarding tiltrotors, there are highly safety-redundant models, such as EVA's X01 (France) with 16 independent tiltrotors (VERTICAL FLIGHT SOCIETY, 2019c) and Lilium's Eagle (Germany) with 36 (LILIUM, 2019) (shown in Figure 13). Lean designs, such as DeLorean Aerospace's DR-7 (USA) with only two tiltrotors (DELOREAN AEROSPACE, 2018) (Figure 14) also emerged in this market. Carter Copter also has a tiltrotor design, Hex, with six tiltrotors equally distributed on three fixed wings.

Figure 13 - Lilium's Eagle.



Source: Lilium (2018).

Figure 14 - DeLorean Aerospace's DR-7.



Source: (DELOREAN AEROSPACE, 2018)

1.4 A MORE GREEN AVIATION

Still there is not an optimal design for each of these three concepts, neither a definite classification considering power efficiency per power installed, maximum speed, autonomy and safety. While very redundant tiltrotor models (as EVA's X01 and Lilium's Eagle – Figure 13) are safer, with no single point of failure, their power installed per kilogram per thrust provided are lower than Carter Aviation Technologies' SR/C's simpler and less safe redundant design.

Since batteries' energy density are still much lower than fuel's, AEA autonomy is significantly smaller than its equivalents with internal combustion engines. Besides, hover mode demands much more power than cruise flight. Hover is less efficient than cruise because all lift thrust is provided from rotors, while on cruise flight, all thrust is used for forward movement, and wings provide aerodynamic support. A Bartini's study has shown a simulation of energy consumption on hover and cruise for an average eVTOL (BARTINI, 2019):

- Battery density: 0,2 kWh/kg
- Battery capacity: 64 kWh
- Power output: 320 kW
- Thrusters: 8 of 40 kW each
- Energy used per flight: 51 kWh
- 1 minute in hover: 5,3 kWh
- 30 min in cruise: 45,9 kWh
- Energy consumption in cruise: 1,5 kWh/min
- Lift to Drag ratio: 4 – 5
- Flight time: 30 minutes
- Cruise speed: 300 km/h
- Disc loading: 146 kg/m²
- Take-off weight 1100 kg

In terms of range, each minute on hover means reducing 15 to 20 kilometers of cruise autonomy. This justifies the importance of researching ways to minimize power usage on AEA. A performance improvement makes AEA designs a realistic option for companies worldwide, since they become economically viable and fit long-range mission requirements. This enables that conventional petroleum-based aircrafts be gradually replaced, contributing to more sustainable aviation in the short and medium term.

In this sense, this dissertation addresses a way to optimize the energy consumption in a typical mission of an aerial taxi aircraft. The approach and landing procedure was chosen to be the subject of an optimization genetic algorithm, while final programming is being developed to be adapted for take-off and flight level changes in future works.

An AEA tiltrotor eVTOL mathematical model is built as a proof of concept, based on a generic tiltrotor aircraft with most of its aerodynamic data derived from wind-tunnel testing of the NASA XV-15, and appropriately scaled to a geometry of a typical aerial taxi VTOL. Finally, the concept assumes a full electric powerplant. Adequate electric powerplant considerations and propellers theory are shown. The purpose is developing a representative method of energy consumption calculation.

The aerodynamic, inertial and propulsion data are used to fit dynamic equations of motion. Starting at the general forms of Newton's second law, the generic forms of the longitudinal Equations of Motion (EOM) are derived.

Although a tiltrotor design is used as a proof of concept, the algorithm is programmed in a way that it is possible to change the optimization to be applied for other design concepts, even those with independent motors for hover and cruise flight phases. For a given trajectory, the best set of control variables are calculated to provide the time history response for aircraft's elevator position, rotors RPM and thrust direction (or vertical and horizontal thrust, for independent motors designs) that, if followed, results in the minimum electrical power consumption through that landing path.

The trajectory varies according to the operation and changes as the approach procedures and landing sites change. In this way, the trajectory definition is arbitrary provided that aircraft air data and position follow a typical profile to be carried out by an aerial taxi eVTOL. Thus, an elliptical path is chosen, as well as position and air data constraints for ballistic equations development. Safety, comfort and design constraints are also assumed to give the highest representativeness to the solution.

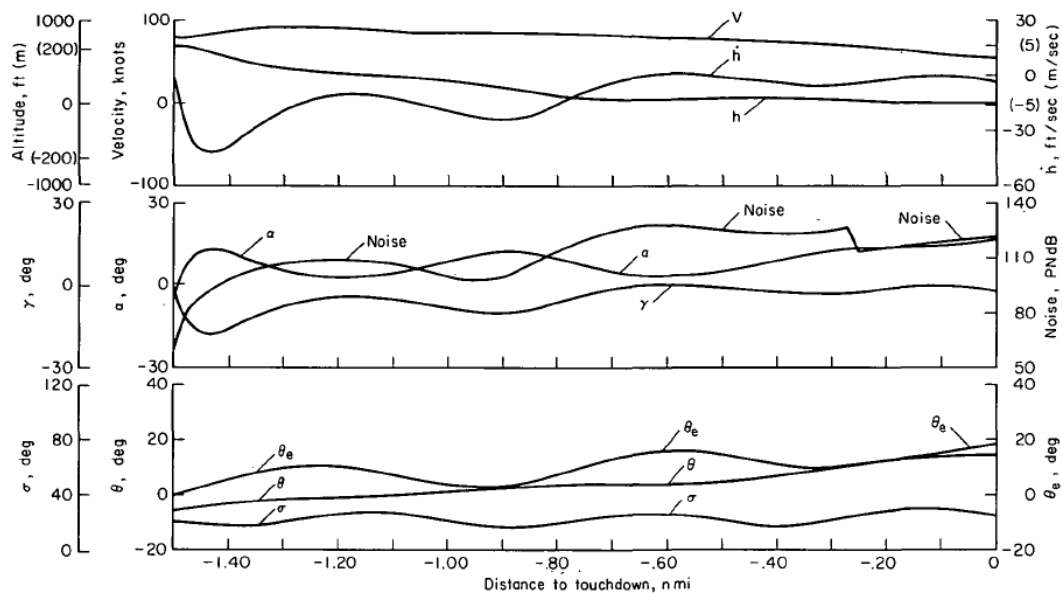
The longitudinal EOM are solved for each step along the landing path. There are an infinite set of solutions for elevator position, RPM and thrust direction that comply with the equations and the one that minimizes energy consumption is the final algorithm result.

Still there are challenges that might be explored in future works, such as improvements in comfort and safety, trajectory finders, automatic controllers development able to perform the proposed landing task, powerplant and actuators specifications and certification requirements that are out of the scope of this dissertation.

2 LITERATURE REVIEW

Jacob (1972) has proposed trajectories to a STOL aircraft, with criteria to minimize flight time, fuel consumption and noise and defined design, comfort and safety constraints and touchdown limitations on the runway. It resulted in a simultaneous time history optimization of three control variables: the attitude pitch angle, the throttle angle and the thrust angle. Figure 15 shows examples of minimum fuel consumption trajectories with design and touchdown. Afterwards, a realistic landing profile of a STOL aircraft was studied.

Figure 15 - Minimum fuel consumption with design and touchdown constraints according to Heinrich G. Jacob.



Source: Jacob (1972, p. 18).

Jacob symbols has the following meaning:

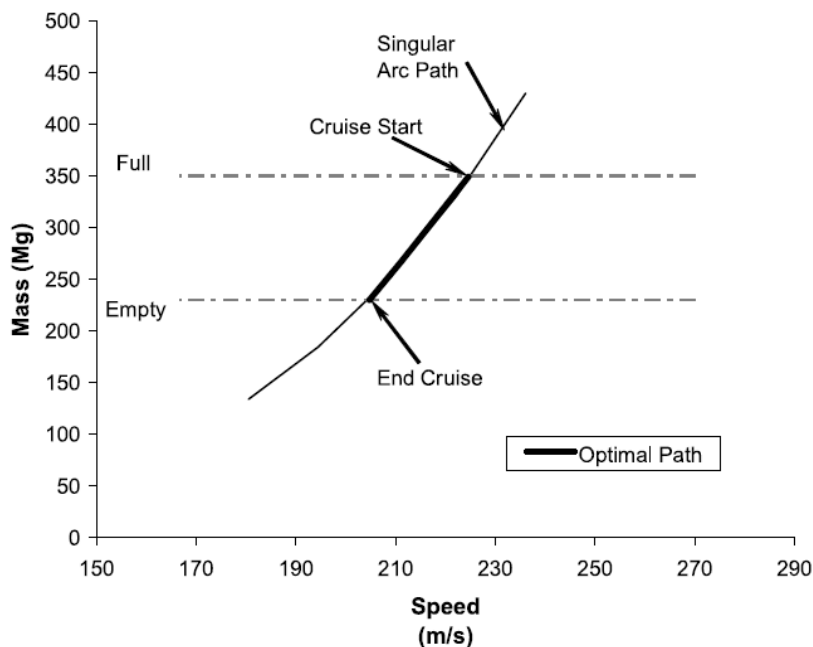
- V True airspeed
- \dot{h} Rate of sink
- h Pressure altitude
- γ Flight path angle
- α Angle of attack
- θ Pitch angle
- σ Thrust angle
- θ_e Throttle angle.

Bole and Svoboda (2000) studied an automatic landing system for a Bombardier craft, the CL-327, dividing the problem into 3 parts: change of GPS navigation source to DGPS, trajectory generator and a controller to provide control of the movement of the craft along the trajectory generated. A linear trajectory (glide slope) was chosen, and a simple PID controller was implemented, indifferent to energy consumption profile.

Kendoul, Fantoni and Lozano (2006) have modeled dynamic equations and developed a controller aiming to stabilize and trajectory track a small-scale tiltrotor aircraft design with two engines. The control laws developed was well succeeded in order to carry out the proposed task, but the authors had no specific concern in minimizing the energy expenditure to fulfill the task.

Pargett and Ardema (2007) have proposed a flight path performance optimization, focusing on the cruise flight phase of aircrafts with classical internal combustion engines, resulting on a trajectory that has a better energy efficiency. They have shown that a 7,3% fuel economy could be achieved if the proposed path was followed, which would increase autonomy by 9,8%. A correlation example of an optimal path is show in Figure 16.

Figure 16 - Cruise optimal path according to Mark D.Ardema.



Source: Pargett and Ardema (2007, p. 4)

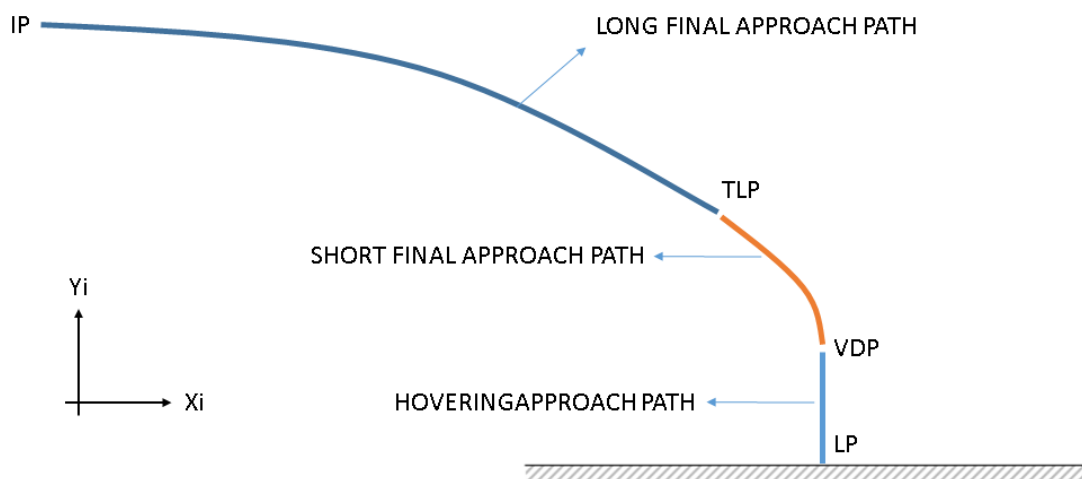
Kim, Kim and Kim (2010) developed a trajectory controller for all flight modes of a tiltrotor design (hovering, conversion and airplane mode), focusing on a landing scenario.

3 PROBLEM DESCRIPTION

3.1 LANDING PROFILE

In order to facilitate the full problem analysis, the landing trajectory is divided into three main segments: Long Final Approach Path (LFAP), Short Final Approach Path (SFAP) and Hovering Approach Path (HAP). Figure 17 illustrates these three generic segments.

Figure 17 - Landing Profile.



Source: Created by the author.

The first portion of the trajectory defines the Long Final Approach Path (LFAP) and connects two waypoints: the Interception Point (**IP**) and the Thrust Lifting Point (**TLP**). The interception point represents the first trajectory waypoint. At IP, the aircraft will start its long final landing approach with cruise configuration. As long as the long final approach is followed, it is supposed that the aircraft starts to be configured to the cruise to hover transition phase, that will depend on the design. The LFAP segment ends at TLP, where the vehicle is fully configured for transition, but still with remaining forward thrust.

The line connecting TLP up to the Vertical Descent Point (**VDP**) defines the second segment of the landing trajectory, the Short Final Approach Path (SFAP). This is the conversion segment until full hovering configuration. During the SFAP, the motors nacelle will start rotating for a tilt-rotor (or wings for a tilt-wing or yet, power will increase in hover motors for an independent motors design). More electrical power will be delivered to increase rotors

rotation as to aid the airframe for lifting purposes, up to the point whereupon no more lift is extracted by pure aerodynamics and motors are ready to sustain the airplane completely in the VDP.

Finally, the third and final approach and landing segment is defined as the Hovering Approach Path (HAP). At this segment, the aircraft flies vertically from VDP up to the Landing Point (LP) and finishes the whole approach and landing procedure.

The angle of descent relative to the horizontal is able to vary between 0 and 90 degrees (negative flight path angle, pointing downwards) for both LFAP and SFAP. The geometry also encompasses the heading or bearing angle, which can be anything from zero to 360 degrees. Once defined, the heading is fixed during the whole landing path. Whole definition of general equations and assumptions considers a two dimensional problem, which means that the aircraft's motion is treated as longitudinal only. Finally, both the LFAP and the SFAP range have full adjustability and only a maximum value is defined for a representativeness reason (LFAP maximum range: 8000 m; SFAP maximum range is 500 m). Table 2 summarizes these assumptions:

Table 2 - Limits assumed to the optimization algorithm.

FULL APPROACH AND LANDING PROFILE ASSUMPTIONS

Flight Path Angle, γ	$-90^\circ \leq \gamma \leq 0^\circ$
Heading/Bearing, μ	$0 \leq \mu \leq 360^\circ$ (fixed)
LFAP _{RANGE}	$0 \leq \text{SFAP}_{\text{RANGE}} \leq 8000 \text{ m}$ (~5.4 NM)
SFAP _{RANGE}	$0 \leq \text{SFAP}_{\text{RANGE}} \leq 500 \text{ m}$ (~0.27 NM)

Source: Created by the author.

Despite LFAP and HAP definitions, only SFAP is the target for the optimization algorithm in development shown in this thesis. Full definitions aim future works, where takeoff and flight level changes phases will also be a subject of study.

3.2 OPTIMIZATION SCOPE

The whole Landing Profile was divided into three different segments: the Long Final Approach Path (LFAP), the Short Final Approach Path (SFAP) and the Hovering Approach Path

(HAP). The central point of further optimization is the SFAP portion of the whole approach and landing procedure.

This is initially a flight dynamics problem. It is necessary to develop a representative model of electric aircraft, with the objective of evaluating different ways to travel the SFAP route. State variables, such as positions, speeds and accelerations, are arbitrary. Therefore, once a course is arbitrated, there are a number of possible ways to control the aircraft in order to cover this course, since it will be possible to control the thrust generated by the motors, the direction of that thrust and the pitch attitude.

For an independent motors model, varying the thrust direction means varying the thrust generated by the motors dedicated to the hover and those dedicated to the cruise. The vector addition of the thrust components of each motor will result in a vector with defined magnitude and direction. In tiltwing or tiltrotor type models it is possible to directly control the direction of the motors, by means of shafts coupled to the structure of the wings or nacelles that allow the rotation of the set. The pitch attitude is most commonly controlled via elevators, although there are models with fully motor dependent control.

Once the model is defined, it is proposed that SFAP be divided into time steps, with a Δt duration each. For each step of the trajectory, the dynamics equations of motion are solved with a set of control variables that comply with the governing equations. In the end, each solution of the problem is composed by time history arrays of the control variables.

Since there are a number of possible solutions, the one of interest is the one that minimizes the energy consumption during the whole procedure. In other words, minimizes electric power usage and, consequently, the operation cost. In order to find the better suit for a real problem, where not only the power usage is minimized, but it still represents a real practicable scenario, the optimal solution must comply with all the safety, comfort and design constraints.

The mean electric energy delivered from batteries throughout the SFAP is then a key element. For each step, the instantaneous power demanded by electric motors during Δt seconds can be calculated. The summation of the energy for each step yields in the total energy consumption for the whole course. The following equation summarizes that rationale:

$$\Delta E_T = \int_0^{t_f} P_{BATT}(t) dt = \sum_{t=0}^{t=t_f} P_{BATT}(t) \Delta \varepsilon \quad (\Delta \varepsilon \rightarrow 0) \quad (3.1)$$

P_{BATT} Batteries power for each step

In summary, the optimization algorithm must perform a search in a number of possible solutions and find the one that suits best, or gives the lowest energy expenditure. In Methodology section, it is discussed the software choice and the search method implemented to solve the problem, whereas this section has the objective to provide the basis to perceive the model and the codes elaborated further on.

3.3 AIR TAXI TRAVEL MODEL

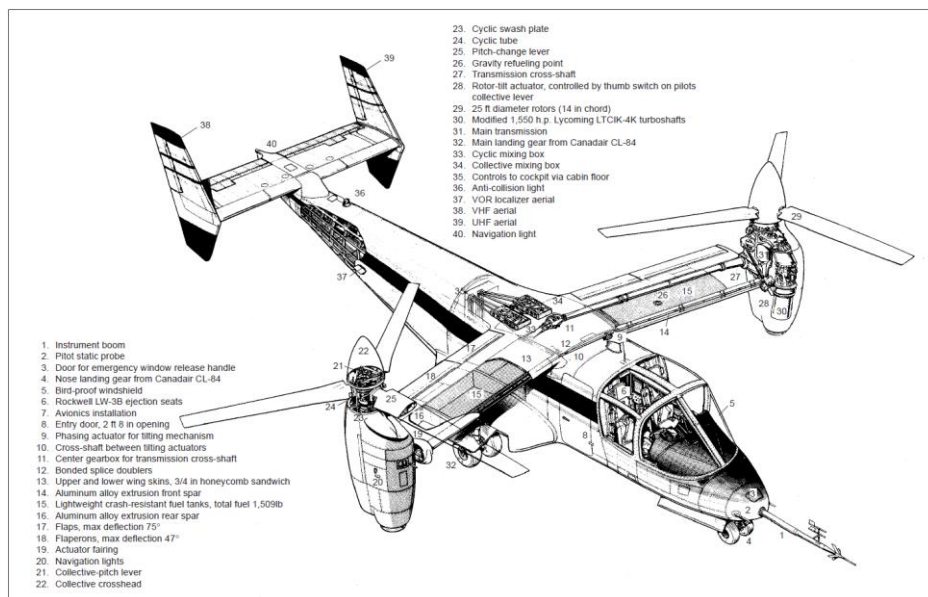
3.3.1 The Concept

The aim is to optimize energy consumption for eVTOL aircrafts. In the goal to use the most representative data to be part of the final algorithm proposed many strategies were discussed. In actual fact, there are several design variations that one would propose. Nevertheless, the one that best suited the demand of availability and representativeness was choosing a generic tiltrotor aircraft model, appositely built in an air taxi travel market eVTOL measurements, with most of its aerodynamic data gathered from wind tunnel testing of a well-known and massively researched real aircraft, the NASA XV-15 project. All modeling inputs then fits a set of derived equations of motion. Many researches on the NASA X-15 were conducted and are available at NASA technical reports server (NASA, 2019). The model developed uses an approach similar to that of Ferguson's (FERGUSON, 1988), but making a beeline for an air taxi travel concept. These efforts will lead to a fully vectored thrust eVTOL aircraft, exemplified by a general tiltrotor design configuration, with rotating electric engines. This model guides the empirical tests of the programming structure. Next, a brief introduction is done regarding the NASA XV-15 project.

3.3.2 NASA XV-15 Project

In August 1950, from the need to extend and enhance helicopter capabilities, especially for air support of the U.S. military field operations, a convertiplane program was established in the U.S. as a result of the joint U.S. Army and U.S. Air Force. There was a design competition whereupon a few prototypes were exhibited and took place of it the McDonnell XV-1 compound helicopter (McDonnell Aircraft Co.), the XV-2 stoppable rotor aircraft (Sikorsky Aircraft) and the Bell XV-3 tiltrotor aircraft (submitted by the Bell Helicopter Company). The XV-3 tiltrotor emerged from this program as a strong contender. However, it had significant stability problems. It was not until the discovery of new techniques and the incorporation of new materials technology that a major design concept advance was reached. As a result of such an advance, the XV-15 tiltrotor aircraft project, which was launched in 1971 at NASA Ames Research Center, was proposed.

Figure 18 - General layout of NASA XV-15.



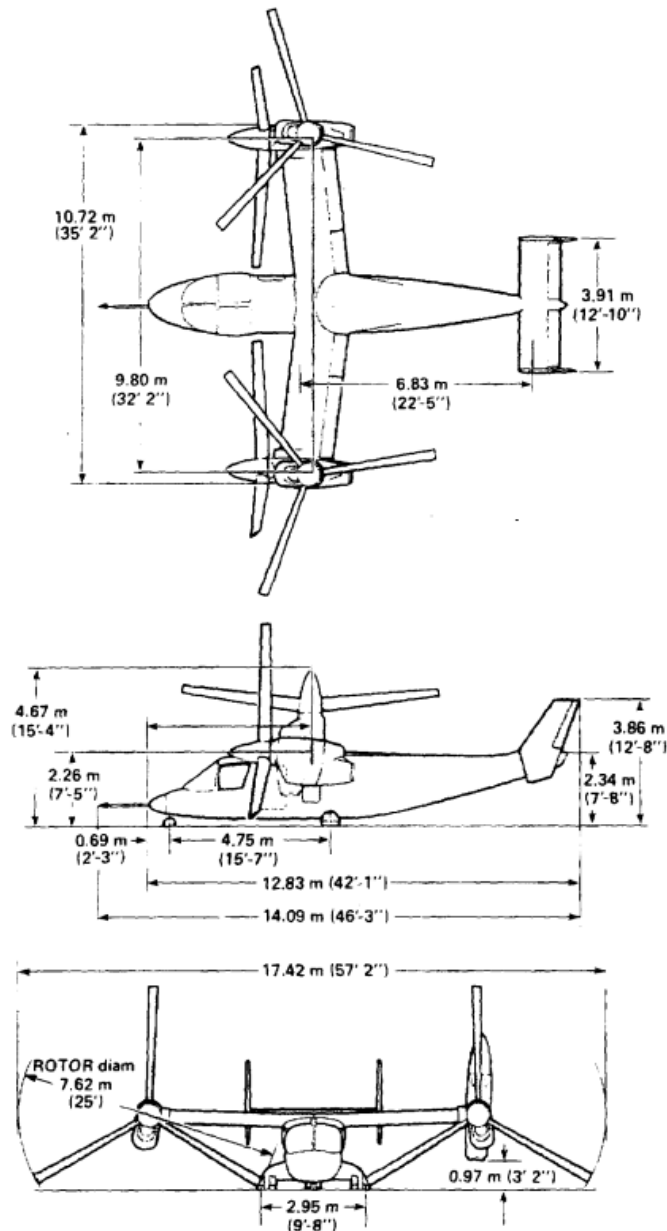
Source: Maisel, Giulianeti & Dugan (2000, p. 126)

The XV-15 tiltrotor research aircraft is a two-seat VTOL that has a large diameter, low disc loading, wingtip mounted proprotors that provide the thrust for vertical lift and forward flight. This aircraft is powered by twin Lycoming T-53 turboshaft engines that are connected by a cross-shaft and drive three-bladed, 25 ft diameter metal rotors, whose size was extensively tested in a wind tunnel. The engines and main transmissions are located in wingtip nacelles to minimize the operational loads on the cross-shaft system and, with the rotors, tilt as a single unit.

When in the VTOL mode, the XV-15 climbs vertically into the air like a helicopter. In this mode, the XV-15 can lift off and hover for approximately one hour. This aircraft has the ability to either fly as a helicopter, in the partially converted airplane mode, or as a propeller airplane, when it converts from the helicopter to the airplane mode. In the airplane mode, the XV-15 can cruise for more than two hours.

The set of general characteristics of the XV-15 are presented herein, for wide knowledge purposes (FERGUSON, 1988; MAISEL; GIULIANETI; DUGAN, 2000; WEIBERG; MAISEL, 1980). A number of them are used and properly adapted in the generic eVTOL model.

Figure 19 - XV-15 Geometry.



Source: Weiberg & Maisel (1980, p. 70)

Powerplant

Two Lycoming LTC1K-41K turboshaft engines (modified T53L13B)

Horsepower ratings

Contingency (2 minutes) 1802 SHP

Takeoff (10 minutes). 1550 SHP

Normal (max. continuous) 1250 SHP

Wing

Span. 32 ft 2 in

Area 181.0 ft²

Chord (constant) 5.25 ft

Airfoil section NACA 64A223

Sweep -6.5 degrees

Dihedral. 2.0 degrees

Aspect ratio. 6.12

Width 57 ft 2 in (to outer tip of proprotor disc)

Height 12 ft 8 in

Horizontal tail

Span. 12ft 10 in

Area 50.25 ft²

Chord. 3 ft 11 in

Airfoil section NACA 64A015

Aspect ratio. 3.27

Vertical tail

Area. 50.5 ft² (25.25 ft²/panel)

Airfoil section NACA 0009

Mean Aerodynamic Chord 3.72 ft

Aspect Ratio 2.33

Proprotor

No. of proprotors 2, interconnected

Blades/proprotor 3

Diameter 25 ft

Chord (constant)	14.0 in
Solidity	0.089
Twist, geometric (spinner to tip).	36 degrees
Delta 3 angle.	-15.0 degrees
<u>Rotational speed</u>	
Helicopter mode	589 rpm
Airplane mode.	517 rpm

Inertia

Design	13,000 lb
Empty (actual).	10,083 lb
Actual gross (at engine start)	13,248 lb
Fuel	1,436 lb
Moment of Inertia $I_{YY} _{\varphi=90^\circ}$	21,360 lb, varies with mast angle

Performance

Maximum speed:	300 knots (345 mph, 557 km/h)
Stall speed:	100 knots when in airplane mode (115 mph, 185 km/h)
Range:	445 nmi (515 mi, 825 km)
Service ceiling:	29,500 ft (8,840 m)
Disc loading:	13.2 lb/ft ² (73 kg/m ²)
Power loading:	1.35 kg/kW
Hovering altitude:	8,800 ft (2,635 m) out of ground effect

3.4 PROPELLERS

3.4.1 Introduction

For lightweight aircrafts, propeller-driven designs prevail. Actually, when the speed range is up to 450 knots propellers is the most efficient choice (KIMBERLIN, 2003). Aerial taxi eVTOLs are part of this group. Kimberlin (2003, p. 63) also suggests that propellers may become viable in the near future even for large-scale air transport:

Recent NASA research has shown it possible to extend the cruise speed of propeller-driven aircraft to 0.8 Mach while maintaining a propeller efficiency in excess of 80%.

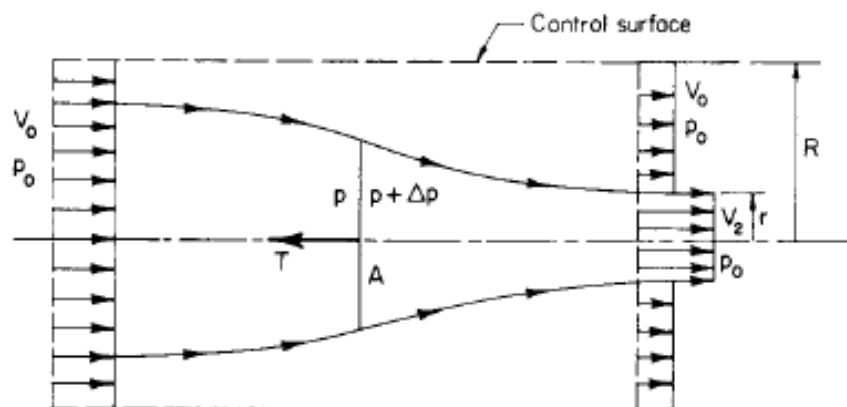
Therefore for certain applications the propeller will be around indefinitely, and may be reintroduced in such areas as air transport.

This section has the intention to show the background used for propulsion analysis in the model elaboration and in the final programming. However, it is not the purpose developing a whole propellers theory withal. For further details, sources such as McCormick Jr. (1967) and Kimberlin (2003) are recommended. Enough content for a comprehensive view of propulsion assumptions and equations used in the codes is presented instead.

3.4.2 Momentum Theory

This first theory provides the basis to calculate the propeller efficiency. The classical momentum theory uses the approach of energy and momentum principles. A set of assumptions are made:

Figure 20 - Airstream passing through a propeller with control surface.



Source: McCormick Jr. (1967, p. 74).

1. The thrust loading is uniform over the propeller disk. In other words, propeller has an infinity number of blades;
2. Propeller does not add rotation to the flow. Reasonable if considered a pair of counter rotating propellers;
3. Inviscid flow;
4. Incompressible flow;
5. Static pressure in and out the slipstream in sections far ahead and behind of the propeller is the same to the undisturbed free-stream static pressure (no profile losses);

Most of these assumptions are unrealistic. However, the momentum theory predicts the ideal or maximum propeller efficiency, which is suitable to be used for energy consumption calculation data for the present work. Since propeller efficiency varies with a number of factors such as number of blades, geometry and material, it is preferable to use a general efficiency calculation. The final program can be adapted though, with few and easy modifications, to account for propeller efficiency curves pertaining to a specific aircraft data.

Next the equations are shown. The mass flow through the propeller, the thrust, the power input and the power output can be calculated as follows:

$$\dot{M}_{FLOW} = \rho A(V_0 + w) \quad (3.2)$$

$$T = \rho A(V_0 + w)2w \quad (3.3)$$

$$P_i = T(V_0 + w) \quad (3.4)$$

$$P_{USE} = TV_0 \quad (3.5)$$

\dot{M}_{FLOW} Air mass per unit time

ρ Air density

A Propeller disc area

V_0 Airflow non-disturbed velocity (propeller inflow)

w Induced velocity (velocity increment added by the propeller)

T Thrust generated by the propeller

P_i Power input (power that the propeller supplies to the fluid)

P_{USE} Power output (useful power)

Lastly, the ideal efficiency is defined as the ratio of the useful power by the total power supplied to the flow by the propeller.

$$\eta_i = \frac{P_{USE}}{P_i} \quad (3.6)$$

$$\eta_i = \frac{1}{1 + \frac{w}{V_0}} \quad (3.7)$$

The induced velocity dimensionless ratio w/V_0 is then calculated as follows:

$$\frac{w}{V_0} = \frac{1}{2} (\sqrt{(1 + C_{MT})} - 1) \quad (3.8)$$

$$C_{MT} = \frac{T}{\frac{1}{2} \rho A V_0^2} \quad (3.9)$$

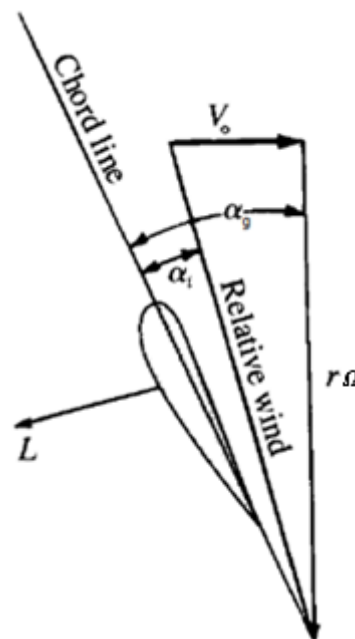
The term C_{MT} is a dimensionless coefficient that shows the dependency of the induced velocity, and hence the ideal efficiency, upon the disk loading T/A and the undisturbed flow dynamic pressure $\frac{1}{2} \rho V_0^2$.

3.4.3 Blade Element Theory

The blade element theory addresses dimensionless coefficients that are easily related to more familiar aerodynamic ones in airfoil theory, such as lift, drag and momentum coefficients. Propeller data provided by most companies are usually expressed using many of the parameters derived in this theory to refer to engine characteristics and so is also done in thrust and power charts in this work.

Initially, the advance ratio, which is the parameter analogous to the angle of attack in wing aerodynamics, can be understood referring to the following diagram:

Figure 21 - Blade element velocity and relative wind diagram.



Source: Adapted from Anderson Jr. (1999, p. 157).

$$\tan(\alpha_g - \alpha_i) = \frac{V_0}{\Omega r_i} = \frac{V_0}{\pi n d_i} \quad (3.10)$$

α_g	Geometric angle of attack
α_i	Actual angle of attack of blade element
r_i	Radius from hub to blade element
d_i	Diameter from one blade element to the opposite one
Ω	Rotation speed in rad/s or degrees/s
n	Rotation speed in rev/s

If the equation is written for the tip blade element then the diameter in the denominator is the proper propeller diameter D . The definition of advance ratio is then:

$$J = \tan(\beta - \alpha) \pi = \frac{V_0}{nD} \quad (3.11)$$

The advance ratio J , slip function or progression factor is a ratio of velocity terms, one standing for translation and the other for rotation. Note that the propeller velocity due to rotation is $\Omega R = (2\pi R/D)nD$. The higher is the advance ratio, more the aircraft moves with one propeller turn. A large J means that the forward velocity is large compared to the tip speed.

The thrust, the torque and the power are defined as follows:

$$T = \rho n^2 D^4 C_T = \rho (nD)^2 D^2 C_T \quad (3.12)$$

$$Q = \rho n^2 D^5 C_Q = \rho (nD)^2 D^2 D C_Q \quad (3.13)$$

$$P_{USE} = \Omega Q = \rho n^3 D^5 C_P = \rho (nD)^2 D^2 n D (2\pi C_Q) \quad (3.14)$$

Where

$$C_P = 2\pi C_Q \quad (3.15)$$

The dimensionless coefficients C_T , C_Q and C_P are functions of a number of factors, namely:

$$C_T = C_T(Re, J) \quad (3.16)$$

$$C_Q = C_Q(Re, J, \text{blade geometry}) \quad (3.17)$$

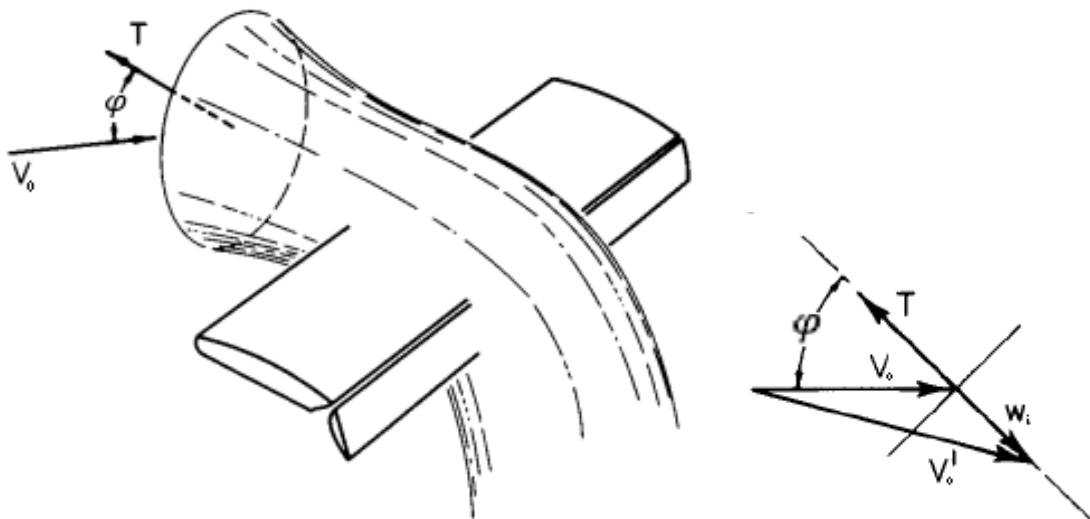
$$C_P = C_P(Re, J, \text{blade geometry}) \quad (3.18)$$

3.4.4 Vectored Propellers

In a tiltrotor VTOL aircraft, the thrust is vectored and can vary through a range of zero to slightly more than 90 degrees in some concepts. As the thrust angle φ varies, the induced velocity and power demanded by the propeller changes to generate the same amount of thrust T .

The wing and propeller in the Figure 22 are in combination. The propeller is right in front of a wing and a generic thrust angle φ is considered. The propeller slipstream influences the flow behavior over the wing and an analytical solution to the aerodynamic force, lift and drag, is unlikely in view of the real fluid flow. The propeller alone is evaluated then, where this theory will be applicable. When the content is brought to aerodynamic means, an empirical result is used in this work, a wind tunnel testing.

Figure 22 - Wing in combination with a propeller at an angle of attack φ .



Source: McCormick Jr. (1967, p. 212).

It is assumed that the propeller is far enough the wing. That means that the velocities in and out the propeller are not influenced by the wing disturbance in the flow. An upwash correction shall be made if that is the real case.

A velocity w_i is induced at the thrust direction. The resultant velocity V'_0 is used along Glauert's hypothesis and it can be demonstrated that the following equation holds:

$$\left(\frac{w_i}{w_0}\right)^4 + 2\left(\frac{w_i}{w_0}\right)^3 \frac{V_0}{w_0} \cos\varphi + \left(\frac{w_i}{w_0}\right)^2 \left(\frac{V_0}{w_0}\right)^2 = 1 \quad (3.19)$$

The term w_0 is the velocity in a static condition induced by the propeller to generate a thrust T and it is defined as follows:

$$w_0 = \sqrt{\frac{T}{2\rho A}} \quad (3.20)$$

Furthermore, the ideal power P_i , or the total power that the propeller supplies to the fluid, must be evaluated through the thrust direction and is the product of the thrust and the velocity normal to the disk:

$$P_i = T(V_0 \cos\varphi + w_i) \xrightarrow{\div P_0} \frac{P_i}{P_0} = \frac{V_0}{w_0} \cos\varphi + \frac{w_i}{w_0} \quad (3.21)$$

Where P_0 is the power to produce T statically, or:

$$P_0 = T w_0 \quad (3.22)$$

Correlations (3.19) and (3.21) are of particular interest when determining w_i and P_i for designs with vectored thrust. They are used in rotors aerodynamics modeling, rotor wake determination and energy expenditure computation throughout the entire range of motors tilt.

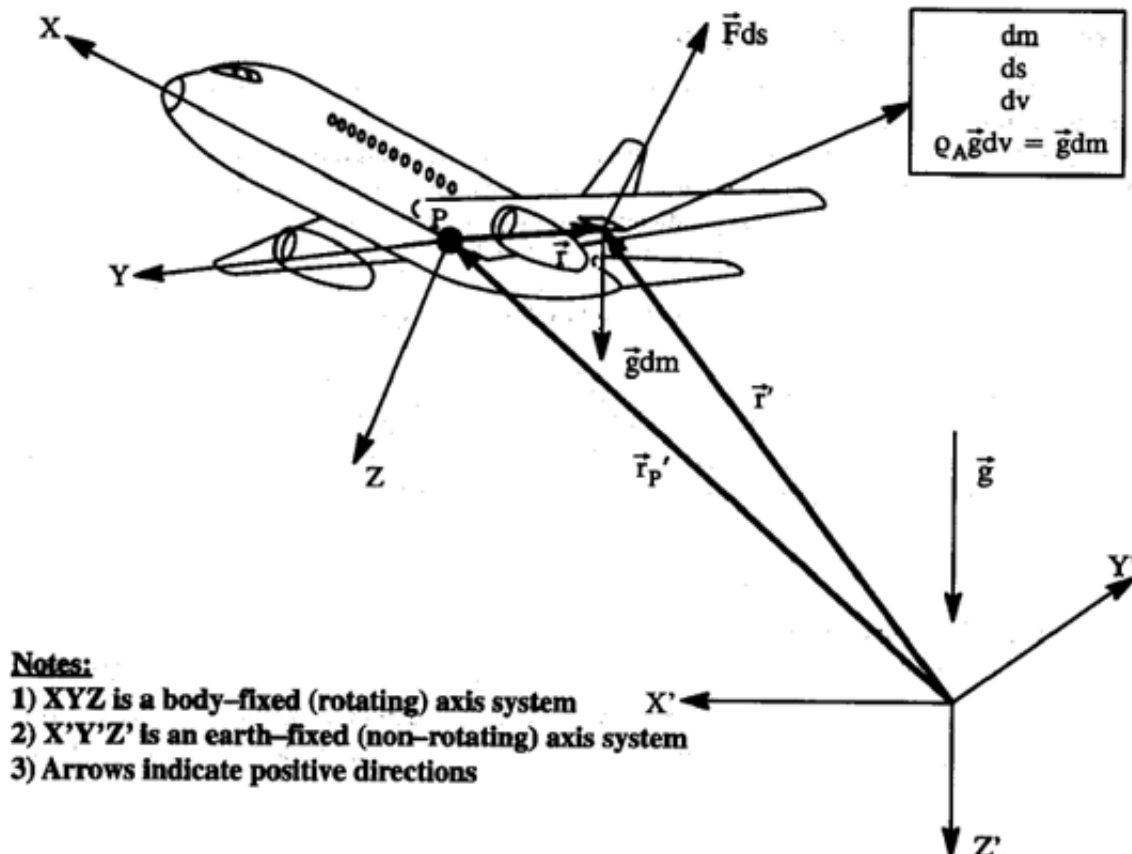
3.5 AXIS DEFINITIONS

Upon the coordinate systems commonly defined in aircraft flight dynamics, four are of special interest. These axes are the ones where the equations of motion are evolved, namely:

1. Body-Axis Coordinate System XYZ ;
2. Earth-Axis Coordinate System $X'Y'Z'$;
3. Wind-Axis Coordinate System $X_W Y_W Z_W$;
4. Mast-Axis Coordinate System $X_M Y_M Z_M$;

Figure 23 – Earth-axis and body-axis coordinate systems. depicts the former two axis systems. The body-axis system is fixed in the airplane and is allowed to rotate. The X -axis points out the nose through the principal inertia direction in the XZ plane while Y runs out the right wing direction and is perpendicular to X . Z -axis is perpendicular to either X and Y and points downwards. Earth-axis system is fixed on earth, non-rotating and is the inertial reference system used.

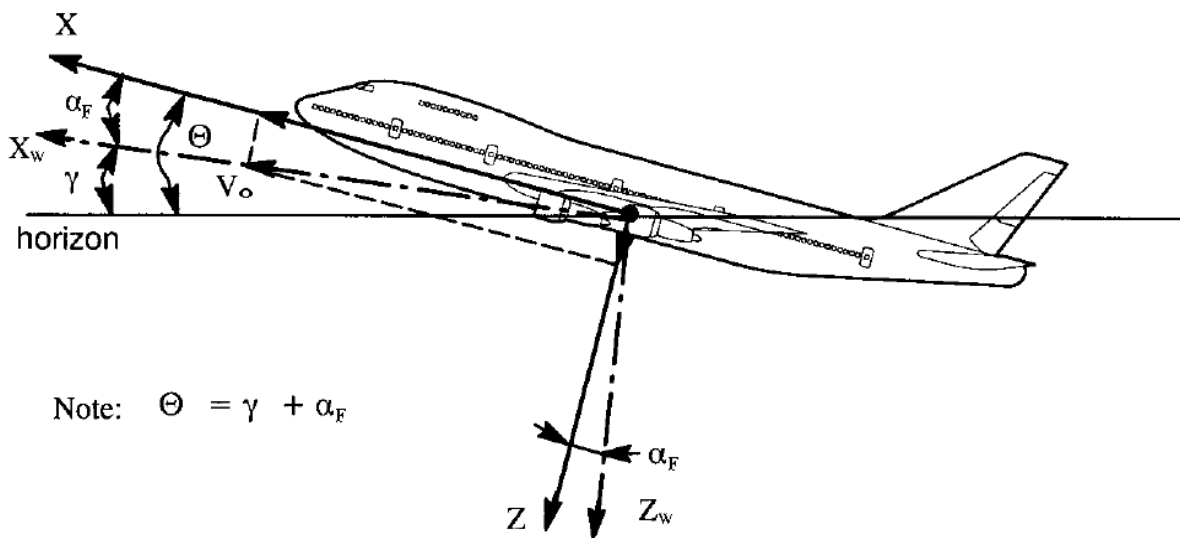
Figure 23 – Earth-axis and body-axis coordinate systems.



Source: Roskam (2001, p. 4)

The third coordinate system is the wind-axis $X_W Y_W Z_W$, which is a modification of the body-axis system. The X_W -axis is always aligned to the wind direction, the same of the true airspeed. Figure 24 - Definition of the wind-axis system - longitudinal motion. shows how the $X_W Y_W Z_W$ is defined for the longitudinal motion, for a steady state, wings level, straight line flight condition with no sideslip. In this case (zero sideslip), the Y_W -axis coincide with the Y -axis of the XYZ system.

Figure 24 - Definition of the wind-axis system - longitudinal motion.

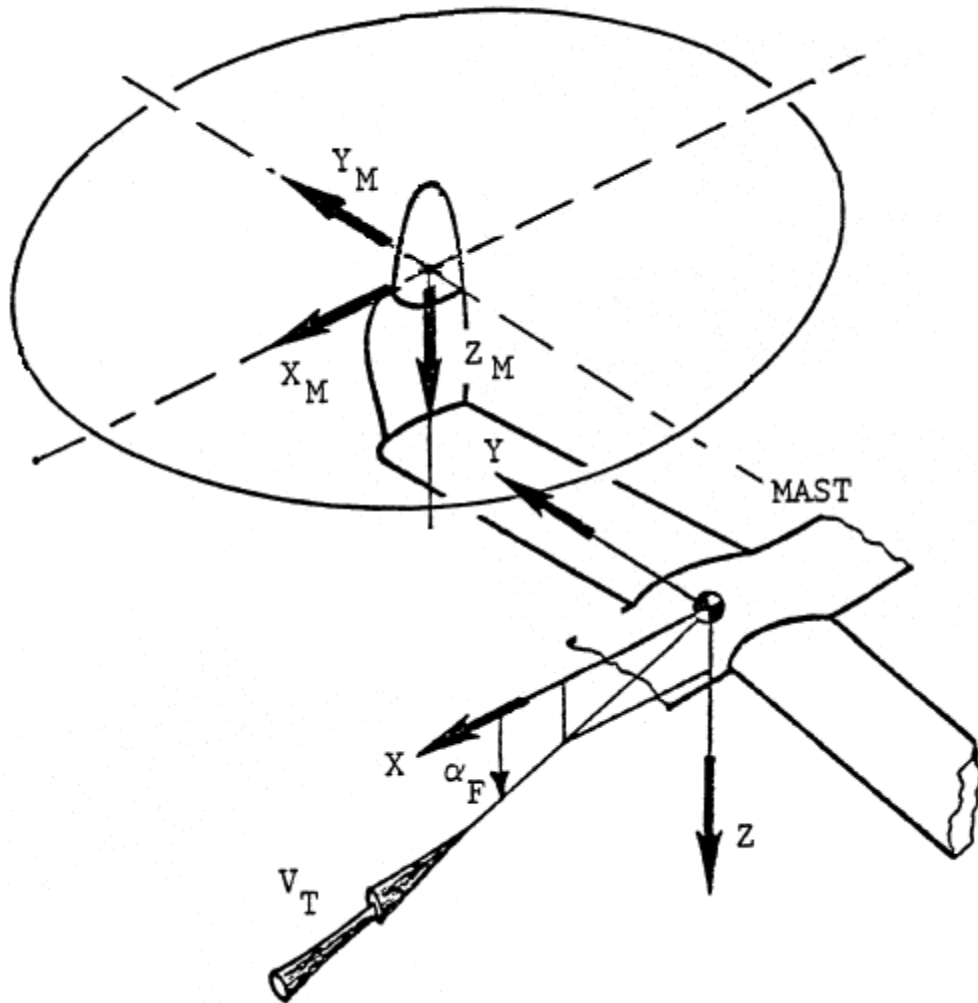


Source: Adapted from Roskam (2001, p. 66)

- θ Euler angle with respect to pitch motion, or the pitch angle
- α_F Fuselage angle of attack

Finally, the fourth coordinate system is the mast-axis system $X_M Y_M Z_M$ and is used to derive the rotor equations. $X_M Y_M Z_M$ is fixed in the rotor's mast and allowed to rotate. Right and left sides are completely symmetrical about aircraft plane of symmetry. The definition of this system is shown in Figure 25.

Figure 25 - Mast-axis coordinate system.



Source: Adapted from Ferguson (1988, p. A-13).

3.6 SHORT FINAL APPROACH PATH DEFINITIONS

3.6.1 Introduction

The Short Final Approach Path is the main object of study. First, the aircraft equations of motion are derived and the necessary relationships to understand the overall problems are discussed. After, additional constraints are defined. These constraints are a representation of what an eVTOL aircraft design is supposed to face under a realistic approach and landing procedure.

3.6.2 Governing Equations

Starting at the general forms of Newton's second law, the generic forms of the longitudinal Equations of Motion (EOM) are derived. Actually, the most general form of the EOM considers a full six degree of freedom dynamics. However, the approach and landing problem herein treated is assumed as two dimensional. Thus, the lateral-directional variables are not taken into account. Etkin and Reid (1996) and Roskam (2001) evolved a full detailed derivation of these equations. However, as done for propellers theory, the purpose is not to show the whole derivation, but only present the assumptions and the final set of terms that must be used to understand and solve the approach and landing problem.

The general form of Newton's second law for the translational and rotation motions are:

$$\vec{F}_R = \frac{d(m\vec{V})}{dt} \quad (3.23)$$

$$\vec{M}_R = \frac{d(\vec{L})}{dt} \quad (3.24)$$

\vec{F}_R	Resultant Force
\vec{M}_R	Resultant Moment
\vec{L}	Angular Momentum

The net force applied is calculated as the rate of change along time of linear momentum while the net applied moments are defined as the rate of change of angular momentum.

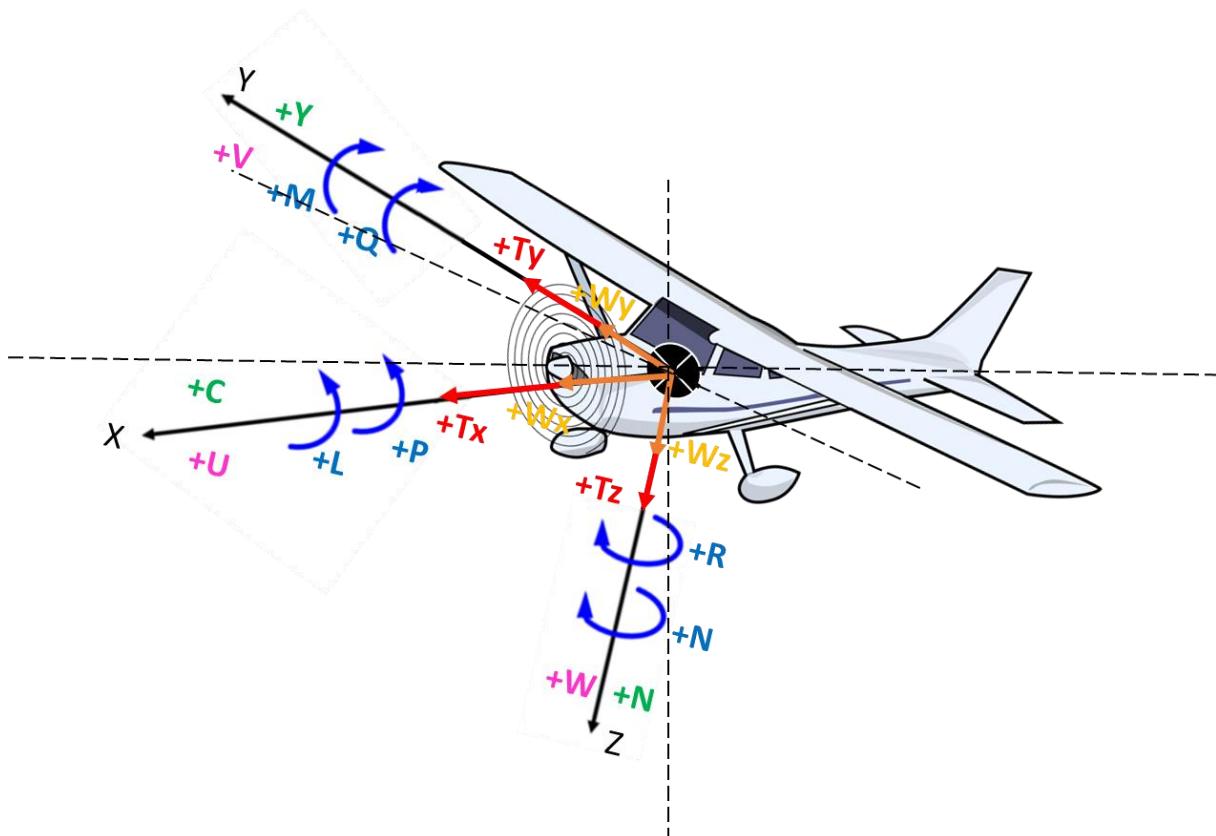
The definition of the forces, moments, airspeeds, angular rates and inertias assumed in relation to the body-axis coordinate system in a generic way are shown in the next table and will follow the sign convention shown in Figure 26 - Sign convention for the forces, moments, airspeeds and angular rates on body-axis reference frame..

Table 3 - Variables index).

AXIS	X	Y	Z
Translational Airspeeds	U	V	W
Angular Rates	P	Q	R
Aerodynamic Forces	C	Y	N
Propulsive Forces	T_x	T_y	T_z
Gravitational Force	W_x	W_y	W_z
Rolling, Pitching and Yawing Moments	L	M	N
Moments of Inertia	I_{xx}	I_{yy}	I_{zz}
Products of Inertia	I_{yz}	I_{xz}	I_{xy}

Source: Created by the author.

Figure 26 - Sign convention for the forces, moments, airspeeds and angular rates on body-axis reference frame.



Source: Created by the author.

Foremost, a number of assumptions are stated:

- I. The time spent during an approach and landing procedure is short and the aircraft's mass does not change during a typical procedure²;
- II. A flat and non-rotating Earth is considered and the earth-axis frame is suitable as an Inertial Reference Frame.
- III. Any structure deformation will be neglected³;
- IV. The pylons or wings conversion always happen in a steady state conversion rate⁴;

Assumption III does not imply in considering the airplane as a rigid body, since changes in inertia terms with time due to moving parts can still take place. Most of inertia changes, such as propellers rotation, can be disregarded and still hold a representative model for the purposes herein pursued. However, the Center of Gravity (CG) variation when pylons or wings rotate - for tiltrotors and tiltwings - affects considerably the results and is acknowledged. Thereby, assumption IV ensures that when accounting for this CG position variation, the CG acceleration, in turn, does not change with pylons or wings rotation. At last, after math evolvment of equations (3.23) and (3.24), it is possible to write the Newtonian version of the aircraft EOM's:

$$\begin{cases} F_x = m(\dot{U} + QW - RV) \\ F_z = m(\dot{W} + PV - QU) \\ M_y = \dot{Q}I_{yy} - PR(I_{zz} - I_{xx}) + (P^2 - R^2)I_{xz} \\ F_y = m(\dot{V} + RU - PW) \\ M_x = \dot{P}I_{zz} - QR(I_{zz} - I_{yy}) - (\dot{R} + PQ)I_{xz} \\ M_z = \dot{R}I_{zz} - PQ(I_{yy} - I_{xx}) - (QR - \dot{P})I_{xz} \end{cases} \quad (3.25)$$

The first three equations regards to the aircraft's longitudinal motion, while the last three are applied for the lateral-directional motion. For the approach and landing problem, a couple more assumptions can be done in order to obtain further simplified equations and still have a good representation of the aircraft's dynamics. They are:

² In actual fact, for electric designs this assumption is unnecessary, but is here presented in order to give wide coverage to the solution. For conventional aircrafts, this assumption may not be adequate in cases where the fuel flow is high and/or the procedure is time consuming. On the other hand, the typical short final approach proposed takes less than 60 seconds. According to Roskam (2001, p. 5) "this assumption is justified as long as the mass change is sufficiently small over a time period of 30 – 60 seconds".

³ Structural deformation, as wing bending, is disregarded.

⁴ If this is not the case, additional terms would be added in equations that would take the thrust rotation mechanism influence in aircraft's CG linear and angular motion into account.

- V. The atmosphere is calm and no wind is present during the procedure⁵;
 VI. The XZ plane is a plane of symmetry. In other words: $I_{XY} = I_{YZ} = 0$ ⁶;

All that stated, it is able to derive the six degrees of freedom EOM's, which represent a set of more simplified terms. In particular, the ones applicable for the longitudinal motion are:

$$\begin{cases} \dot{U} = -QW + RV + g \frac{C}{W_{GROSS}} + g \frac{T_X}{W_{GROSS}} - g \sin\theta \\ \dot{W} = -PV + QU + g \frac{N}{W_{GROSS}} + g \frac{T_Z}{W_{GROSS}} + g \cos\theta \\ \dot{Q} = \frac{I_{ZZ} - I_{XX}}{I_{YY}} PR - \frac{I_{XZ}}{I_{YY}} (P^2 - R^2) + \frac{M_{TCG}}{I_{YY}} + \frac{M_{ACG}}{I_{YY}} \end{cases} \quad (3.26)$$

g Gravitational acceleration

W_{GROSS} Aircraft gross weight

θ Euler angle with respect to pitch motion, or the pitch angle

M_{TCG} Propulsive pitching moment with respect to the CG

M_{ACG} Aerodynamic pitching moment with respect to the CG

The aerodynamic forces and moments in these equations, and so the thrust, are already considered with the respective signal. In addition, the forces and moments in the Newtonian version were already expanded into the aerodynamic and thrust forces in the equations above. In the Methodology section, whereupon the eVTOL tiltrotor mathematical model is described in detail, these terms are expanded in several elements, each one related to a different aircraft's region.

Finally, the lateral-directional motion is suppressed from the equations and the final form of the equations of motion applied are:

⁵ This assumption is not always true and real procedures can, in actual fact, face high tailwind, headwind or crosswind components. Since the focus is to validate the methodology, the assumption is made. Still the wind shall be taken into account depending on the application. If that is the case, the wind velocity shall be summed to the aircraft's body-axis airspeed in order to achieve \dot{X} , \dot{Y} and \dot{Z} . Nevertheless, the equations are still able to take into account the effect of gusts.

⁶ This is valid for most arising eVTOL designs;

$$\begin{cases} \dot{U} = -\dot{\theta}W + \frac{C}{M} + \frac{T_X}{M} - g\sin\theta \\ \dot{W} = \dot{\theta}U + \frac{N}{M} + \frac{T_Z}{M} + g\cos\theta \\ \ddot{\theta} = \frac{M_{TCG}}{I_{YY}} + \frac{M_{ACG}}{I_{YY}} \end{cases} \quad (3.27)$$

One must note that Q was replaced by $\dot{\theta}$ and \dot{Q} by $\ddot{\theta}$. The relationship of these variables are given by the kinematic equations that correlate angles and angular rates of body-axis and earth-axis systems:

$$\begin{cases} P = \dot{\phi} - \dot{\psi} \sin \theta \\ Q = \dot{\theta} \cos \theta + \dot{\psi} \cos \theta \sin \phi \\ R = \dot{\psi} \cos \theta \cos \phi - \dot{\theta} \sin \phi \end{cases} \quad (3.28)$$

ϕ Euler angle with respect to rolling motion, or the bank angle

ψ Euler angle with respect to yawing motion, or the yaw angle

The second equation in (3.28) leads to $Q = \dot{\theta}$ when a pure longitudinal motion is considered. In addition, its derivative allows to deduce $\dot{Q} = \ddot{\theta}$. Equations in (3.27) already take into account these conclusions.

The aerodynamic total forces and moments are a summation of several airframe regions – the fuselage, the wings (divided in two portions, upon the freestream and the rotor wake), the pylons, the spinners, the horizontal stabilizers, the vertical stabilizers, the main landing gears and the nose landing gears.

$$N = N_F + N_{iW} + N_{WFS} + N_{PYL} + N_{SD} + N_{HT} + N_{VT} + N_{MG} + N_{NG} \quad (3.29)$$

$$C = C_F + C_{iW} + C_{WFS} + C_{PYL} + C_{SD} + C_{HT} + C_{VT} + C_{MG} + C_{NG} \quad (3.30)$$

$$\begin{aligned} M_{ACG} = M_F + M_F|_{CA} + M_{iW} + M_{WFS} + M_W|_{AC} + M_{iPYL} + M_{SD} + M_{HT} + M_{HT}|_{CA} \\ + M_{VT} + M_{MG} + M_{NG} \end{aligned} \quad (3.31)$$

In Methodology section, the right hand sides of equations (3.29), (3.30) and (3.31) are expressed as a function of the motion variables.

3.6.3 Conditions Described

In order to finish describing the approach and landing problem to be optimized, the definitions of the boundary conditions for the eVTOL to comply during the SFAP procedure are depicted. Again, the conditions were chosen in a way that the procedure remains as practicable as possible.

The initial conditions where the aircraft is supposed to be at the TLP are:

$$\begin{cases} X(t_0) = X_0 \\ Z(t_0) = Z_0 \\ V_T(t_0) = V_{T0} \\ \gamma(t_0) = \gamma_0 \end{cases} \quad (3.32)$$

These values have the role of constraints in the trajectory programming. The aircraft begins trimmed at position (X_0, Z_0) flying with airspeed V_{T0} and flight path angle γ_0 . The assumptions that true airspeed and gamma are known are equivalent to prescribe \dot{X} and \dot{Z} .

During the Short Final Approach Path the aircraft transitions from cruise to hovering configuration (conversion phase). The pitch angle and, as a consequence, the angle of attack, is allowed to vary beyond the aerodynamic stall in a way that the generated drag assists an air braking. At VDP the eVTOL reaches a trimmed condition where a pure hovering movement eventually begins to finish the landing procedure tracking the Hovering Approach Path. At VDP the conditions are:

$$\begin{cases} X(t_F) = X_F \\ Z(t_F) = Z_F \\ \dot{X}(t_F) = \dot{X}_F \\ \ddot{X}(t_F) = \ddot{X}_F \\ \dot{\theta}(t_F) = \dot{\theta}_F \\ \ddot{\theta}(t_F) = \ddot{\theta}_F \end{cases} \quad (3.33)$$

Note, in turn, that vertical movement is not limited by constraints, which means that aircraft is allowed to reach VDP with remaining vertical speed or acceleration before stating hover maneuvering.

In addition to the assumptions made in the Landing Profile section, some aircraft design constraints are defined as well, to make the problem solution the most representative.

Table 4 - Safety, Comfort and Design Constraints

SAFETY, COMFORT AND DESIGN CONSTRAINTS	
Thrust angle φ	$0 \text{ deg} \leq \varphi \leq 95 \text{ deg}^7$
Thrust angle rate $\dot{\varphi}$	$ \dot{\varphi} \leq 60 \text{ deg/s}^8$
Maximum rate of sink \dot{Z}	600 ft/min
Maximum pitch angle θ_{MAX}	$\theta_{MAX} = 45 \text{ deg}$
Minimum pitch angle θ_{MIN}	$\theta_{MIN} = -10 \text{ deg}$
Pitch rate $\dot{\theta}$	$ \dot{\theta} \leq 10 \text{ deg/s}^9$
Elevator deflexion rate $\dot{\delta}_E$	$ \dot{\delta}_E \leq 50 \text{ deg/s}$

Source: Created by the author.

3.7 AXIS TRANSFORMATIONS

The EOMs deduced in the previous section positioned the forces and moments in relation to the body-axis coordinate system and the state variables (positions, speeds and accelerations) were also presented for an aircraft fixed reference frame, what makes necessary to transform terms to this system before solving the equations. First, the inertial velocities and accelerations (earth-axis) can be related to the body-axis U, \dot{U}, W and \dot{W} .

$$\begin{cases} U = \dot{X} \cos \theta + \dot{Z} \sin \theta \\ W = \dot{X} \sin \theta - \dot{Z} \cos \theta \end{cases} \quad (3.34)$$

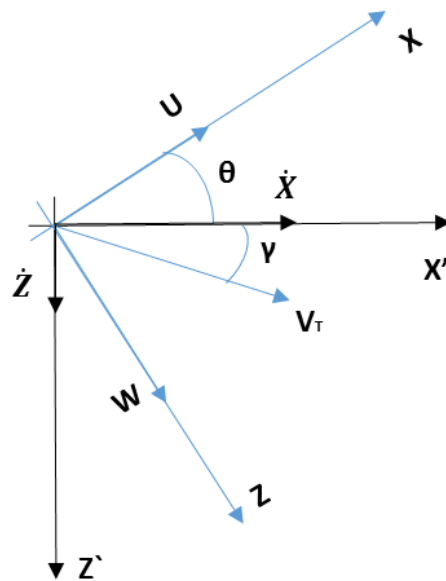
$$\begin{cases} \dot{U} = (\ddot{X} + \dot{Z}\dot{\theta}) \cos \theta + (\ddot{Z} - \dot{X}\dot{\theta}) \sin \theta \\ \dot{W} = (\ddot{X} + \dot{Z}\dot{\theta}) \sin \theta + (-\ddot{Z} + \dot{X}\dot{\theta}) \cos \theta \end{cases} \quad (3.35)$$

⁷ XV-15 design constraint (FERGUSON, 1988).

⁸See Jacob (1972, p. 9).

⁹ Idem.

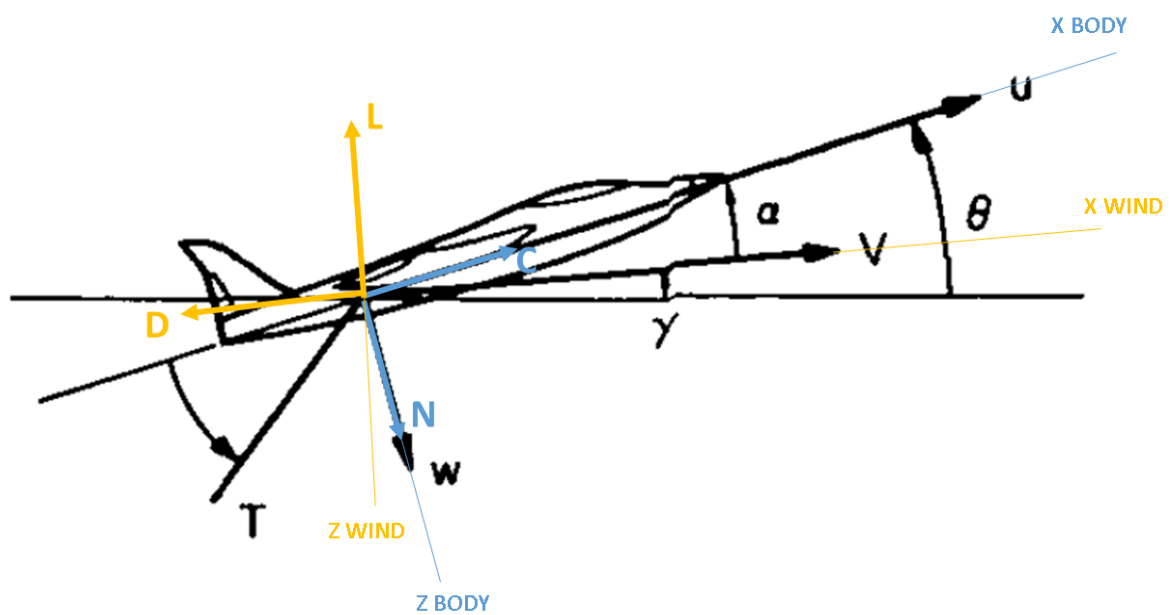
Figure 27 - Velocities in body and earth-axis systems.



Source: Created by the author.

Which gives the axis transformation between earth to body coordinate systems. Concerning the aerodynamic forces and moments, they are commonly written in terms of lift and drag in the wind-axis coordinate system. C and N can be related to these conventional aerodynamic forces. The free body diagram in Figure 28 is done in order to make the derivation clear.

Figure 28 - Relation between aerodynamic forces in different aircraft fixed reference frames.



Source: Adapted from Jacob (1972, p. 6).

$$\begin{cases} N = -L\cos\alpha - D\sin\alpha \\ C = L\sin\alpha - D\cos\alpha \end{cases} \quad (3.36)$$

Lastly, the longitudinal velocities in the mast-axis coordinate systems are transformed to its correspondents in body-axis as according to equations (3.36).

$$\begin{cases} U = U_{HM} \sin \varphi - W_{HM} \cos \varphi \cos \phi_M \\ W = U_{HM} \cos \varphi + W_{HM} \sin \varphi \cos \phi_M \end{cases} \quad (3.36)$$

ϕ_M Lateral mast tilt (angle between mast Z_M -axis and body Z -axis)

U_{HM} Horizontal speed along mast X -axis

W_{HM} Vertical speed along mast z -axis

3.8 GENETIC ALGORITHMS

3.8.1 Introduction

The Genetic Algorithm (GA), proposed by Holland, (1973), is a biologically inspired stochastic algorithm search. This type of algorithm is inspired by Charles Darwin's theory of natural selection (DARWIN, 1859), which states that the fittest organisms – the organisms that are better suited to a given environment - have a greater chance of producing offspring and pass forward their genetic information. Basically, a genetic algorithm is divided in the following steps:

1. Initialize the population by generating random individuals;
2. Select parents for the mating pool (size of mating pool is the same of population size);
3. Shuffle the mating pool;
4. For each consecutive pair in the mating pool apply crossover with probability p_C , otherwise copy parents;
5. For each offspring apply mutation (with probability p_M independently for each gene);
6. Replace the whole population with the resulting offspring;
7. Repeat steps 2 to 6 until a given stopping criterion is met.

3.8.2 Representation

The first step involved in a genetic algorithm is the representation. Representation can be understood as the mapping of biology into a computational problem. For this representation, one must follow the metaphors of genetics: gene and chromosome. The smallest piece of information represents the gene while the whole information represents the chromosome, that is, the set of genes.

There are three types of representations: binary, integer and real-valued representations. Focus is given to binary and real-valued ones. For information on integer representation, see Eiben and Smith (2015). For the binary representation, each individual (candidate solution) is represented as a bit-string. Note that the length of the string, that is, the number of bits, is determined according to the desired precision. It is worth mentioning that high precision implies not only long chromosomes, but also high tendency for a slow evolution. Note that if the value is real-valued, it is also possible to use the binary approach. In this case, the following equation is used to decode the bit string of a given individual into a floating-point value.

$$x_{LB} + \frac{y_{UB} - x_{LB}}{2^n - 1} \left(\sum_{j=0}^{n-1} a_{n-j} 2^j \right) \in [x_{LB}, y_{UB}] \quad (3.37)$$

x_{LB} Lower bound of the domain

y_{UB} Upper bound of the domain

a_{n-j} $(n - j)$ -th bit (gene) of an individual's bit string

3.8.3 Fitness Function

Fitness or cost function is a procedure used to evaluate how close an individual in the population is to the solution of a given problem. Technically, it is a function or procedure that assigns a score to an individual in order to define its quality as a candidate solution. For instance, for the problem of finding the value x that maximizes $f(x) = -x^2$, $f(x)$ is the fitness function itself.

3.8.4 Parent Selection

Parent selection is the step responsible for mimicking the environmental pressure aspect of Darwin's theory. In other words, is the selection of the best fit individuals of a given environment, who have the greater chance of producing offspring closer to the final solution and keep passing forward their genetic information. Hence, it is a basic requirement that parent selection algorithms make distinction among individuals according to their fitness. Two kinds of strategies commonly used for individuals' selection are tournament and roulette selections. The tournament strategy consists of randomly select (with replacement) at least two individuals of the population and the ones with higher scores are considered the winners and become parents. Another strategy is the roulette selection. This method follows the same concept of repeatedly spinning a roulette wheel, where the sizes of the pockets reflect the selection probabilities. The method can be adjusted to choose more fit individuals. The algorithm generic illustrated in Figure 29.

Figure 29 - Roulette algorithm diagram.

Pre-condition: for each chromosome c_i is possible to quantify a fitness f_i . The whole population, that is, all the chromosomes, is sorted based on fitness.

$total_fitness \leftarrow \sum_{i=1}^N f_i$

$r \leftarrow \text{random_value}(0, total_fitness)$

$partial_fitness \leftarrow 0$

$i \leftarrow 0$

repeat

$i \leftarrow i + 1$

$partial_fitness \leftarrow partial_fitness + f_i$

until $partial_fitness \geq r$

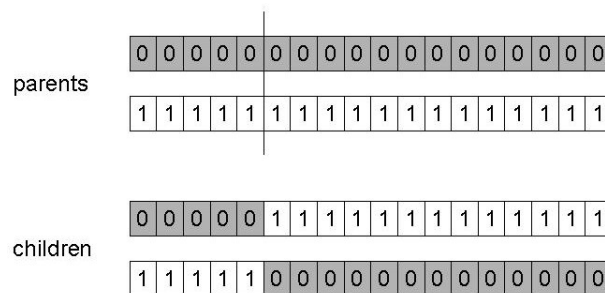
return c_i

3.8.5 Crossover

Selected the parents, the next step is applying some kind of crossover in order to produce offspring. Crossover is an important step because it is one of the mechanisms responsible for population diversity. Diversity is a crucial aspect when it comes to evolution theory since new individuals are generated in such a way that the best ones survive, reproduce, and so evolution takes place. For the binary representation, three kinds of crossover operations are the most common: one-point crossover (HOLLAND, 1992), n-point crossover and uniform crossover (SYSWERDA, 1989).

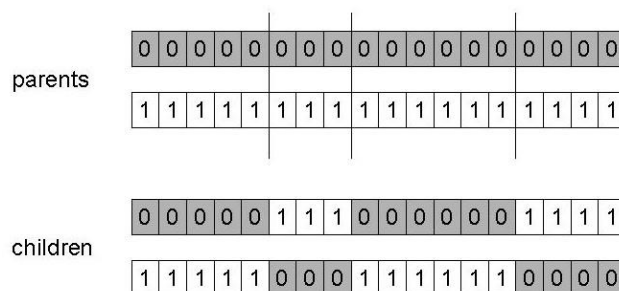
The former is applied to two parents and produces two children by choosing a random crossover-point along the strings and swapping the bits of the parents after this point (see Figure 30. The generalization for this operator is called the n-point crossover (Figure 31).

Figure 30 - One-point crossover.



Source: Created by the author.

Figure 31 - N-point crossover (example with $n = 3$).

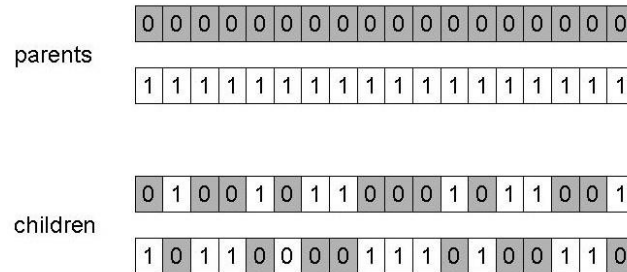


Source: Created by the author.

Conversely, the latter, or the uniform crossover method, works by treating each gene independently and making a random choice regarding which parent it should be inherited from. This is implemented by generating a string of l random variables from a uniform distribution over $[0,1]$. In each position, if the value is below a parameter p (usually 0.5), the

gene is inherited from the first parent. Otherwise from the second. The second offspring is created using the inverse mapping. This kind of operator is illustrated in Figure 32.

Figure 32 - Uniform crossover.



Source: Created by the author.

3.8.6 Mutation

Diversity is also achieved by means of mutations. They are small random variations that occur during reproduction. These variations create new individuals, generally not possible to be born through crossover only. In terms of search space, mutation is an important operator to help avoiding concentration around a local optimum. For each offspring delivered by crossover, mutation operates by altering each gene independently with a small probability p_M . For the binary representation, mutation can be simulated by flipping each gene independently with that small probability. For the real-valued representation, the most straightforward strategy to determine a new value for the i -th gene is drawing uniformly such a value from $[x_{LB}, y_{UB}]$, the domain of the i -th gene. Another strategy is drawing this new value from a Gaussian distribution with mean zero and user-specified standard deviation, in such a way that the resulting value is within the domain $[x_{LB}, y_{UB}]$. For information on other strategies for mutation, see Eiben and Smith (2015).

3.8.7 Stopping Criterion

A common criterion to stop a GA is waiting the algorithm reach a point such that no significant evolution is observed after a given number of iterations. That is, when the best fitness does not exhibit a significant improvement after a given number of iterations. The threshold value for defining what significant improvement means can be given, for instance, in terms of percentage of fitness variation.

4 METHODOLOGY

4.1 INTRODUCTION

Henceforth, this section presents the methodology used to build the model of the eVTOL aircraft in detail, as well as the search method chosen to find the optimal solution to the approach and landing problem described in the previous section.

The aircraft model was organized into several interconnecting parts, so that the model dynamic solution is a result of the integration of the various parts. The EOMs, the safety, comfort and design constraints and the inputs and outputs of the search algorithm communicate during the simulation of the movement along the trajectory. Several ways of controlling the aircraft to comply with the route are tested, until the solution of minimum energy expenditure is found and delivered as an output of the algorithm.

The mathematical model structure was divided into several parts or subsystems herein itemized:

1. Aircraft State Parameters;
2. Inertia and Balance;
3. Powerplant;
4. Fuselage Aerodynamics;
5. Wing-Pylon Aerodynamics;
6. Empennage Aerodynamics;
7. Landing Gear Aerodynamics;
8. Equations of Motion;
9. Machine Learning.

Each subsystem of the model structure is developed on its mathematical equations, whereupon variables from other subsystems are used every time a relationship exists. Aircraft State Parameters defines all the position, speeds and accelerations for the longitudinal motion. The propulsion and electric systems are treated separately into three different subsystems. The first one, the Powerplant, discusses the electric motors selection and holds

the deck data. The second expands the aerodynamics of the rotors, whereas the Batteries Energy Expenditure subsystem shows the general power calculation under efficiency considerations.

A number of subsystems consider all the airframe aerodynamics. Tables of the main aerodynamic coefficients are depicted. Before solving the equations of motion, aerodynamic forces calculated in terms of lift and drag in the wind-axis system are transformed into their correspondent body-axis system forces and kinematic ground based parameters into their body-axis correspondents either.

The Equations of Motion subsystem performs the forces and moments summation and the EOMs solution. For each step, a trim routine runs solving the equations according to aircraft model. The entire path solution must pass through validation criteria in order to comply with safety, comfort and design constraints. Finally, the Machine Learning subsystem receives a spreadsheet data with all the solutions found and carry out data classification, regression modeling and optimization through search codes which outputs the optimum solution.

Microsoft Excel software (MICROSOFT, 2013a) is used to build the eVTOL model, which encompass subsystems 1 to 8. The Machine Learning codes were implemented in R, using RStudio software (RSTUDIO, 2019) by means of methods for classification and regression. A genetic algorithm, also programmed in R, uses the models created for classification and regression prediction as inputs and search for the optimum solution.

4.2 AIRCRAFT STATE PARAMETERS

In the previous section, describing both the initial and final conditions for the Short Final Approach Path, constraints were defined for the Thrust Lifting Point and Vertical Descent Point. In addition to these, two more hypothesis are made regarding first, the path profile and second, the acceleration in the horizontal direction.

To formulate the SFAP in terms of equations, one must state first that the profile choice is arbitrary, provided that it makes the role of a probable route chosen by the pilot or the

automatic controller, based on previous waypoints. Thus, as a proof of concept, an elliptical path is chosen and the equations are derived for it.

In summary, the whole set of constraints for trajectory programming are:

- I. Initial conditions – statements (3.32);
- II. Final conditions – statements (3.33);
- III. Maximum rate of sink \dot{Z} – Table 4 - Safety, Comfort and Design ConstraintsTable 4 - ;
- IV. The trajectory profile satisfies the equation of an ellipse;

Boundary conditions I to IV allows one to proceed with the set of equations that dictate the elliptical path. Condition III, in turn, is addressed in the codes using a methodology of ensemble classification. Section 4.10.1 shows the details about how this restriction is formulated. The first ellipse quarter is the portion selected to represent the whole path. This quarter is translated to the left in a magnitude equal to its semi-major axis. The starting and final points are known and are (X_0, Z_0) and (X_F, Z_F) respectively. The difference between X_F and X_0 gives the total distance traveled horizontally, or the procedure range. X_0 is then placed as the total range and the final position X_F as zero. Altogether, the associated mathematical problem yields:

$$\frac{(X + a)^2}{a^2} + \frac{(Z - Z_F)^2}{b^2} = 1 \quad (4.1)$$

a Ellipse semi-major axis

b Ellipse semi-minor axis

Now, equations for vertical position, speed and acceleration can be derived for both vertical and horizontal motions. The former, or the vertical motion, is a result upon solving (4.1) for $Z(t)$. $\dot{Z}(t)$ and $\ddot{Z}(t)$ are the first and second time derivatives of $Z(t)$.

$$Z(t) = \frac{b}{a} \sqrt{a^2 - (X(t) + a)^2} + Z_F \quad (4.2)$$

$$\dot{Z}(t) = -\frac{b^2 (X + a)\dot{X}}{a^2 (Z - Z_F)} \quad (4.3)$$

$$\ddot{Z}(t) = -\frac{b^2 [\dot{X}^2 + \ddot{X}(X + a)]}{a^2 (Z - Z_F)} - \frac{\dot{Z}^2}{(Z - Z_F)} \quad (4.4)$$

Reviewing equations (4.1) and (4.3) along with the trajectory constraints leads to semi-minor axis b and semi-major axis a expressions. First, using the constraints of known \dot{X}_0 and \dot{Z}_0 , calculated from V_{TO} and γ_0 and evaluating $\dot{Z}(t)$ at $t = 0$. Lastly, evaluating $Z(t)$ at $t = 0$. The last step is to solve equations for a and b . Carrying out these steps the ellipse axes are expressed as follows:

$$a = \frac{X_0[X_0 - \frac{\dot{X}_0}{\dot{Z}_0}(Z_0 - Z_F)]}{\frac{\dot{X}_0}{\dot{Z}_0}(Z_0 - Z_F) - 2X_0} \quad (4.5)$$

$$b = \sqrt{-\frac{a^2 \dot{Z}_0(Z_0 - Z_F)}{\dot{X}_0(X_0 + a)}} \quad (4.6)$$

4.3 INERTIA AND BALANCE

4.3.1 Scaling

The tiltrotor eVTOL model must have geometric measurements typical of those arising air taxi travel designs, which is feasible by adapting the XV-15 aircraft to the size of the intended concept. Its actual size and powerplant are not adequate for the purpose pursued. But its weight and balance, geometric and aerodynamic data are of great value to make the model robust and representative of a VTOL design. Thus, describing the way of scaling its size to suit the one of a typical air taxi eVTOL is the desired outcome of this section.

Normally, the scaling process is done in order to build smaller replicas of a full-size aircraft and study its flight dynamics characteristics. They are useful to the first phases of aircraft design. Obviously, in order to obtain valid results, a prototype must be built in a specific manner, in such a way its motions are similar to those of the full-scale article. This premise makes the same process, relative to the NASA XV-15, applicable to the conception of the mathematical tiltrotor eVTOL model.

The scaled prototype must react to external forces and move so the relative positions of its components have geometric similarity of those expected for the full-scale subject after a proportional period of time. This similarity of dynamic behavior and geometry is known as

dynamic similitude. Note that, dynamic similitude implies that, in addition to geometric aspects, scale ratios of force and mass are preserved.

When properly constructed and tested, the flight path and angular displacements of the scaled prototype and the vehicle will be geometrically identical, even though the time required for selected motions are different and may demand application of mathematical factors in order to interpret the results.

The simplest type of dynamic free-flight model uses the incompressible flow assumption. It does not attempt to simulate flexible structural properties such as aeroelastic bending modes or flutter properties. This comply with the considerations made when describing the approach and landing problem. The scale factors assuming an incompressible flow are given in

Table 5 - Scale factors for incompressible flow assumption..

Table 5 - Scale factors for incompressible flow assumption.

PROPERTY	SCALE FACTOR
Linear dimension	n
Relative density	1
Froude number	1
Angle of attack	1
Linear acceleration	1
Weight, mass	n^3/σ
Moment of inertia	n^5/σ
Linear velocity	$n^{0.5}$
Angular velocity	$1/n^{0.5}$
Time	$n^{0.5}$
Reynolds number	$n^{1.5}v/v_0$
Multiply full-scale values by the indicated scale factors to determine model values.	

Source: Adapted from (CHAMBERS, 2009, p. 11)

n Ratio of model-to-full-scale dimensions

σ	Ratio of air density
ν	Kinematic viscosity
ν_0	Kinematic viscosity at sea level

Some similitude limitations can be faced when scaling an aircraft. The discrepancy between the scaled concept and the real design in the Reynolds number is the most significant aspect that affects the results, since Reynolds effects are dependent upon geometric characteristics and, in many times, can deliver complex analysis in evaluating its effects. One of the most affected data is the lift polar, or the CL vs Angle of Attack curve. When, for instance, the model is being used to predict the maximum lift coefficient that the full scale aircraft will achieve and its dynamic behavior near and above aerodynamic stall. However, since the scaling process for the eVTOL mathematical model already takes credit of aerodynamic data of the full-scale article, the NASA XV-15, this limitation does not suit.

The scale geometric factor chosen was 2, or $n = 2$. In that way, all geometric data is divided by 2, weight by 8 and moments of inertia by 32, while aerodynamic coefficients are maintained. The ratio of air density is considered unitary ($\sigma = 1$).

4.3.2 Modeling

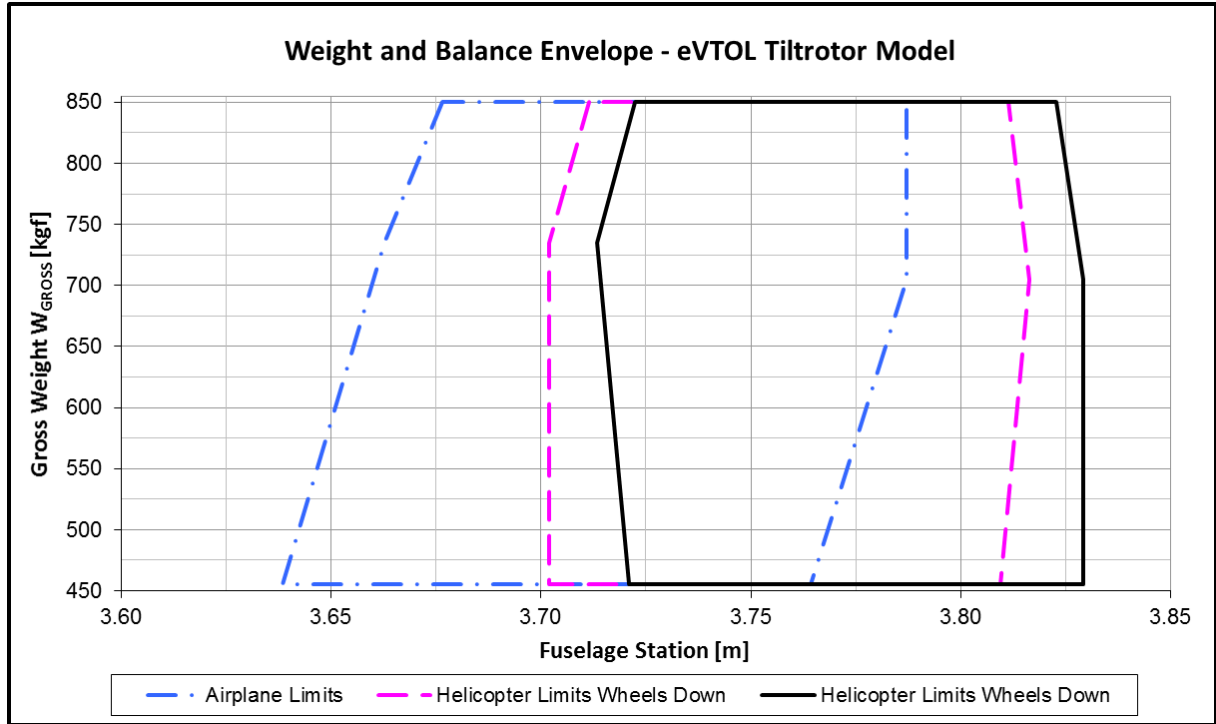
The Weight and Balance subsystem defines parameters of aircraft weight, inertia and center of gravity. It also provides modeling for CG location and inertia changes due to pylon tilt.

Initially, using the scale factor $n = 2$ for geometric and weight data of the NASA XV-15 aircraft, the weight and balance envelope, also known as W-CG diagram, is defined in Figure 33. It depicts the CG longitudinal location in terms of fuselage station representation as a function of the eVTOL tiltrotor gross weight.

The two flight phases must be taken into account in a tiltrotor design, the airplane (cruise) mode and the helicopter (hover) mode. The W-CG diagram has different formats depending on the flight mode. In other words, the permitted CG positions for a specific gross weight value vary if the aircraft is in cruise or hover regime. In addition, it also changes if landing gears are retracted or extended when hovering. Notwithstanding this configuration

dependence in the W-CG envelope, the only one applicable for the short final segment is the ‘Helicopter Limits Wheels Down’ diagram. Next, description for CG displacement as a function of pylon tilt angle, CG location and moment of inertia I_{YY} change due to pylon tilt are provided.

Figure 33 - Weight and Balance envelope for the eVTOL tiltrotor model.



Source: Created by the author using Microsoft Excel (MICROSOFT, 2013a).

- CG Displacement as a Function of Thrust Angle

$$X_{CG} = Z_K \sin(90 - \varphi) + X_K(1 - \cos(90 - \varphi)) \quad (4.7)$$

$$Z_{CG} = Z_K(1 - \cos(90 - \varphi)) - X_K \sin(90 - \varphi) \quad (4.8)$$

Where

$$Z_K = \frac{W_{PYL}}{W_{GROSS}} (WL_{NAC} - WL_{PYL}) \quad (4.9)$$

$$X_K = \frac{W_{PYL}}{W_{GROSS}} (FS_{NAC} - FS_{PYL}) \quad (4.10)$$

X_{CG} CG fuselage station displacement due to pylon tilt

Z_{CG} CG water line displacement due to pylon tilt

W_{PYL}	Weight of both pylons for a tilt rotor
FS_{NAC}	Fuselage station of engine nacelle shaft pivot point for a tilt rotor
FS_{PYL}	Fuselage station of pylon center of gravity for a tilt rotor
WL_{NAC}	Water line of pylon center of gravity for a tilt rotor
WL_{PYL}	Water line of engine nacelle shaft pivot point for a tilt rotor

- CG Location

$$FS_{CG} = FS_{CG}|_{\varphi=90^\circ} + X_{CG} \quad (4.11)$$

$$WL_{CG} = WL_{CG}|_{\varphi=90^\circ} + Z_{CG} \quad (4.12)$$

$FS_{CG}|_{\varphi=90^\circ}$ CG fuselage station of hover mode

$WL_{CG}|_{\varphi=90^\circ}$ CG water line of hover mode

- Moment of Inertia I_{YY} Change Due to Pylon Tilt and Lateral Mast Tilt Angle

$$I_{YY} = I_{YY}|_{\varphi=90^\circ} - K_I(90 - \varphi) \quad (4.13)$$

$$\phi_M = \frac{\phi_M|_{\varphi=90^\circ}}{90} \varphi + \phi_M|_{\varphi=0^\circ} \quad (4.14)$$

$I_{YY}|_{\varphi=90^\circ}$ Hover mode pitching moment of inertia, body-axis

K_I Pitch inertia coefficient for varying inertia with φ for a tilt rotor

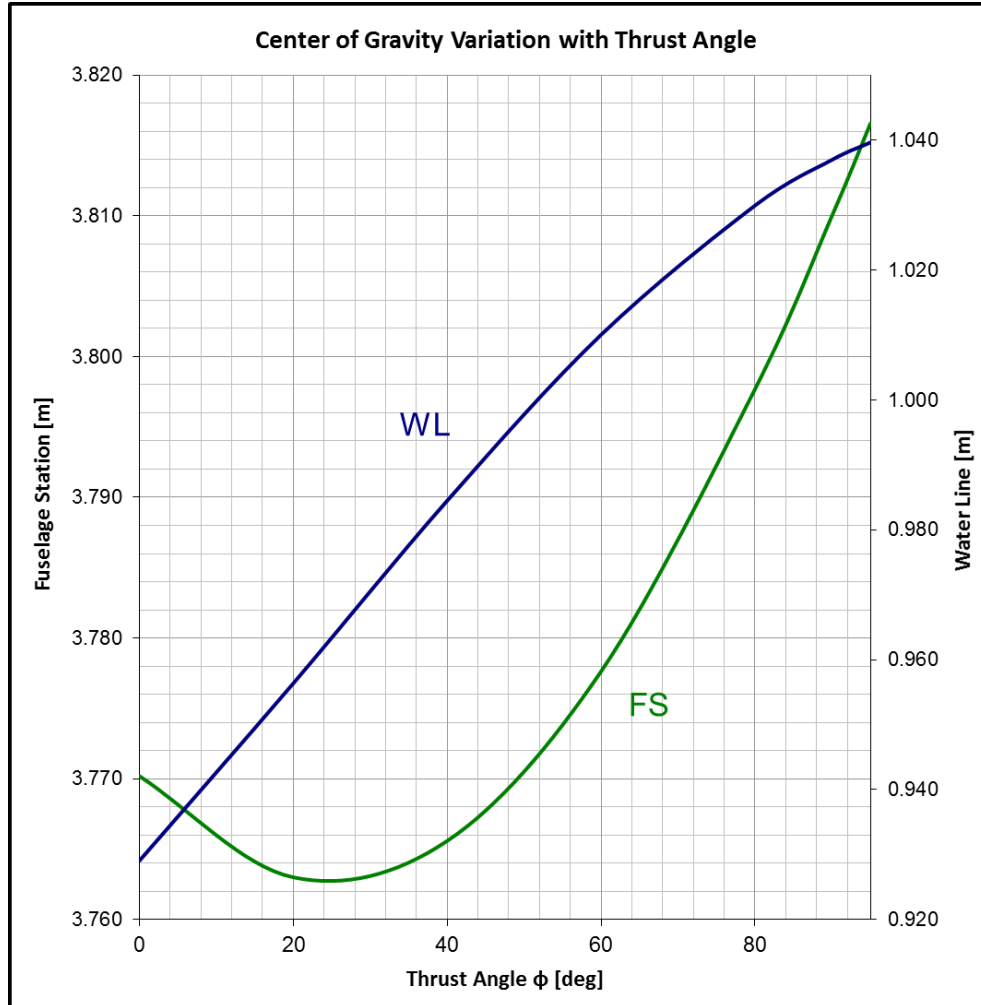
$\phi_M|_{\varphi=90^\circ}$ Hover mode lateral mast tilt angle

$\phi_M|_{\varphi=0^\circ}$ Airplane mode lateral mast tilt angle

Center of gravity variation with thrust angle according to equations (4.11) and (4.12) is depicted in the sequence considering the whole pylon tilt range from 0 to 95 degrees.

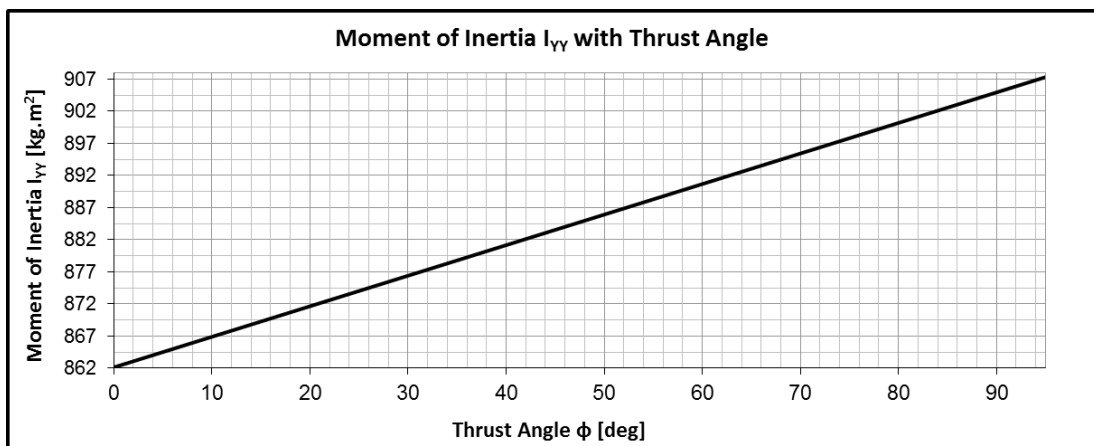
Whereas equation (4.18) leads to a linear variation of moment of inertia I_{YY} with thrust angle ϕ . Values for all involved variables are provided in the Simulation and Results section.

Figure 34 - CG variation with pylon tilt.



Source: Created by the author using Microsoft Excel (MICROSOFT, 2013a).

Figure 35 - I_{YY} variation with pylon tilt.



Source: Created by the author using Microsoft Excel (MICROSOFT, 2013a).

4.4 POWERPLANT

4.4.1 Motors Selection

For a propeller-driven aircraft, a relevant parameter for measuring performance is the power loading. Power loading is the reciprocal of power-to-weight ratio, which is the thrust per unit mass multiplied by the velocity of any aircraft. In the aeronautical literature, power loading is given by W_{GROSS}/P_{ENG} , where W_{GROSS} is the gross weight of the aircraft and P_{ENG} is the engine power. Thus, the power loading parameter indicates that a low value is associated to high performance in terms of maximum speed, takeoff and climb. This means that for a given gross weight of an aircraft, the higher the engine power, the higher the maximum speed and the faster will be both takeoff and climb. Note, however, that a low value of power loading also indicates high fuel burn for a fuel-powered engine or high electricity consumption for a battery-powered engine. As can be seen from Table 6, typical values of power loading ranges from 10 to 15 pounds per horsepower for most aircraft types.

Table 6 - Typical power loading by design.

Aircraft type	Typical P/W		Typical power loading lb/hp
	hp/lb	Watt/g	
Powered sailplane	0.04	0.07	25
Homebuilt	0.08	0.13	12
General aviation - single engine	0.07	0.12	14
General aviation - twin engine	0.17	0.3	6
Agricultural	0.09	0.15	11
Twin turboprop	0.2	0.33	5
Flying boat	0.1	0.16	10

Source: Adapted from Raymer (1992).

The original XV-15 engine is a turboshaft Lycoming that drives a propeller with 1250 *hp* in normal cruise operation and 1550 *hp* during takeoff. Since the concept is being scaled and it is an eVTOL model, an electric engine with proper dimensions is selected for it. The whole powerplant is based on electric propulsion.

When scaling a prototype or aircraft, it is possible to demonstrate using Table 5 scale factors for linear velocity and linear dimension that the aerodynamic force, and therefore its components lift and drag, is multiplied by the same factor as the weight n^3 . Once the thrust must counterbalance the drag, this means that the Thrust to Weight ratio T/W_{GROSS} of the scaled concept can be preserved as the same of the original aircraft, the NASA XV-15. The same applies for power loading.

$$\text{Installed Power} = 2 * 1550 \text{ hp} = 3100 \text{ hp} \quad (4.15)$$

$$\text{Design Gross Weight} = 13000 \text{ lbs} \quad (4.16)$$

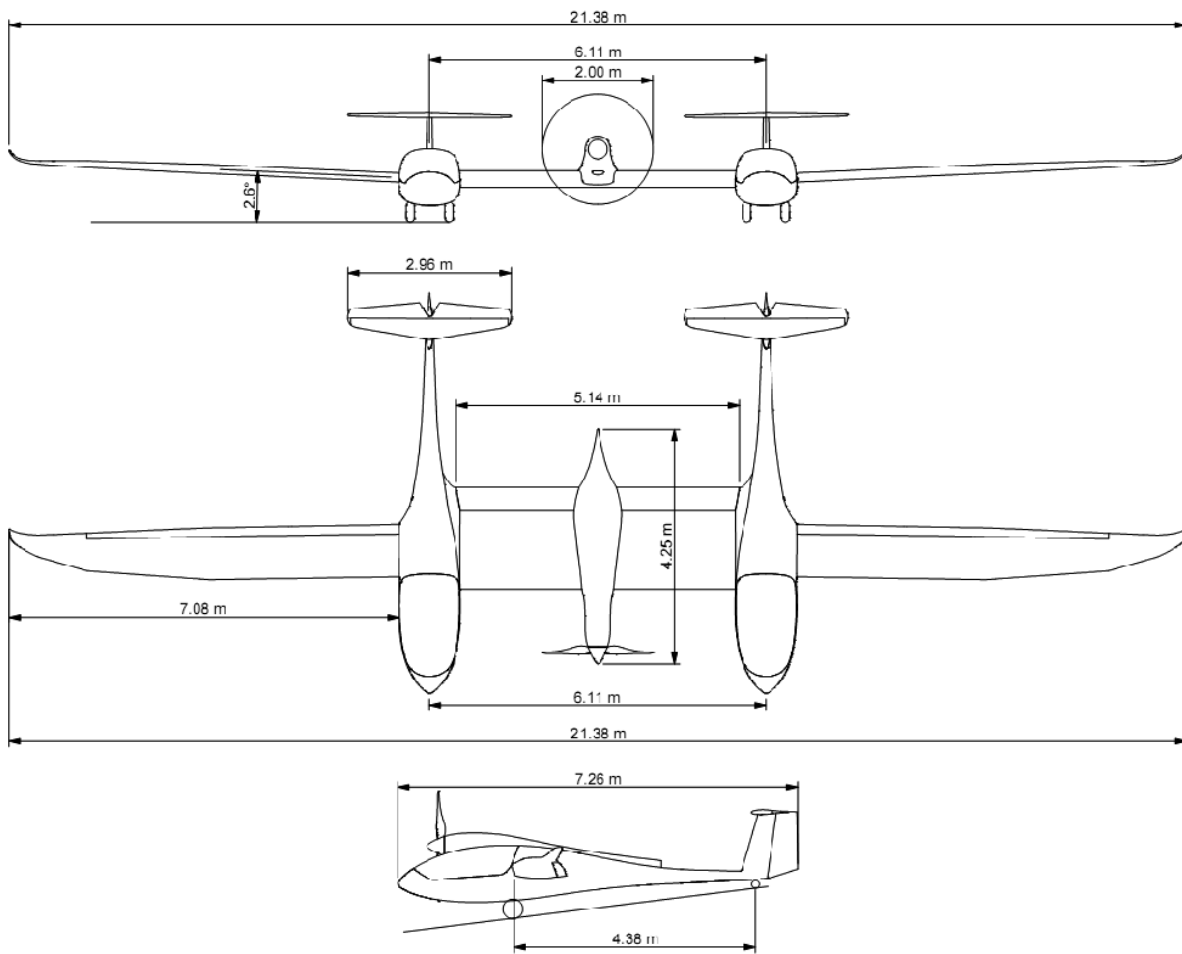
$$\text{Power Loading} = W/P = 13000/3100 = 4.2 \text{ lb/hp} \quad (4.17)$$

Which is near the statistical data provided by Raymer (1992) for general aviation – twin engine, the closest design of those listed. Data for emerging eVTOLs concepts are still raising and are difficult to find from reliable sources. The scaled concept weights 1625 lbs (XV-15 gross weight divided by 8). In order to keep the same power loading the concept powerplant must have an installed power of:

$$\text{eVTOL Installed Power} = 1625/4.2 = 387 \text{ hp or } 193 \text{ hp (per engine)}; \quad (4.18)$$

Altogether, the AEA Pipistrel Taurus G4, winner of the 2011 NASA Green Flight Challenge has a specific power demand that comply with those aimed for the model (TOMAZIE et al., 2011). Its 201 hp electric engine is chosen then as the one to be part of the eVTOL model. It is a fixed-pitch propeller design that behaves much like a constant-speed propeller on an equivalent reciprocating engine. That is because electric propulsion can deliver power at flexible RPM.

Figure 36 - Pipistrel Taurus G4



Source: Tomazie *et al.* (2011, p. 876).

4.4.2 Rotor Aerodynamics

The combination of rotors and airframe produces interferences that affects directly the aircraft motion. It is investigated deeply and embodied by means of mathematical correlations in the model the effect of the rotor wake on the wing and horizontal stabilizer lift and drag. The rotors mathematical model is based on Castles and New (1952) McCormick Jr. (1967) Ferguson (1988) Kimberling (2003).

The rotor wake and airframe interaction with the ground affects the pitch moment regarding the aircraft longitudinal motion. However, it is considered that the distance of the VLP from the ground is far enough to neglect these interaction effects. When evaluating the complete landing with the HAP portion in future works, this remark shall be reconsidered.

The rotor induced velocity at the wing and horizontal stabilizer are a function of the isolated uniform propeller induced velocity and rotor parameters such as the inflow and advance ratios.

- Rotor Wake

$$R_W = R_D \left\{ 0.78 + 0.22 \exp \left[- \left(0.3 + \frac{2l_m}{R_D} \sqrt{0.129C_T + 7.74C_T} \right) \right] \right\} \quad (4.19)$$

R_W Rotor wake contraction ratio

R_D Disc radius

l_M Mast length

- Rotor Wake at Wing in Mast-Axis

$$w_i|_{R/W} = (K_0 + K_1\mu + K_2\mu^2 + K_3\lambda_i + K_4\lambda_i^2)(w_i) \quad (4.20)$$

$w_i|_{R/W}$ Induced velocity at the wing in mast-axis due to the rotor

K_{0-4} Constants in the rotor/wing wake equation

μ In-plane velocity ratio at the mast-axis $X_M Y_M$ plane

λ_i Inflow ratio

w_i Uniform induced velocity, mast-axis

- Inflow and In-Plane Velocity Ratios

$$\mu = \frac{V_{TPP}}{\Omega' R_D} \quad (4.21)$$

$$\lambda_i = \frac{V_{NTPP} + w_i}{\Omega' R_D} \quad (4.22)$$

Where,

$$\Omega' = \Omega + \dot{\theta} \sin \varphi \sin \phi_M \quad (4.23)$$

$$V_{TPP} = \sqrt{U_{HM}^2 + V_{HM}^2} \quad (4.24)$$

$$V_{NTPP} = -W_{HM} \quad (4.25)$$

$$U_{HM} = U_{HB} \sin \varphi + W_{HB} \cos \varphi \cos \phi_M \quad (4.26)$$

$$V_{HM} = W_{HB} \sin \phi_M \quad (4.27)$$

$$W_{HM} = -U_{HB} \cos \varphi + W_{HB} \sin \varphi \cos \phi_M \quad (4.28)$$

$$U_{HB} = U - \dot{\theta} L_{ZH} \quad (4.29)$$

$$W_{HB} = W - \dot{\theta} L_{XH} \quad (4.30)$$

$$L_{XH} = (FS_{CG} - FS_{NAC}) + l_M \cos \varphi \cos \phi_M \quad (4.31)$$

$$L_{ZH} = (WL_{NAC} - WL_{CG}) + l_M \sin \varphi \cos \phi_M \quad (4.32)$$

V_{TPP} True airspeed tangential component to the mast-axis $X_M Y_M$ plane

V_{NTPP} True airspeed normal component to the mast-axis $X_M Y_M$ plane

Ω' Rotor speed corrected for angular rate

U_{HM} Horizontal speed along mast X_M -axis

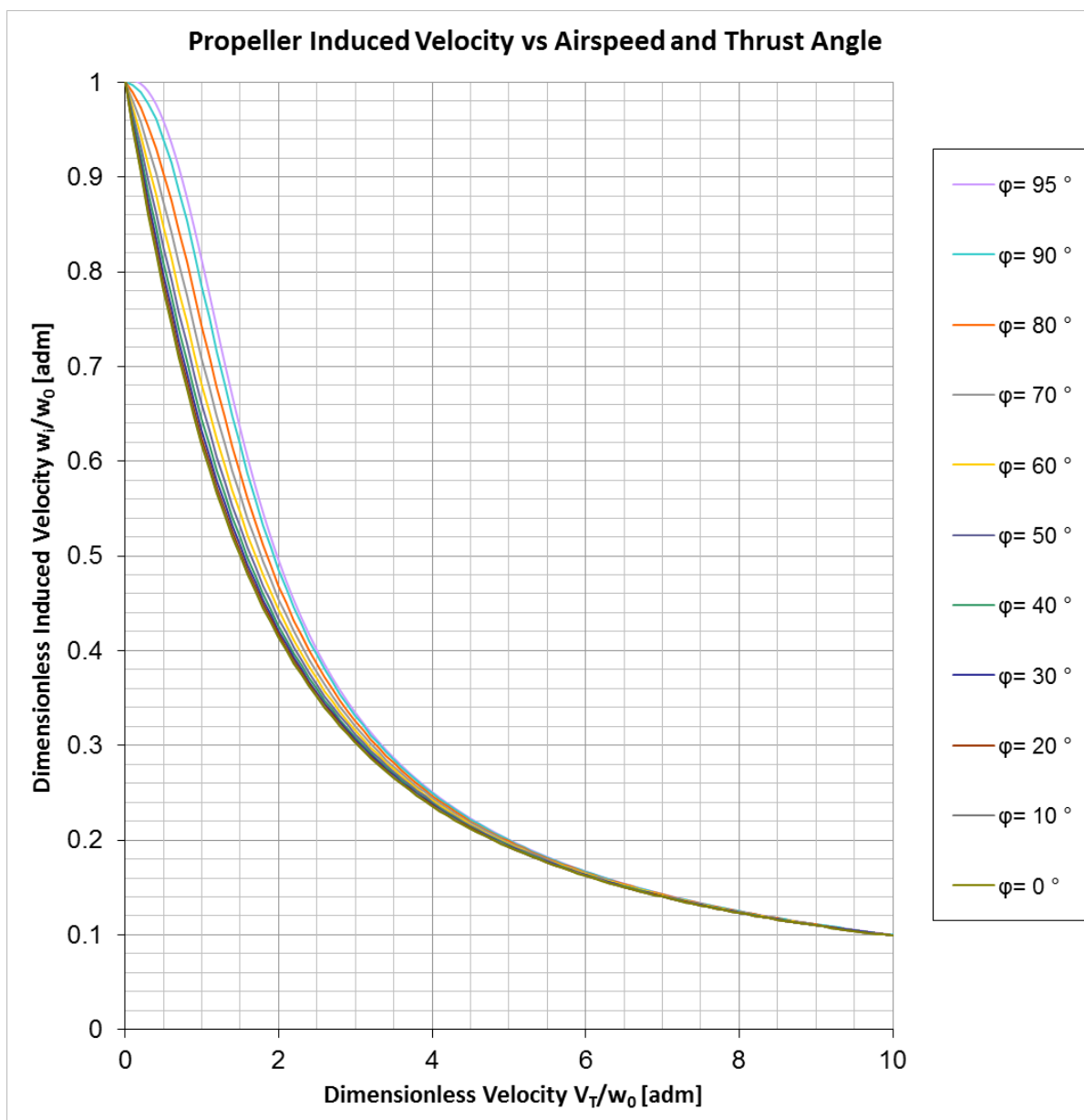
V_{HM} Lateral speed along mast Y_M -axis

W_{HM} Vertical speed along mast Z_M -axis

No distinction is made between the right and left rotors, which means that the engines inputs and outputs are symmetrical in the eVTOL model. Furthermore, for a simpler reading, the uniform induced velocity is referred as induced velocity only.

In section 3.4.4 theory regarding vectored propellers was evolved. Equations (3.19) and (3.21) can be solved numerically where dimensionless ideal power P_i/P_0 and dimensionless induced velocity w_i/w_0 are found as a function of the independent variables V_0/w_0 and φ , the dimensionless airflow non-disturbed velocity and the thrust angle respectively. For now, the induced velocity curve is plotted as a function of V_0/w_0 , whereas power is detailed in section 4.4.4. Each curve represents a fixed value of φ .

Figure 37 - Propeller induced velocity versus speed and thrust angle.



Source: Created by the author using Microsoft Excel (MICROSOFT, 2013a).

For a propeller-driven aircraft, the airflow non-disturbed velocity V_0 is the proper true airspeed V_T . In order to evaluate the velocity increment produced by a propeller w_i the graph depicted in Figure 37 shall be utilized as follows: for an aircraft flying with true airspeed V_T and the propeller generating a thrust T , first the induced velocity to produce the thrust T statically must be calculated. Hence, with V_T/w_0 the plot for the current thrust angle φ is consulted to obtain w_i/w_0 and then w_i .

Figure 38 - w_i/w_0 determination diagram.

$$(T, \varphi, V_T) \rightarrow w_0 = \sqrt{\frac{T}{2\rho A}} \rightarrow \frac{V_T \varphi \text{ plots } w_i}{w_0} \rightarrow w_i = \left(\frac{w_i}{w_0}\right) w_0$$

Source: Created by the author.

- Components of Rotor Wake at Wing in Body-Axis

$$U_i|_{R/W}^B = w_i|_{R/W} \cos \varphi \cos \phi_M \quad (4.33)$$

$$W_i|_{R/W}^B = -w_i|_{R/W} \sin \varphi \cos \phi_M \quad (4.34)$$

$U_i|_{R/W}^B$ Induced x-velocity at the wing in body-axis due to the rotor

$W_i|_{R/W}^B$ Induced z-velocity at the wing in body-axis due to the rotor

- Rotor Wake at Horizontal Stabilizer in Mast-Axis

$$w_i|_{R/H} = \left(\frac{w_i|_{R/H}}{w_i}\right) \left(\frac{1}{\tau_i S_{HT} + 1}\right) (w_i) \quad (4.35)$$

Where,

$$\frac{w_i|_{R/H}}{w_i} = f(\alpha_F, \varphi, V_T) \quad [\text{Table A-1}] \quad (4.36)$$

$$\tau_i = \frac{l_{XRH}}{U} \quad (4.37)$$

$$l_{XRH} = [FS_{HT} - (FS_{NAC} - l_M \cos \varphi)] \quad (4.38)$$

$w_i|_{R/H}$ Induced mast Z_M -axis rotor wake velocity on the horizontal stabilizer

$\frac{w_i|_{R/H}}{w_i}$ Ratio of the induced mast Z_M -axis rotor wake velocity on the horizontal stabilizer to the uniform induced velocity at the rotor

S_{HT} Horizontal stabilizer area

FS_{HT} Fuselage station of the horizontal stabilizer center of pressure

- Components of Rotor Wake at Horizontal Stabilizer in Body-Axis

$$U_i|_{R/H}^B = w_i|_{R/H} \cos \varphi \cos \phi_M \quad (4.39)$$

$$W_i|_{R/H}^B = -w_i|_{R/H} \sin \varphi \cos \phi_M \quad (4.40)$$

$U_i|_{R/H}^B$ Induced x-velocity at the horizontal stabilizer in body-axis due to the rotor

$W_i|_{R/H}^B$ Induced z-velocity at the horizontal stabilizer in body-axis due to the rotor

The components of rotor wake at the wing (4.33) and (4.34) and at the horizontal stabilizer (4.39) and (4.40) are the application of the axis transformation from mast to body-axis - equations (3.36) - regarding the induced velocity due to the rotors.

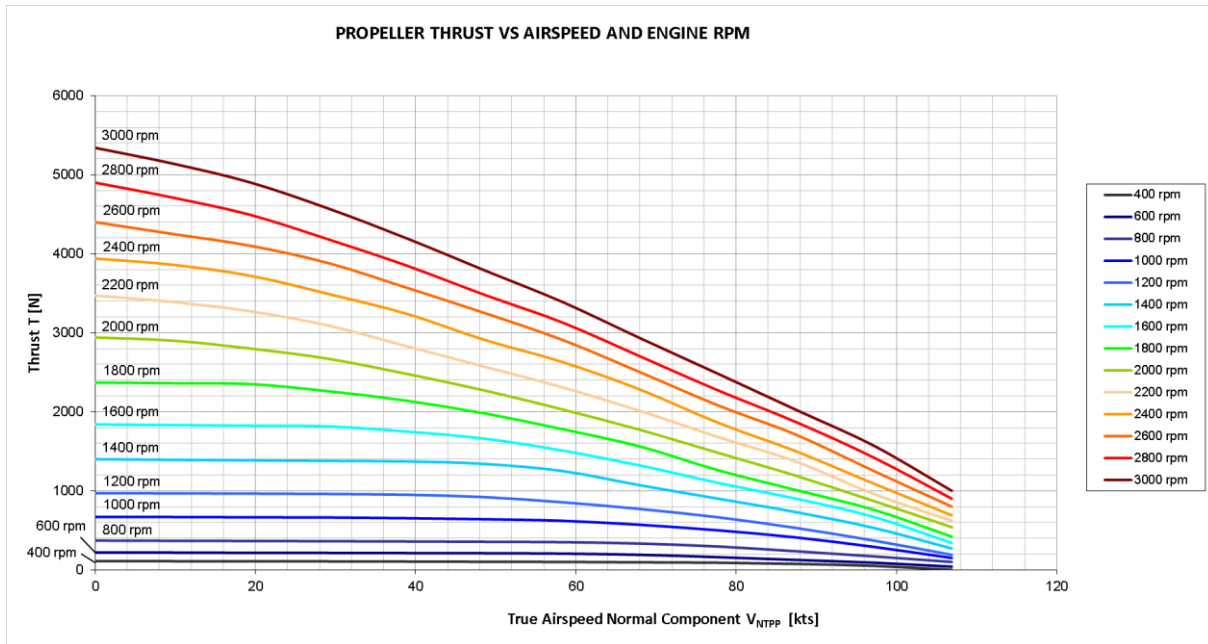
The $\frac{w_i|_{R/H}}{w_i}$ ratio is a function of the fuselage angle of attack, the thrust angle and the true airspeed and its data is presented on Appendix A, Tables Table A- 1, Table A- 2 and Table A- 3.

4.4.3 Engine Deck

For the electric engine chosen in section 4.4.1 Tomazie *et al.*(2011) provides the thrust as a function of indicated airspeed and RPM. The information was adapted for the developed generic tilt rotor and it is shown in Figure 39. One must note that the speed in X-axis of Figure 39 is the true airspeed normal component to the mast-axis $X_M Y_M$ plane. In other words, the engine deck provides a way to calculate thrust in the equations of motion as a function of true airspeed, engines RPM and thrust angle:

$$T = T(V_T, \varphi, RPM, \phi_M, \dot{\theta}) \quad (4.41)$$

RPM Engine rotation speed in rpm

Figure 39 - Propeller Thrust vs V_{NTPP} and RPM.

Source: Adapted from Tomazie *et al.* (2011, p. 872).

Ferguson (1988) also provides data tables to set an upper bound limit on thrust coefficient C_T as a function of in-plane velocity ratio μ and thrust angle φ . But, according to him, “for simulated flight conditions not requiring high thrust, e.g, high-g maneuvers, these tables have no effect on the calculated results”. Since the object of evaluation is a landing procedure, it was assumed that this kind of data has no effect on calculated thrust.

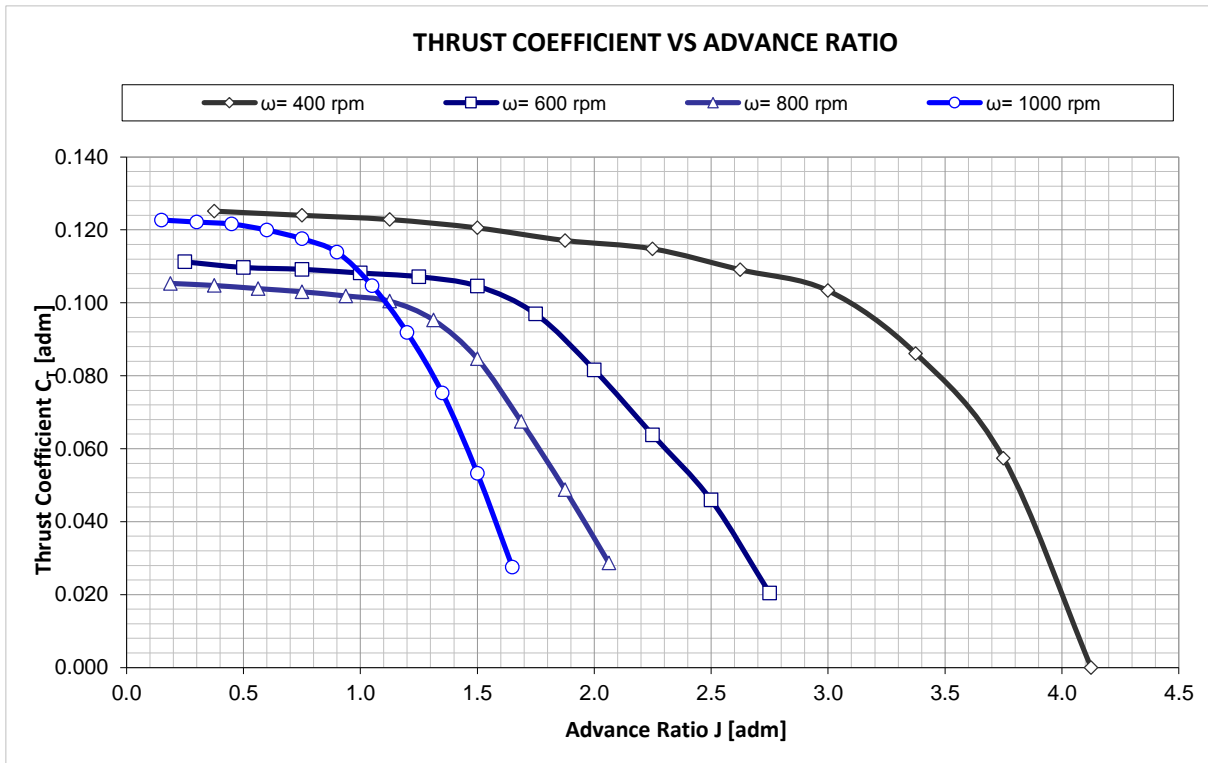
As for the aerodynamic forces, the thrust forces also can be expressed in terms of its components in the body-axis coordinate system.

$$\begin{cases} T_X = T \cos \varphi \cos \phi_M \\ T_Z = -T \sin \varphi \cos \phi_M \end{cases} \quad (4.42)$$

Where T is the magnitude of the thrust generated by the propeller.

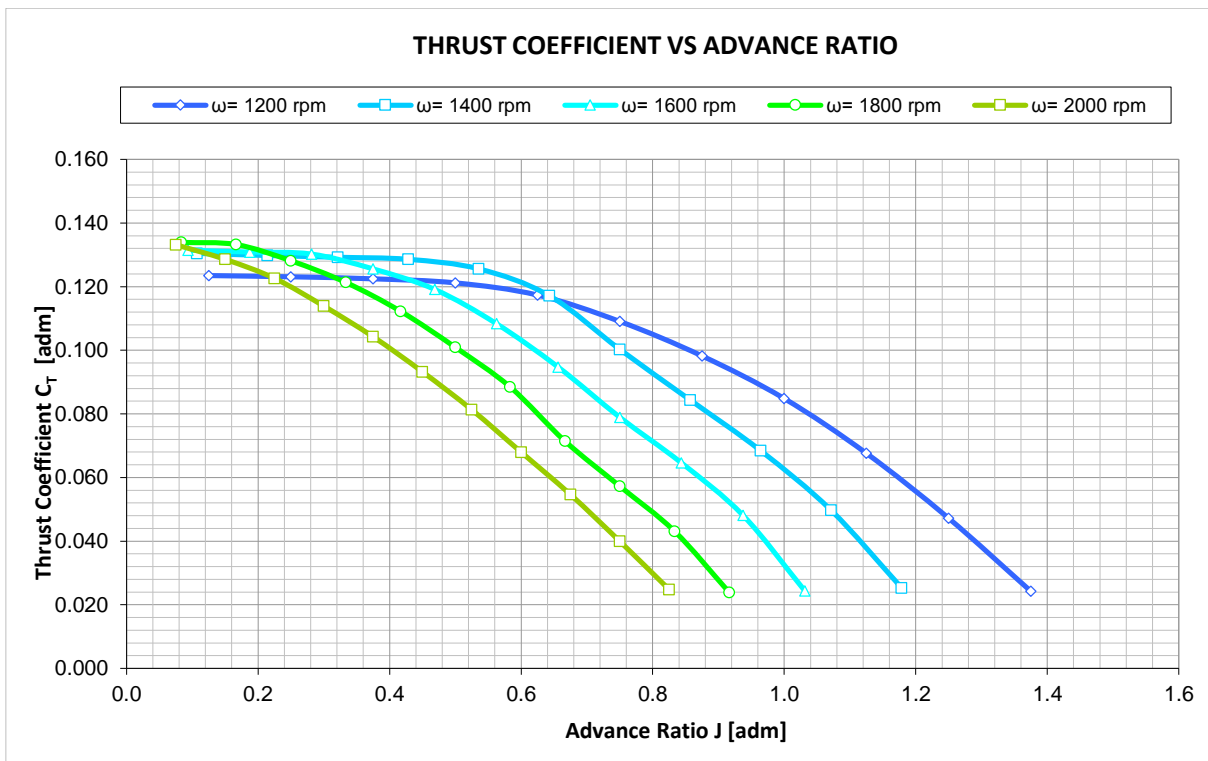
Based on propeller theory developed in section 3.4 and data provided by Tomazie *et al.* (2011) the non-dimensional coefficients of thrust were derived for dynamic cases (RPM greater than 400 *rpm*). The whole engine characteristics is presented in the plots below. It is plotted the variation of thrust coefficient C_T with advance ratio J for each engine RPM, where V_{NTPP} is used as V_0 in equation (3.11).

Figure 40 - Thrust coefficient C_T for 400, 600, 800 and 1000 rpm.

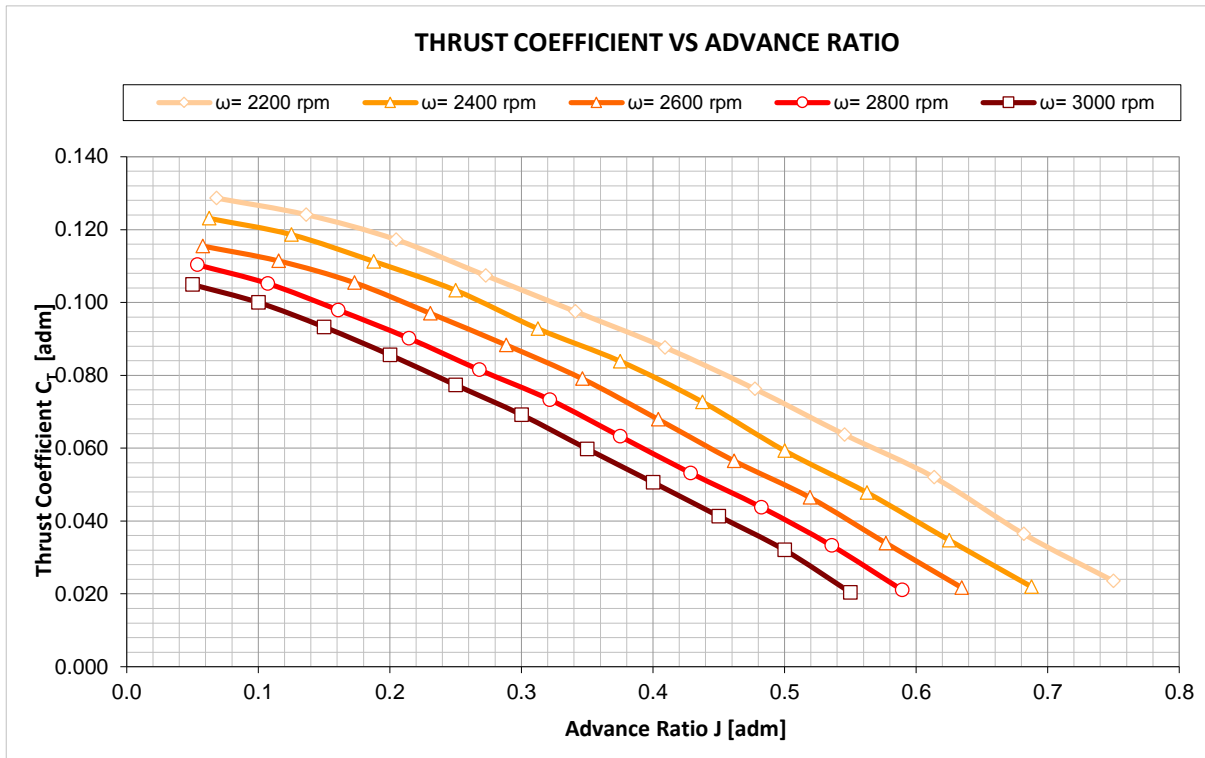


Source: Created by the author using Microsoft Excel (MICROSOFT, 2013a).

Figure 41 - Thrust coefficient C_T for 1200, 1400, 1600 and 1800 and 2000 rpm.



Source: Created by the author using Microsoft Excel (MICROSOFT, 2013a).

Figure 42 - Thrust coefficient C_T for 2200, 2400, 2600 and 2800 and 3000 rpm.

Source: Created by the author using Microsoft Excel (MICROSOFT, 2013a).

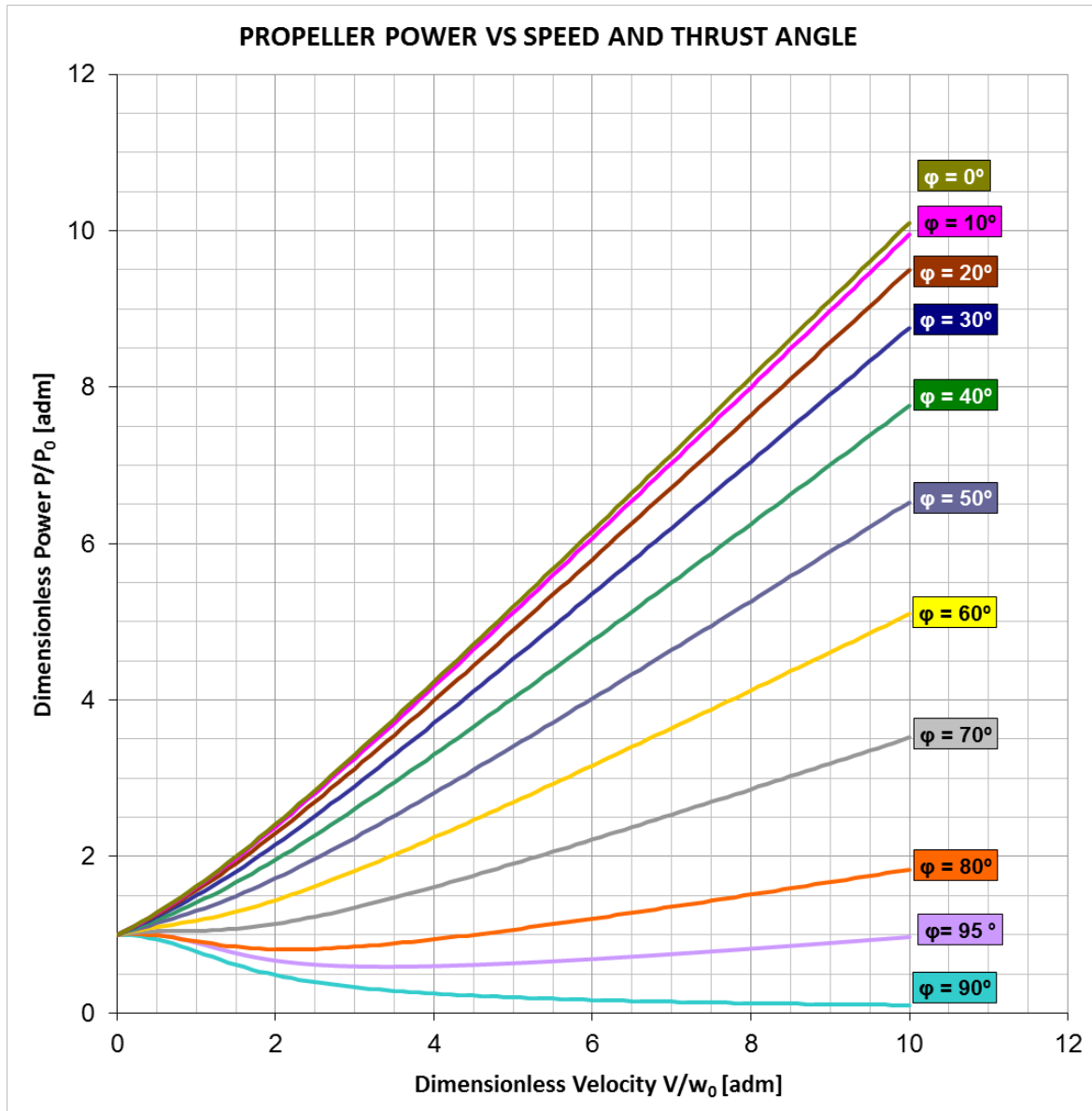
4.4.4 Energy Expenditure

The electric motors RPM is directly proportional to the power delivered from batteries and, the higher it is, the more electric power is demanded. This parameter is one of the control variables of the optimization algorithm and represents the capacity of controlling generated thrust. Once thrust is known, the power that the propeller supplies to the fluid, or the ideal power, can be determined.

As mentioned in section 4.4.2, equations (3.19) and (3.21) can be solved numerically where dimensionless ideal power P_i/P_0 is found as a function of the independent variables V_T/w_0 and φ .

The ideal power produced by a propeller P_i is calculated using the graph depicted in Figure 43 and the procedure of Figure 44. For a true airspeed V_T and the propeller generating a thrust T , find the induced velocity to produce the thrust T statically and then V_T/w_0 . Using the plots, the one correspondent to the current thrust angle φ is consulted to obtain P_i/P_0 and finally P_i .

Figure 43 - Propeller power versus speed and thrust angle.



Source: Created by the author using Microsoft Excel (MICROSOFT, 2013a).

Figure 44 - P_i/P_0 determination diagram.

$$(T, \phi, V_T) \rightarrow w_0 = \sqrt{\frac{T}{2\rho A}} \rightarrow \frac{V_T}{w_0} \phi \text{ plots } \frac{P_i}{P_0} \rightarrow P_i = \left(\frac{P_i}{P_0}\right) P_0$$

Source: Created by the author.

In order to find the energy expenditure on batteries, it is be considered a typical all electric powerplant chain with batteries, power controller, electric motor, gearbox and propeller. The correspondent efficiencies are:

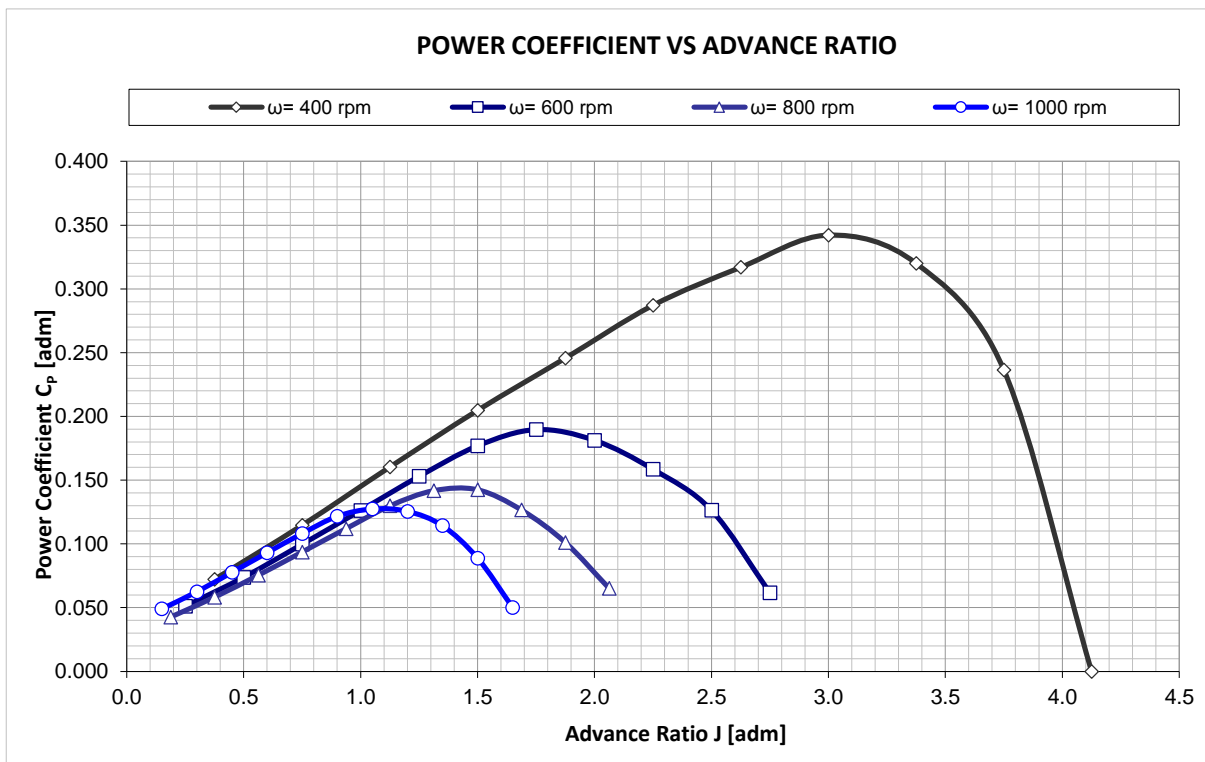
$$\begin{cases} \eta_{POWCONT} = 98\% \\ \eta_{MOTOR} = 95\% \\ \eta_{GEARBOX} = 98\% \end{cases} \quad (4.43)$$

The values are based on Patterson German and Moore (2012) and Hepperle (2012) and are a way in determining the total batteries energy delivered during the whole approach and landing procedure. When it comes to the entire powerplant chain, it is possible to separate the fraction of energy that can be converted into useful power or, in other words, the portion of power that effectively generates thrust.

An efficiency propeller map provided by a blades manufacturer can be used for a singular application. However, a theoretical approach is chosen instead since the aim is not to provide data for a specific aircraft, but for any electric powered design.

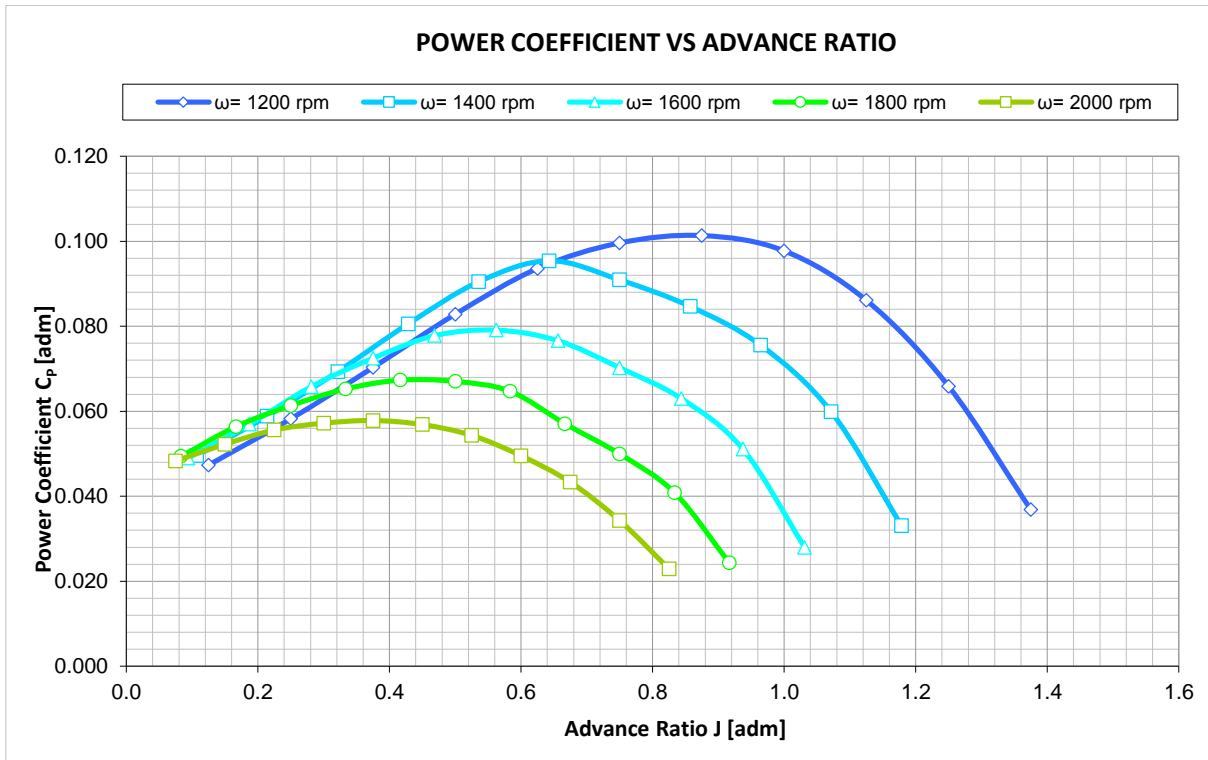
Now with efficiencies proposed, the non-dimensional power coefficients are depicted for dynamic cases in the next plots. Again the advance ratio J takes into account V_{NTPP} . Static thrust and power coefficients are plotted as well.

Figure 45- Power coefficient C_p for 400, 600, 800 and 1000 rpm.



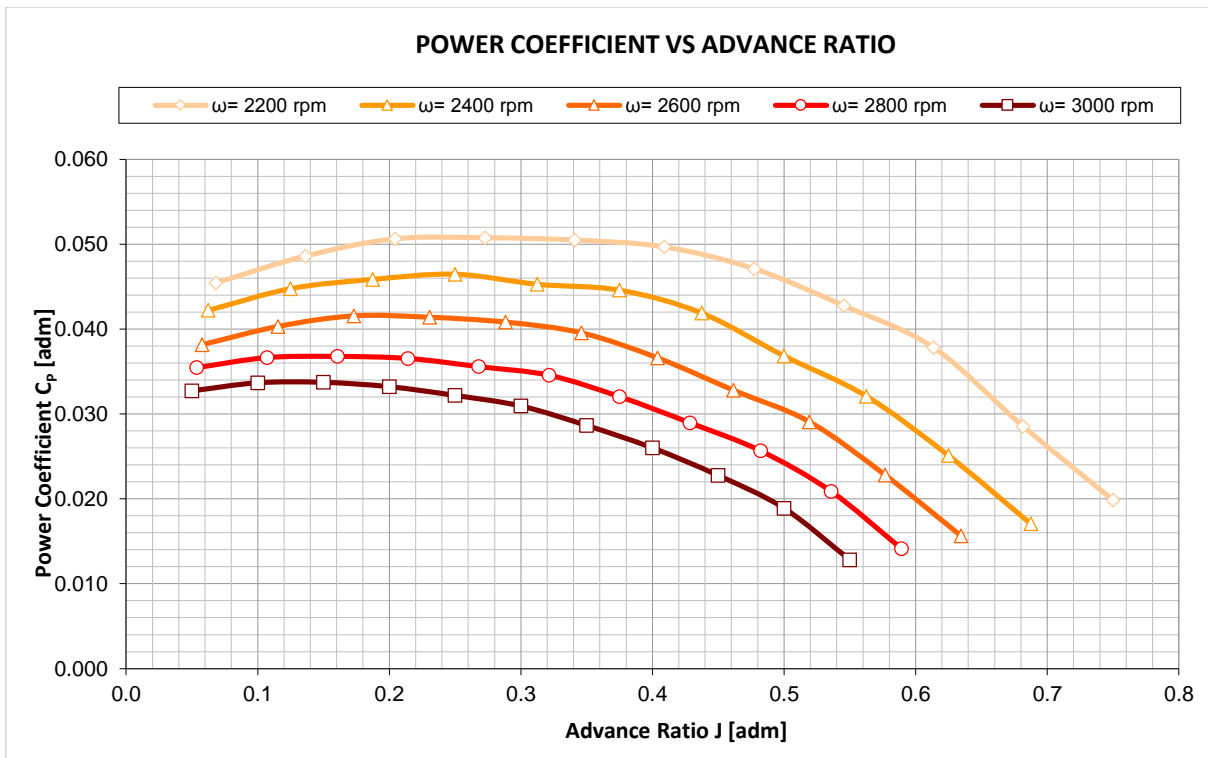
Source: Created by the author using Microsoft Excel (MICROSOFT, 2013a).

Figure 46 - Power coefficient C_p for 1200, 1400, 1600, 1800 and 2000 rpm.



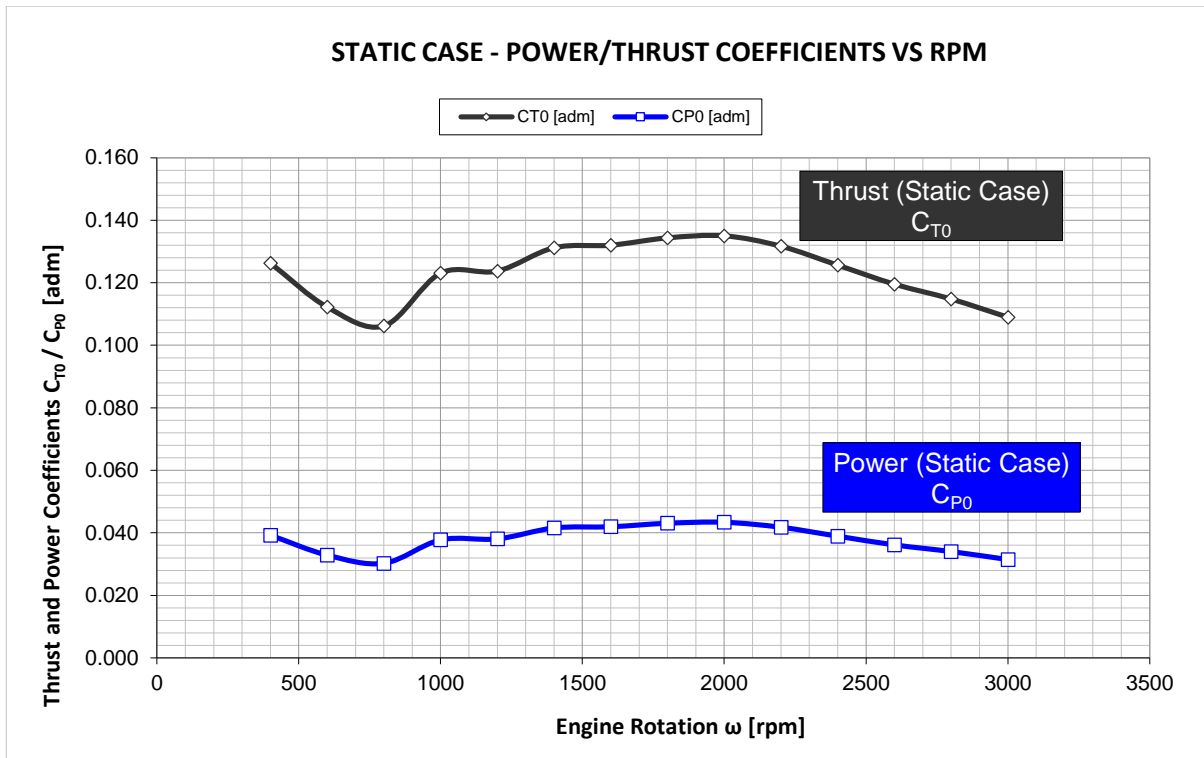
Source: Created by the author using Microsoft Excel (MICROSOFT, 2013a).

Figure 47 - Power coefficient C_p for 2200, 2400, 2600, 2800 and 3000 rpm.



Source: Created by the author using Microsoft Excel (MICROSOFT, 2013a).

Figure 48 –Power and thrust coefficients for the static case.



Source: Created by the author using Microsoft Excel (MICROSOFT, 2013a).

4.5 FUSELAGE AERODYNAMICS

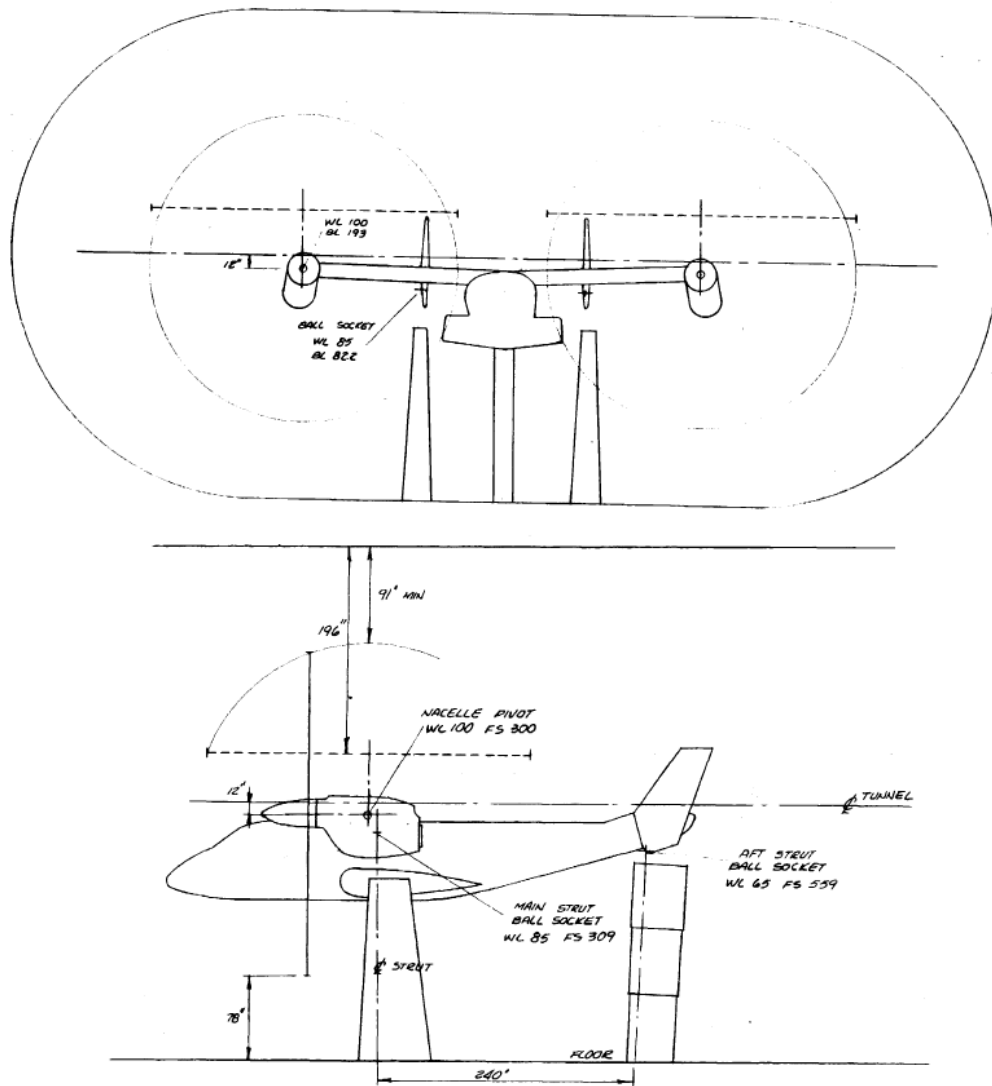
4.5.1 Aerodynamics Structure

The aerodynamic model and equations used were based on Ferguson (1988). The aerodynamics of the tiltrotor concept is implemented separately, so that there are five aerodynamic subsystems in the model: Fuselage Aerodynamics, Wing-Pylon Aerodynamics, Horizontal Stabilizer Aerodynamics, Vertical Stabilizer Aerodynamics and Landing Gear Aerodynamics.

It uses most of aerodynamic data obtained by means of wind tunnel testing raised up by Weiberg and Maisel (1980). They carried out a series of runs in the Ames 40- by 80- feet Wind Tunnel in order to evaluate the NASA XV-15 aerodynamics. The maximum tunnel velocity was 170 knots. The test consisted of 51 runs in 54 hours of wind-on time, in which 19 were with rotors on. When applicable, the data is scaled for the generic eVTOL tiltrotor model

built. The equations for aerodynamic forces and moments are all referenced to the wind-axis coordinate system.

Figure 49 – Wind-tunnel mounting.



Source: Weiberg and Maisel (1980, p. 90-91)

4.5.2 Equations

- Dynamic Pressure and Angle of Attack

$$q_F = \frac{1}{2} \rho V_T^2 \quad (4.44)$$

$$\alpha_F = \theta - \gamma \quad (4.45)$$

q_F Fuselage dynamic pressure

- Lift, Drag and Pitching Moment In Wind-Axis

$$L_F = q_F(L_\alpha + L_{BFO} + L_{LANG}) \quad (4.46)$$

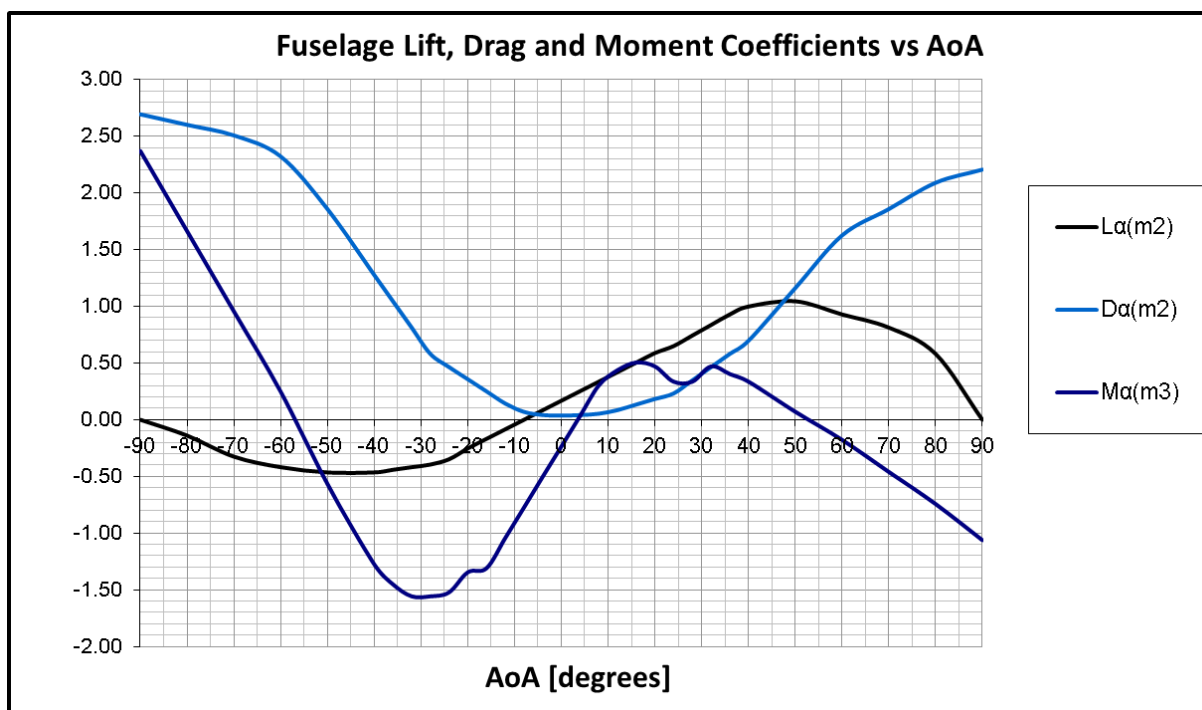
$$D_F = q_F(D_\alpha + D_{BFO} + D_{LANG}) \quad (4.47)$$

$$M_F|_{CA} = q_F(M_\alpha + M_{BFO}) \quad (4.48)$$

L_F	Fuselage lift (wind-axis)
L_α	Fuselage lift variation with angle of attack α_F
L_{BFO}	Fuselage lift at $\alpha_F = 0 \text{ deg}$
L_{LANG}	Extra fuselage lift
D_F	Fuselage drag (wind-axis)
D_α	Fuselage drag variation with angle of attack α_F
D_{BFO}	Fuselage drag at $\alpha_F = 0 \text{ deg}$
D_{LANG}	Extra fuselage drag
L_F	Fuselage lift (wind-axis)
L_α	Fuselage lift variation with angle of attack α_F
L_{BFO}	Fuselage lift at $\alpha_F = 0 \text{ deg}$
$M_F _{CA}$	Fuselage pitching moment with respect to the fuselage aerodynamic center
M_α	Fuselage pitching moment variation with angle of attack α_F
M_{BFO}	Fuselage pitching moment at $\alpha_F = 0 \text{ deg}$

The terms L_α , D_α and M_α are function of the fuselage angle of attack and its data is presented on Appendix A, Table A- 4 and Figure 50. The other terms are constants. The data less than or equal to $\alpha_F = 20 \text{ deg}$ are based on wind tunnel, for greater values the data is approximated.

Figure 50 - Fuselage lift, drag and pitching moment coefficients vs AoA.



Source: Created by the author using Microsoft Excel (MICROSOFT, 2013a).

4.6 WING-PYLON AERODYNAMICS

4.6.1 Introduction

Wing-pylon lift, drag and pitching moment are derived into two different theoretical sets: the part affected by the rotors wake and the one submitted to the freestream flow. In addition, calculation regarding the assembly between wing and pylon is made explicit by an interference drag. And lastly, the spinners drag are also taken into account.

4.6.2 Wings Aerodynamics Affected by Rotor Wake

A series of equations and procedures are described in the sequence with two main deliverables: the wing area affected by rotor wake S_{iW} and the longitudinal center of pressure location X_{iW} .

- Initial Parameters

$$G = \tan^{-1}[\cos \phi_M \tan(90 - \varphi)] \quad (4.49)$$

$$SG = \sin G \quad (4.50)$$

$$CG = \cos G \quad (4.51)$$

$$ZL = l_M \cos \phi_M CG \quad (4.52)$$

If $\sin \varphi = 0$ then $G = 1.5708$.

G, SG, CG, ZL Auxiliary parameters in rotor wake determination

- Velocities at the Wing

$$U_W = -(U + w_i|_{R/W})(SG) \quad (4.53)$$

$$W_W = -W + w_i|_{R/W} \cos \phi_M (CG) \quad (4.54)$$

If $W_W < 0.0001$, then $W_W = 0.0001$.

U_W Auxiliary x-velocity at the wing in rotor wake determination

W_W Auxiliary z-velocity at the wing in rotor wake determination

- Wing Geometry Information

$$X_{TE} = -\bar{\epsilon} - l_m SG - \left(\frac{U_W}{W_W}\right) (ZL)(K_{RW}) \quad (4.55)$$

$$X_{LE} = c_W + X_{TE} \quad (4.56)$$

$$R_{WX} = R_W \left\{ \left[\left(\frac{U_W}{W_W}\right) \sin \phi_M \right]^2 + \left[CG - \left(\frac{U_W}{W_W}\right) [(SG)(\cos \phi_M)] \right]^2 \right\}^{0.5} \quad (4.57)$$

$$R_{WY} = R_W [(SG)(\sin \phi_M)]^2 + (\cos \phi_M)^2)^{0.5} \quad (4.58)$$

$$F_{RW} = \frac{R_{WY}}{R_{WX}} \quad (4.59)$$

$$SDEL = \sin \delta \quad (4.60)$$

$$CDEL = |\cos \delta| \quad (4.61)$$

Where,

$$\bar{e} = FS_{WTE} - FS_{NAC} \quad (4.62)$$

$$\delta = \tan^{-1} \left[\frac{\left(\frac{U_W}{W_W}\right) \sin \phi_M}{CG - \left(\frac{U_W}{W_W}\right) (\cos \phi_M) (SG)} \right] \quad (4.63)$$

K_{RW} Rotor skew angle velocity distribution factor

X_{TE} Trailing edge distance in X_{iW} equation

c_w Wing chord

FS_{WTE} Fuselage station of wing trailing edge

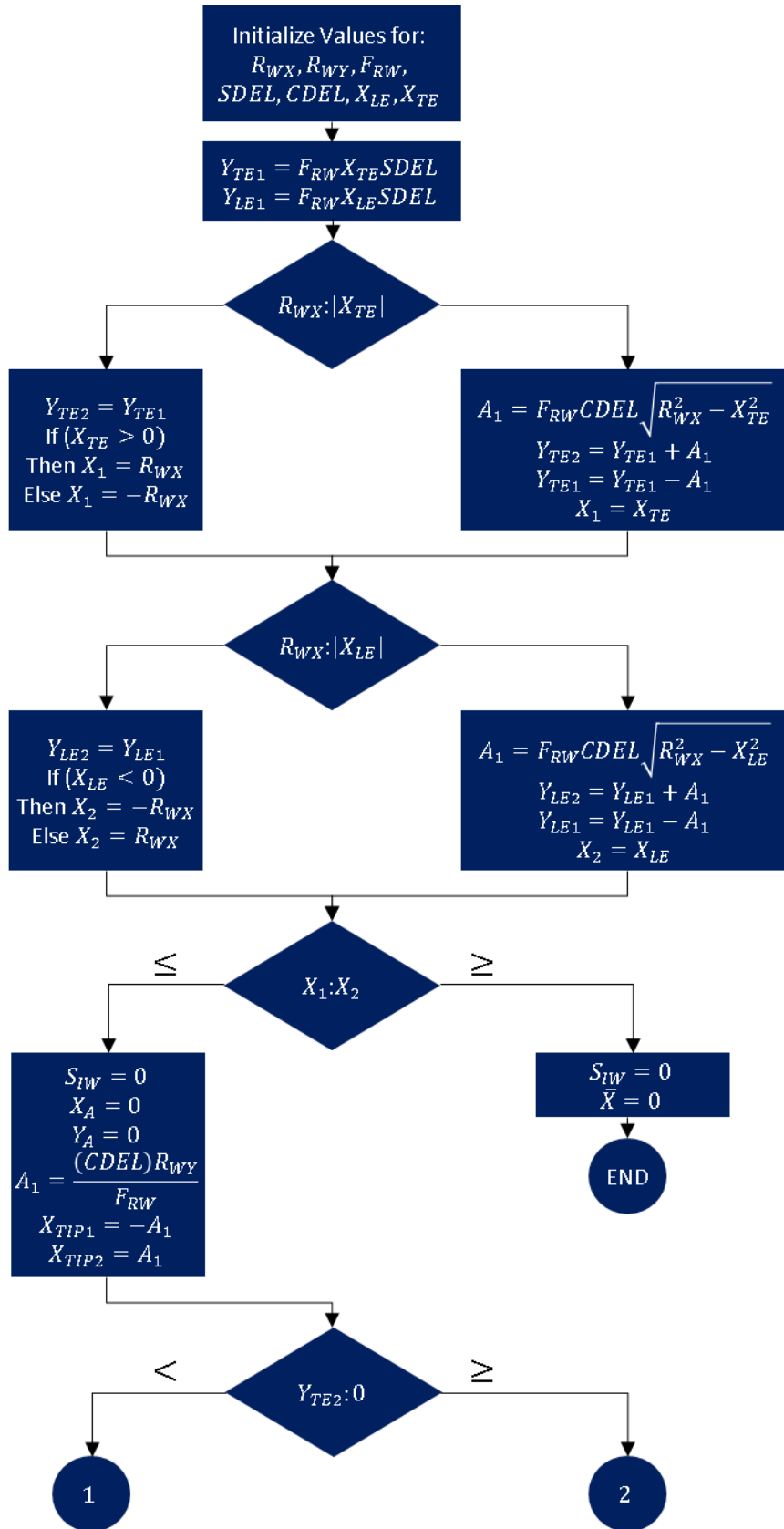
$X_{LE}, R_{WX}, R_{WY}, F_{RW}, SDEL, CDEL$ Initialization parameters in procedures for calculating X_{iW} and S_{iW}

- Procedures for Calculating the Wing Area S_{iW}
 - a. If $\varphi \geq 60 \text{ deg}$, follow flow chart of Figure 51 to determine S_{iW} and X_{iW} .
 - b. If $\varphi < 60 \text{ deg}$, then $S_{iW} = 0$
 - c. Procedures $P1$ to $P5$ called in Figure 51 flow chart receive as inputs the variables XA_1, XA_2, XA_3, XA_4 and return values for S_{iW} and \bar{X} , which is used, in turn, to calculate X_{iW} as follows:

$$X_{iW} = \bar{X} + FS_{CG} - FS_{WTE} - X_{TE} \quad (4.64)$$

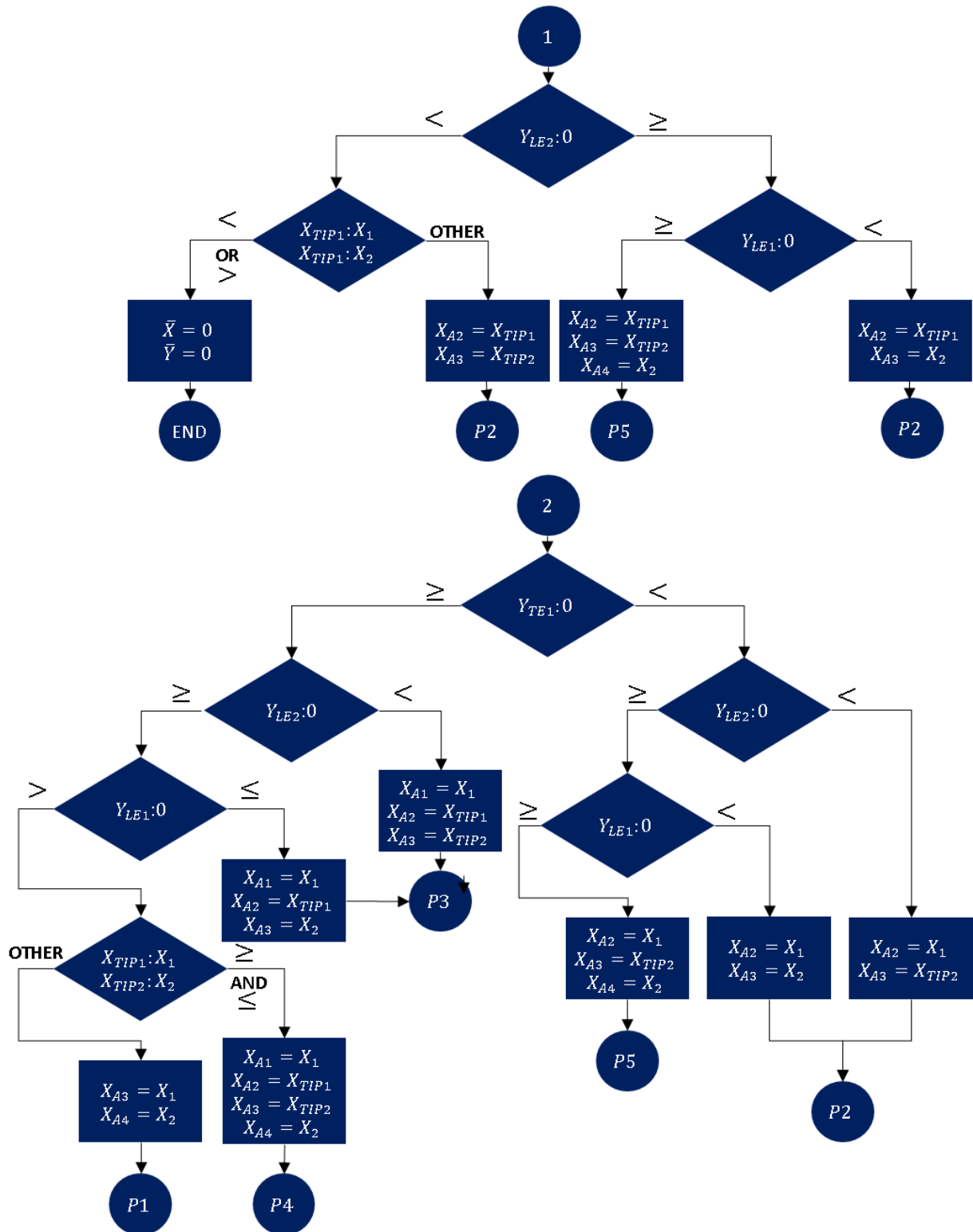
In Figure 52 one can verify what each procedures $P1$ to $P5$ do in detail and functions $F1$ and $F2$ were programmed in Visual Basic for Applications (VBA) using Microsoft Excel software (MICROSOFT, 2013a) and the codes are presented in Appendix B.

Figure 51 - Flow chart of wing aerodynamics affected by rotor wake.



Source: Created by the author using Microsoft PowerPoint (MICROSOFT, 2013b).

Figure 51 - Flow chart of wing aerodynamics affected by rotor wake (CONCLUDED).



Source: Created by the author using Microsoft PowerPoint (MICROSOFT, 2013b).

Figure 52 - Procedures for calculating wing area and CP location.

<p>Procedure P1:</p> <p>Call F1: $INPUT (X_{A3}, X_{A4}) \rightarrow OUTPUT(S_{iW}, X_A)$</p> <p>Procedure P2:</p> <p>Call F2: $INPUT (X_{A2}, X_{A3}) \rightarrow OUTPUT(S_{iW}, X_A)$</p> <p>Procedure P3:</p> <p>Call F1: $INPUT (X_{A1}, X_{A2}) \rightarrow OUTPUT(S_{iW}, X_A)$</p> <p>Call F2: $INPUT (X_{A2}, X_{A3}) \rightarrow OUTPUT(S_{iW}, X_A)$</p> <p>Procedure P4:</p> <p>Call F1: $INPUT (X_{A1}, X_{A2}) \rightarrow OUTPUT(S_{iW}, X_A)$</p> <p>Call F2: $INPUT (X_{A2}, X_{A3}) \rightarrow OUTPUT(S_{iW}, X_A)$</p> <p>Call F1: $INPUT (X_{A3}, X_{A4}) \rightarrow OUTPUT(S_{iW}, X_A)$</p> <p>Procedure P5:</p> <p>Call F2: $INPUT (X_{A2}, X_{A3}) \rightarrow OUTPUT(S_{iW}, X_A)$</p> <p>Call F1: $INPUT (X_{A3}, X_{A4}) \rightarrow OUTPUT(S_{iW}, X_A)$</p> <p>$\bar{X} = X_A/S_{iW}$</p> <p>$X_{iW} \leftarrow$ equation (4.71)</p>

Source: Created by the author

- Total Velocity and Angle of Attack

$$V_{T_{iW}} = \left((U + U_i|_{R/W}^B)^2 + (W + W_i|_{R/W}^B)^2 \right)^{0.5} \quad (4.65)$$

$$\alpha_{iW} = \tan^{-1} \left(\frac{W + W_i|_{R/W}^B}{U + U_i|_{R/W}^B} \right) \quad (4.66)$$

$V_{T_{iW}}$ True airspeed in wing rotor wake region

α_{iW} Angle of attack of the wing portion immersed in rotor wake

- Lift and Drag In Wind-Axis

$$L_{iW} = q_{iW} S_{iWT} C_{LW} K_{FW} \quad (4.67)$$

$$D_{iW} = q_{iW} S_{iWT} C_{DW} K_{FW} \quad (4.68)$$

Where,

$$q_{iW} = \frac{1}{2} \rho V_{TiW}^2 \quad (4.69)$$

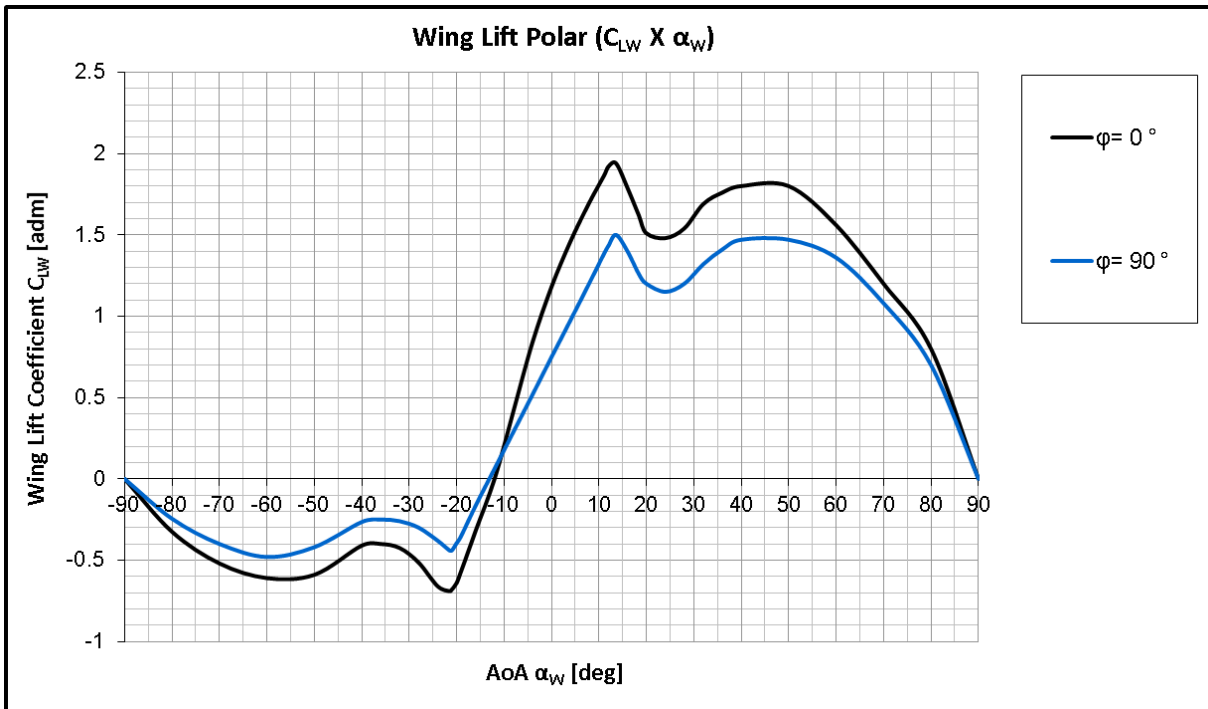
$$K_{FW} = K_{FW0} - K_{FWDF} \delta_F \quad (4.70)$$

L_{iW}	Lift of the wing portion immersed in rotor wake
S_{iWT}	Total wing area affected by rotor wake
K_{FW}	Rotor downwash/wing for flap effects factor
D_{iW}	Drag of the wing portion immersed in rotor wake
q_{iW}	Dynamic pressure in wing rotor wake region
K_{FW0}	Constant in rotor downwash/wing equation for flap effects
K_{FWDF}	Slope in rotor downwash/wing equation for flap effects
δ_F	Flaps position

Since no distinction is made between the right and left rotors effects, lift and drag on both sides of the wings are identical and, in this way, $S_{iWT} = 2S_{iW}$. Furthermore, C_{LW} and C_{DW} are dependent upon thrust angle, flaps setting, Mach number and wing angle of attack. For the SFAP trajectory, no configuration change is done (constant flaps) and Mach number M_N varies below 0.2. Therefore, coefficient data is presented on Appendix A, Tables Table A-5 and Table A-6, varying with angle of attack and thrust angle only.

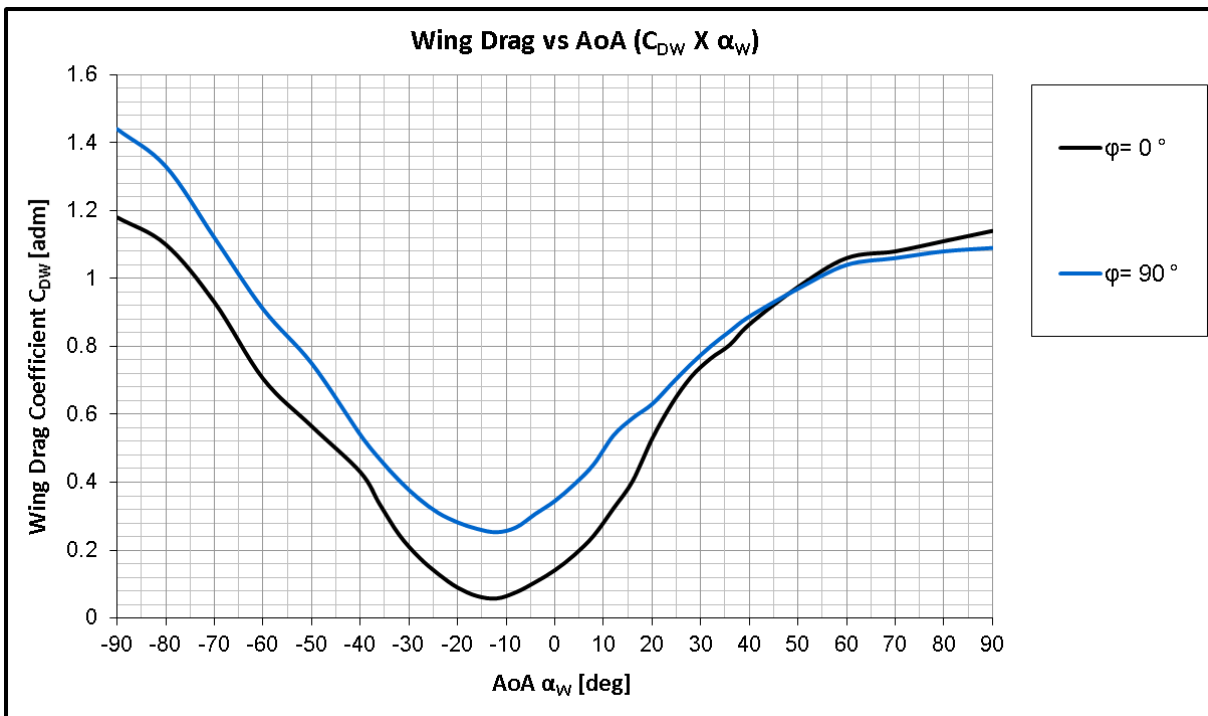
The coefficients for wing lift, drag and pitching moment were obtained through use of wind tunnel testing for angles of attack up to stall. Above it, an approximation is done based on test data.

Figure 53 - Wing lift polar for different thrust angles.



Source: Created by the author using Microsoft Excel (MICROSOFT, 2013a).

Figure 54 – Wing drag vs wing angle of attack for different thrust angles.



Source: Created by the author using Microsoft Excel (MICROSOFT, 2013a).

4.6.3 Wings Aerodynamics in Freestream

- Area of the Wing in Freestream Flow and Dynamic Pressure

$$S_{WFS} = S_W - S_{iWT} \quad (4.71)$$

$$q_{WFS} = q_F \quad (4.72)$$

S_{WFS} Wing area upon the freestream flow

S_W Total wing area

q_{WFS} Dynamic pressure in wing region upon freestream flow

- Angle of Attack of the Wing in Freestream Flow

$$\alpha_{WFS} = \alpha_F - K_{XRW}(X_{RW}) \left[\frac{0.258C_T}{(\text{MAX}(0.15, \mu))^2} \right] \quad (4.73)$$

Where,

$$X_{RW} = X_{RW0} + (90 - \varphi)(X_{RW1} + (90 - \varphi)X_{RW2}) \quad (4.74)$$

α_{WFS} Angle of attack of the wing in freestream flow

$K_{XRW}, X_{RW}, X_{RW0}, X_{RW1}, X_{RW2}$ Constants in rotor downwash/wing equation

X_{RW} Rotor downwash/wing effect on AoA of the wing in freestream flow

- Lift, Drag and Pitching Moment (Freestream) In Wind-Axis

$$L_{WFS} = q_{WFS}S_{WFS}C_{LW} \quad (4.75)$$

$$D_{WFS} = q_{WFS}S_{WFS}C_{DW} \quad (4.76)$$

$$M_W|_{CA} = (q_{iW}S_{iW} + q_{WFS}S_{WFS})C_{MW}c_W \quad (4.77)$$

L_{WFS} Lift of the wing portion upon the freestream flow field

C_{LW} Wing lift coefficient

D_{WFS}	Drag of the wing portion upon the freestream flow field
C_{DW}	Wing drag coefficient
$M_W _{CA}$	Wing pitching moment with respect to the wing aerodynamic center
C_{MW}	Wing pitching moment coefficient

One must note that angle of attack equation takes into account a rotor downwash effect on the entire wing. Coefficients for lift and drag are the same used for the rotor wake region, except that Table A- 5 and Table A- 6 must be consulted using α_{WFS} instead of α_{iW} . Pitching moment equation is a generalization of both wing parts. Lastly, C_{MW} is presented on Table A- 7 of Appendix A and is a function of φ .

4.6.4 Wing-Pylon Interference Drag

There is an interference drag generated by the interaction between the wings and the pylons and it is accounted by the following equation.

- Wing-pylon Interference Drag

$$D_{PYLN} = D_{PYINT} q_{iW} \quad (4.78)$$

D_{PYLN} Drag between the interaction of the tilt rotor pylon and wing

D_{PYINT} Wing-pylon interference drag coefficient

The term D_{PYINT} is a function of the thrust angle φ and is presented in Table A- 8 of Appendix A.

4.6.5 Spinner Drag

- Velocities, Dynamic Pressure and Angle of Attack on Spinners in Mast Axis

$$U_{MSP} = U \sin \varphi + W \cos \varphi \cos \phi_M \quad (4.79)$$

$$W_{MSP} = -w_i - U \cos \varphi + W \sin \varphi \cos \phi_M \quad (4.80)$$

$$V_{TSP} = \sqrt{U_{MSP}^2 + W_{MSP}^2} \quad (4.81)$$

$$q_{SP} = \frac{1}{2} \rho V_{TSP}^2 \quad (4.82)$$

$$\alpha_{MSP} = \left[\tan^{-1} \frac{|U_{MSP}|}{|W_{MSP}|} \right] \quad (4.83)$$

U_{MSP} Horizontal speed on spinner along mast X_M -axis

W_{MSP} Vertical speed on spinner along mast Z_M -axis

V_{TSP} True airspeed upon spinners region

q_{SP} Dynamic pressure upon spinners region

α_{MSP} Angle of attack upon spinners region, mast-axis

- Velocities, Dynamic Pressure and Angle of Attack on Spinners in Mast-Axis

$$SD = 2q_{SP} [SD/q|_{\varphi=0} + (SD/q) \sin^3 \alpha_{MSP}] \quad (4.84)$$

SD/q Coefficient to account for thrust angle variation in spinners drag equation

4.6.6 Wing Wake Deflection on Horizontal Tail

- Wing Wake Deflection Angle

$$\epsilon_{W/H} = \epsilon_{W/HOGE} \left[\frac{1}{(1 - M_N^2)^{0.5}} \right] \quad (4.85)$$

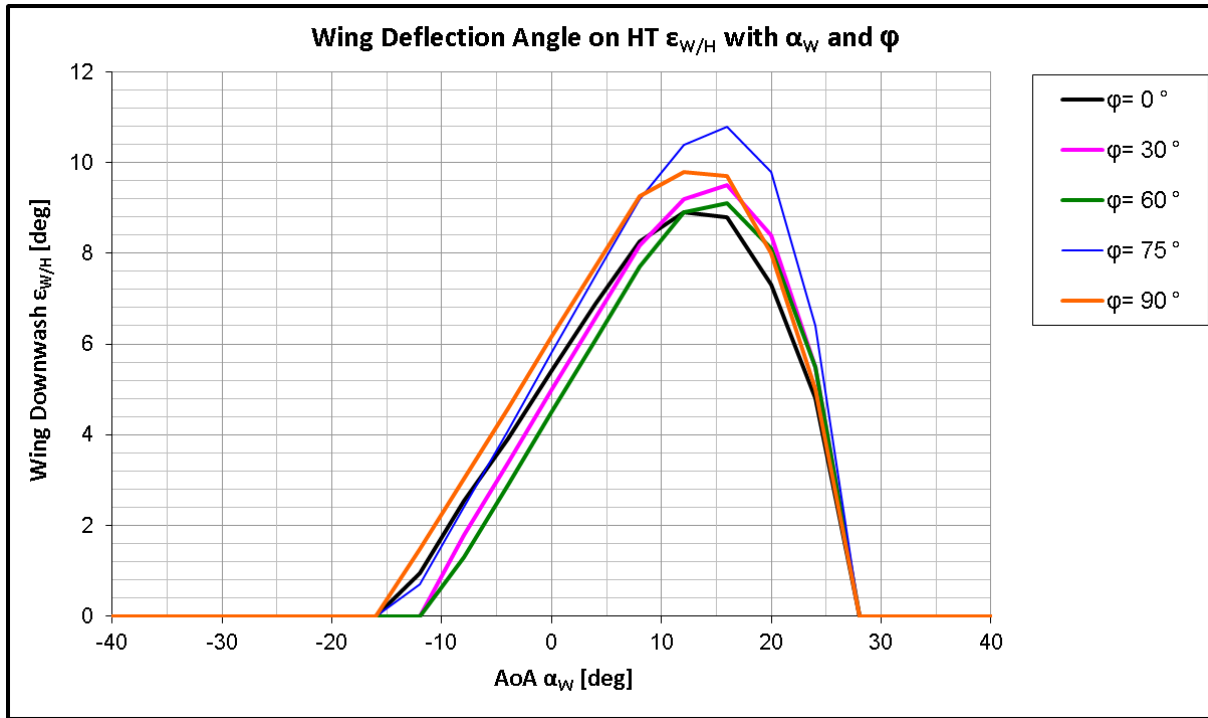
$\epsilon_{W/H}$ Wing wake deflection angle at the horizontal stabilizer

$\epsilon_{W/HOGE}$ Wing wake deflection angle at the horizontal stabilizer

Since Mach number M_N varies below 0.2 in the SFAP, its effects in the wing wake deflection angle $\epsilon_{W/H}$ is minimal. It varies with flaps setting δ_F , angle of attack of the wing in

freestream flow α_{WFS} and thrust angle φ . Table A- 9 (Appendix A) shows the data, as well as Figure 55.

Figure 55 - Wing wake deflection angle on Horizontal Tail.



Source: Created by the author using Microsoft Excel (MICROSOFT, 2013a).

4.7 EMPENNAGE AERODYNAMICS

The model empennage is consisted by two horizontal stabilizers (HT's) and two vertical stabilizers (VT's). The dynamic pressure and the angle of attack for both the HT and the VT takes into account wing-pylon wake, thrust angle, rotor wake, fuselage attitude and angular velocities. For the longitudinal model, the only force of the VT that is taken into consideration is its drag. On the other hand, the HT is modeled in regard to its lift, drag and pitching moment in order to compose the forces and moments terms in the equations of motion.

4.7.1 Horizontal Stabilizer

- Velocities on HT

$$U_{HT} = U + U_i |_{R/H}^B + \dot{\theta} Z_{HT} \quad (4.86)$$

$$W_{HT} = W + W_i |_{R/H}^B + \dot{\theta} X_{HT} \quad (4.87)$$

$$V_{HT} = \sqrt{U_{HT}^2 + W_{HT}^2} \quad (4.88)$$

Where,

$$Z_{HT} = -(WL_{HT} - WL_{CG}) \quad (4.89)$$

$$X_{HT} = FS_{HT} - FS_{CG} \quad (4.90)$$

U_{HT} Horizontal speed along body X -axis on HT

W_{HT} Vertical speed along body Z -axis on HT

V_{HT} True airspeed magnitude on HT

FS_{HT} Fuselage station of HT center of pressure

WL_{HT} Water line of HT center of pressure

- Dynamic Pressure and Angle of Attack on HT

$$q_{HT} = \frac{1}{2} \rho K_{HNU} \left[(U \sqrt{\eta_{HS}} + \dot{\theta} Z_{HT})^2 + (W \sqrt{\eta_{HS}} + \dot{\theta} X_{HT})^2 \right] \quad (4.91)$$

$$\alpha_{HT} = i_{HT} + \left[\tan^{-1} \frac{W_{HT}}{U_{HT}} \right] - \epsilon_{W/H} + K_E \tau_E \delta_E \quad (4.92)$$

Where,

$$K_E = X_{KE} \quad (|\delta_E| > 15 \text{ deg}) \quad (4.94)$$

$$K_E = X_{KE} - \left[D_{KE} \left(\frac{|\delta_E| - 15}{15} \right) \right] \quad (|\delta_E| > 15 \text{ deg}) \quad (4.95)$$

q_{HT} Dynamic pressure upon HT region

K_{HNU} HT loss multiplier of dynamic pressure

η_{HS}	Dynamic pressure ratio at the HT
α_{HT}	HT angle of attack
i_{HT}	HT incidence angle
δ_E	Elevator deflection angle
τ_E	Elevator effectiveness
X_{KE}	Elevator effectiveness factor
D_{KE}	Elevator effectiveness reduction factor for $ \delta_E > 15 \text{ deg}$

▪ Lift, Drag and Pitching Moment on HT in Wind Axis

$$L_{HT} = q_{HT} S_{HT} (C_{LHT} + C_{LHT_W} \dot{W}) \quad (4.96)$$

$$D_{HT} = q_{HT} S_{HT} C_{DHT} \quad (4.97)$$

$$M_{HT|CA} = q_{HT} S_{HT} C_{MHT} C_{HT} \quad (4.98)$$

Where,

$$C_{MHT} = C_{MHT0} + C_{MHTA} \alpha_{HT} \quad (4.99)$$

$$C_{LHT_W} = D_{WB} \left(\frac{\partial C_{LHT}}{\partial \alpha_{HT}} \right) \left(\frac{\partial \epsilon_{W/H}}{\partial \alpha_{WFS}} \right) \left(\frac{PCPM|_{M_N}}{PCPM|_{M_N=0}} \right) \left(\frac{X_{HT}}{U_{HT}^2} \right) \quad (4.100)$$

L_{HT}	HT lift
C_{LHT}	HT lift coefficient
C_{LHT_W}	HT stability derivative with vertical acceleration \dot{W} or the wing/body damping
D_{HT}	HT drag
C_{DHT}	HT drag coefficient
$M_{HT CA}$	HT pitching moment with respect to the HT aerodynamic center
C_{MHT}	HT pitching moment coefficient

S_{HT}	HT reference area
c_{HT}	HT chord
D_{WB}	Coefficient in the wing/body damping equation
$PCPM$	Mach number effect on the $(\partial \epsilon_{W/H} / \partial \alpha_{WFS})$ derivative

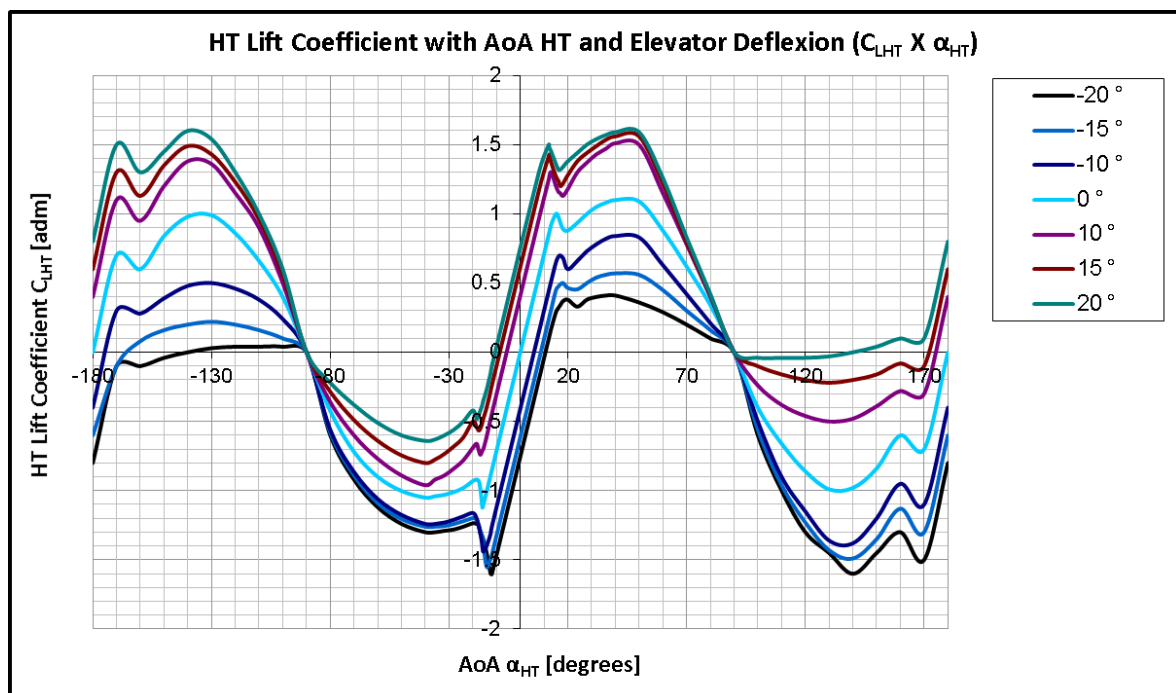
The dynamic pressure ratio on the HT is a function of fuselage angle of attack α_F , thrust angle φ and general true airspeed V_T . Table A- 10 to Table A- 14 on Appendix A summarizes the data. The elevator effectiveness factor X_{KE} is a function of Mach number and its data is also described on Appendix A, Table A- 15. In the wing/body damping equation, the term $PCPM$ depends on the Mach number (Table A- 16, Appendix A).

For lift and pitching moment equations, the last term in (4.92) is neglected, since $M_N < 0.2$ in SFAP. In the drag equation, though, it is taken into consideration. Horizontal stabilizer lift and drag coefficients C_{LHT} and C_{DHT} depends on elevator deflection angle δ_E and HT angle of attack α_{HT} . Review data in Table A- 17 and Table A- 18 (Figure 56 and Source: Created by the

author using Microsoft Excel (MICROSOFT, 2013a).

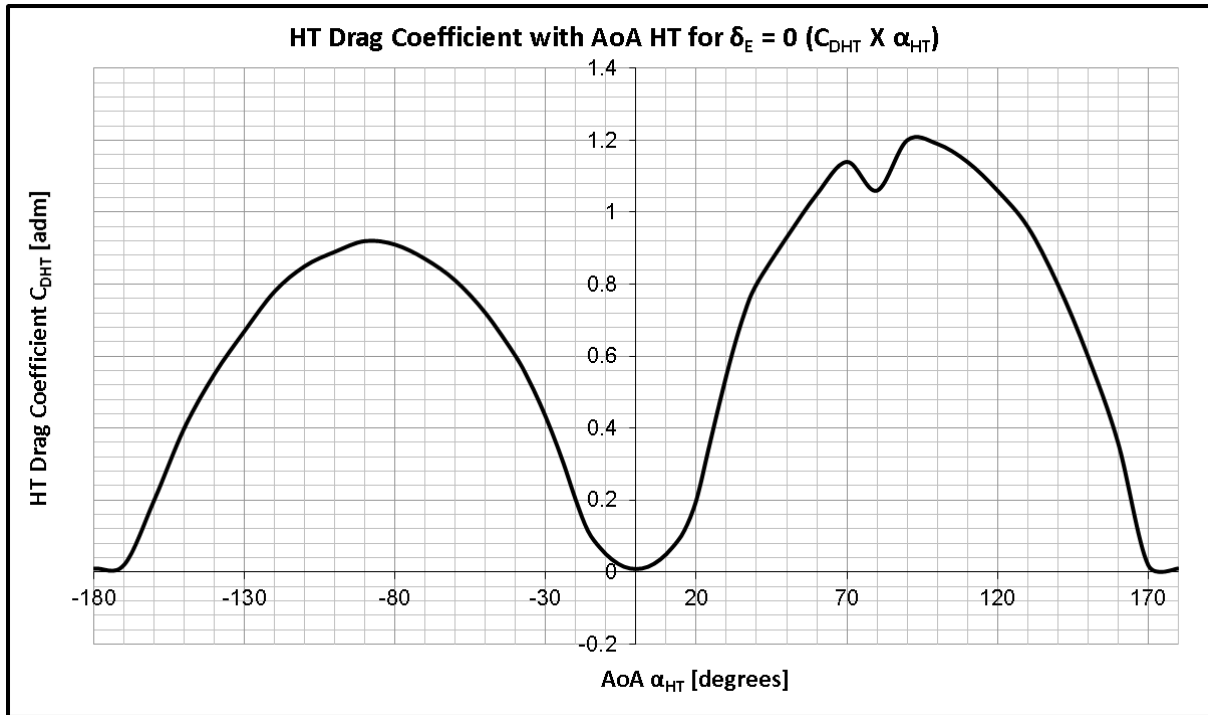
Figure 57).

Figure 56 – HT lift coefficient variation with α_{HT} and δ_E .



Source: Created by the author using Microsoft Excel (MICROSOFT, 2013a).

Figure 57 – HT drag coefficient variation with α_{HT} for $\delta_E = 0$.



Source: Created by the author using Microsoft Excel (MICROSOFT, 2013a).

4.7.2 Vertical Stabilizer

- Geometric Distance from CG to VT

$$Z_{VT} = -(WL_{VT} - WL_{CG}) \quad (4.101)$$

$$X_{VT} = FS_{VT} - FS_{CG} \quad (4.102)$$

FS_{VT} Fuselage station of VT center of pressure

WL_{VT} Water line of VT center of pressure

- Dynamic Pressure and Angle of Attack on HT

$$q_{VT} = \frac{1}{2} \rho K_{VNU} \left[(U\sqrt{\eta_{VS}} + \dot{\theta}Z_{VT})^2 + (W\sqrt{\eta_{VS}} + \dot{\theta}X_{VT})^2 \right] \quad (4.103)$$

$$\alpha_{VT} = \alpha_{HT} \quad (4.104)$$

q_{VT} Dynamic pressure upon VT region

K_{VNU} VT loss multiplier of dynamic pressure

η_{VS} Dynamic pressure ratio at the VT

α_{VT} VT angle of attack

▪ Fin Drag in Wind Axis

$$D_{VT} = q_{VT} S_{VT} C_{DVT} \quad (4.105)$$

Where,

$$C_{DVT} = (C_{DV} |_{\delta_R=0}) \left[K_{\beta R} \left(1 - \frac{\partial \sigma}{\partial \beta_F} \right) \right] \quad (4.106)$$

D_{VT} VT drag

C_{DVT} VT drag coefficient

S_{VT} VT reference area

δ_R Rudder deflection angle

$K_{\beta R}$ Rotor sidewash factor on dynamic pressure

$\left(1 - \frac{\partial \sigma}{\partial \beta_F} \right)$ VT sidewash factor

Table A- 19 Table A- 20 on Appendix A are the data raised up for the rotor sidewash factor on dynamic pressure $K_{\beta R}$ and the vertical stabilizer sidewash factor $\left(1 - \frac{\partial \sigma}{\partial \beta_F} \right)$. The dynamic pressure ratio on the VT is taken as the same as its equivalent ratio for HT η_{HS} and the same data, as per in Table A- 10 to Table A- 14 on Appendix A, are reviewed.

4.8 LANDING GEARS AERODYNAMICS

This subsystem is comprised in accounting for drag and its influence in pitching moment due to nose and main landing gears. Through the trajectory in study there is no gears retraction nor extension and no ground contact neither. They remain extended the for the entire SFAP.

4.8.1 Nose Landing Gears

- NLG Drag in Wind Axis

$$D_{NG} = q_F D_{0_{NGD}} \quad (4.107)$$

D_{NG} NLG drag

$D_{0_{NGD}}$ Drag coefficient of NLG extended

4.8.2 Main Landing Gears

- MLG Drag in Wind Axis

$$D_{MG} = q_F [D_{0_{MGD}} + D_{POD}] \quad (4.108)$$

D_{MG} MLG drag

$D_{0_{MGD}}$ Drag coefficient of MLG extended

D_{POD} Landing gear pod drag

One must note that equation for main landing gear drag stands for only one side. Thus, it is necessary multiplying it by 2 in order to account for the total aerodynamic drag generated by the main landing gears.

4.9 EQUATIONS OF MOTION

4.9.1 Forces Summation

After the aerodynamic forces are computed in wind-axis system, the model converts them into the body-axis system using equations (3.36). For each aerodynamic subsystem, its lift and drag forces L_i and D_i are transformed into N_i and C_i , the correspondent forces along the body Z -axis and X -axis respectively.

The force summation including all subsystems components is then carried out as per equations (3.29) and (3.30) and final body-axis aerodynamic forces are the result. For thrust, equations (4.42) lead to the X and Z body-axis components of forces and the outputs are used in the EOM's.

4.9.2 Pitching Moment Summation

Each pitching moment produced by aerodynamic forces is calculated using the general equation:

$$M_i = N_i X_i + C_i Z_i \quad (4.109)$$

Where the moment arms are the distance between the aircraft center of gravity to the application point of the resultant aerodynamic force for a specific subsystem, or its center of pressure¹⁰:

$$Z_i = -(WL_i - WL_{CG}) \quad (4.110)$$

$$X_i = FS_i - FS_{CG} \quad (4.111)$$

The moment summation is the result of equation (3.31). Note that (3.31) sums the moments around the AC for the tiltrotor fuselage, wings and horizontal stabilizer. Analogous procedure is performed for thrust forces T_X and T_Y and to its moment around aircraft center of gravity M_{TCG} .

¹⁰ For subsystems that calculate the aerodynamic moment, the distance between the aerodynamic center and the center of pressure is considered small enough to be neglected in the final moment summation.

4.9.3 Trim Routine

Once determined all terms in (3.27), the model computes the solution for each step of time for a given attitude solving the equations. The output is a set of control variables that comply with them for each step. The total set is composed by the time history response of the elevator position δ_E , the rotors RPM and thrust direction φ through the entire SFAP.

The algorithm used to perform the trim calculations was the Nonlinear Optimization by Mesh Adaptive Direct Search (NOMAD), which is a gradient-free minimization method. Direct search methods for solving the trim problem are widely used according to De Marco, Duke and Berndt (2007). The NOMAD codes are available for Microsoft Excel software (MICROSOFT, 2013a) as an open source software add-in programmed in VBA developed by Mason (2012).

NOMAD is the implementation of the Mesh Adaptive Direct Search algorithm (MADS) created by Audet and Dennis (2006). This method is based on a rigorous convergence theory of nonsmooth calculus for minimizing a function f under general constraints. A complete description about NOMAD can be found in Le Digabel (2011).

An application of a nonlinear, constrained and multiobjective problem using MADS was developed by Torres *et al* (2011). They led a research aiming on minimizing the environmental footprint (noise nuisance in the protected zones near airports, local air quality, and global warming) finding the optimum trajectory for commercial aircraft departure procedures. The study was carried out with data provided by Airbus Operations, S.A.S. The general multiobjective problem using MADS is described in Audet, Savard and Zghal (2010).

4.9.4 Controls Validation

The solutions of the SFAP problem contains the control variables time history, but some of them do not comply with the safety, comfort and design constraints of Table 4. It was necessary to use a distinct approach for each one. While thrust angle φ , maximum and minimum pitch angles θ_{MAX} and θ_{MIN} were put as restrictions on the trim routine, thrust angle rate $\dot{\varphi}$, maximum rate of sink \dot{Z} , maximum pitch rate $\dot{\theta}$ and elevator deflexion rate $\dot{\delta}_E$ were evaluated after the full solution was computed, as a pass/fail criteria. When violation is detected, the model labels the solution with a specific flag.

4.9.5 Spreadsheet Data

In order to feed data for further classification and processing in RStudio software (RSTUDIO, 2019) the model was used to compute a set of one thousand possible solutions for the SFAP problem. For each one, the total procedure time was let to vary between 22.5 s¹¹ and 60 s and the attitude between 45 *deg* and -10 *deg*.

The total energy expenditure is an output of the powerplant subsystem that consumes the *RPM* and φ data. The optimization is then used to test all the different solutions and determine the one that minimizes the electrical power consumption of the eVTOL tiltrotor aircraft.

The total model output data contains the time and the attitude arrays, the controls validation flags, the calculated total energy and the set of control variables for each solution and serves as input data for the classification and regression models described in the next section.

4.10 MACHINE LEARNING

The machine learning field allows one to determine the desired inputs in order to cause a response based on the achievement of a target value. According Altay Guvenir and Uysal (2000), machine learning approaches are used to solve many real-life problems by means of regression and classification methods to develop predictive models.

Prediction is one of the main objects of study in machine learning and data mining. For problems where it is necessary to determine a real-valued or continuous target feature, the process of creating a prediction model is generally known as regression. On the other hand, classification differs from regression in that the predicted variable is categorical, that is, assumes a limited number of possibilities. For instance, a variable that can assume the colors blue, red and green is categorical.

Aiming on solving the SFAP problem, it was necessary to use both classification and regression models. While classifiers played the role to predict whether a new solution would

¹¹ Minimum time calculated by the model using the trim routine to accomplish the entire SFAP.

infringe any safety, comfort or design constraint, the regression model was able to point out the total energy expenditure throughout the SFAP.

4.10.1 Methods for Classification

The process of predicting a qualitative, or categorical, response is known as classification. According to James *et al.* (2013) “predicting a qualitative response for an observation can be referred to as classifying that observation, since it involves assigning the observation to a category, or class”. The observation flags indicating constraints violation, then, are classified into two different categories: true or false. In the manner of a Boolean variable. True indicates violation and false the opposite.

There are a number of techniques for classification that can be proposed for the SFAP. In most real cases, it is impracticable to determine previously the classifier that best suit the problem in question. Thus, it is common to first promote an analysis to find the more accurate classifier based on training set of input data.

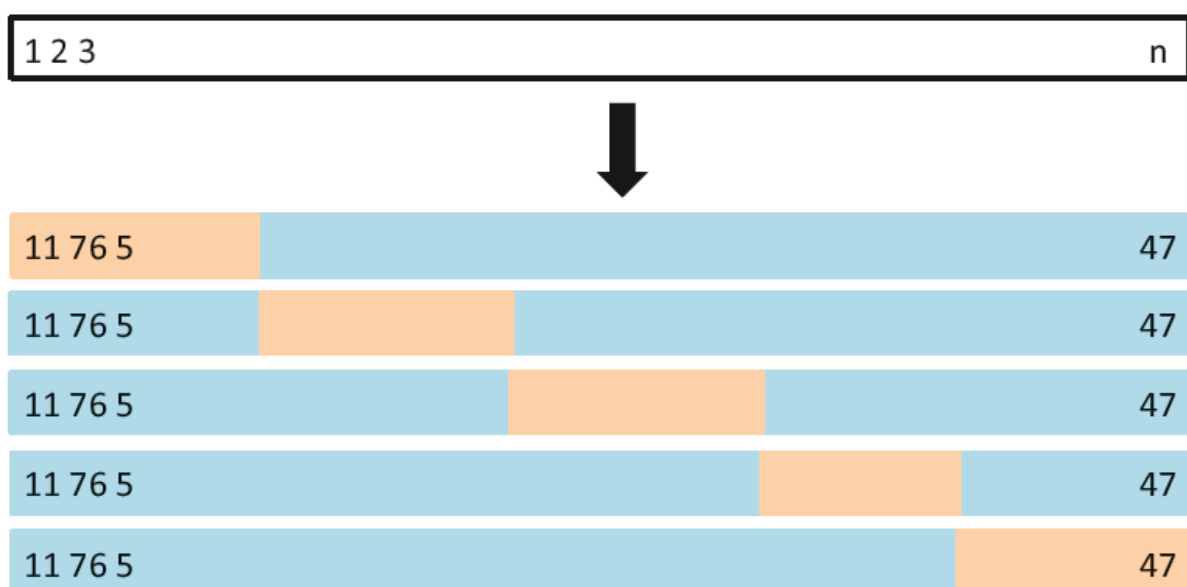
Four different methods are tested in terms of their precision: the K-Nearest Neighbors (KNN), the Quadratic Discriminant Analysis (QDA), the Classification and Regression Tree (CART) and the Random Forest (RF). Details on these methods are found in James *et al.* (2013). A comparison between them is done using a ROC curve. In spite of its historic name (Receiver Operating Characterists) which is a legacy from communications theory, the ROC curve determines the overall performance of a classifier, which is given by the AUC number, the area under the curve. The larger the AUC, the better the classifier. A classifier with an AUC of 0.5, for example, operates no better than chance.

Prediction accuracy of already known observations are not the final goal of an efficient classifier. Its capacity to predict new unknown observations is what one seeks instead. Thus, in the process of building a classification model, it is necessary to split the data input into two different segments: the training and the test data sets. The former is used to train, or teach the method how to estimate the class of the qualitative variable. The latter, in turn, is used to evaluate whether the classifier was well trained. The input data is then divided into 70% for training and 30% for testing.

Even within the training set, there are different approaches in order to accomplish an efficient training before starting predictions of new observations. The one chosen for the purposes herein pursued is the k-fold cross validation (10-fold, in particular). According to James *et al.* (2013, p. 181):

[...] This approach involves randomly dividing the set of observations into k groups, or folds, of approximately equal size. The first fold is treated as a validation set, and the method is fit on the remaining k – 1 folds. The mean squared error, MSE, is then computed on the observations in the held-out fold. This procedure is repeated k times; each time, a different group of observations is treated as a validation set. This process results in k estimates of the test error, $MSE_1, MSE_2, \dots, MSE_k$.

Figure 58 – A 5-fold CV. Validation folds are shown in beige. Training folds in blue.



Source: James *et al.* (2013, p. 181).

4.10.2 Methods for Regression

Most of the theory applied to classification methods still hold for regression. Regression is the choice for predicting the total energy expenditure through the flight path. The difference from classifiers is that the amount of energy is a continuous real-valued parameter, which makes the regression the appropriate technique to address it.

The methods evaluated for regression are the Random Forest (RF) and Generalized Additive Model (GAM). The GAM is a way to deal with multiple predictors, such as the

regression splines, smoothing splines and local regression. It is a common approach when treating nonlinear sophisticated predictions. The Random Forest tree-based method is used in the same manner as for classifying, but now as to foresee a real-valued parameter.

For regression, the data is divided into 80% for training and 20% for testing. The best suited model is evaluated in terms of its R-squared and MSE's. The training is also carried out in the basis of a 10-fold cross validation.

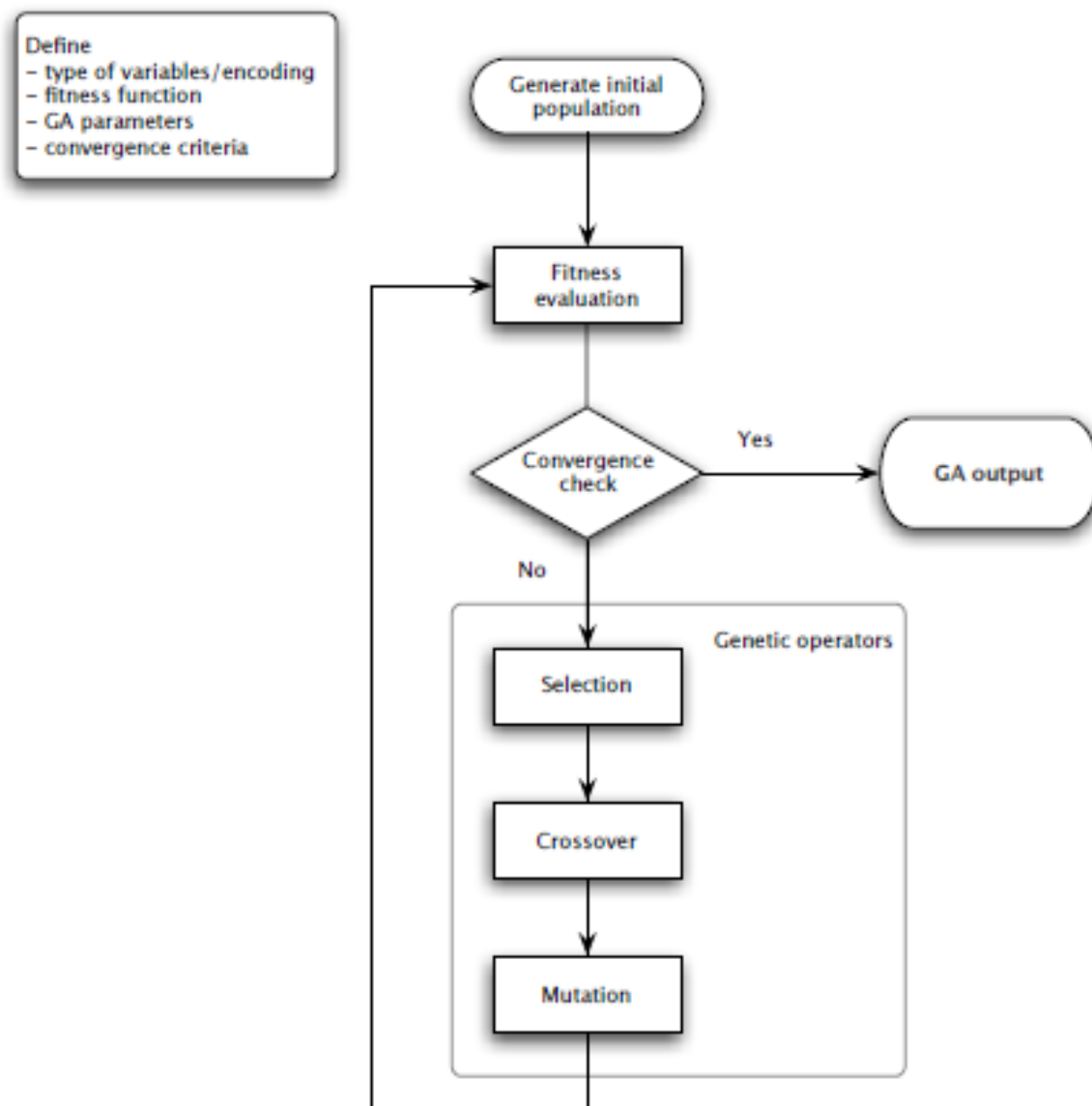
4.10.3 GA Algorithm for Optimization

The machine learning methodology is the key for a fast prediction. It can also be applied for further applications, when dealing with take-off or flight level changes for instance, or even with other different trajectories for approach and landing. An optimization analysis considering the full model equations would have been of too much computational time and effort, and would probably have made impracticable running an optimization algorithm several times for any possible model, or algorithm parameter changes. The efforts in developing such procedures encourage a practicable application of the methodology herein developed. Once models for classification and regression are well trained with satisfactory accuracy, it might be attached to real flight control computers embedded to eVTOL aircrafts. Once defined real waypoints to travel, a low computational cost makes it possible to compute the optimum solution prior to flying through these points and eventually promoting lower operational costs and greater flight autonomy.

In that way, the classifiers prediction of safety, comfort and design constraints and the regression model energy expenditure calculation are used, together, to calculate a genetic algorithm cost function. First, Figure 59 shows a genetic algorithm schematic. This is a representation of the steps presented in section 3.8. The programming used the package GA and a full description of its functionalities are found in Scrucca (2013).

It follows the GA parameters settings: real-valued population, nonlinear-rank selection, local arithmetic crossover and uniform random mutation. Eiben and Smith (2015) brings deep details on the theory of these settings. Furthermore, for crossover operator information, see Picek, Jakobovic and Golub (2013).

Figure 59 - Schematic of genetic algorithm.



Source: Scrucca (2013, p. 4)

The algorithm works as follows: initially a population is generated with random individuals (also called members, or chromosomes); the fitness for each member is evaluated and a convergence check indicates whether the GA has finished or not. In case of no convergence, the three genetic operators (selection, crossover and mutation) are applied. Lastly, it comes back to the fitness evaluation and convergence check until the criterion is met or the maximum number of iterations is reached.

In the SFAP problem, the flight path is divided into steps. Each member represents a possible solution for the trajectory and contains values for the pitch attitude and time for each

step. The main fitness calculation is the total energy expenditure throughout the trajectory. The final GA output is, then, the solution with the minimum energy expenditure along the path.

The controls validation flags are addressed inside the fitness function calculation. As the iterations take place, every new solution is tested by means of its fitness. If any of the classifiers points out a violation, the fitness function receives a forbidding cost, which makes it unfeasible.

5 RESULTS

5.1 CODES IN R

5.1.1 Introduction

In this section, the main results are shown and discussed. The codes created during the process to find the GA output and the aircraft's response in terms of its subsystems characteristics (fit to the optimum energy solution) are brought in detail. This response is the aircraft dynamic behavior when submitted to the optimized parameters found in R. They were used to feed the eVTOL model after the GA run.

5.1.2 Classification

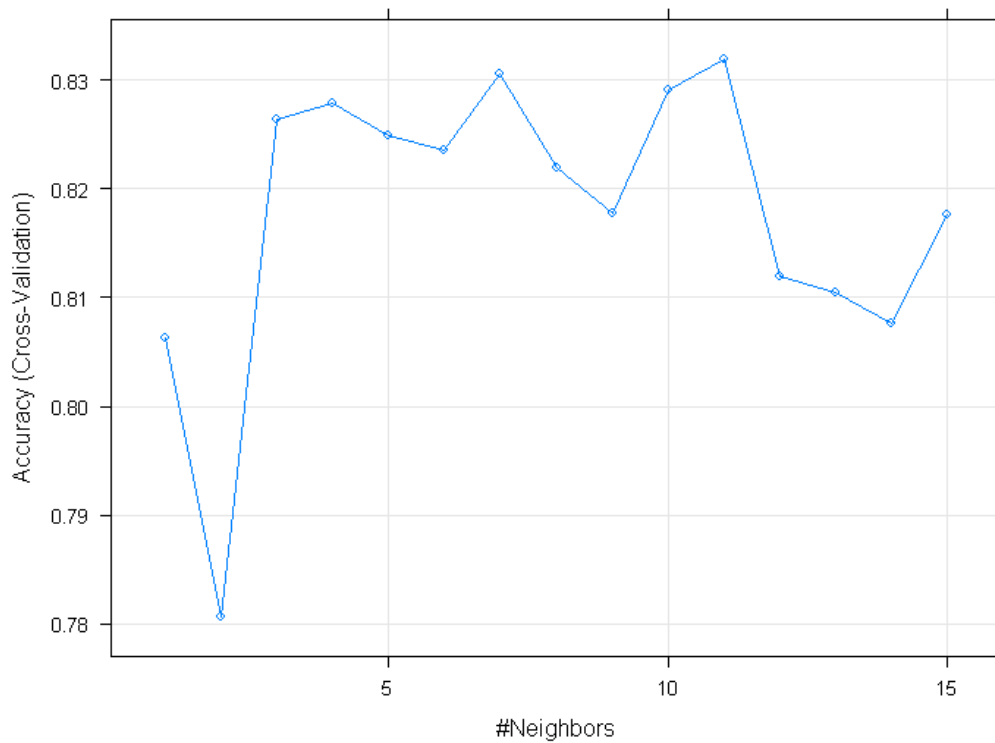
For all constraints in Table 4 - Safety, Comfort and Design ConstraintsTable 4, all solutions met the criteria for thrust angle rate $\dot{\varphi}$ and elevator deflexion rate $\dot{\delta}_E$. Therefore, these restrictions were not evaluated with classifiers. However, the maximum pitch rate $\dot{\theta}$ and the maximum rate of sink \dot{Z} were not met within these limits in several of the solutions contained in the spreadsheet data input and, thus, had to be treated and classified.

The data presented below show the process of building the classification models that were tested for each of these controls validation flags.

- Maximum Pitch Rate $\dot{\theta}$

According to Table 4, the maximum value for the pitch rate is 10 *deg/s*. Initially, in order to build a KNN classifier, a survey was carried out to determine the number of closest neighbors, per construction, that optimize its performance (Figure 60). It can be seen from the plot that the choice of 11 neighbors is the most appropriate.

Figure 60 - Accuracy of KNN classifier for maximum pitch rate as a function of neighbors number.

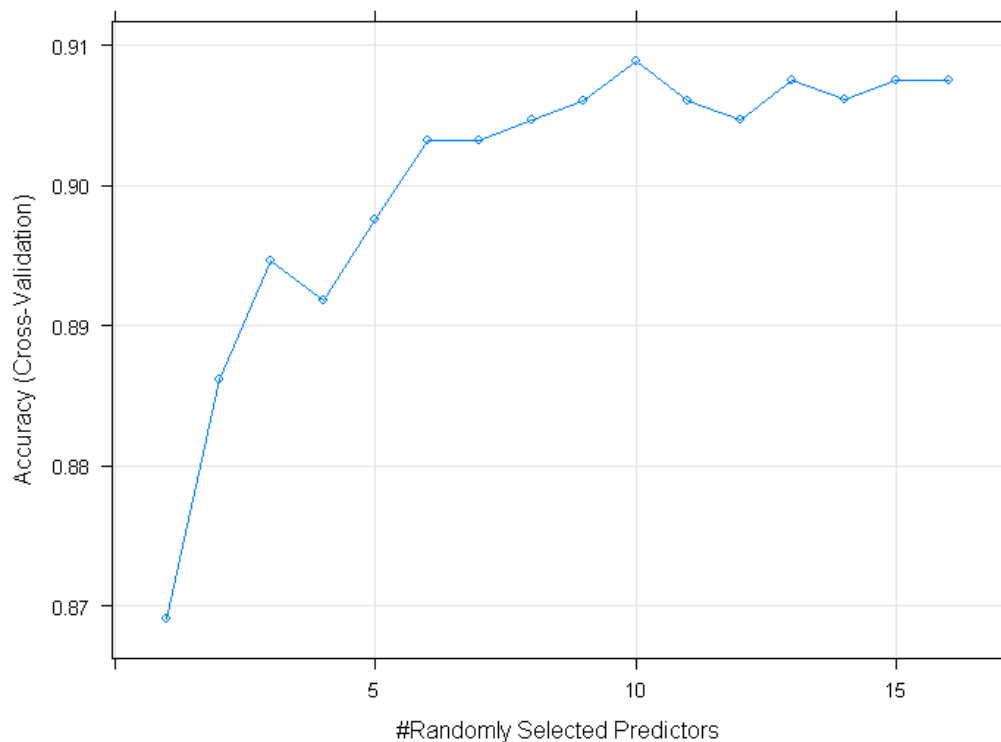


Source: Created by the author using RStudio software (RSTUDIO, 2019).

The Random Forest method is based-tree and, therefore, suggests a prior determination of the number of trees (sub models) and the number of variables that will compose each tree. Random Forests are ensemble classifiers that combine predictions of its trees. Therefore, it is possible to choose optimal numbers that maximize accuracy. The way to determine these values is contained in Figure 61 and Figure 62, in which one must note that 10 variables, or predictors, and 50 trees are the optimal numbers.

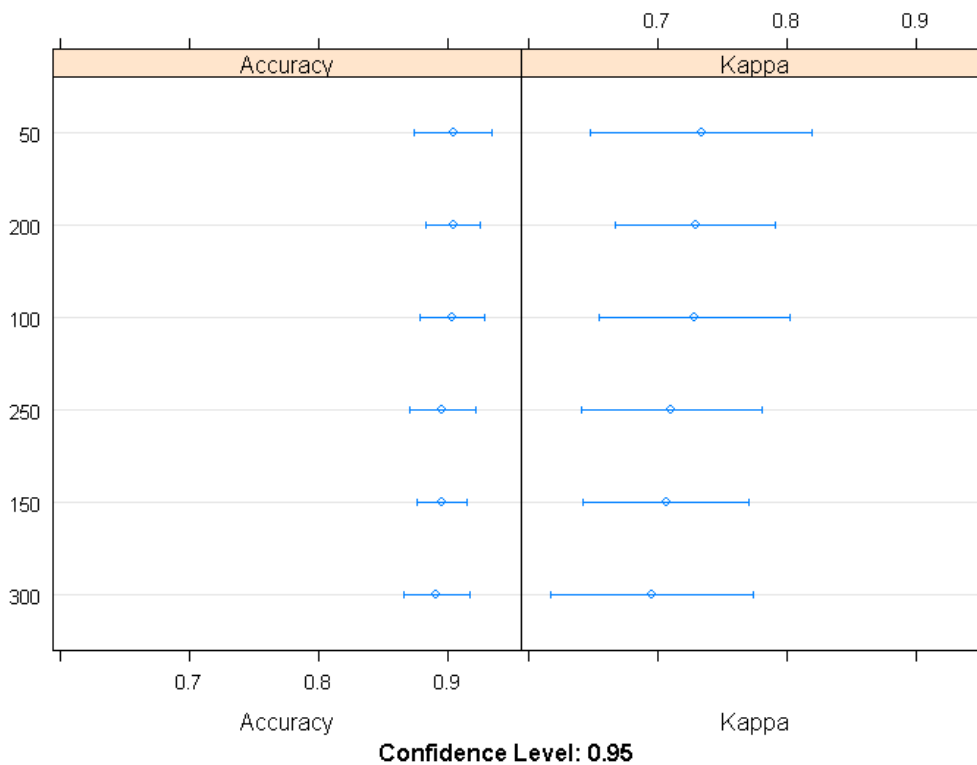
Lastly, the performances of the KNN, QDA, CART and RF classifiers are compared using ROC plots. As previously stated in section 4.10.1, the input data is then divided into 70% for training and 30% for testing. While each classifier model are trained using the training data, the ROC plots considers the test data, or the remaining 30%. The one that performs best is the one that maximizes the AUC, or the area under the curve. Thus, the selected to integrate the GA, regarding classification of maximum pitch rate, is the RF, which resulted in an AUC of 0.977.

Figure 61 - Accuracy of RF classifier for maximum pitch rate as a function of selected predictors.



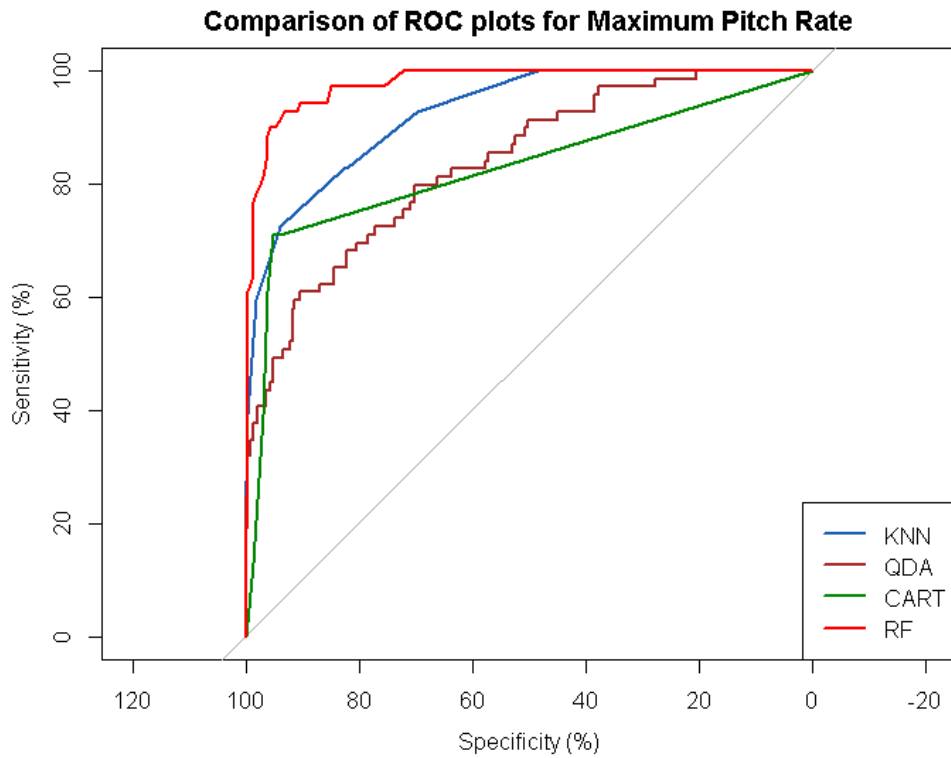
Source: Created by the author using RStudio software (RSTUDIO, 2019).

Figure 62 – Accuracy and Kappa of RF classifier for maximum pitch rate as a function of the number of trees.



Source: Created by the author using RStudio software (RSTUDIO, 2019).

Figure 63 – Comparison of ROC plots for maximum pitch rate.



Source: Created by the author using RStudio software (RSTUDIO, 2019).

- Maximum Sink Rate \hat{Z}

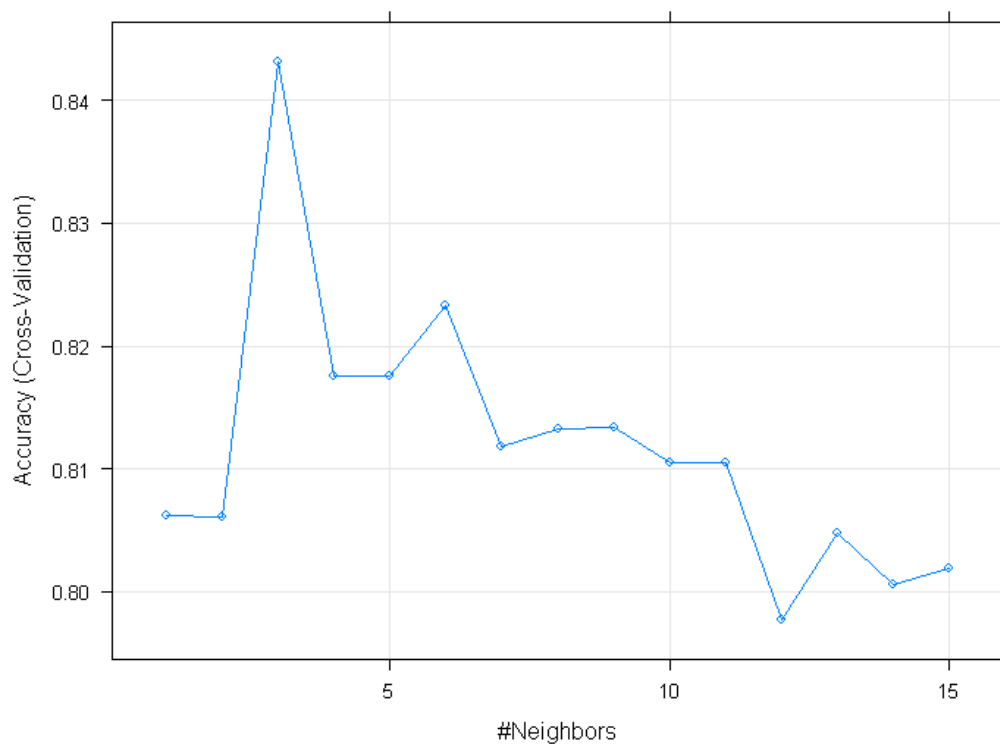
An analogous methodology is used to determine the maximum sink rate classifier. For KNN, the number that optimizes its performance is 3 neighbors, that is, the training of the model must be based on a classification of each single data taking into account 3 nearest neighbors.

In the case of the RF, Figure 65 and Source: Created by the author using RStudio software (RSTUDIO, 2019).

Figure 66 show that the best way to train the RF is with 150 trees and 3 variables per tree.

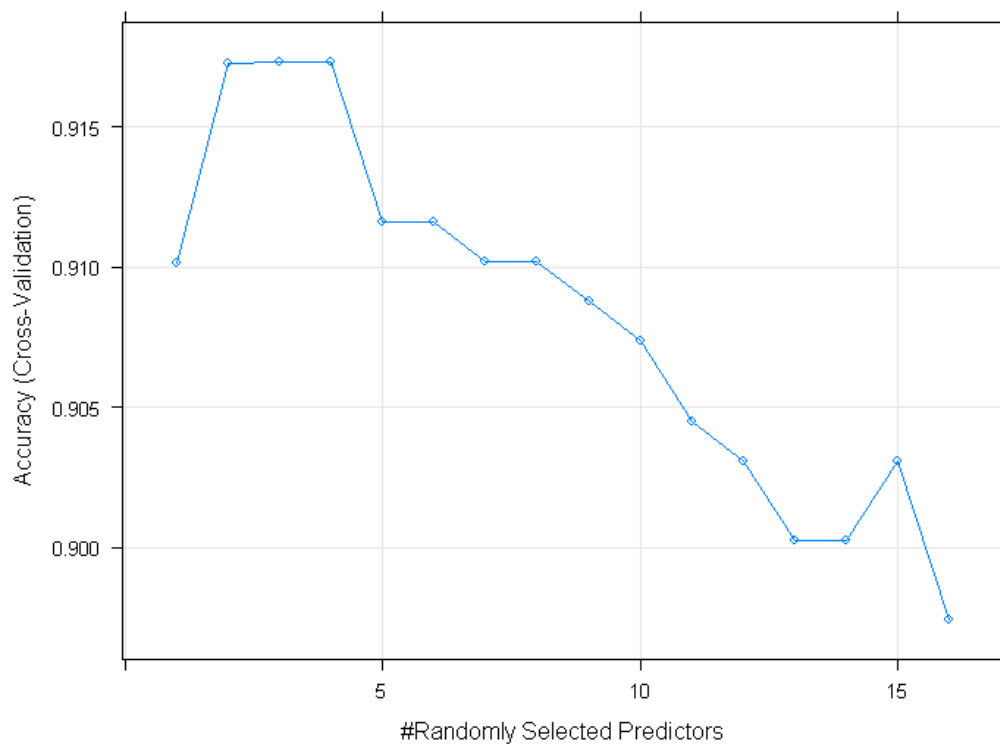
Finally, the comparison via ROC plots for the maximum sink rate, also based on the test data, suggests the choice of RF to integrate the final optimization algorithm, the same type chosen for the maximum pitch rate classifier.

Figure 64 - Accuracy of KNN classifier for maximum sink rate as a function of neighbors' number.



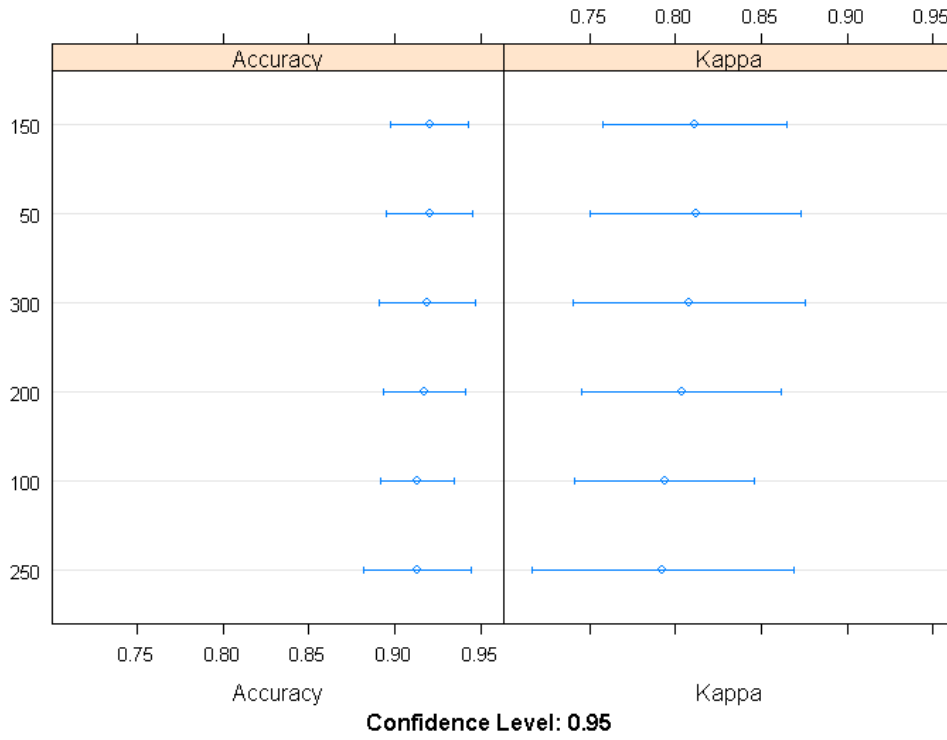
Source: Created by the author using RStudio software (RSTUDIO, 2019).

Figure 65 - Accuracy of RF classifier for maximum sink rate as a function of selected predictors.



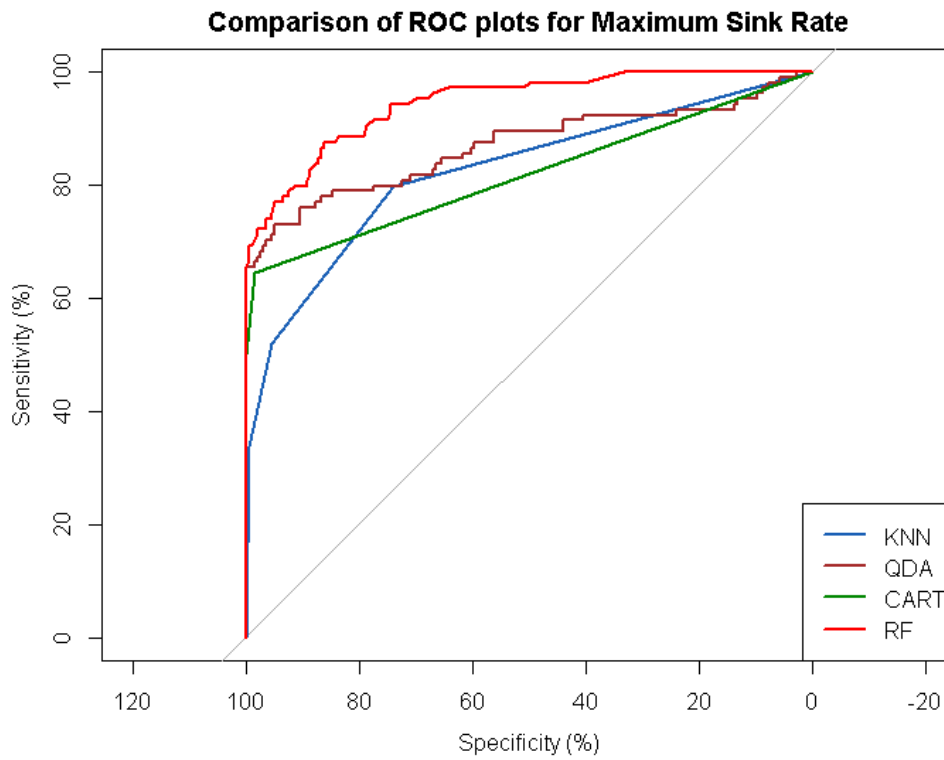
Source: Created by the author using RStudio software (RSTUDIO, 2019).

Figure 66 – Accuracy and Kappa of RF classifier for maximum sink rate as a function of the number of trees.



Source: Created by the author using RStudio software (RSTUDIO, 2019).

Figure 67 - Comparison of ROC plots for maximum sink rate.



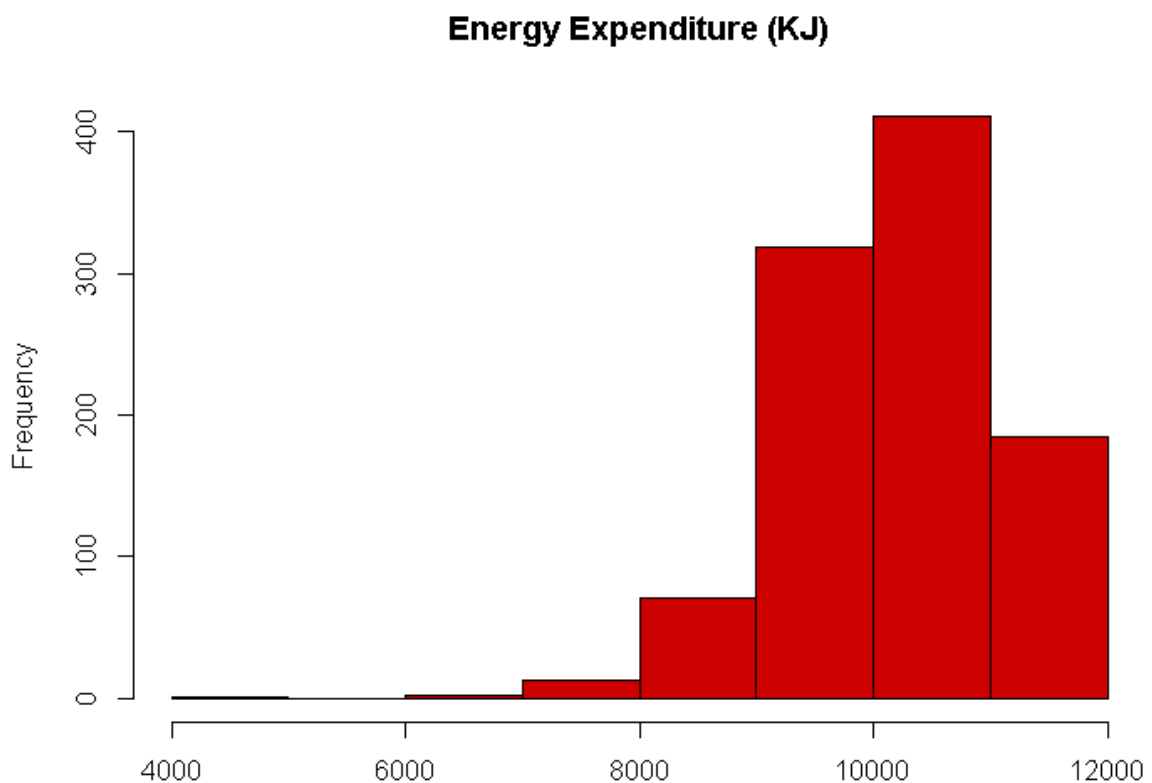
Source: Created by the author using RStudio software (RSTUDIO, 2019).

5.1.3 Regression

The regression model is responsible for predicting the energy expended during the entire trajectory studied. Initially, in order to study the sample distribution of energy data, an exploratory analysis of the data is performed (Figure 68). It is noticed that the values of this variable are concentrated in the region between 10000 to 12000 *KJ* and, in addition, there are some outliers close to 4000 *KJ*.

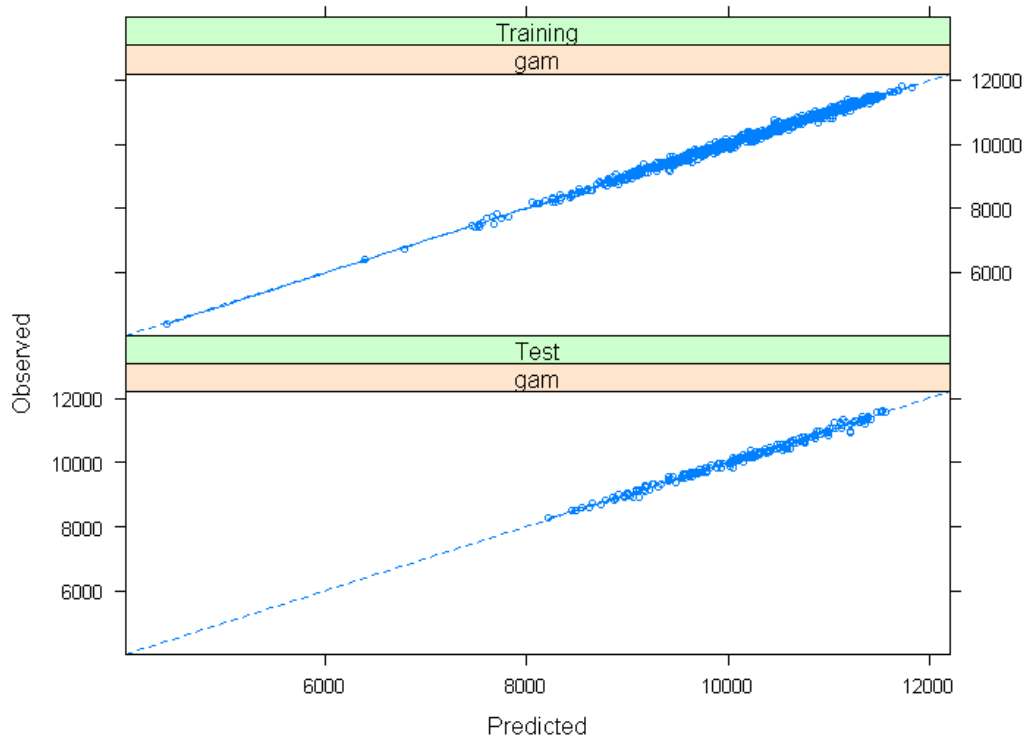
Two types of regression methods are tested, GAM and RF. The performance of the GAM model can be seen in Figure 69. In this figure, the model performance is tested in both training and test data. The interpretation of this schematic suggests that the closer the points are to the 45 *deg* straight line, the better the performance of the regression model.

Figure 68 - Energy expenditure sample distribution (all solutions of spreadsheet data).



Source: Created by the author using RStudio software (RSTUDIO, 2019).

Figure 69 - Accuracy of GAM for the training and the test sets.



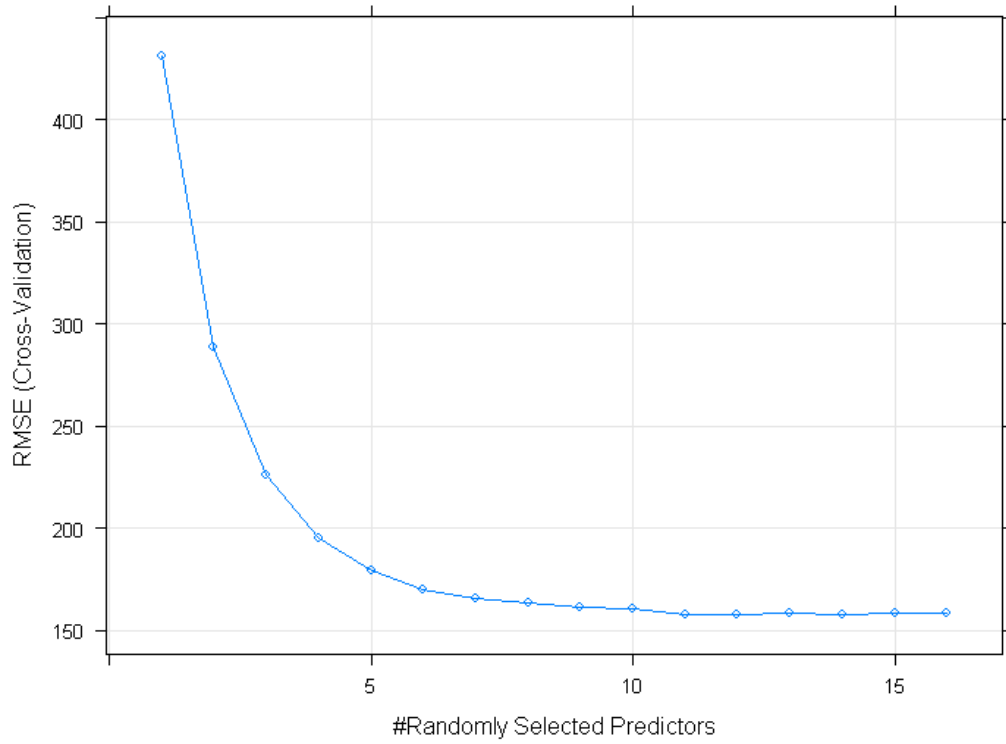
Source: Created by the author using RStudio software (RSTUDIO, 2019).

The second type of regression model built was the RF. In order to find the values that maximize the performance of this model, first the number of variables per tree and the number of trees to be used is determined, as well as done for the classifiers. In this case, 14 variables and 300 trees are the values that minimize the Root Mean Square Error (RMSE).

A measurement similar to what was done for the GAM can also be made for the RF regarding its accuracy of prediction for the training and test data. As with the GAM model, the data seems to fit the 45 *deg* straight line well.

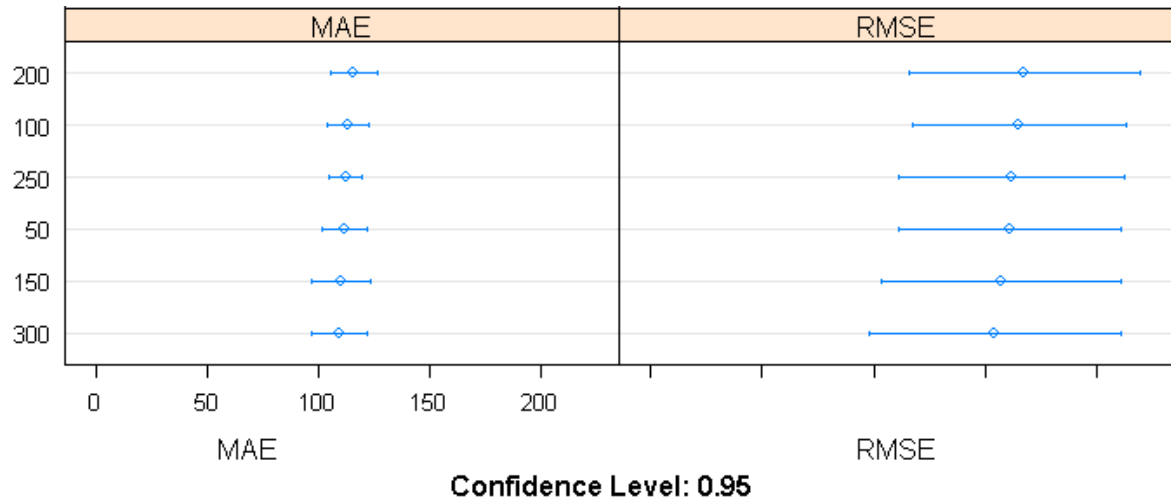
The time and attitude data were divided into arrays, so that each position in the array represents a time or attitude step. The set of all positions of the time and attitude arrays represent the variables that the built models are based on to achieve their prediction results. In the case of the RF models, it is possible to observe the influence that the last step of time has on the value of total energy spent, possibly because it is very close to the region where pure hover movement begins.

Figure 70 – RMSE of RF for energy expenditure as a function of selected predictors.



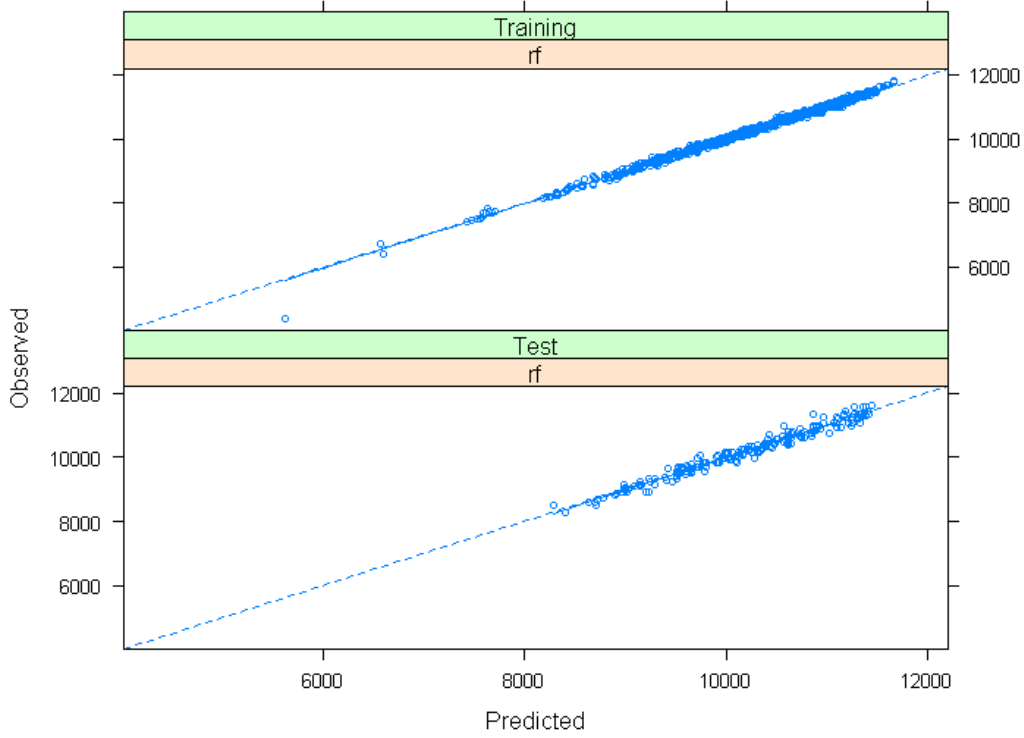
Source: Created by the author using RStudio software (RSTUDIO, 2019).

Figure 71 – RMSE and MAE of RF for energy prediction.



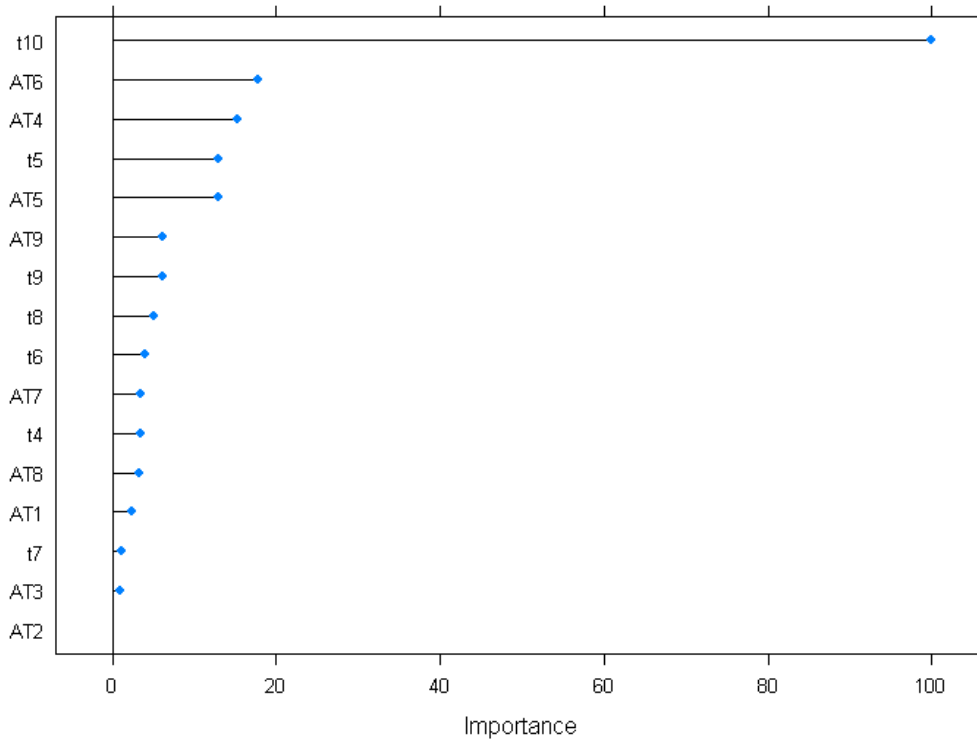
Source: Created by the author using RStudio software (RSTUDIO, 2019).

Figure 72 – Accuracy of RF for the training and the test sets.



Source: Created by the author using RStudio software (RSTUDIO, 2019).

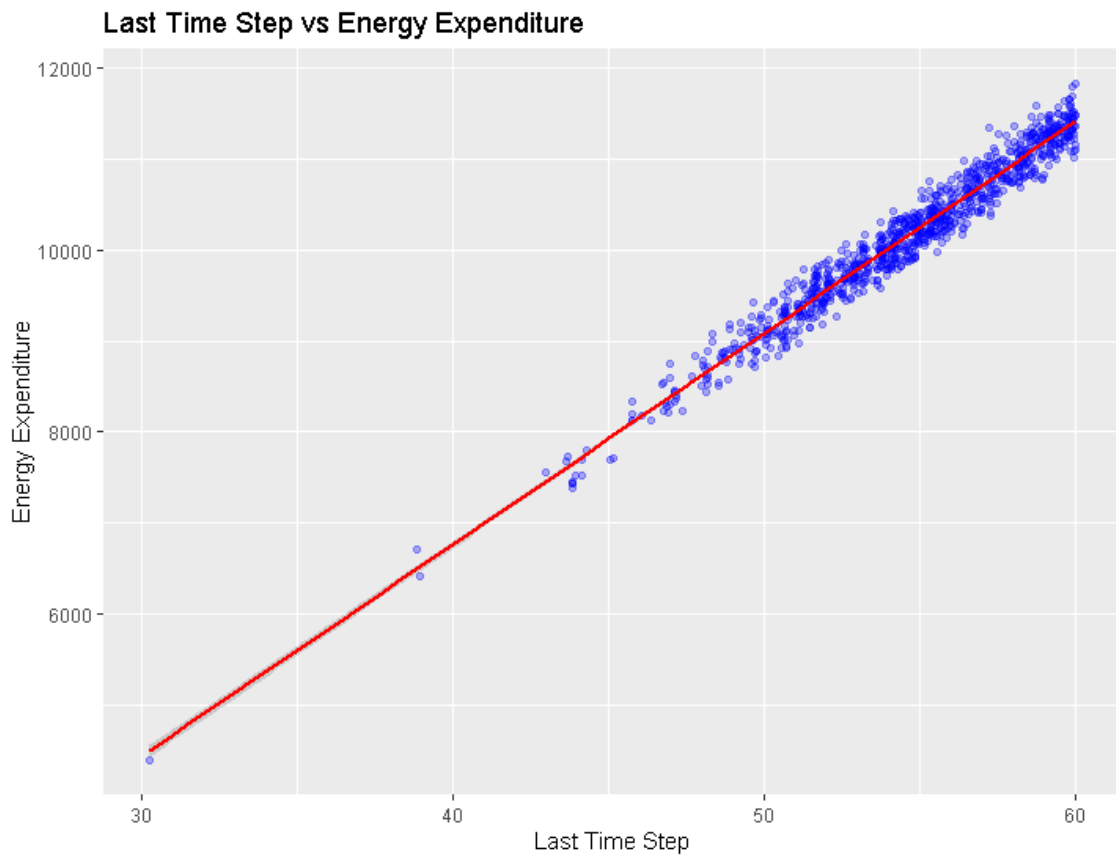
Figure 73 – Importance of variables on RF regression model. "AT" means attitude and "t" time.



Source: Created by the author using RStudio software (RSTUDIO, 2019).

In fact, when assessing a direct energy dependence diagram with the last step of time, the correlation between the two variables visually fits a line very well, which indicates that minimizing time at the final moments of the trajectory should minimize significantly the total energy expended.

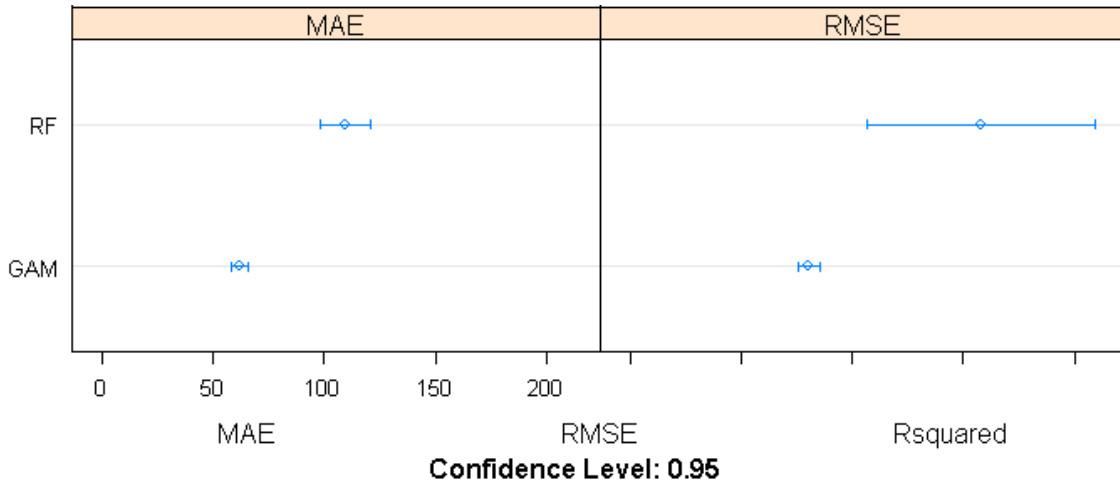
Figure 74 – Dependence of energy on the last time step.



Source: Created by the author using RStudio software (RSTUDIO, 2019).

Conclusively, a comparison between the regression models suggests that precision and accuracy in the GAM model are better, which can be inferred by measuring the R-squared and RMSE indicators. An assessment of Figure 76, leads one to notice that both the average R-squared is higher, and its dispersion spread-out around the mean value is lower for the GAM type regression model. Its value for the GAM resulted in 0.9912018, while the RMSE in 73.4232664.

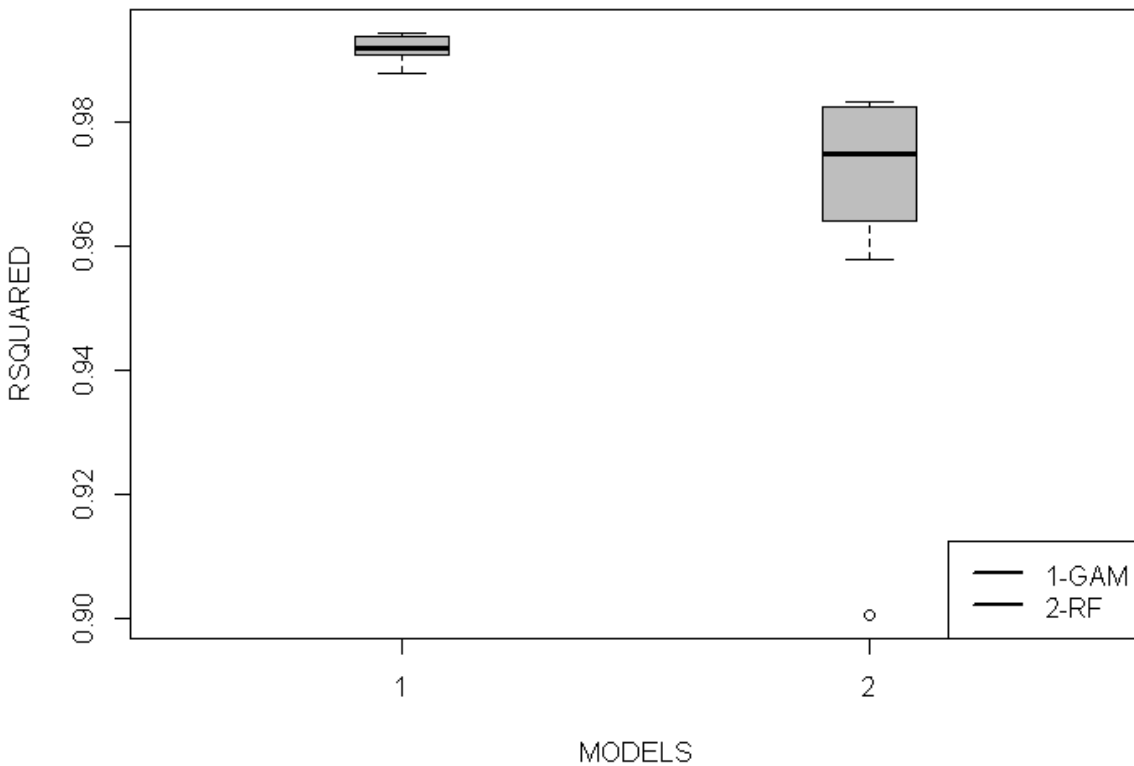
Figure 75 – RMSE and MAE for GAM and RF.



Source: Created by the author using RStudio software (RSTUDIO, 2019).

Figure 76 – Boxplots of R-squared for GAM and RF regression.

Boxplots for R-squared for GAM and Random Forest Regression

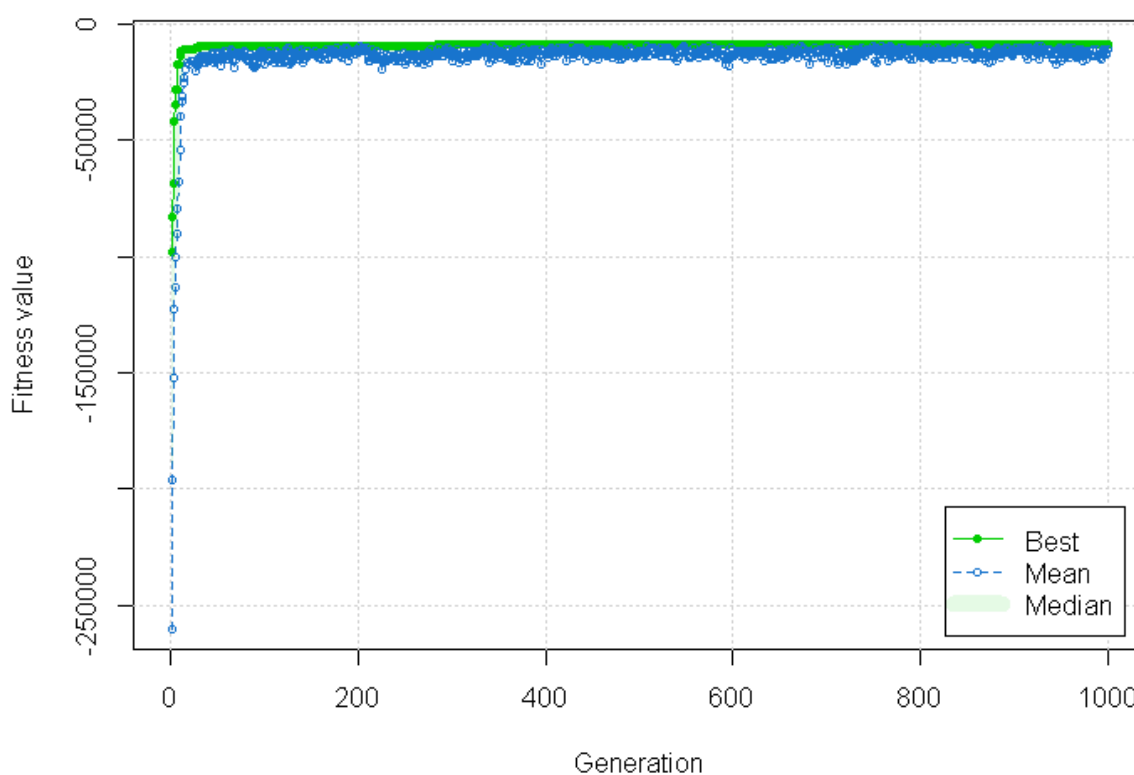


Source: Created by the author using RStudio software (RSTUDIO, 2019).

5.1.4 Optimization

The optimization took place using both the classification and the regression models previously presented. It stands for an evolutionary algorithm, configured with a population of 100 individuals and with mutation and crossover operators set to 10% and 70% respectively. Instead of defining a convergence parameter, it was decided to work only with a maximum number of iterations, maintained at 1000. Thus, the evolution of the algorithm is shown in Figure 77.

Figure 77 – Genetic Algorithm evolution.



Source: Created by the author using RStudio software (RSTUDIO, 2019).

The energy optimization resulted in a value of 8724.08 KJ, or 2.42 kWh for a trajectory of 50.35 s. The mean expenditure, when considering all the solutions, was of 10306.15 KJ (2.86 kWh), which gives a performance save of 15.35%. When compared to the maximum energy solution (11932.32 KJ, or 3.31 kWh) the improvement is even better, and becomes of 27.19%.

The GA does not test every new possible solution into the eVTOL model, in the sense that the gain in computational cost has the drawback that some steps of the proposed

solution might not be directly trimmable by the aircraft model in exact numbers. In practice, this means that the GA output values, if fed back into the original eVTOL model, result in a dynamic response slightly different from that predicted by the optimization algorithm. However, even after data feedback and trimming, the total energy expenditure was of 9116.20 *KJ*, or 2.53 *kWh*, which still results in a performance save of 11.55%. The dynamic response of the aircraft, already trimmed by the model assuming this variation, is presented in detail for each subsystem in the following section.

It is possible to observe that with approximately 300 iterations, the solution with the minimum energy found by the GA was already very close to the final result. This means that, in the case of practical applications, it would still be possible to reduce the number of iterations if there are any computational processing limitations, or even in order to seek better performance on a Flight Management System (FMS) embedded in a real eVTOL. Defining a convergence criterion is encouraged too.

5.2 eVTOL MODEL BUILT

In order to comply with the equations presented for all subsystems in the Methodology section, typical values for the constraints and parameters described in each one were applied for the simulation example. The simulation efforts led to the results depicted henceforth. They are presented in tables and plots formats. The calculated procedure total time was 50.35 *s*, after optimization. It was sorted in 10 steps up to VDP and one last step for final pitch adjustment. The time history plots and table rows go through each time step.

5.2.1 Aircraft State Parameters

- Initial Conditions at TLP – Values for Statements (3.32):

Parameter	Value
X_0	$-1640 \text{ ft } (-500 \text{ m})$
Z_0	$360 \text{ ft } (110 \text{ m})$
V_{T0}	70 kt
γ_0	-3 deg

- Final Conditions at VDP – Values for Statements (3.33):

Parameter	Value
X_F	0 ft
Z_F	50 ft
\dot{X}_F	0 kt/s
\ddot{X}_F	0 kt/s^2
$\dot{\theta}_F$	0 deg/s
$\ddot{\theta}_F$	0 deg/s^2

- Positions, Speeds and Accelerations

Table 7 - Trajectory data for positions, speeds, accelerations and attitude.

AIRCRAFT STATE PARAMETERS							
Time	Trajectory Parameters (Positions/Speeds/Accelerations/Attitude)						
t (s)	X (ft)	Z (ft)	X' (knots)	Z' (ft/min)	X'' (m/s ²)	Z'' (m/s ²)	θ (deg)
0.00	-1640	360	69.90	-371.00	-3.69	-0.06	12.21
2.70	-1321	340	50.52	-376.01	-1.89	-0.02	30.77
5.50	-1083	320	40.24	-378.67	-1.71	0.03	19.85
9.36	-820	292	27.39	-335.23	-0.84	0.02	30.71
15.75	-525	250	16.94	-291.34	-0.44	0.02	18.26
22.64	-328	211	11.00	-256.17	-0.26	0.02	0.85
27.94	-230	186	8.32	-239.03	-0.28	0.04	1.19

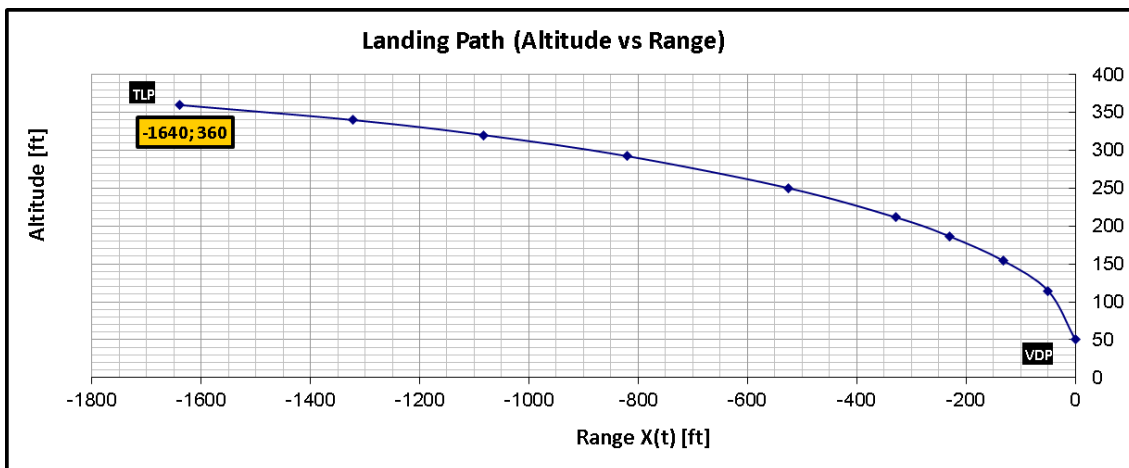
Table 7 - Trajectory data for positions, speeds, accelerations and attitude (CONTINUED).

AIRCRAFT STATE PARAMETERS							
Time	Trajectory Parameters (Positions/Speeds/Accelerations/Attitude)						
t (s)	X (ft)	Z (ft)	X' (knots)	Z' (ft/min)	X''(m/s ²)	Z'' (m/s ²)	θ (deg)
34.94	-131	154	4.46	-174.60	0.14	-0.08	-0.42
45.84	-49	114	7.47	-489.39	-0.98	0.31	5.86
49.75	0	50	0.00	0.00	0.00	0.00	-0.14
50.35	0	50	0.00	0.00	0.00	0.00	-1.48

Table 7 - Trajectory data for positions, speeds, accelerations and attitude (CONCLUDED).

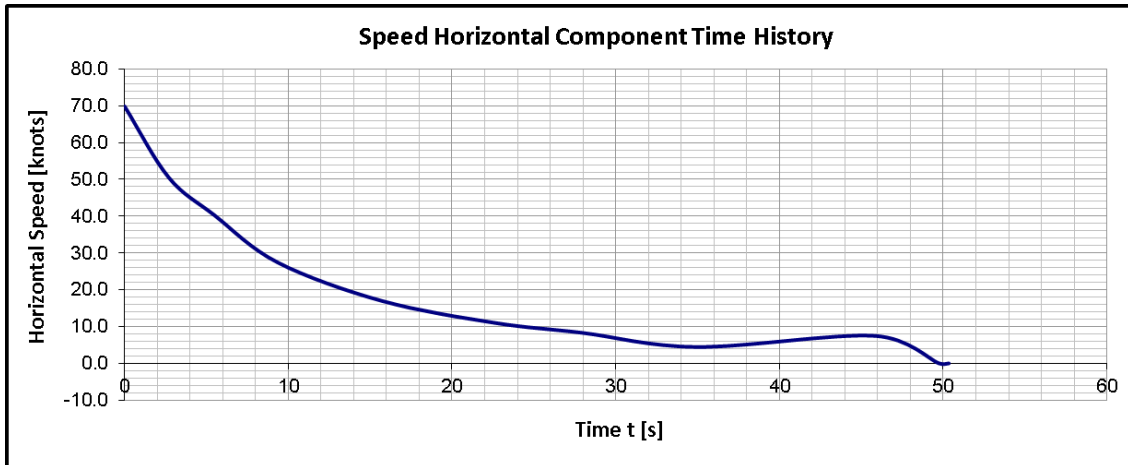
AIRCRAFT STATE PARAMETERS		
Time		
t (s)	θ' (deg/s)	θ''(deg/s ²)
0.00	6.87	-3.99
2.70	-3.90	2.40
5.50	2.81	-1.23
9.36	-1.95	-0.09
15.75	-2.53	0.38
22.64	0.06	-0.06
27.94	-0.23	0.12
34.94	0.58	-0.19
45.84	-1.54	2.96
49.75	0.50	-0.83
50.35	0.00	0.00

Figure 78 - Landing path (Altitude Z(t) vs Range X(t)).



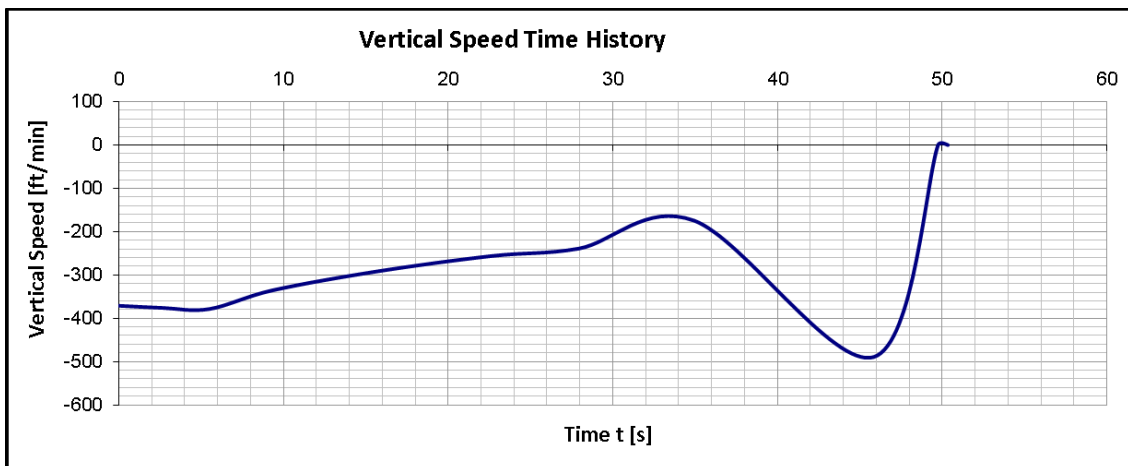
Source: Created by the author using Microsoft Excel (MICROSOFT, 2013a).

Figure 79 - Speed horizontal component – earth-axis $\dot{X}(t)$ time history.



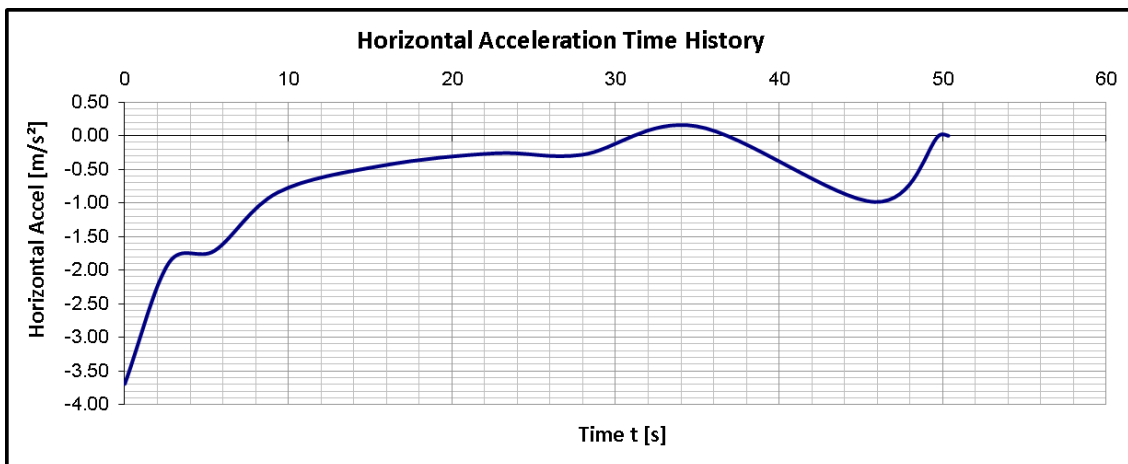
Source: Created by the author using Microsoft Excel (MICROSOFT, 2013a).

Figure 80 – Vertical speed – earth-axis $\dot{Z}(t)$ time history.



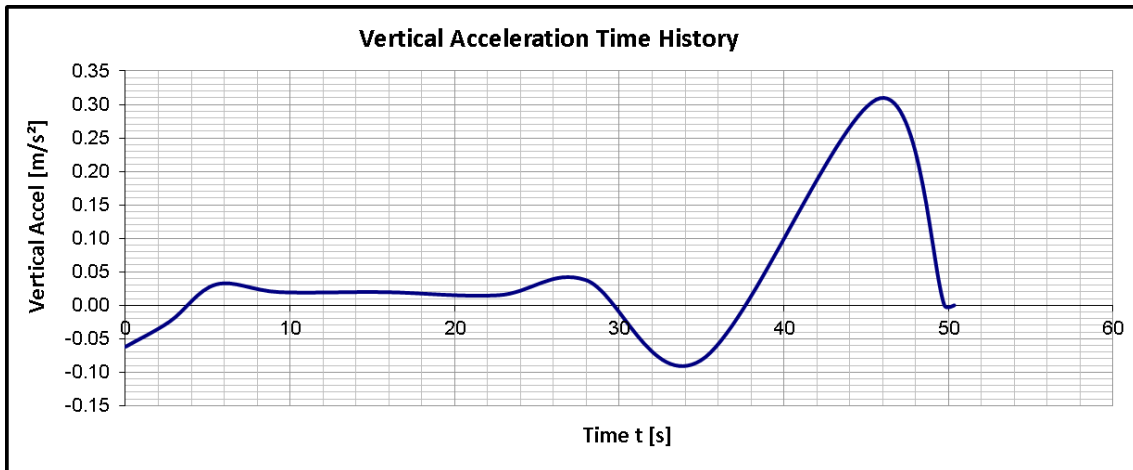
Source: Created by the author using Microsoft Excel (MICROSOFT, 2013a).

Figure 81 - Horizontal acceleration – earth-axis $\ddot{X}(t)$ time history.



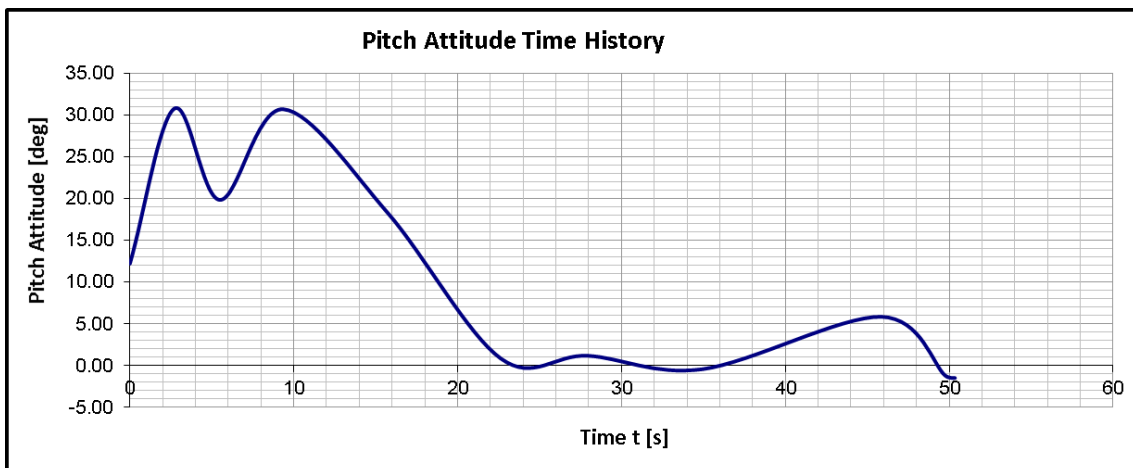
Source: Created by the author using Microsoft Excel (MICROSOFT, 2013a).

Figure 82 - Vertical acceleration time history.



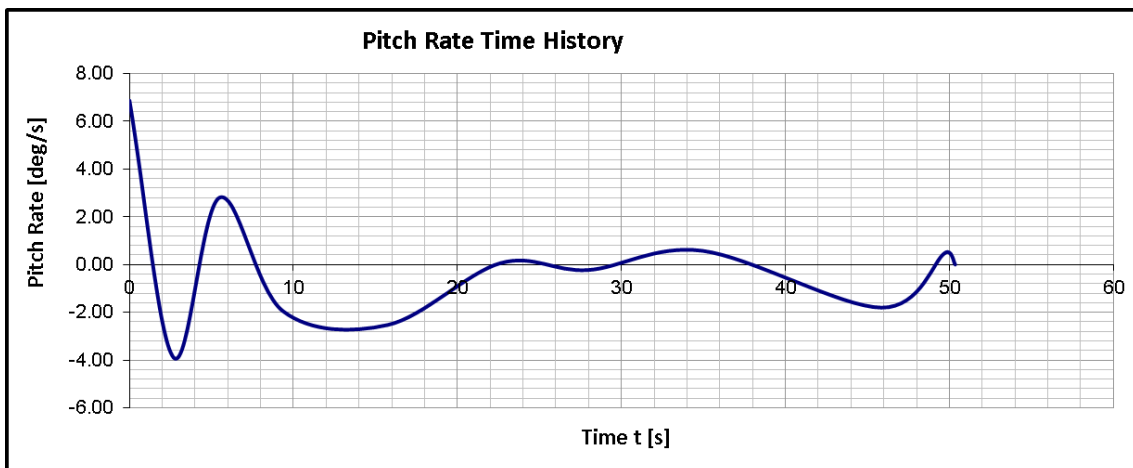
Source: Created by the author using Microsoft Excel (MICROSOFT, 2013a).

Figure 83 – Pitch attitude time history.



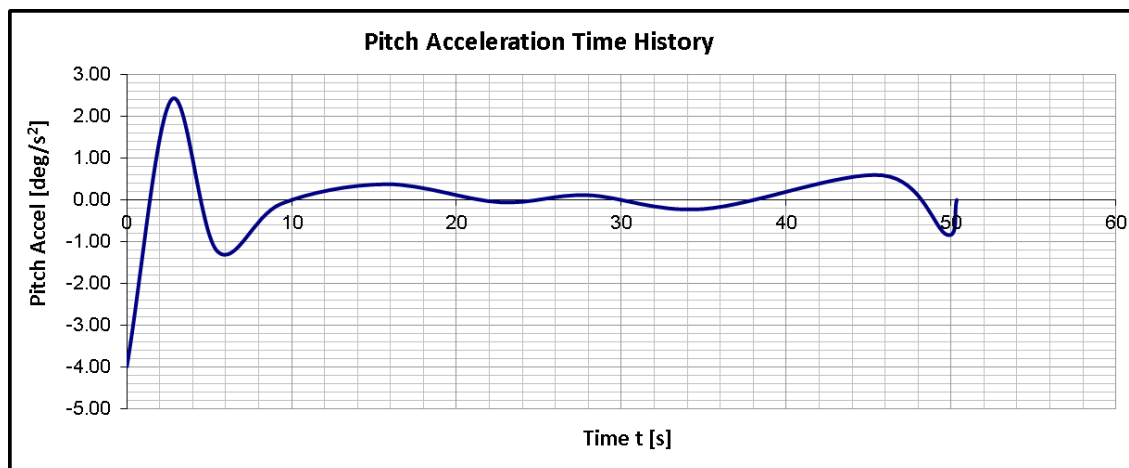
Source: Created by the author using Microsoft Excel (MICROSOFT, 2013a).

Figure 84 – Pitch Rate time history.



Source: Created by the author using Microsoft Excel (MICROSOFT, 2013a).

Figure 85 – Pitch Acceleration time history.



Source: Created by the author using Microsoft Excel (MICROSOFT, 2013a).

In the final step a pitch rate of 0.5 deg/s is used with constant pitch acceleration in order to reach the final hover conditions according to (3.33) at VDP and be ready to start the pure hover movement through the HAP.

5.2.2 Control Variables

The minimum energy path uses most of its elevator pitch up capacity initially and, then, the pitch down in order to return to low attitude positions (reference positive is trailing edge down). The RPM increases as the hover movement approaches. Analogous behavior is observed for the thrust angle φ , with a difference at the beginning, where some time is used to capture a smooth tilt.

- Control Variables:

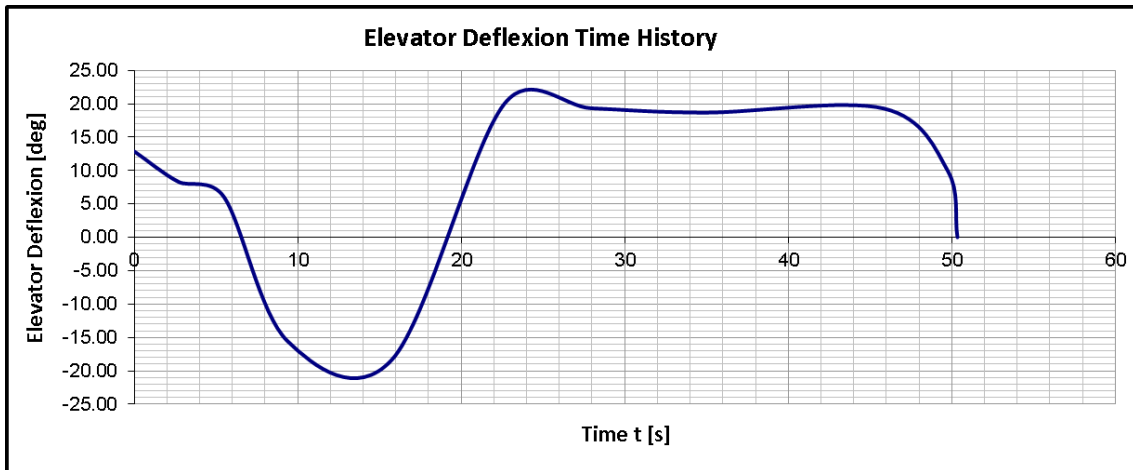
Table 8 - Control variables after optimization.

EQUATIONS OF MOTION			
Time	Control Variables		
t(s)	δ_E (deg)	RPM	φ (deg)
0.00	12.9	879	86.9
2.70	8.3	1477	46.6
5.50	6.0	1906	72.7
9.36	-15.5	2078	59.4
15.75	-18.3	2458	75.2
22.64	20.0	2462	91.3
27.94	19.3	2495	90.9
34.94	18.7	2511	90.0

Table 8 - Control variables after optimization (CONCLUDED).

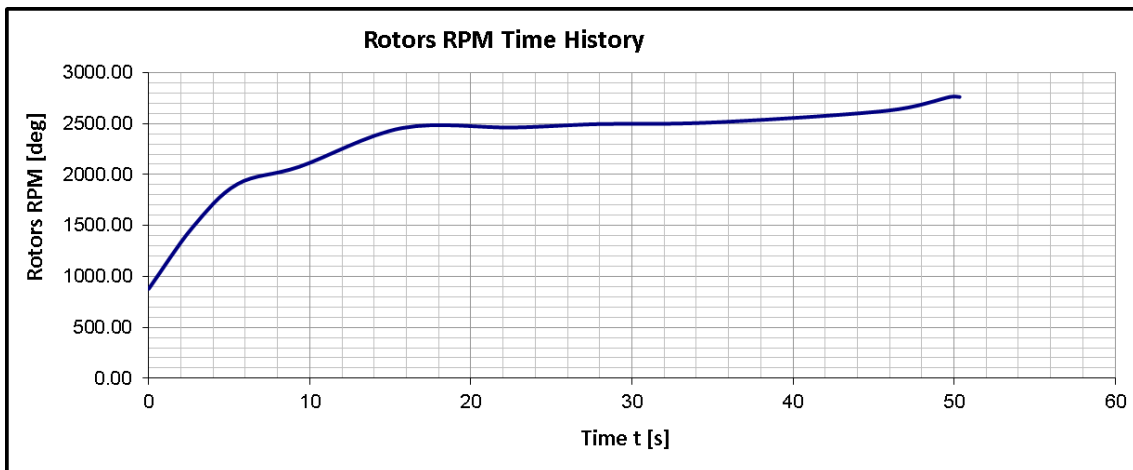
EQUATIONS OF MOTION			
Time	Control Variables		
t (s)	δ_E (deg)	RPM	φ (deg)
45.84	19.3	2627	90.1
49.75	10.0	2762	90.8
50.35	0.0	2761	91.0

Figure 86 – Elevator deflexion time history.



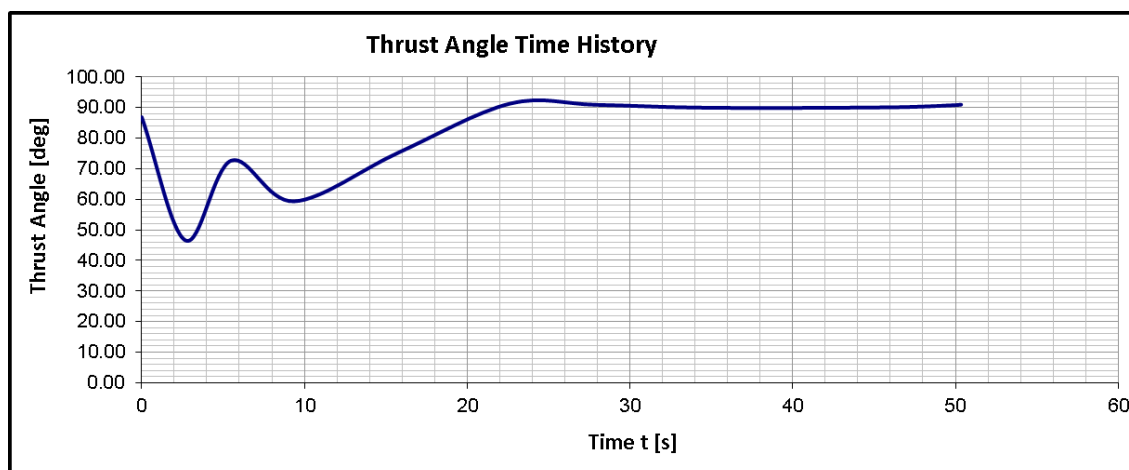
Source: Created by the author using Microsoft Excel (MICROSOFT, 2013a).

Figure 87 – Rotors RPM time history.



Source: Created by the author using Microsoft Excel (MICROSOFT, 2013a).

Figure 88 – Thrust angle time history.



Source: Created by the author using Microsoft Excel (MICROSOFT, 2013a).

5.2.3 Inertia and Balance

- Constants:

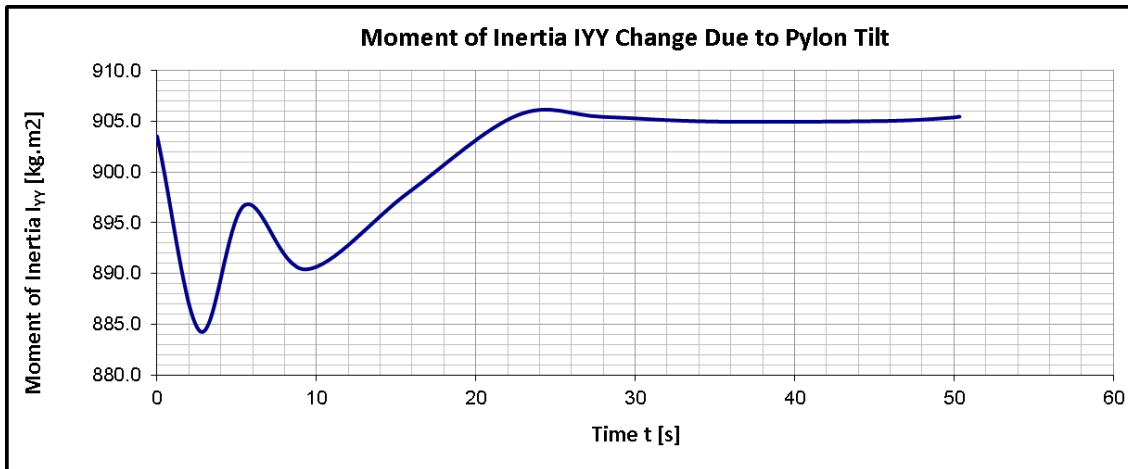
Parameter	Value
W_{GROSS}	737 kgf
W_{PYL}	238 kgf
$FS_{CG} _{\varphi=90^\circ}$	3.81 m
$WL_{CG} _{\varphi=90^\circ}$	1.04 m
FS_{NAC}	3.81 m
WL_{NAC}	1.27 m
FS_{PYL}	3.70 m
WL_{PYL}	1.50 m
$I_{YY} _{\varphi=90^\circ}$	905 kg.m ²
K_I	0.48 kg.m ² /deg
$\phi_M _{90^\circ}$	1.0 deg
$\phi_M _{0^\circ}$	0.0 deg

▪ Moment of Inertia I_{YY} and CG Displacement:

Table 9 - Inertia and balance data for I_{YY} and CG displacement.

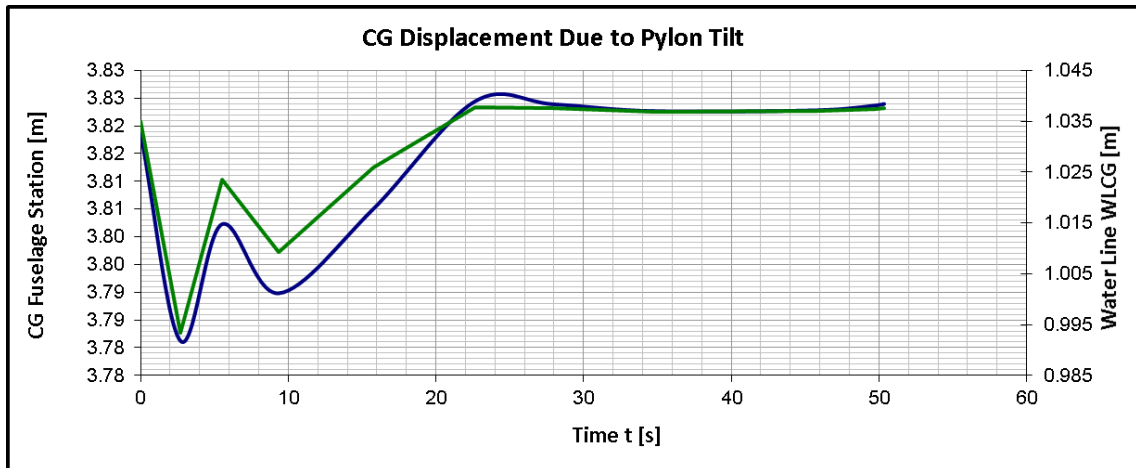
INERTIA AND BALANCE			
Time	Inertia and CG		
t (s)	$I_{YY}(\text{kg.m}^2)$	FS_{CG} (m)	WL_{CG} (m)
0.00	903.5	3.819	1.035
2.70	884.3	3.781	0.993
5.50	896.8	3.802	1.023
9.36	890.4	3.790	1.009
15.75	898.0	3.805	1.026
22.64	905.6	3.824	1.038
27.94	905.5	3.824	1.038
34.94	905.0	3.823	1.037
45.84	905.0	3.823	1.037
49.75	905.4	3.824	1.037
50.35	905.5	3.824	1.038

Figure 89 - Moment of inertia I_{YY} change due to pylon tilt.



Source: Created by the author using Microsoft Excel (MICROSOFT, 2013a).

Figure 90 - CG displacement due to pylon tilt.



Source: Created by the author using Microsoft Excel (MICROSOFT, 2013a).

5.2.4 Powerplant

- Constants:

Parameter	Value
K_0	1.6
K_1	0
K_2	0
K_3	0
K_4	0
l_M	0.711 m
$\eta_{POWCONT}$	98%
η_{MOTOR}	95%
$\eta_{GEARBOX}$	98%
R_D	1.0 m

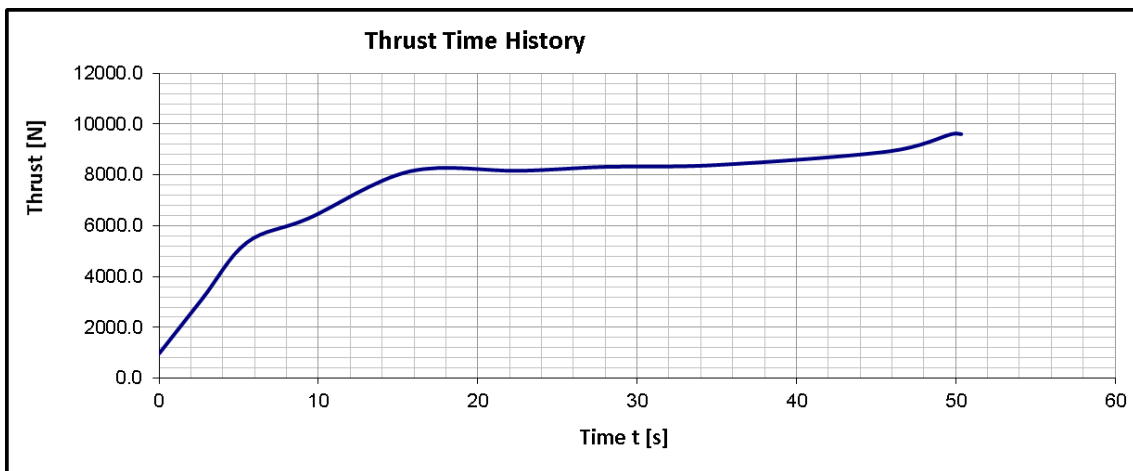
▪ Thrust, Power and Energy:

Table 10 - Thrust, power and energy.

POWERPLANT		
Time	Thrust and Power	
t(s)	T (N)	P _{BATT} (kW)
0.00	975.7	4.0
2.70	3124.3	83.8
5.50	5342.4	111.0
9.36	6292.4	158.9
15.75	8144.8	210.1
22.64	8164.6	205.1
27.94	8319.1	211.6
34.94	8391.4	214.6
45.84	8933.2	234.2
49.75	9611.0	263.4
50.35	9606.9	263.2

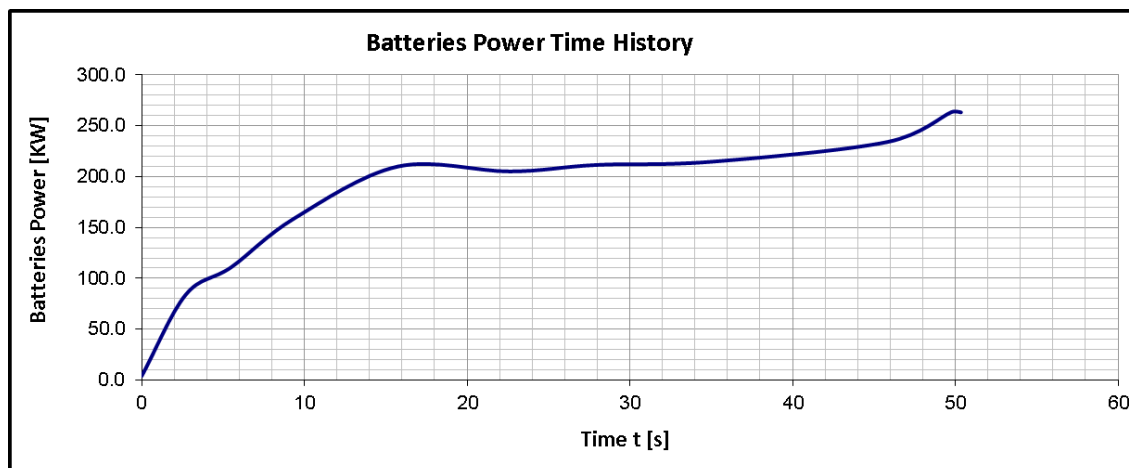
The total energy $\Delta E_T = 9116.20 \text{ KJ}$ is the minimum value of energy for the SFAP after optimization and trimming. The last step energy is calculated by means of a consideration that the aircraft is going to return from the last step attitude to a trimmed θ_F from $\dot{\theta} = 0.5 \text{ deg/s}$ to $\dot{\theta}_F$ with constant pitch acceleration and moved by a static power P_{0_BATT} .

Figure 91 – Total thrust time history



Source: Created by the author using Microsoft Excel (MICROSOFT, 2013a).

Figure 92 – Batteries power time history



Source: Created by the author using Microsoft Excel (MICROSOFT, 2013a).

5.2.5 Fuselage Aerodynamics

- Constants:

Parameter	Value
FS_F	3.72 m
WL_F	1.07 m
L_{LANG}	0 m ²
D_{LANG}	0.012 m ²
L_{BFO}	0 m ²
D_{BFO}	0 m ²
M_{BFO}	0 m ³

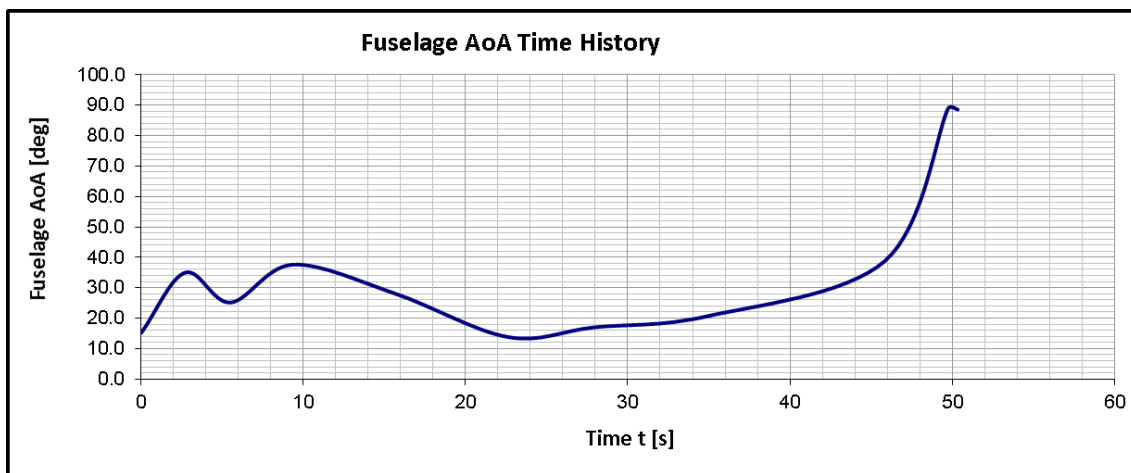
Table 11 - Fuselage AoA, lift, drag and pitching moment.

FUSELAGE AERODYNAMICS				
Time AoA, Lift, Drag and Pitching Moment				
t (s)	α_F (deg)	L_F (N)	D_F (N)	$M_{F CA}$ (N.m)
0.00	15.2	383.4	88.82	386.08
2.70	35.0	372.9	222.16	173.30
5.50	25.2	177.6	66.70	88.18
9.36	37.6	117.1	75.33	46.07

Table 11 - Fuselage AoA, lift, drag and pitching moment (CONCLUDED).

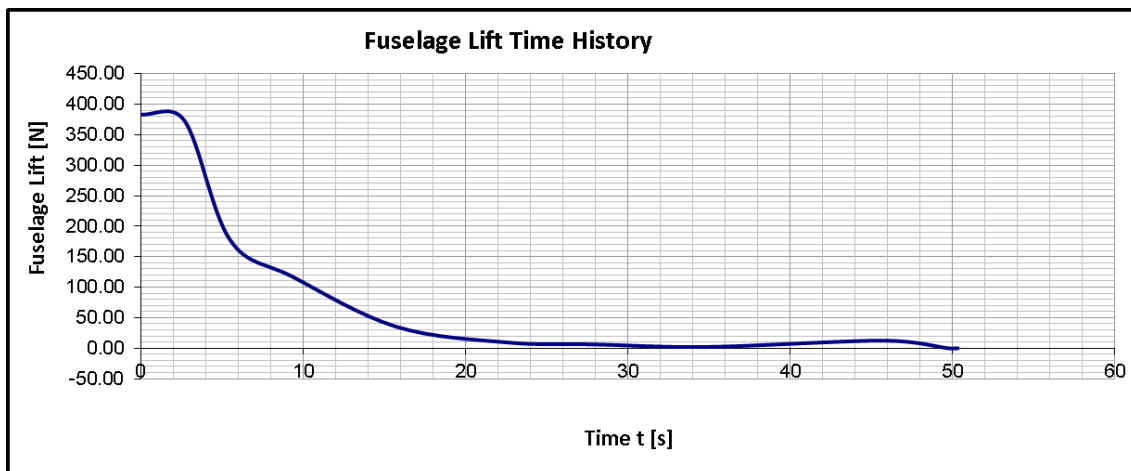
FUSELAGE AERODYNAMICS				
Time	AoA, Lift, Drag and Pitching Moment			
t (s)	α_F (deg)	L_F (N)	D_F (N)	$M_{F CA}$ (N.m)
15.75	27.9	35.2	15.86	15.98
22.64	13.8	9.4	1.96	9.60
27.94	17.0	6.3	1.63	5.98
34.94	20.7	2.2	0.67	1.65
45.84	38.8	12.5	8.30	4.57
49.75	88.8	0.0	0.00	0.00
50.35	88.5	0.0	0.00	0.00

Figure 93 – Fuselage AoA time history



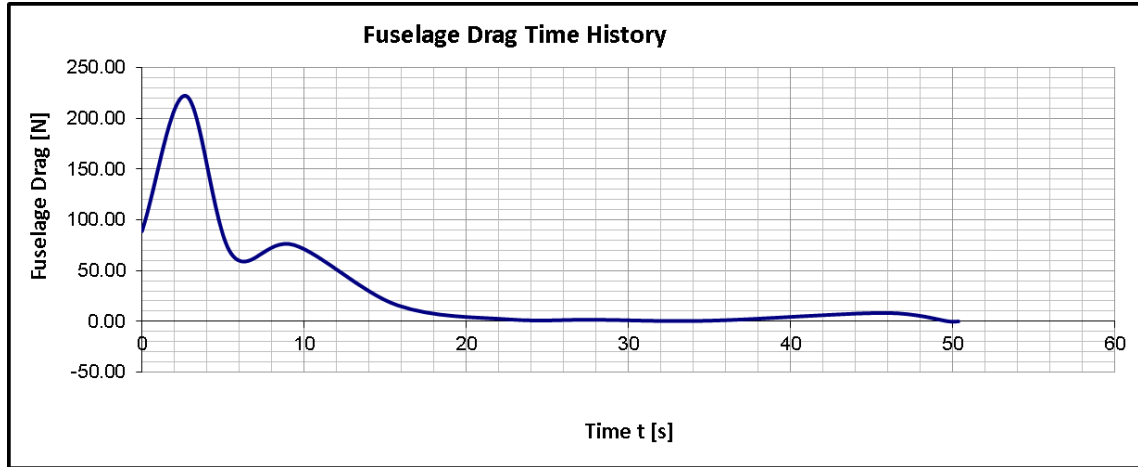
Source: Created by the author using Microsoft Excel (MICROSOFT, 2013a).

Figure 94 – Fuselage lift time history



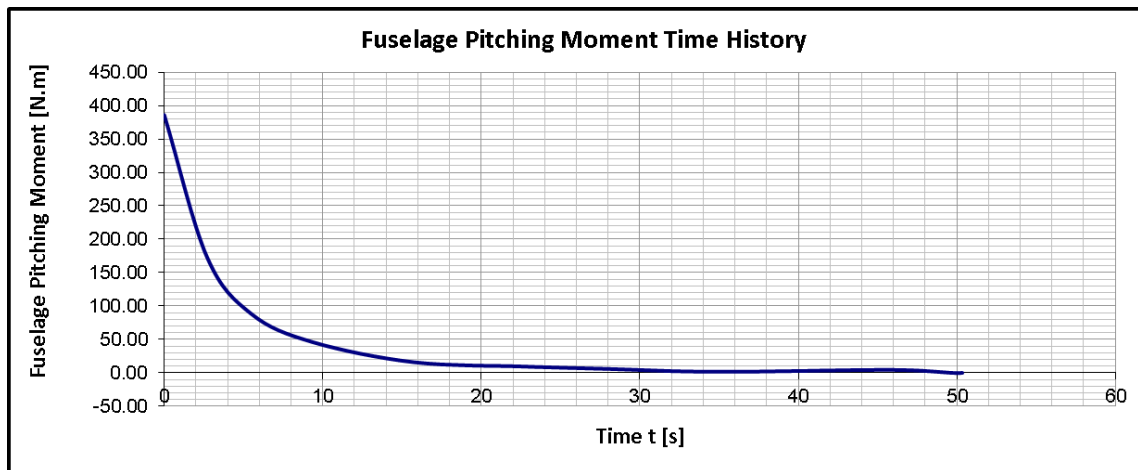
Source: Created by the author using Microsoft Excel (MICROSOFT, 2013a).

Figure 95 – Fuselage drag time history



Source: Created by the author using Microsoft Excel (MICROSOFT, 2013a).

Figure 96 – Fuselage pitching moment time history



Source: Created by the author using Microsoft Excel (MICROSOFT, 2013a).

5.2.6 Wing-Pylon Aerodynamics

- Constants:

Parameter	Value
FS_{WFS}	3.70 m
WL_{WFS}	1.22 m
FS_{WTE}	4.30 m
$\bar{\epsilon}$	0.485 m

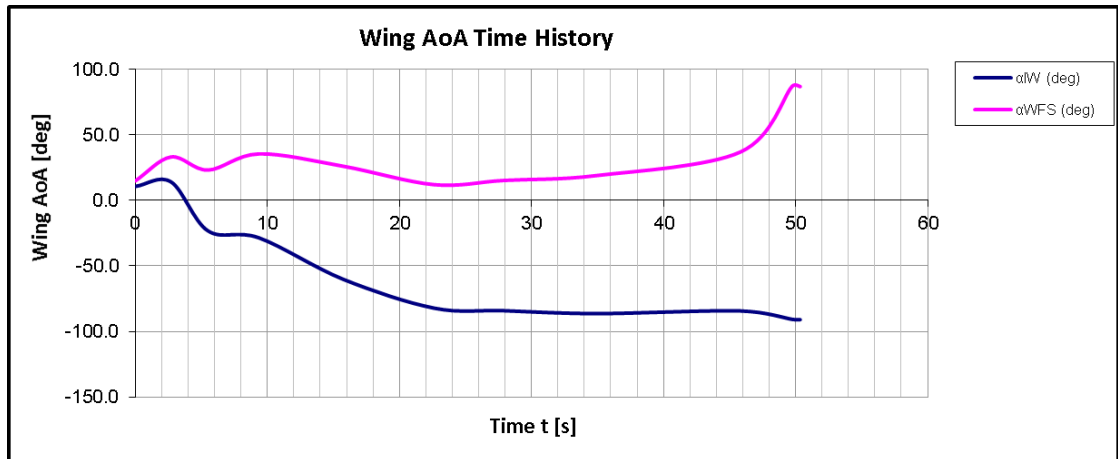
▪ Constants (CONCLUDED):

Parameter	Value
K_{RW}	3.0
K_{FW0}	1.4
K_{FWDF}	-0.0035 1/deg
K_{XRW}	0.26
X_{RW0}	0.0806
X_{RW1}	0.00003341
X_{RW2}	0.000007386
$SD/q _{\varphi=0}$	0.02 m ²
SD/q	0.12 m ²
S_W	4.204 m ²
c_W	0.80 m

Table 12 - Wing-Pylon AoA, lift, drag and pitching moment.

WING-PYLON AERODYNAMICS							
Time	AoA, Lift, Drag and Pitching Moment						
t (s)	α_{IW} (deg)	α_{WFs} (deg)	L_{IW} (N)	L_{WFs} (N)	D_{IW} (N)	D_{WFs} (N)	$M_{W CA}$ (N.m)
0.00	10.7	15.0	757.43	4282.03	311.97	1671.73	-262.77
2.70	14.2	33.2	0.00	2637.49	0.00	1377.96	-113.63
5.50	-23.2	23.2	0.00	1347.72	0.00	733.26	-74.92
9.36	-28.5	35.6	0.00	781.89	0.00	425.20	-25.01
15.75	-60.2	26.1	-508.60	188.28	725.73	108.99	-34.76
22.64	-82.2	12.1	-279.91	86.58	796.80	32.78	-47.17
27.94	-84.2	15.3	-216.68	50.59	884.89	20.69	-46.34
34.94	-86.3	19.0	-142.13	13.40	983.11	6.72	-46.02
45.84	-84.3	37.1	-208.90	53.58	1291.17	32.19	-46.14
49.75	-90.8	87.2	35.28	0.00	2074.72	0.00	-54.29
50.35	-91.0	86.9	45.42	0.00	2070.90	0.00	-54.21

Figure 97 – Wing AoA time history



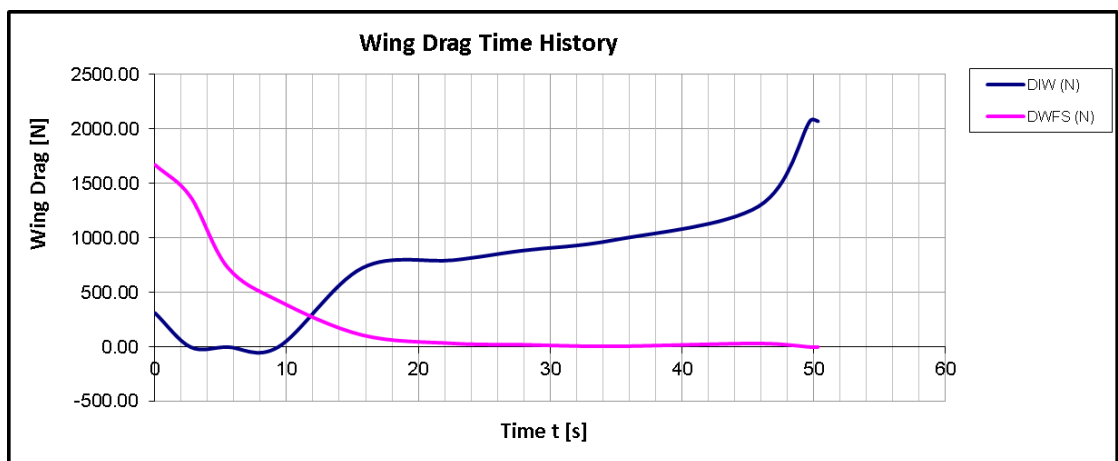
Source: Created by the author using Microsoft Excel (MICROSOFT, 2013a).

Figure 98 – Wing lift time history



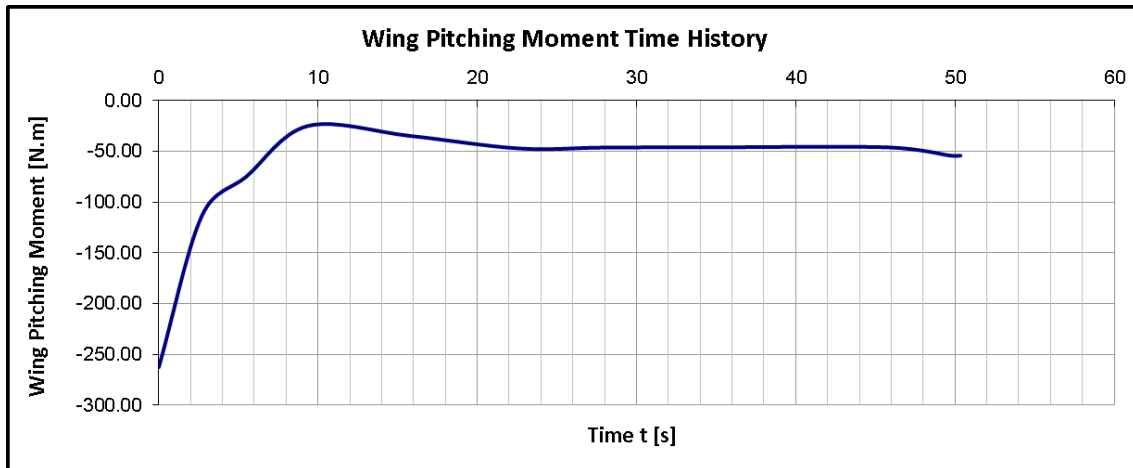
Source: Created by the author using Microsoft Excel (MICROSOFT, 2013a).

Figure 99 – Wing drag time history



Source: Created by the author using Microsoft Excel (MICROSOFT, 2013a).

Figure 100 – Wing pitching moment time history



Source: Created by the author using Microsoft Excel (MICROSOFT, 2013a).

5.2.7 Empennage Aerodynamics

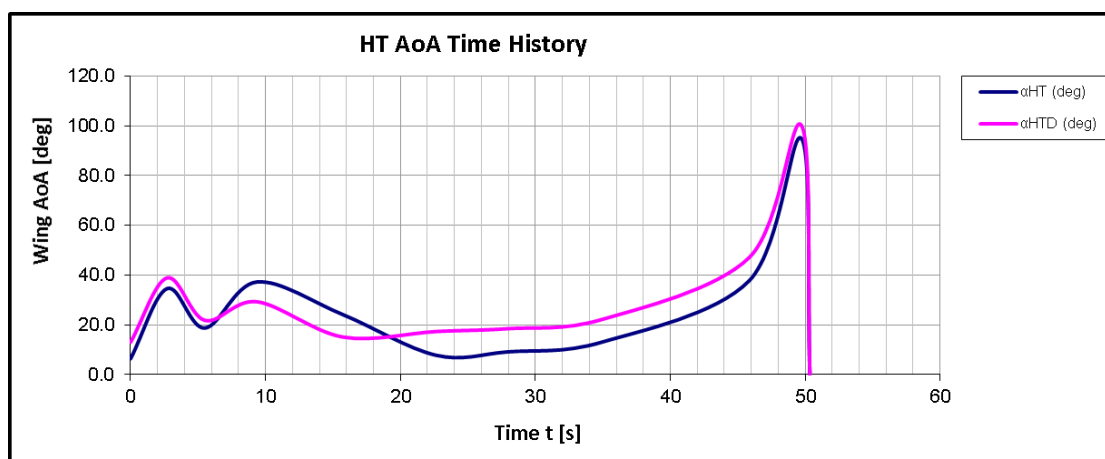
- Constants:

Parameter	Value
FS_{HT}	7.11 m
WL_{HT}	1.31 m
FS_{VT}	7.24 m
WL_{VT}	1.47 m
S_{HT}	1.17 m ²
S_{VT}	1.18 m ²
c_{HT}	0.60 m
i_{HT}	0 deg
τ_E	0.518
D_{KE}	0.24
K_{HNU}	0.8
D_{WB}	1.0
K_{VNU}	1.0
C_{MHT0}	0.0
C_{MHTA}	0.5
$C_{DV} _{\delta_R=0}$	0.0071

Table 13 - Empennage AoA, lift and Drag

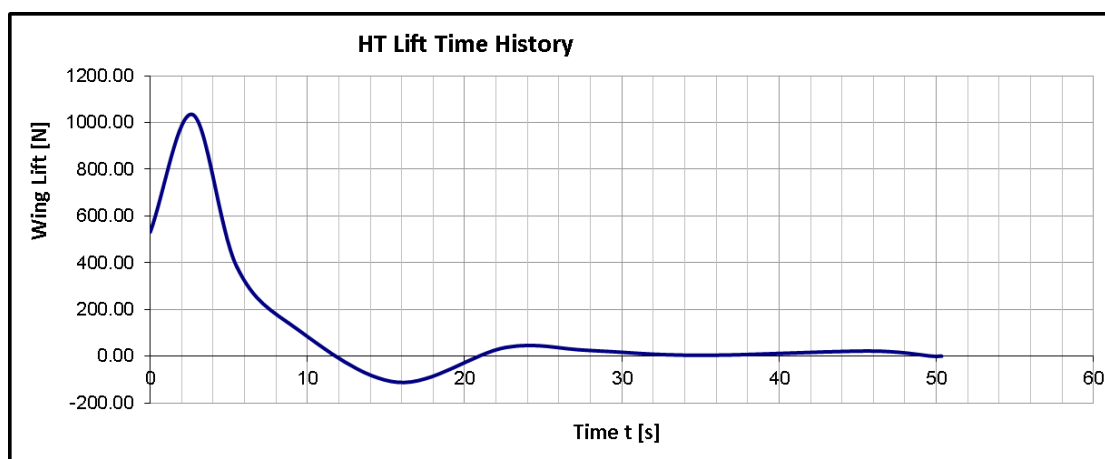
EMPENNAGE AERODYNAMICS						
Time AoA, Lift and Drag						
t (s)	α_{HT} (deg)	α_{HTD} (deg)	L_{HT} (N)	D_{HT} (N)	D_{VT} (N)	$M_{HT CA}$ (N.m)
0.00	6.4	13.0	531.45	48.66	2.28	1153.72
2.70	34.5	38.8	1034.27	296.26	-0.44	3933.96
5.50	18.7	21.8	383.43	70.59	-1.33	1501.54
9.36	37.2	29.2	115.00	58.94	0.47	1259.21
15.75	24.0	15.0	-111.85	4.71	0.47	325.93
22.64	7.7	17.3	37.78	3.44	0.26	56.04
27.94	9.1	18.4	24.50	2.14	0.14	34.90
34.94	13.0	22.1	3.63	1.00	0.04	14.11
45.84	37.7	47.0	21.99	10.37	0.12	131.02
49.75	94.7	99.9	0.00	0.00	0.00	0.01
50.35	0.0	0.0	0.00	0.00	0.00	0.00

Figure 101 – HT AoA time history



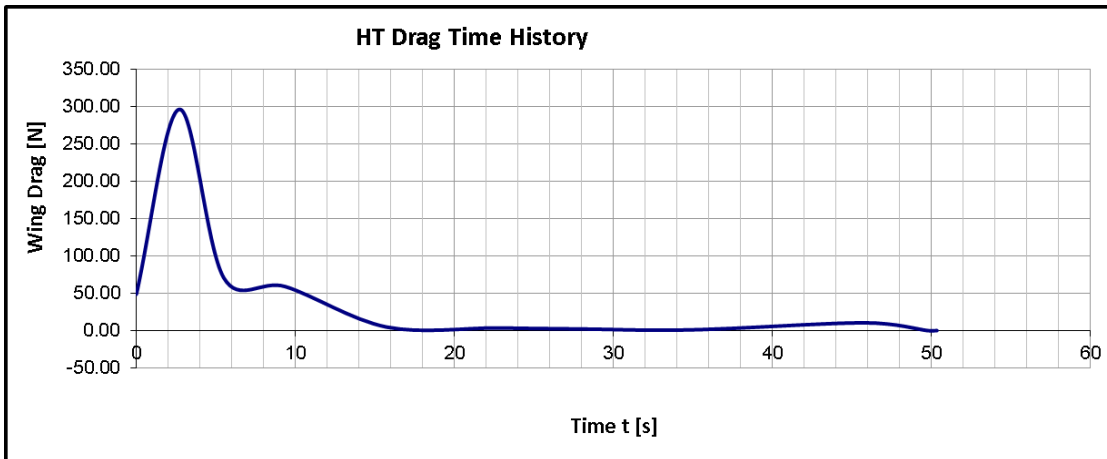
Source: Created by the author using Microsoft Excel (MICROSOFT, 2013a).

Figure 102 – HT lift time history



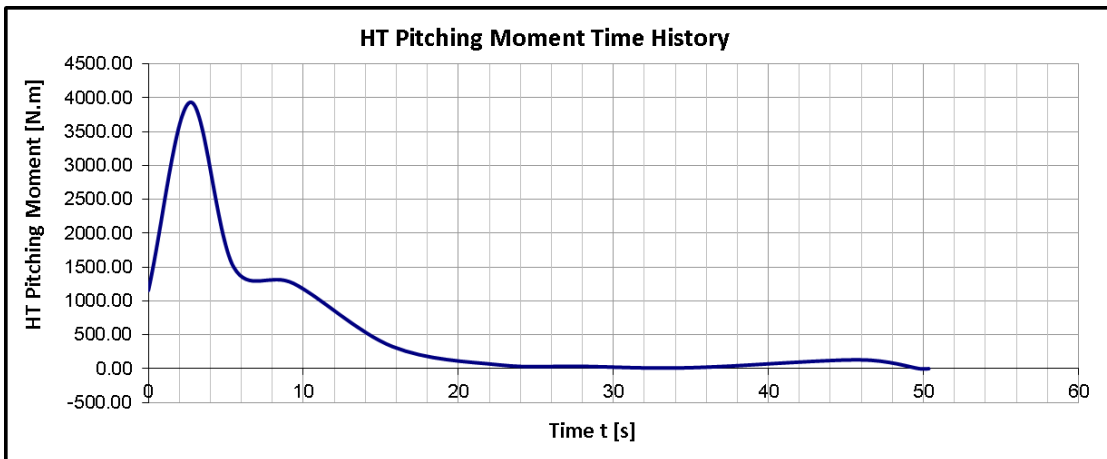
Source: Created by the author using Microsoft Excel (MICROSOFT, 2013a).

Figure 103 – HT drag time history



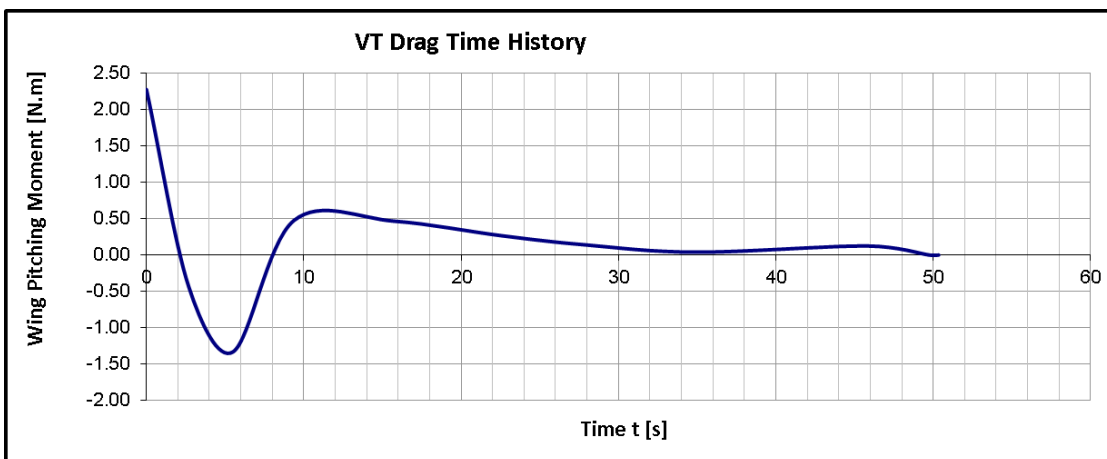
Source: Created by the author using Microsoft Excel (MICROSOFT, 2013a).

Figure 104 – HT pitching moment time history



Source: Created by the author using Microsoft Excel (MICROSOFT, 2013a).

Figure 105 – VT drag time history



Source: Created by the author using Microsoft Excel (MICROSOFT, 2013a).

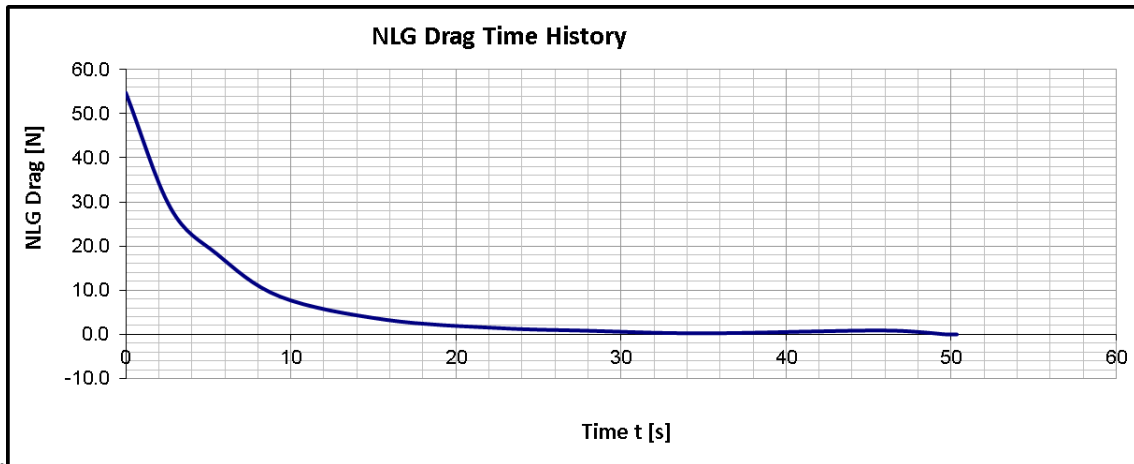
5.2.8 Landing Gears Aerodynamics

- Constants:

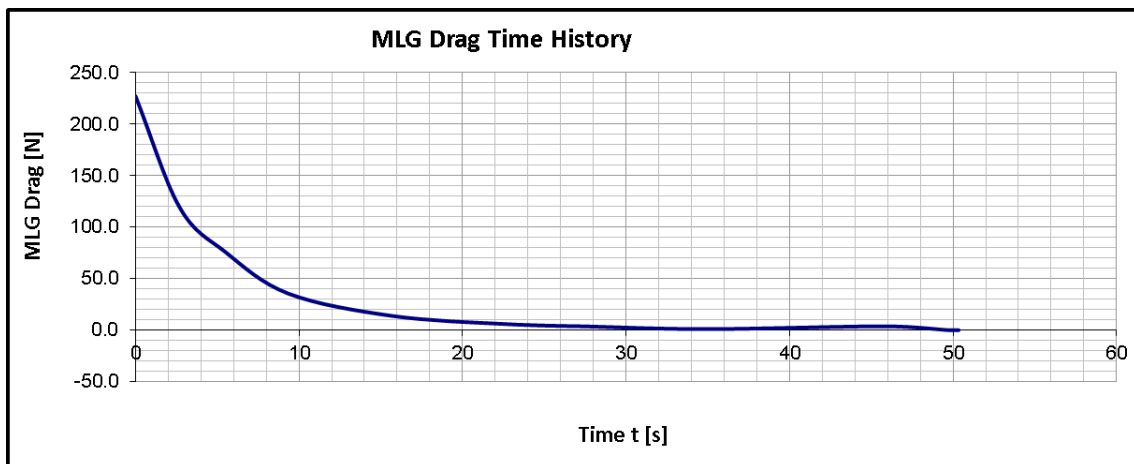
Parameter	Value
FS_{NG}	1.77 m
WL_{NG}	0.06 m
FS_{MG}	4.14 m
WL_{MG}	0.10 m
$D_{0_{NGD}}$	0.02 m ²
$D_{0_{MGD}}$	0.07 m ²
D_{POD}	0.03 m ²

Table 14 - Landing gears drag;

GEARS AERODYNAMICS		
Time	Drag	
t (s)	D _{NG} (N)	D _{MG} (N)
0.00	54.8	227.3
2.70	28.7	119.1
5.50	18.3	75.8
9.36	8.5	35.4
15.75	3.3	13.7
22.64	1.4	5.9
27.94	0.8	3.5
34.94	0.3	1.1
45.84	0.9	3.7
49.75	0.0	0.0
50.35	0.0	0.0

Figure 106 – NLG drag time history

Source: Created by the author using Microsoft Excel (MICROSOFT, 2013a).

Figure 107 – MLG drag time history

Source: Created by the author using Microsoft Excel (MICROSOFT, 2013a).

6 CONCLUSION

A full review of the current eVTOL designs, of the arising air taxi travel market and of fully electric powerplants was done. The seek for performance improvements tends to grow as the number of researches and designs in electric aviation rise and AEA might be a realistic option for global companies in the short and medium term.

The XV-15 project was worldwide disclosed after the sale of the Bell Helicopters design to NASA, and its aerodynamic data, available to the scientific community, was of major importance to the generic tiltrotor eVTOL mathematical model built. Most of it was gathered by means of wind-tunnel testing, with methodology for parameters identification in flight tests and, therefore, are extremely reliable and makes the aircraft dynamic model representative.

The creation of a totally electric powerplant enabled the computation of the energy expenditure using the engine deck of a real electric motor built-in the Pipistrel Taurus G4. Furthermore, the energy storage (batteries) and conversion system, electric power controller, gearbox and propeller were also considered in the power generation chain.

Results has shown high dependence on safety, comfort and design constraints, since there were possible solutions for the SFAP problem that are able to reduce significantly the energy spent throughout the flight path, but also overcome one or more of these constraints. The need to comply with restrictions, make it rather costly to accomplish the approach and landing task proposed.

Notwithstanding the performance improvement slightly different when trimming the model after optimization, the efforts were in the way of making the application of the methodology herein developed practicable, ready to be embedded to a real eVTOL FMS. Running the algorithm using machine learning instead of evaluating each GA individual directly in the generic tiltrotor model, was the key to turn a processing that could have taken days to complete into a less than 5 minutes optimizer.

In that way, every new trajectory computed by the FMS, can be previously optimized in order to promote low cost, safe and comfortable flights fulfilling the taxi travel market demand and contributing to a more green aviation.

Finally, there are opportunities for future works, such as:

1. Application of optimization for other flight phases such as level changes and takeoff;
2. Tests with other models, including independent motors and rotary wings;
3. Comparison between similar rotary wing and rotary thrust models;
4. Definition of an optimal trajectory, varying horizontal and vertical positions;
5. Implementation of a flight controller that follows the set of control variables proposed;
6. Construction of a small-scale conceptual design for eVTOL model integration with matching data obtained in flight trials for model refinement purposes.

REFERENCES¹²

- AIRBUS. **Vahana**. 2019b. Disponível em: <https://vahana.aero/>. Acesso em: 7 ago. 2019.
- AIRIS AEROSPACE. **AIRIS AEROSPACE**. 2019. Disponível em: www.airisaero.com. Acesso em: 29 jul. 2018.
- ALTAY GUVENIR, H.; UYSAL, I. Regression on feature projections. **Knowledge-Based Systems**, [S. l.], v. 13, n. 4, p. 207–214, 2000. DOI: 10.1016/S0950-7051(00)00060-5.
- ANDERSON JR., John D. Aircraft Performance and Design. *In*: Boston: WCB/McGraw-Hill, 1999. p. 157.
- ARDEMA, Mark D.; ASUNCION, Bryan C. Flight path optimization at constant altitude. *In*: **Springer Optimization and Its Applications**. [s.l: s.n.]. v. 33p. 21–32. DOI: 10.1007/978-0-387-95857-6_2.
- AUDET, Charles; DENNIS, J. Mesh Adaptive Direct Search Algorithms for Constrained Optimization. **SIAM Journal on Optimization**, [S. l.], v. 17, p. 188–217, 2006. DOI: 10.1137/060671267.
- AUDET, Charles; SAVARD, Gilles; ZGHAL, Walid. A mesh adaptive direct search algorithm for multiobjective optimization. **European Journal of Operational Research**, [S. l.], v. 204, n. 3, p. 545–556, 2010. DOI: 10.1016/j.ejor.2009.11.010.
- AURORA. **PAV - Passenger Air Vehicle**. 2019. Disponível em: <http://www.aurora.aero/pav-evtol-passenger-air-vehicle/>. Acesso em: 30 jun. 2018.
- BACCHINI, Alessandro; CESTINO, Enrico. Electric VTOL configurations comparison. **Aerospace**, [S. l.], v. 6, n. 3, p. 1–19, 2019. DOI: 10.3390/aerospace6030026. Disponível em: www.mdpi.com/journal/aerospace.
- BARTINI. **Bartini**. 2019. Disponível em: <https://bartini.aero/>. Acesso em: 2 jul. 2018.
- BOGLIETTI, A.; CAVAGNINO, A.; TENCONI, A.; VASCHETTO, S. The safety critical electric machines and drives in the more electric aircraft: A survey. *In*: IECON PROCEEDINGS

¹²According to Associação Brasileira de Normas Técnicas (ABNT NBR 6023).

(INDUSTRIAL ELECTRONICS CONFERENCE) 2009, **Proceedings** [...]. [s.l: s.n.] p. 2587–2594. DOI: 10.1109/IECON.2009.5415238.

BOLE, Michael; SVOBODA, Jaroslav. Design of a reconfigurable automated landing system for VTOL unmanned air vehicles. *In*: NATIONAL AEROSPACE AND ELECTRONICS CONFERENCE, PROCEEDINGS OF THE IEEE 2000, **Proceedings** [...]. [s.l: s.n.] p. 801–806. DOI: 10.1109/naecon.2000.894996.

CAO, Wenping; MECROW, Barrie C.; ATKINSON, Glynn J.; BENNETT, John W.; ATKINSON, David J. Overview of electric motor technologies used for more electric aircraft (MEA). **IEEE Transactions on Industrial Electronics**, [S. l.], v. 59, n. 9, p. 3523–3531, 2012. DOI: 10.1109/TIE.2011.2165453.

CARTER AVIATION TECHNOLOGIES. **Carter Copter**. 2019. Disponível em: <http://carteraero.com/home2/>. Acesso em: 29 jul. 2018.

CASTLES JR, W.; NEW, N. A Blade-Element Analysis for Lifting Rotors that is Applicable for Large Inflow and Blade Angles and Any Reasonable Blade Geometry. **NACA TN 2656**, [S. l.], 1952.

CHAMBERS, Joseph R. Modeling Flight: The Role of Dynamically Scaled Free-Flight Models in Support of NASA's Aerospace Programs. **Nasa Sp 2009-575**, Washington, D. C., p. 202, 2009.

COOKSON, G.; PISHUE, B. **INRIX Global Traffic Scorecard**. [s.l: s.n.]. Disponível em: <https://media.bizj.us/view/img/10360454/inrix2016trafficscorecarden.pdf>.

DARWIN, C. R. **On the origin of species by means of natural selection, or the preservation of favoured races in the struggle for life**. 1st. ed. London: John Murray, 1859.

DE MARCO, Agostino; DUKE, Eugene L.; BERNDT, Jon S. A general solution to the aircraft trim problem. *In*: COLLECTION OF TECHNICAL PAPERS - 2007 AIAA MODELING AND SIMULATION TECHNOLOGIES CONFERENCE 2007, **Proceedings** [...]. [s.l: s.n.] p. 792–831. DOI: 10.2514/6.2007-6703.

DEFESANET. **Embraer X Revela Primeiro Conceito do eVTOL**. 2018. Disponível em: <https://www.defesanet.com.br/embraer/noticia/29219/Embraer-X-Revela-Primeiro-Conceito-do-eVTOL/>. Acesso em: 6 ago. 2019.

DELOREAN AEROSPACE. **DR-7 VTOL**. 2018. Disponível em:

<http://www.deloreanaerospace.com/>. Acesso em: 1 jul. 2018.

DUFOUR. **Dufour Aerospace**. 2019. Disponível em: <https://dufour.aero/vision/>. Acesso em: 30 jul. 2018.

EIBEN, A. E.; SMITH, J. E. **Introduction to Evolutionary Computing**. 2nd. ed. Berlin: Springer-Verlag Berlin Heidelberg, 2015. DOI: 10.1007/978-3-662-44874-8.

EMBRAER. **EmbraerX**. 2019. Disponível em: <https://embraerx.embraer.com/global/en>. Acesso em: 29 jun. 2019. ETKIN, B.; REID, L. D. **Dynamics of flight: Stability and control**. 3rd. ed. New York: Wiley, 1995.

ETKIN, B.; REID, L. D. **Dynamics of flight: Stability and control**. 3rd. ed. New York: Wiley, 1995. 400 p.

FERGUSON, Samuel W. A Mathematical Model for Real Time Flight Simulation of a Generic Tilt-Proprotor Aircraft. **Nasa CR 166536**, Mountain View, California, p. 533, 1988.

G1. **Embraer mostra novo design de “carro voador” nos EUA**. 2019. Disponível em: <https://g1.globo.com/sp/vale-do-paraiba-regiao/noticia/2019/06/11/com-novo-design-carro-voador-da-embraer-vai-fazer-voos-de-teste-em-2020-nos-eua-e-australia.ghtml>. Acesso em: 5 ago. 2019.

HEPPERLE, Martin. **Electric Flight - Potential and Limitations**. German Aerospace Center: Institute of Aerodynamics and Flow Technology, Brunswick, 2012. DOI: STO-MP-AVT-209.

HOEHNER, Christine M.; BARLOW, Carolyn E.; ALLEN, Peg; SCHOOTMAN, Mario. Commuting distance, cardiorespiratory fitness, and metabolic risk. **American Journal of Preventive Medicine**, [S. l.], v. 42, n. 6, p. 571–578, 2012. DOI: 10.1016/j.amepre.2012.02.020.

HOLLAND, J. H. Genetic algorithms and the optimal allocation of trials. **SIAM J. of Computing**, [S. l.], v. 2, p. 88–105, 1973.

HOLLAND, J. H. **Adaptation in Natural and Artificial Systems: An Introductory Analysis with Applications to Biology, Control and Artificial Intelligence**. [s.l.] : MIT Press, 1992. 211 p.

INSIDENOVA. **Aurora Flight Sciences adding 135 jobs in Manassas**. 2019. Disponível em: https://www.insidenova.com/news/business/prince_william/aurora-flight-sciences-adding-jobs-in-manassas/article_86007e1a-90fc-11e8-abbc-5b1aa0e85ead.html. Acesso em: 22 mar.

2019.

JACOB, H. G. An Engineering Optimization Method with Application to Stol-Aircraft Approach and Landing Trajectories. **Nasa TN D-6978**, Mountain View, California, p. 43, 1972.

JAMES, Gareth; WITTEN, Daniela; HASTIE, Trevor; TIBSHIRANI, Robert. **An Introduction to Statistical Learning : with Applications in R**. New York: Springer, 2013. 426 p.

KENDOUL, F.; FANTONI, I.; LOZANO, R. Modeling and control of a small autonomous aircraft having two tilting rotors. **IEEE Transactions on Robotics**, [S. l.], v. 22, n. 6, p. 1297–1302, 2006. DOI: 10.1109/TRO.2006.882956.

KIM, B. M.; KIM, B. S.; KIM, N. W. Trajectory tracking controller design using neural networks for a tiltrotor unmanned aerial vehicle. **Proceedings of the Institution of Mechanical Engineers, Part G: Journal of Aerospace Engineering**, [S. l.], v. 224, n. 8, p. 881–896, 2010. DOI: 10.1243/09544100JAERO710.

KIMBERLIN, Ralph D. **Flight Testing Of Fixed-Wing Aircraft**. Blacksburg, Virginia: American Institute of Aeronautics and Astronautics, Inc., 2003. DOI: 10.2514/4.861840. 435 p.

LE DIGABEL, Sébastien. Algorithm 909: NOMAD: Nonlinear optimization with the MADS algorithm. **ACM Transactions on Mathematical Software**, [S. l.], v. 37, n. 4, p. 44:–44:15, 2011. DOI: 10.1145/1916461.1916468.

LILIUM. **Lilium**. 2019. Disponível em: <https://lilium.com/>. Acesso em: 1 jul. 2018.

MAISEL, M. D.; GIULIANETTI, D. J.; DUGAN, D. C. **The History of the XV-15 Tilt Rotor Research Aircraft from Concept to Flight**. Washington, D. C.: National Aeronautics and Space Administration, 2000.

MASON, Andrew J. OpenSolver - An Open Source Add-in to Solve Linear and Integer Programmes in Excel. In: OPERATIONS RESEARCH PROCEEDINGS 2012, **Proceedings** [...]. eds. Klatte, Diethard, Lüthi, Hans-Jakob, Schmedders, Karl, Springer Berlin Heidelberg [s.l.: s.n.] p. 401–406. DOI: 10.1007/978-3-642-29210-1_64. Disponível em: <http://opensolver.org>

MCCORMICK JR., Barnes W. **Aerodynamics of V/STOL Flight**. New York: Academic Press, Inc., 1967. 328 p.

MICROSOFT Office Professional Plus 2013: Microsoft Excel for Windows 2013. Versão

15.0.5153.1000. [S. l.]: Microsoft Corporation, 2013. Disponível em: microsoft.com.

MICROSOFT Office Professional Plus 2013: Microsoft PowerPoint for Windows 2013. Versão 15.0.5093.1000. [S. l.]: Microsoft Corporation, 2013. Disponível em: microsoft.com. **NASA**. 2018.

NASA. **NASA Technical Reports Server**. 2019. Disponível em: <https://www.nasa.gov/>. Acesso em: 27 jun. 2018.

NTU. **Pesquisa Mobilidade da População Urbana**. Brasília. Disponível em: <https://www.ntu.org.br/novo/upload/Publicacao/Pub636397002002520031.pdf>.

PARGETT, Douglas; ARDEMA, Mark. Flight Path Optimization at Constant Altitude. **Journal of Guidance Control and Dynamics**, [S. l.], v. 30, p. 1197–1201, 2007. DOI: 10.2514/1.28954.

PATTERSON, Michael D.; GERMAN, Brian J.; MOORE, Mark D. Performance analysis and design of on-demand electric aircraft concepts. *In*: 12TH AIAA AVIATION TECHNOLOGY, INTEGRATION AND OPERATIONS (ATIO) CONFERENCE AND 14TH AIAA/ISSMO MULTIDISCIPLINARY ANALYSIS AND OPTIMIZATION CONFERENCE 2012, **Proceedings** [...]. [s.l.: s.n.] p. 1–28. DOI: 10.2514/6.2012-5474.

PEREIRA, R. H. M.; SCHWANEN, T. Commute Time in Brazil (1992-2009): differences between metropolitan areas, by income levels and gender. Brasília: Instituto de Pesquisa Econômica Aplicada, 2015.

PICEK, Stjepan; JAKOBOVIC, Domagoj; GOLUB, Marin. On the recombination operator in the real-coded genetic algorithms. *In*: 2013 IEEE CONGRESS ON EVOLUTIONARY COMPUTATION, CEC 2013 2013, Cancun. **Proceedings** [...]. Cancun: IEEE, 2013. p. 3103–3110. DOI: 10.1109/CEC.2013.6557948.

RAYMER, D. P. **Aircraft Design A Conceptual Approach**. Washington, D. C.: American Institute of Aeronautics and Astronautics, Inc., 1992. 745 p.

ROSETO, J. A. et al. Moving towards a more electric aircraft. **IEEE Aerospace and Electronic Systems Magazine**, [S. l.], v. 22, n. 3, p. 3–9, 2007.

ROSETO, J. A.; ORTEGA, J. A.; ALDABAS, E.; ROMERAL, L. Moving towards a more electric aircraft. **IEEE Aerospace and Electronic Systems Magazine**, [S. l.], v. 22, n. 3, p. 3–9, 2007. DOI:

10.1109/MAES.2007.340500.

ROSKAM, J. **Airplane Flight Dynamics and Automatic Flight Controls. Part I.** 3rd. ed. Lawrence: DARcorporation, 2001. 576 p.

RSTUDIO. Versão 15.0.5093.1000. [S. l.]: Versão 1.3.959, 2019, Disponível em: <https://rstudio.com/>

SCRUCCA, L. GA: A Package for Genetic Algorithms in R. **Journal of Statistical Software**, [S. l.], v. 53, n. 4, p. 1–37, 2013. DOI: [doi:http://dx.doi.org/10.18637/jss.v053.i04](http://dx.doi.org/10.18637/jss.v053.i04).

SYSWERDA, G. Uniform crossover in genetic algorithms. *In*: 3RD INTERNATIONAL CONFERENCE ON GENETIC ALGORITHMS 1989, **Proceedings** [...]. [s.l: s.n.] p. 2–9.

TARIQ, M. et al. Aircraft batteries: current trend towards more electric aircraft. **IEEE Electrical Systems in Transportation**, [S. l.], v. 7, n. 2, p. 93–103, 2017. DOI: [doi:http://dx.doi.org/10.18637/jss.v053.i04](http://dx.doi.org/10.18637/jss.v053.i04).

TAYLOR, Charles E. Adaptation in Natural and Artificial Systems: An Introductory Analysis with Applications to Biology, Control, and Artificial Intelligence. Complex Adaptive Systems. John H. Holland. **The Quarterly Review of Biology**, Cambridge, v. 69, n. 1, p. 88–89, 1994. DOI: 10.1086/418447.

TECHNOLOGIES, ASX: Airspace Experience. **MOBi-ONE**. 2019. Disponível em: <https://www.iflyasx.com/>.

TOMAZIE, T.; PLEVNIK, V.; TOMAZIE, J.; POPIT, F.; KOLAR, V.; KIKELJ, R.; LANGELAAN, J.; MILES, K. Pipistrel Taurus G4: on Creation and Evolution of the Winning Aeroplane of NASA Green Flight Challenge 2011. **Journal of Mechanical Engineering**, [S. l.], v. 57, n. 12, p. 869–878, 2011. DOI: 10.5545/sv-jme.2011.212.

TORRES, R.; CHAPTAL, J.; BÈS, C.; HIRIART-URRUTY, J. B. Optimal, Environmentally Friendly Departure Procedures for Civil Aircraft. **Journal of Aircraft**, [S. l.], v. 48, n. 1, p. 11–22, 2011. DOI: 10.2514/1.C031012.

UBER. **UBER Elevate: Fast-Forwarding to a Future of On-Demand Urban Air Transportation**. 2016. Disponível em: <https://www.uber.com/elevate.pdf>.

VENTURI. **HopFlyt Venturi**. 2019. Disponível em: <http://hopflyt.com/>.

VERTICAL FLIGHT SOCIETY. **AirisOne**. 2019a. Disponível em: <https://evtol.news/airisone/>. Acesso em: 30 jun. 2018.

_____. **AirspaceX MOBi**. 2019b. Disponível em: <https://evtol.news/airspacex/>. Acesso em: 30 jul. 2018.

_____. **EVA X01**. 2019c. Disponível em: <https://evtol.news/eva-x01/>. Acesso em: 1 jul. 2018.

_____. **Wisk (Kitty Hawk) Cora**. 2019d. Disponível em: <https://evtol.news/kitty-hawk-cora/>.

VERTIPEDIA. **Vertipedia**. 2018. Disponível em: vertipedia.vtol.org. Acesso em: 27 jun. 2018.

WEIBERG, James A.; MAISEL, Martin D. **Wind-Tunnel Tests of the XV-15 Tilt Rotor Aircraft**. [s.l.: s.n.].

WISK. **Wisk**. 2019. Disponível em: <https://wisk.aero/>. Acesso em: 29 jun. 2018.

Table A- 3 - Rotor wake on horizontal stabilizer, $\frac{w_{i|R/H}}{w_i}$, $\phi = 60 \text{ deg}$.

Rotor Wake on Horizontal Stabilizer ($W_{i R/H}/W_i$)						
$\phi = 60 \text{ deg}$						
$W_{i R/H}/W_i$	V_T (kts)					
α_F (deg)	0 kt	20 kt	40 kt	60 kt	80 kt	100 kt
-180	0.000	0.000	0.000	0.000	0.000	0.000
-30	0.000	0.000	0.000	0.000	0.000	0.000
-28	0.000	-0.020	-0.030	-0.040	-0.050	-0.050
-24	0.000	-0.040	-0.060	-0.060	-0.100	-0.100
-20	0.000	-0.050	-0.080	-0.140	-0.150	-0.150
-16	0.000	-0.070	-0.150	-0.200	-0.260	-0.260
-12	0.000	-0.080	-0.200	-0.250	-0.380	-0.380
-8	0.000	-0.080	-0.220	-0.350	-0.440	-0.440
-4	0.000	-0.080	-0.260	-0.430	-0.480	-0.480
0	0.000	-0.080	-0.300	-0.450	-0.520	-0.520
4	0.000	-0.070	-0.300	-0.450	-0.600	-0.600
8	0.000	-0.060	-0.240	-0.300	-0.440	-0.440
12	0.000	-0.060	-0.150	-0.240	-0.280	-0.280
16	0.000	-0.040	-0.060	-0.100	-0.140	-0.140
20	0.000	0.000	0.000	0.000	0.000	0.000
180	0.000	0.000	0.000	0.000	0.000	0.000

NOTE: Rotor wake on horizontal stabilizer for $\phi = 30 \text{ deg}$ and $\phi = 0 \text{ deg}$ is null ($\frac{w_{i|R/H}}{w_i} = 0$).

Table A- 4 – Fuselage aerodynamics with angle of attack α_F

Concept Fuselage Aerodynamics with α_F			
α_F (deg)	L_α (m ²)	D_α (m ²)	M_α (m ³)
-90	0.00	2.69	2.37
-80	-0.14	2.60	1.66
-70	-0.33	2.51	0.96
-60	-0.42	2.32	0.25
-50	-0.46	1.86	-0.57
-40	-0.46	1.28	-1.27
-36	-0.44	1.05	-1.45
-32	-0.42	0.81	-1.56
-28	-0.39	0.58	-1.56
-24	-0.35	0.46	-1.52
-20	-0.25	0.36	-1.35
-16	-0.17	0.25	-1.31
-12	-0.08	0.14	-1.04
-8	0.00	0.07	-0.78
-4	0.08	0.04	-0.50
0	0.17	0.04	-0.24
4	0.25	0.04	0.03
8	0.34	0.05	0.30
12	0.42	0.09	0.44
16	0.50	0.13	0.50
20	0.59	0.18	0.47
24	0.65	0.23	0.34

Table A- 4 – Fuselage aerodynamics with angle of attack α_F (CONCLUDED).

Concept Fuselage Aerodynamics with α_F				
α_F (deg)	L_α (m ²)	D_α (m ²)	M_α (m ³)	
28	0.74	0.35	0.34	
32	0.84	0.46	0.47	
36	0.93	0.58	0.40	
40	1.00	0.70	0.34	
50	1.05	1.16	0.07	
60	0.93	1.63	-0.18	
70	0.81	1.86	-0.46	
80	0.58	2.09	-0.74	
90	0.00	2.21	-1.06	

Table A- 5 - Wing drag coefficient.

Wing-Pylon Drag Coefficient C_{DW}		
C_{DW} α_w (deg)	ϕ (deg)	
	$\phi = 0^\circ$	$\phi = 90^\circ$
-90	1.18	1.44
-80	1.1	1.33
-70	0.93	1.12
-60	0.705	0.91
-50	0.565	0.75
-40	0.43	0.54
-36	0.335	0.468
-32	0.245	0.405
-28	0.18	0.352
-24	0.13	0.31
-20	0.09	0.282
-16	0.065	0.263
-12	0.058	0.253
-8	0.076	0.267
-4	0.106	0.307
0	0.141	0.345
4	0.186	0.394
8	0.243	0.453
12	0.322	0.537
16	0.404	0.589
20	0.528	0.63
24	0.63	0.69
28	0.71	0.748
32	0.764	0.8
36	0.805	0.845
40	0.865	0.888
50	0.975	0.97
60	1.06	1.04
70	1.08	1.06
80	1.11	1.08
90	1.14	1.09

Table A- 6 - Wing lift coefficient.

Wing-Pylon Lift Coefficient C_{LW}			
C_{LW}	ϕ (deg)		
	α_w (deg)	$\phi = 0^\circ$	$\phi = 90^\circ$
	-90	0	0
	-80	-0.325	-0.245
	-70	-0.52	-0.4
	-60	-0.61	-0.48
	-50	-0.59	-0.42
	-40	-0.41	-0.265
	-36	-0.4	-0.25
	-32	-0.425	-0.26
	-28	-0.515	-0.3
	-24	-0.66	-0.38
	-21.5	-0.69	-0.44
	-21	-0.68	-0.44
	-20	-0.64	-0.395
	-19.2	-0.58	-0.36
	-16	-0.32	-0.165
	-12	0	0.0628
	-8	0.42	0.291
	-4	0.84	0.518
	0	1.18	0.749
	4	1.46	0.975
	8	1.7	1.205
	11	1.86	1.38
	12	1.92	1.433
	13.6	1.94	1.5
	16	1.79	1.4
	18.4	1.62	1.26
	20	1.51	1.2
	24	1.48	1.15
	28	1.54	1.2
	32	1.69	1.32
	36	1.76	1.41
	40	1.8	1.47
	50	1.8	1.47
	60	1.56	1.36
	70	1.2	1.08
	80	0.8	0.7
	90	0	0

Table A- 7 - Wing pitching moment coefficient.

Wing-Pylon C_{MW}	
C_{MW}	α_w (deg)
φ (deg)	$\alpha_w = ANY$
$\varphi = 0^\circ$	-0.17
$\varphi = 30^\circ$	-0.11
$\varphi = 60^\circ$	-0.06
$\varphi = 75^\circ$	-0.09
$\varphi = 90^\circ$	-0.11

Table A- 8 - Wing-pylon interference drag coefficient.

Wing-Pylon D_{PYINT}	
D_{PYINT} (m ²)	α_w (deg)
φ (deg)	$\alpha_w = ANY$
$\varphi = 0^\circ$	0.023
$\varphi = 5^\circ$	0.079
$\varphi = 10^\circ$	0.132
$\varphi = 15^\circ$	0.186
$\varphi = 20^\circ$	0.244
$\varphi = 25^\circ$	0.279
$\varphi = 30^\circ$	0.302
$\varphi = 35^\circ$	0.308
$\varphi = 40^\circ$	0.311
$\varphi = 45^\circ$	0.314
$\varphi = 60^\circ$	0.314
$\varphi = 75^\circ$	0.314
$\varphi = 90^\circ$	0.314
$\varphi = 95^\circ$	0.314

Table A- 9 - Wing Wake Deflection Angle on HT with α_w and φ .

Wing Wake Deflection Angle on HT with α_w and φ					
$\epsilon_{W/HOGE}$					
α_w (deg)	$\varphi = 0^\circ$	$\varphi = 30^\circ$	$\varphi = 60^\circ$	$\varphi = 75^\circ$	$\varphi = 90^\circ$
-90	0	0	0	0	0
-16	0	0	0	0	0
-12	0.95	0	0	0.7	1.47
-8	2.54	1.78	1.3	2.4	3.03
-4	3.92	3.38	2.9	4.1	4.59
0	5.4	4.98	4.5	5.8	6.15
4	6.88	6.58	6.1	7.5	7.71
8	8.26	8.18	7.7	9.2	9.27
12	8.9	9.2	8.9	10.4	9.8
16	8.8	9.5	9.1	10.8	9.7
20	7.3	8.4	8.1	9.8	8
24	4.8	5.5	5.5	6.4	5
28	0	0	0	0	0
90	0	0	0	0	0

Table A- 12 - Dynamic pressure ratio at the HT, rotors ON, $\varphi = 60$ deg

Dynamic Pressure Ratio at the Horizontal Stabilizer (η_{HT}), Rotors ON						
$\varphi = 60$ deg						
η_H	V_T (kts)					
α_F (deg)	0 kt	20 kt	40 kt	60 kt	80 kt	100 kt
-180	1.00	1.00	1.00	1.00	1.00	1.00
-40	1.00	1.00	1.00	1.00	1.00	1.00
-30	1.00	1.00	1.00	1.00	1.00	1.00
-28	1.00	1.00	1.00	1.00	1.00	1.00
-24	1.00	1.00	1.00	1.00	1.00	1.00
-20	1.00	1.00	1.00	1.00	1.00	1.00
-16	1.00	1.00	1.00	1.00	1.00	1.00
-12	1.00	1.00	1.00	1.00	1.00	1.00
-8	1.00	1.00	1.00	1.00	1.00	1.00
-4	1.00	1.00	1.00	1.00	1.00	1.00
0	1.00	1.00	1.00	1.00	1.00	1.00
4	1.00	1.00	1.00	1.00	1.00	1.00
8	1.00	1.00	1.00	1.00	1.00	1.00
12	1.00	1.00	1.00	1.00	1.00	1.00
16	1.00	1.00	1.00	1.00	1.00	1.00
20	1.00	1.00	1.00	1.00	1.00	0.80
30	1.00	1.00	1.00	1.00	1.00	1.00
180	1.00	1.00	1.00	1.00	1.00	1.00

Table A- 13 - Dynamic pressure ratio at the HT, rotors ON, $\varphi = 30$ deg

Dynamic Pressure Ratio at the Horizontal Stabilizer (η_{HT}), Rotors ON						
$\varphi = 30$ deg						
η_H	V_T (kts)					
α_F (deg)	0 kt	20 kt	40 kt	60 kt	80 kt	100 kt
-180	1.00	1.00	1.00	1.00	1.00	1.00
-40	1.00	1.00	1.00	1.00	1.00	1.00
-30	1.00	1.00	1.00	1.00	1.00	1.00
-28	1.00	1.00	1.00	1.00	1.00	1.00
-24	1.00	1.00	1.00	1.00	1.00	1.00
-20	1.00	1.00	1.00	1.00	1.00	1.00
-16	1.00	1.00	1.00	1.00	1.00	1.00
-12	1.00	1.00	1.00	1.00	1.00	1.05
-8	1.00	1.00	1.00	1.00	1.00	1.05
-4	1.00	1.00	1.00	1.00	1.00	1.05
0	1.00	1.00	1.00	1.00	1.00	1.05
4	1.00	1.00	1.00	1.00	1.00	1.05
8	1.00	1.00	1.00	1.00	1.00	1.05
12	1.00	1.00	1.00	1.00	1.00	1.05
16	1.00	1.00	1.00	1.00	1.00	1.05
20	1.00	1.00	1.00	1.00	1.00	0.80
30	1.00	1.00	1.00	1.00	1.00	1.00
180	1.00	1.00	1.00	1.00	1.00	1.00

Table A- 14 - Dynamic pressure ratio at the HT, rotors ON, $\varphi = 0 \text{ deg}$

Dynamic Pressure Ratio at the Horizontal Stabilizer (η_{HT}), Rotors ON						
$\varphi = 0 \text{ deg}$						
η_H	V_T (kts)					
α_F (deg)	0 kt	20 kt	40 kt	60 kt	80 kt	100 kt
-180	1.00	1.00	1.00	1.00	1.00	1.00
-40	1.00	1.00	1.00	1.00	1.00	1.00
-30	1.00	1.00	1.00	1.00	1.00	1.00
-28	1.00	1.00	1.00	1.00	1.00	1.00
-24	1.00	1.00	1.00	1.00	1.00	1.00
-20	1.00	1.00	1.00	1.00	1.00	1.00
-16	1.00	1.00	1.00	1.00	1.00	1.00
-12	1.00	1.00	1.00	1.00	1.00	1.00
-8	1.00	1.00	1.00	1.00	1.00	1.00
-4	1.00	1.00	1.00	1.00	1.00	1.00
0	1.00	1.00	1.00	1.00	1.00	1.00
4	1.00	1.00	1.00	1.00	1.00	1.00
8	1.00	1.00	1.00	1.00	1.00	1.00
12	1.00	1.00	1.00	1.00	1.00	1.00
16	1.00	1.00	1.00	1.00	1.00	1.00
20	1.00	1.00	1.00	1.00	1.00	0.80
30	1.00	1.00	1.00	1.00	1.00	1.00
180	1.00	1.00	1.00	1.00	1.00	1.00

Table A- 15 - Elevator Effectiveness factor X_{KE} .

Elevator Effectiveness Factor (X_{KE})	
M_N	X_{KE}
0	1
0.2	1
0.4	0.965
0.5	0.95
0.6	0.93
0.7	0.9

Table A- 16 - M_N effect on $\delta\varepsilon_{W/H} / \delta\alpha_{WFS}$.

M_n Effect on $\delta\varepsilon_{W/H} / \delta\alpha_{WFS}$	
M_N	PCPM
0	0.0799
0.2	0.0799
0.4	0.0856
0.5	0.0905
0.6	0.0994

Table A- 17 - HT lift coeficiente C_{LHT} .

HT Lift Coefficient C_{LHT}							
C_{LHT}	δ_E (deg)						
α_{HT} (deg)	-20 °	-15 °	-10 °	0 °	10 °	15 °	20 °
-180	-0.8	-0.6	-0.4	0	0.4	0.6	0.8
-170	-0.1	-0.1	0.3	0.7	1.1	1.3	1.5
-160	-0.1	0.08	0.28	0.6	0.95	1.13	1.3
-150	-0.04	0.16	0.39	0.84	1.2	1.35	1.45
-140	0	0.2	0.48	0.98	1.38	1.49	1.6
-130	0.03	0.22	0.5	0.99	1.36	1.43	1.54
-120	0.04	0.2	0.46	0.86	1.15	1.23	1.3
-110	0.04	0.16	0.38	0.66	0.9	0.96	1
-100	0.04	0.1	0.24	0.4	0.5	0.56	0.6
-90	0	0	0	0	0	0	0
-80	-0.6	-0.58	-0.56	-0.425	-0.36	-0.285	-0.22
-70	-0.92	-0.89	-0.865	-0.72	-0.6	-0.49	-0.38
-60	-1.12	-1.09	-1.06	-0.9	-0.77	-0.64	-0.51
-50	-1.24	-1.205	-1.175	-1.002	-0.89	-0.745	-0.6
-40	-1.3	-1.26	-1.24	-1.05	-0.96	-0.8	-0.64
-36	-1.3	-1.26	-1.24	-1.04	-0.92	-0.775	-0.63
-32	-1.29	-1.255	-1.23	-1.03	-0.89	-0.735	-0.6
-28	-1.28	-1.24	-1.21	-1.01	-0.84	-0.68	-0.56
-24	-1.26	-1.22	-1.185	-0.98	-0.78	-0.615	-0.5
-20	-1.235	-1.198	-1.16	-0.93	-0.69	-0.5	-0.42
-18.4	-1.24	-1.21	-1.2	-0.92	-0.66	-0.54	-0.48
-17.5	-1.25	-1.25	-1.26	-0.93	-0.71	-0.565	-0.45
-16.8	-1.31	-1.29	-1.31	-0.99	-0.74	-0.55	-0.42
-16	-1.33	-1.33	-1.4	-1.12	-0.71	-0.51	-0.38
-15.6	-1.35	-1.38	-1.44	-1.1	-0.7	-0.48	-0.35
-14.2	-1.45	-1.55	-1.4	-1.0082	-0.61	-0.4	-0.27
-12.5	-1.6	-1.49	-1.31	-0.8875	-0.48	-0.28	-0.15
-12	-1.60318	-1.464375	-1.26025	-0.852	-0.44375	-0.239625	-0.10082
8	-0.18318	-0.044375	0.15975	0.568	0.97625	1.180375	1.311918
12	0.10082	0.239625	0.44375	0.852	1.25	1.42	1.5
12.2	0.11502	0.253825	0.45795	0.8662	1.27	1.43	1.48
13	0.17182	0.310625	0.51475	0.923	1.3	1.37	1.45
15	0.29	0.45	0.65	1	1.2	1.27	1.36
16	0.32	0.475	0.69	0.98	1.16	1.24	1.32
16.8	0.34	0.49	0.7	0.94	1.15	1.2	1.32
18	0.37	0.5	0.68	0.89	1.13	1.22	1.34
20	0.38	0.465	0.6	0.88	1.18	1.28	1.38
24	0.33	0.455	0.66	0.935	1.3	1.38	1.44
28	0.38	0.5	0.73	1	1.37	1.44	1.5
32	0.4	0.54	0.78	1.05	1.43	1.49	1.54
36	0.41	0.56	0.82	1.08	1.47	1.535	1.57
40	0.41	0.57	0.84	1.1	1.51	1.56	1.59
50	0.36	0.56	0.83	1.09	1.5	1.56	1.59
60	0.29	0.45	0.63	0.88	1.15	1.22	1.26
70	0.2	0.3	0.42	0.62	0.78	0.8	0.83
80	0.1	0.16	0.21	0.34	0.4	0.41	0.42
90	0	0	0	0	0	0	0
100	-0.6	-0.56	-0.5	-0.4	-0.24	-0.1	-0.04
110	-1	-0.96	-0.9	-0.66	-0.38	-0.16	-0.04

Table A- 17 - HT lift coeficiente C_{LHT} (CONCLUDED).

HT Lift Coefficient C_{LHT}							
C_{LHT}	δ_E (deg)						
α_{HT} (deg)	-20 °	-15 °	-10 °	0 °	10 °	15 °	20 °
120	-1.3	-1.23	-1.15	-0.86	-0.46	-0.2	-0.04
130	-1.45	-1.43	-1.36	-0.99	-0.5	-0.22	-0.03
140	-1.6	-1.49	-1.38	-0.98	-0.48	-0.2	0
150	-1.45	-1.35	-1.2	-0.84	-0.39	-0.16	0.04
160	-1.3	-1.13	-0.95	-0.6	-0.28	-0.08	0.1
170	-1.5	-1.3	-1.1	-0.7	-0.3	-0.1	0.1
180	-0.8	-0.6	-0.4	0	0.4	0.6	0.8

Table A- 18 - HT drag coefficient C_{DHT} .

HT Drag Coefficient C_{DHT}	
C_{DHT}	δ_E (deg)
α_{HT} (deg)	0 °
-180	0.01
-170	0.02
-160	0.2
-150	0.4
-140	0.55
-130	0.67
-120	0.78
-110	0.85
-100	0.89
-90	0.92
-80	0.91
-70	0.87
-60	0.81
-50	0.72
-40	0.6
-36	0.54
-32	0.47
-28	0.39
-24	0.3
-20	0.2
-16	0.115
-12	0.068
-8	0.035
-4	0.015
0	0.00875
4	0.015
8	0.035
12	0.068
16	0.115
20	0.2
24	0.34
28	0.48
32	0.61
36	0.72
40	0.8

Table A- 18 - HT drag coefficient C_{DHT} (CONCLUDED).

HT Drag Coefficient C_{DHT}	
C_{DHT}	δ_E (deg)
α_{HT} (deg)	0 °
50	0.93
60	1.05
70	1.14
80	1.06
90	1.2
100	1.19
110	1.14
120	1.06
130	0.96
140	0.8
150	0.6
160	0.36
170	0.02
180	0.01

Table A- 19- Sidewash Factor ($1 - \delta\sigma/\delta\beta_F$).

Sidewash Factor ($1 - \delta\sigma/\delta\beta_F$)					
$(1 - \delta\sigma/\delta\beta_F)$	φ (deg)				
α_F (deg)		0	30	60	90
-90		1.000	1.000	1.000	1.000
-10		1.000	1.000	1.000	1.000
-3		1.070	1.020	1.065	1.315
0		0.984	0.945	1.100	1.228
7		0.982	1.030	1.025	0.890
13		0.842	0.915	0.884	0.535
28		1.000	1.000	1.000	1.000
90		1.000	1.000	1.000	1.000

Table A- 20 - Rotor sidewash factor $K_{\beta R}$.

Rotor Sidewash Factor $K_{\beta R}$	
$K_{\beta R}$	β_F (deg)
V_T (kts)	0
0	1.00
20	1.00
40	-0.50
60	0.20
80	0.50
100	0.75
120	1.00

APPENDIX B – VBA codes for tiltrotor model

Figure B- 1 - Functions F1 and F2 in wing area and CP location calculation.

```
Function F1_Siw (ByVal Siw As Double, ByVal C1 As Double, ByVal C2 As Double, ByVal Rwx  
As Double, ByVal Rwy As Double, ByVal CDEL As Double)
```

```
    Dim A1 As Double
```

```
    A1 = F_A1(C1, C2, Rwx, Rwy, CDEL)
```

```
    F1_Siw = Siw + A1
```

```
End Function
```

```
Function F1_Xa (ByVal Xa As Double, ByVal C1 As Double, ByVal C2 As Double, ByVal Rwx  
As Double, ByVal CDEL As Double, ByVal Frw As Double)
```

```
    Dim XA1 As Double
```

```
    XA1 = F_XA1(C1, C2, Rwx, CDEL, Frw)
```

```
    F1_Xa = Xa + XA1
```

```
End Function
```

```
Function F2_Siw (ByVal Siw As Double, ByVal C1 As Double, ByVal C2 As Double, ByVal Rwx  
As Double, ByVal Rwy As Double, ByVal CDEL As Double, ByVal Frw As Double, ByVal SDEL  
As Double)
```

```
    Dim A1 As Double
```

```
    A1 = F_A1(C1, C2, Rwx, Rwy, CDEL)
```

```
    F2_Siw = Siw + (1 / 2) * (A1 + Frw * SDEL * (C2 ^ 2 - C1 ^ 2))
```

```
End Function
```

```
Function F2_Xa (ByVal Xa As Double, ByVal C1 As Double, ByVal C2 As Double, ByVal Rwx  
As Double, ByVal CDEL As Double, ByVal Frw As Double, ByVal SDEL As Double)
```

```
    Dim XA1 As Double
```

```
    XA1 = F_XA1(C1, C2, Rwx, CDEL, Frw)
```

```
    F2_Xa = Xa + (1 / 2) * XA1 + (1 / 3) * Frw * SDEL * (C2 ^ 3 - C1 ^ 3)
```

```
End Function
```

Figure B- 2 - Auxiliary Functions in wing area and CP location calculation.

```
Function F_Tci (ByVal Ci As Double, ByVal Rwx As Double)
```

```
    F_Tci = WorksheetFunction.Asin(Ci / Rwx)
```

```
End Function
```

```
Function F_A1 (ByVal C1 As Double, ByVal C2 As Double, ByVal Rwx As Double, ByVal Rwy  
As Double, ByVal CDEL As Double)
```

```
Dim Tc1, Tc2 As Double
```

```
    Tc1 = F_Tci(C1, Rwx)
```

```
    Tc2 = F_Tci(C2, Rwx)
```

```
    F_A1 = Rwx * Rwy * CDEL * (Sin(Tc2) * Cos(Tc2) - Sin(Tc1) * Cos(Tc1) + Tc2 - Tc1)
```

```
End Function
```

```
Function F_XA1 (ByVal C1 As Double, ByVal C2 As Double, ByVal Rwx As Double, ByVal  
CDEL As Double, ByVal Frw As Double)
```

```
    F_XA1 = (-2 / 3) * Frw * CDEL * ((Rwx ^ 2 - C2 ^ 2) ^ 1.5 - (Rwx ^ 2 - C1 ^ 2) ^ 1.5)
```

```
End Function
```

Source: Created by the author